SYNCHRONOUS IMPULSE NETWORKS

by

Chee-Cheon Chui

A Dissertation Presented to the
FACULTY OF THE GRADUATE SCHOOL
UNIVERSITY OF SOUTHERN CALIFORNIA
In Partial Fulfillment of the
Requirements for the Degree
DOCTOR OF PHILOSOPHY
(ELECTRICAL ENGINEERING)

August 2005

DEDICATION

To my Mom,

whose love and sacrifices I can nolonger reciprocate.

To my Family,

Chee-Yong, Siew-Choon, Yuit-Meng, Chee-Kong, Kah-Yam, Yee-Chin, How-Yee

without them, I would not have chosen to continue until here.

ACKNOWLEDGEMENTS

It has been a long and arduous journey. I am glad to have arrived at this stage of acknowledging the people who have help me tremendously along the way.

I would like to thank my thesis advisor, Prof. Scholtz, whose guidance is crucial to the completion of this piece of research. He has given me enormous freedom to explore different ideas and exercise great patient in correcting my mistakes. Prof. Scholtz has contributed immensely to my intellectual and professional maturity.

I would also like to thank members of my thesis committee, Prof. Chugg and Prof. Haas, who despite their busy schedule, take the times to be in the committee. I am indebted to their commitment and support.

There is a poignant story behind the title of this thesis and I should start the narration from the spring of 2002 when I returned to Los Angeles after having obtained a M.Sc. degree from USC in the previous spring. I was already in the PhD program then and was preparing for my PhD screening exam. I was also on the lookout for a suitable research topic. I did not remember the exact sequence of events, but I vividly remembered on the night or a day after I first discussed with Prof. Scholtz on the possibilities of synchronizing a network of wireless nodes using UWB signals, I received a phone call from my family members. They told me that my Mom had a heart attack and was warded in the intensive care unit of a hospital. I boarded a plane on the night of Feb 4, 2002 (LA time) and after spending two nights with my Mom next to her hospital bed, we have our last breakfast together on the morning of Feb 8, 2004 (Singapore time). It seems to be fated that in lieu of the two years that I was away from Home between spring 2000 and spring 2002, I was given two nights to be with my Mom. These were the precious last two nights of her life.

This work is dedicated to my Mom, and the title of this thesis, "Synchronous Impulse Networks", the acronym - SIN, has the same spelling as her last name.

Life is a journey and it can only go forward, a friend once advice 'you can never turn back the clock'. This work, despite its intention of synchronizing a network of clocks, will tell you that you

can only synchronize the timing of the future and "initial offsets" between clocks is a quantity of the past.

When I was very young, life was financially difficult. I still remembered there were meals consisting of only rice and soya-sauce (a kind of dark sweet sauce that is commonly used to season food in Chinese cooking). There were nights I kept myself awake, looking at the door, hoping my Dad would come home soon and to tell us that he had found a job for tomorrow. He was an odd-job laborer. There were many disappointing moments or I may have fallen asleep before he was back? My Dad passed away when I was twelve.

To us, education is the way forward in order to be out of the poverty trap. I believe my Mom and Dad would be very happy (if in where they are now, they somehow gotten to know about it) that their youngest son is finishing his PhD study soon. And the PhD degree will be from an "angmoh" (a Chinese dialect referring to people of European descents) country.

Without my family members: my eldest brother Chee-Yong, sis-in-law Siew-Choon, sis Yuit-Meng, elder brother Chee-Kong, sis-in-law Kah-Yam, niece Yee-Chin and nephew How-Yee, I would not have chosen to continue until here. Their care, love, encouragement and support are the sources of my strength, my perseverance and provide me with the motivations that have kept me going.

I must also thank my superiors in DSO, Mr. Yio-Puar Sng and Mr. Hee-Siah Bay who have given me all the supports that they can, especially during the time when I was mourning my Mom passed-away. Last but not least, I am indebted to the DSO National Laboratories, Singapore who has sponsored my post-graduate study in USC. The human-resource personnel in DSO have reminded me an important fact of life when they withdrew the overseas allowances due to me when I requested to be back in Singapore to rest my pain during the summer of 2002.

TABLE OF CONTENTS

LIST OF TABLES AND FIGURES

ABBREVIATIONS

AGC	Automatic Gain Control loop
HM	Hierarchical Master-slave
LS	Least Squares
LoS	Line-of-Sight
ML	Maximum Likelihood
MU	Mutually Synchronous
NLoS	Non-Line-Of-Sight
PSD	Power Spectral Density
SIN	Synchronous Impulse Network
SM	Single-Master
SNR	Signal-to-Noise-Ratio
TDMA	Time Divisional Multiple Access
ToA	Time-of-Arrival
UWB	Ultra Wideband
i.i.d.	independently identically distributed
p.d.f.	probability density function
p.r.r.	pulse repetition rate

ABSTRACT

A synchronous impulse network (SIN) is defined to be a network of spatially distributed wireless nodes employing UWB impulse transceivers whose oscillators are "ticking" at the same time/phase. In this research, the ultra-wide bandwidth of UWB signals is exploited to provide high resolution timing synchronization. The network node in the proposed synchronization scheme measures the time-of-arrival (ToA) of UWB monocycles transmitted from other nodes in the network. The measured ToAs are impaired by additive channel noise, oscillator phase noise and may correspond to ToA of signal arrived via non-line-of-sight (NLoS) propagation. To perform time transfer between network nodes, the designated master node transmits frame-synchronization pulses to slave nodes to align slaves' oscillator frame repetition rate with that of master. This is followed by two-way ranging using the master as the transponder to mitigate signal propagation delay. This allows a node in the SIN to estimate, from the measured ToAs, the initial offset differences between itself and the master nodes. It is assumed that the UWB monocycles occupy all the available bandwidth and network nodes transmit UWB impulses only in pre-assigned time slots. Thus the proposed synchronization scheme uses only one physical channel for time transfer and logical channels are formed via time division multiplexing. The 'roving' master concept for time transfer, whereby each node takes a turn as the master node, is also proposed in this research. The main objective of roving the network's nodes is to overcome blockages to network signal propagation paths and to extend the coverage of the synchronous network. The roving masters form either the mutually synchronous (MU) or hierarchical master-slave (HM) time transfer network architectures and their performances are compared with a single-master time-transfer architecture (SM).

CHAPTER I

INTRODUCTION

1.1 Introduction

A synchronous impulse network (SIN) is defined to be a network of distributed wireless nodes employing ultra-wideband (UWB) impulse transceivers whose oscillators are "ticking" at the same time/phase. In this research, the ultra-wide bandwidth of UWB signals is exploited to provide high resolution timing synchronization. It is assumed that the UWB monocycles occupy all the available system bandwidth. Noting that the ultra-wide bandwidth makes frequency division approaches spectrally inefficient especially when there are many nodes in the network. Therefore in the proposed synchronization scheme, nodes in the network are allowed to transmit UWB impulses only at pre-assigned time slots. In this setting, only one physical channel is utilized for time transfer and logical channels are formed via time division multiplexing.

The nodes in the SIN measure the time-of-arrival (ToA) of UWB monocycles from other nodes in the network in the presence of additive channel noise and oscillators' phase noise. The received signal may have arrived via a non-line-of-sight (NLoS) propagation path. To perform time transfer, the master node in the proposed synchronization scheme transmits/broadcasts frame synchronization pulses to slave nodes to align slaves' oscillator frame repetition rate with that of master. This is followed by two-way ranging with the master as the transponder to mitigate signal propagation delay. By measuring the ToAs of the frame-synchronization and ranging pulses, individual node in the SIN is able to explicitly estimate the frame frequency and initial offset differences between its oscillator and other oscillators in the network. The estimated frame frequency and initial offset differences are then used to correct the node's frame-rate oscillator.

The 'roving' master concept is devised in this research with the intention to extend the geographical coverage of the SIN and to overcome blockages to network signal propagation paths. In the roving master approach, each node takes a turn as the master node. The roving masters are used to form either the mutually synchronous (MU) or hierarchical master-slave (HM) time transfer network architectures and their performances are compared with a single-master-to-multiple-slaves time-transfer architecture (SM). This research is envisioned primarily for transceivers with a UWB physical layer, which has gained wide spread interest in academia and industry in recent years.

1.1.1 Motivations

The motivation of this research is to realize a synchronous impulse network (SIN) for applications such as wireless sensor networks [15], array beam forming, reach-back communication [23] and co-operative geo-locationing utilizing UWB impulse transceivers.

While there already exist synchronization algorithms such as those described in [5], [7], [39], [53], [58] and a review paper, [34] to synchronize the timing of a distributed network, most of them utilize narrowband wireless transceivers. Wireless devices utilizing ultra wide-band (UWB) impulses for their radio interfaces are commonly believed to possess the following advantages:

(a) The narrow pulses provide fine time resolution,

(b) the UWB impulse system has the ability to resolve multipath, and therefore has less susceptibility to fading [69] and

(c) the signal energy spreads over an ultra-wide spectrum, hence providing these signals with covert transmission properties such as low probability of intercept and detection (LPI/LPD).

Further, it is pointed out in [58] that a propagation channel that can be characterized easily is pivotal to good practical performance for time-transfer systems. In most channels envisioned, UWB transceivers sending sufficiently narrow impulses do not suffer adversely from inter-pulse

interference, and therefore are likely to perform better than conventional carrier based continuous narrowband systems which are often degraded by inter-symbol interference.

We are also aware of at least two concerted efforts to develop sensor networks using UWB technology [22], [24]. One common reason cited in these commercial UWB developments is the ability to produce UWB transceivers with small 'form factor'[1]. It is argued that UWB transceiver can be build consisting of 'only a UWB transmit/receive chip, UWB antenna, digital baseband processor and embedded firmware and protocols that drive the digital baseband processor'. As a result, fewer components are needed compared to 'carrier based technology that must modulate and demodulate a complex analog carrier waveform.' [http://www.pulselink.net/ov_history.html]

Unlike most recent works such as [17] and [23], which ignored signal propagation delay, this research incorporates signal propagation time into the system model to be analyzed. Ignoring the effect of signal propagation delay unnecessarily restricts the accuracy of time-transfer techniques. The timing bias introduces as a result of ignoring signal propagation delay is in the order of $(\text{distance between nodes})/3\times10^{8}$ sec, which is significant relative to the width of the UWB monocycle. For example, a signal propagation distance of 10 meters represents a delay of $10\times3\times10^{-8}=300$ nanoseconds. Since a UWB monocycle is typically of sub-nanosecond pulse width, the full potential of UWB impulses to provide high timing resolution is not being fully exploited if the effect of propagation delay is not being mitigated.

1.1.2 Network Time Transfer Approaches

Network time transfer has been a much-researched topic since the 1960s [34]. Recently, [7] highlights the importance of network synchronization in large-scale telecommunication system

[1] According to Webopedia encyclopedia on computer technology (http://www.webopedia.com/), form factor refers to the physical size and shape of a device. It is often used to describe the size of circuit boards.

applications. The works cited in [34] provide a mathematical model of the synchronization problem in a distributed network and address the stability of the network. Most modern communication systems are deployed in a networked fashion. With new capabilities introduced by UWB signals, there is interest to analyze the performance of a synchronous network consisting of UWB transceivers.

Reference [23] utilizes UWB impulses to synchronize nodes uniformly placed in a square region. The propagation delay is ignored as the area covered by the network is assumed to be small.

The various synchronization approaches mentioned in the literature are utilized for sensor networks [15], [16], [17], the Global Positioning System (GPS) [60], TDMA in satellite communications [20], and the Network Time Protocol (NTP) [46] utilized in the Internet. Reference [58] details the one-way, common-view and two-way time transfer techniques. A scheme to synchronize a CDMA mobile network is described in [39]. References [15], [16], [17] proposed a principle of time transfer and labeled it as 'post-facto synchronization' and described a time transfer scheme, referred to as Reference Broadcast System (RBS), for wireless sensor networks. The RBS ignores propagation delay.

Under the broad topic of network synchronization, which includes computer network synchronization, there exist other techniques such as 'bit stuffing' and 'elastic store' [5]. These techniques are not to be confused with the subject of this research, which concerns itself with effects of 'transmission jitter and wander' (a terminology borrowed from [5]) in synchronizing wireless nodes.

1.1.3 Overview

We take a system specific approach here, i.e., we start by restricting ourselves to using UWB impulses and the ultra-wide bandwidth of such signals naturally suggests a Time Division Multiple Access (TDMA) scheme for communications in the network. We then proceed to analyze the timing performance of the network attained using the proposed synchronizing scheme. The proposed scheme is a combination of one-way synchronization from the master node to the slave nodes followed by

two-way ranging using the master as the transponder. In [34] and many references therein, time transfer is performed using a phase-locked-loop to acquire the timing of the received carrier-based narrowband signals. Here, the ToA of the transmitted monocycle at the receiver is measured explicitly. These measured ToAs are used to derive estimates of the differences in initial offset and frame frequency between nodes in the network. In addition, our work differs from [34] in the sense that, besides measuring ToA explicitly, there is only one physical channel for time transfer among nodes in the network and logical channels are formed via time division multiplexing. To the best of our knowledge, the effect of channelization by time-multiplexing on the performance of time synchronization has not been addressed in the open literature.

A timing detector [11] that correlates the received signal with a reference signal generated at the receiver is used to measure the ToA. We considered four major sources of impairments to the measurement of the ToA. They are additive noise (e.g. receiver noise), oscillator phase noise, multipath self-interference and NLoS measurements that give a positive bias to the ToA readings [31]. For UWB impulses fully utilizing the FCC indoor spectral mask, the bias on the ToA measurements attributed to multipath self interference is assumed negligible [12].

We seek to place a bound on the achievable timing resolution, which includes the effects of oscillators' time drift and impairments mentioned in the previous paragraph.

Chapter 1 introduces the time function, which defines the time observed by individual network nodes. It is followed by defining the objective of the time transfer/synchronization in this research. Chapter 2 is devoted to measuring the relative ToA of UWB monocycles at the receiver in the presence of additive noise and disturbances. Chapter 3 describes the proposed time synchronization scheme to transfer clock information between a pair of network nodes. Chapter 4 extends the time synchronization scheme to synchronize a network of nodes using various network time transfer architectures. In Chapter 5, the timing errors for different time transfer architectures are formulated. Chapter 6 details the results and observations obtained from computer simulations of the various network time transfer architectures and conclusions are presented in Chapter 7.

1.2 System Model

The system model comprises the timing function that describes the time observed by the transceiver. Throughout this work, we assume that there exists a reference source (time standard) that tells the 'true time' denoted by t. This allows us to describe the time observed by individual transceiver at epoch t relative to the standard time scale [46].

The timing function of a transceiver is a function of its oscillator's initial offset, drift and phase noise. At the same epoch t, each transceiver will read a different time on its clock and time intervals will be of different durations because of differences in their oscillator initial offset and drift. There are also random timing errors between transceivers as a result of oscillator phase noise.

The received and reference signals are defined after the timing function. The reference signal is used to correlate with the received signal to derive the timing difference between the transmitter and the receiver. The system model is completed with a description of the nth order derivative of a Gaussian curve, which is used to model the received UWB monocycle waveform.

1.2.1 Timing Function

It is assumed that the oscillator at each node/transceiver is described by a sinusoid of the form

$$\mathsf{Y}(t)=\mathsf{A}(t)\sin(\Phi(t)), \tag{1.1}$$

where $\mathsf{A}(t)$ and $\Phi(t)$ are the instantaneous amplitude and total phase function of the oscillator respectively with variable t representing the true time. The timing function is assumed to be a function of the oscillator instantaneous phase, and is defined as

$$T(t)=\frac{\Phi(t)}{\omega_o}, \tag{1.2a}$$

where ω_o is the oscillator's nominal frequency. The timing function (1.2a) maps the total phase of the oscillator onto an observable time axis, i.e., the time that is observed by the transceiver. Following [36] and [42], the imperfect timing function generated by the oscillator of transceiver m is modeled as

$$T^{(m)}(t)=\breve{a}^{(m)}(t)-\breve{d}^{(m)}-\breve{\phi}^{(m)}(t)\,, \tag{1.2b}$$

where

$$\breve{a}^{(m)}(t)=\sum_{v=1}^{V}\frac{\breve{a}_v^{(m)}t^v}{v!}\,, \tag{1.2c}$$

is a function of the deterministic parameters of the oscillator and the random timing term is

$$\breve{\phi}^{(m)}(t)=\frac{\breve{\varphi}^{(m)}(t)-\breve{\varphi}^{(m)}(0)}{\omega_o}\,. \tag{1.2d}$$

The parameter $\breve{a}_v^{(m)}$ characterizes the drift of the oscillator. In particular, $(\breve{a}_1^{(m)}-1)$ is known as the normalized settability and $\breve{a}_2^{(m)}$ the normalized drift rate of oscillator m ([42] pp. 134, 139). In [1], $(\breve{a}_1^{(m)}-1)$ is defined as the frequency offset (or skew) and $\breve{a}_2^{(m)}$ the frequency drift.

The random phase jitter of the oscillator[2] is denoted by $\breve{\varphi}^{(m)}(t)$. And $\breve{\phi}^{(m)}(t)$, in unit of seconds, is the random timing jitter at time t. An oscillator is said to be perfect if its timing function is given by $T^{(m)}(t)=t-\breve{d}^{(m)}$.

In equations (1.2a) to (1.2d) and in subsequent analysis, the superscript in parenthesis $(\circ)^{(m)}$ is used to denote transceiver m, and takes on values in the set {m,s} when it is used to denote a pair of transceivers: the master 'm' and slave 's', or {1,2,3,4,…,N} when denoting a particular transceiver in a network of N transceivers. The index '1' is used to refer to the master node when more than one slave is needed to describe the SIN. The oscillator timing function is illustrated in Fig. 1.

[2] The phase jitter is also known as the oscillator's short-term instabilities and has zero mean.

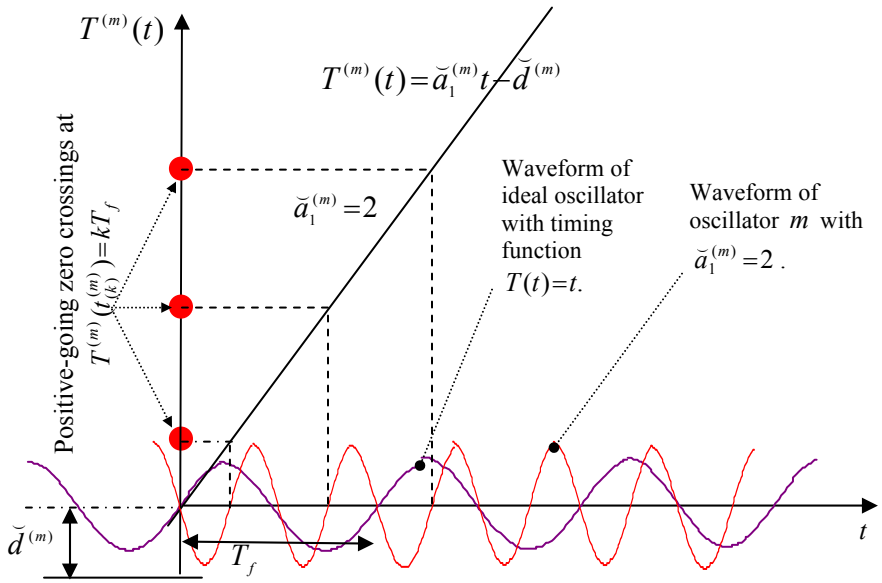

Figure 1: Illustration of oscillator timing function showing the sinusoidal waveforms generated by the transceivers' oscillator on the horizontal axis as a function of t. The vertical axis is the time observed by transceiver m. In this example, assuming the nominal frequency of oscillators is T_f, since $\breve{a}_1^{(m)}=2$, oscillator m makes two complete oscillations during which the ideal oscillator completes one oscillation.

1.2.2 Drift of Oscillator

An oscillator, being a physical device, is known to drift because of aging and external environmental factor. The aging of an oscillator is 'the systematic change in frequency with time due to internal changes in the oscillator'[3]. While the drift of an oscillator refers to 'the systematic change in frequency with time'. The authors of [65] further state that:

[3] This definition in [65] is taken from the glossary of terms and definitions (1990) of the International Radio Consultative Committee (CCIR), now known as the ITU-R.

'*Drift is due to aging plus changes in the environment and other factors external to the oscillator. Aging, not drift, is what one denotes in a specification document and what one measures during oscillator evaluation. Drift is what one observes in an application.*'

In this research, following [65], the drift of an oscillator refers to oscillator aging plus deviations from ideal that arises from external environmental factors.

A highly accurate, precise and stable oscillator with low jitter/variance is desirable for timing purposes. From [65], an accurate oscillator is described as one whereby its frequency of oscillation agrees with its stated values with a high "degree of correctness". The precision of an oscillator is the 'extent to which a given set of measurements of one sample agrees with the mean of the set'. Finally, stability describes 'the amount something changes as a function of parameters such as time, temperature, shock, and the like'.

When a radio network requires accurately aligned clocks, it must perform time transfer periodically to align the timing functions of different oscillators if

a) an accurate, precise and stable oscillator may not be readily available or costly, or

b) aging or environment factors may cause underlying physical properties, e.g. oscillation frequency, of the oscillator to change.

In subsequent analysis, it is assumed that $\breve{a}_v^{(m)} = 0$ for $v > 1$, $\forall m$. This assumption is also stated in the review paper [56] on time synchronization in sensor networks, and utilized in other works [27], [39] and [55] on network time synchronization. The references [27], [39] and [56] did not specify specific reasons for ignoring drift higher than the first order. However, in [55], it is said that the frequency of an oscillator can be assumed to be constant for a period of time in the order of minutes and hours. In [34], when analyzing the behavior of time synchronous network in the presence of channel noise, a "steady" state is assumed whereby the frequency of the oscillator has a constant time-independent mean.

From [42], the drift of oscillators due to aging is in the order of 10^{-10} per day, while oscillators reported in [49] have aging rate ranging from 10^{-9} to 10^{-11} per day. Therefore if time

transfer is performed over a short period of time, e.g. in the order of milliseconds, it is reasonable to assume that the frequency of the oscillator remains constant during time transfer such that $\breve{a}_v^{(m)}=0$ for $v>1$ and $\breve{a}_1^{(m)}$ is a constant parameter to be estimated. This is similar to the steady state assumption invoked in [34]. For this assumption to hold true, it is also necessary to assume that drift induced by external factors, e.g. temperature changes, is not severe. Thus the network nodes are assumed to be deployed in a benign environment that will not induce significant changes to oscillators' drift.

More about oscillator drift can be found in [49], [65] and [66]. The next section describes the objective of time transfer.

1.2.3 Timing Error

The timing error between nodes m and s, measured at time t', at the end of time synchronization process, is given by

$$\begin{aligned} T_\delta^{(m,s)}(t') &= T^{(m)}(t') - T^{(s)}(t') \\ &= (\breve{a}_1^{(m)} - \breve{a}_1^{(s)}) \cdot t' + \breve{d}^{(m)} - \breve{d}^{(s)} + \breve{\phi}^{(m)}(t') - \breve{\phi}^{(s)}(t'). \end{aligned} \tag{1.3}$$

It is assumed that at the end of synchronization

$$\breve{a}_1^{(s)} = \breve{a}_1^{(m)} - \varepsilon_a^{(m,s)}, \tag{1.4}$$

$$\breve{d}^{(s)} = \breve{d}^{(m)} - \varepsilon_d^{(m,s)}, \tag{1.5}$$

where $\varepsilon_a^{(m,s)}$ and $\varepsilon_d^{(m,s)}$ are the time transfer errors. We assume transceivers are stationary during time transfer, as a result $\varepsilon_a^{(m,s)}$ is not a function of time. This allows the estimation techniques, to be described in Chapter 3, to estimate the difference in oscillator frame repetition rate without considering effect of time compression/expansion of signals during transmission. It is therefore reasonable to assume that the estimation error $\varepsilon_a^{(m,s)}$ is a result of zero mean perturbations caused by

additive channel noise and oscillator phase noise and $\mathbf{E}\{\varepsilon_a^{(m,s)}\}=0$. The variance of $\varepsilon_a^{(m,s)}$ is denoted by $\mathbf{V}\{\varepsilon_a^{(m,s)}\}=\mathbf{E}\{(\varepsilon_a^{(m,s)})^2\}$. Let

$$\varepsilon_d^{(m,s)}=\bar{\varepsilon}_d^{(m,s)}+\tilde{\varepsilon}_d^{(m,s)}, \tag{1.6}$$

$$\mathbf{E}\{\varepsilon_d^{(m,s)}\}=\bar{\varepsilon}_d^{(m,s)}. \tag{1.7}$$

The non-zero mean $\mathbf{E}\{\varepsilon_d^{(m,s)}\}\neq 0$ is used to model the timing bias at the end of time synchronization if the time-transfer from m to s is via an NLoS signal propagation path. The variance of the random error $\varepsilon_d^{(m,s)}$ is

$$\begin{aligned}\mathbf{V}\{\varepsilon_d^{(m,s)}\}&=\mathbf{V}\{\tilde{\varepsilon}_d^{(m,s)}\}\\&=\mathbf{E}\{(\tilde{\varepsilon}_d^{(m,s)})^2\}-(\mathbf{E}\{\bar{\varepsilon}_d^{(m,s)}\})^2.\end{aligned} \tag{1.8}$$

From (1.3), the mean of the timing error is

$$\mathbf{E}\{T_\delta^{(m,s)}(t')\}=\bar{\varepsilon}_d^{(m,s)}. \tag{1.9a}$$

Since $T_\delta^{(m,s)}(t')=\varepsilon_a^{(m,s)}t'+\varepsilon_d^{(m,s)}$ and $\left(T_\delta^{(m,s)}(t')\right)^2=(\varepsilon_a^{(m,s)}t')^2+(\varepsilon_d^{(m,s)})^2+2\varepsilon_a^{(m,s)}\varepsilon_d^{(m,s)}t'$, therefore

$$\begin{aligned}\mathbf{E}\left\{(T_\delta^{(m,s)}(t'))^2\right\}&=\mathbf{V}\{\varepsilon_a^{(m,s)}\}\cdot(t')^2+\mathbf{E}\{(\varepsilon_d^{(m,s)})^2\}+2\mathbf{E}\{\varepsilon_a^{(m,s)}\varepsilon_d^{(m,s)}\}t'\\&=\mathbf{V}\{\varepsilon_a^{(m,s)}\}\cdot(t')^2+\mathbf{V}\{\varepsilon_d^{(m,s)}\}+(\bar{\varepsilon}_d^{(m,s)})^2+2\mathbf{E}\{\varepsilon_a^{(m,s)}(\bar{\varepsilon}_d^{(m,s)}+\tilde{\varepsilon}_d^{(m,s)})\}t'\\&=\mathbf{V}\{\varepsilon_a^{(m,s)}\}\cdot(t')^2+\mathbf{V}\{\varepsilon_d^{(m,s)}\}+(\bar{\varepsilon}_d^{(m,s)})^2+2\mathbf{E}\{\varepsilon_a^{(m,s)}\tilde{\varepsilon}_d^{(m,s)}\}t'.\end{aligned} \tag{1.9b}$$

In general, if estimates of $\breve{a}_1^{(m)}$ and $\breve{d}^{(m)}$ are derived from the same corrupted measurements, $\varepsilon_a^{(m,s)}$ and $\tilde{\varepsilon}_d^{(m,s)}$ may be correlated and $\mathbf{E}\{\varepsilon_a^{(m,s)}\tilde{\varepsilon}_d^{(m,s)}\}\neq\mathbf{E}\{\varepsilon_a^{(m,s)}\}\cdot\mathbf{E}\{\tilde{\varepsilon}_d^{(m,s)}\}$. The timing jitter at time t' is defined as the variance of the timing error, i.e.,

$$\begin{aligned}\mathbf{V}\{T_\delta^{(m,s)}(t')\}&=\mathbf{E}\left\{(T_\delta^{(m,s)}(t'))^2\right\}-\left(\mathbf{E}\{T_\delta^{(m,s)}(t')\}\right)^2\\&=\mathbf{V}\{\varepsilon_a^{(m,s)}\}\cdot(t')^2+\mathbf{V}\{\varepsilon_d^{(m,s)}\}+2\mathbf{E}\{\varepsilon_a^{(m,s)}\tilde{\varepsilon}_d^{(m,s)}\}t'.\end{aligned} \tag{1.9c}$$

The objective of time synchronization is to minimize $\mathbf{V}\{T_\delta^{(m,s)}(t')\}$ and $\mathbf{E}\{T_\delta^{(m,s)}(t')\}$, which is equivalent to minimizing $\mathbf{E}\{(T_\delta^{(m,s)}(t'))^2\}$. These entail ensuring the differences in initial offset $|\varepsilon_d^{(m,s)}|=\left|\breve{d}^{(m)}-\breve{d}^{(s)}\right|$ and drift $|\varepsilon_a^{(m,s)}|=\left|\breve{a}_1^{(m)}-\breve{a}_1^{(s)}\right|$ are as small as possible after time transfer.

1.2.4 Received and Reference Signals

Throughout this work, it is assumed that the positive-going zero crossings of an oscillator with timing function given by (1.2b) are used to trigger the transmission of UWB impulses. That is, UWB impulses are transmitted at times $t_{(k)}^{(m)}$ that are solutions to the equation $\Phi^{(m)}(t_{(k)}^{(m)})=2k\pi$ for values of k in $\{0,1,2,3,4,5,...\}$. Then $t_{(k)}^{(m)}$ is written as

$$\begin{aligned} t_{(k)}^{(m)} &= (1/\breve{a}_1^{(m)})kT_f + \breve{d}^{(m)}/\breve{a}_1^{(m)} + \breve{\phi}_{(k)}^{(m)}/\breve{a}_1^{(m)} \\ &= a_1^{(m)}kT_f + d^{(m)} + \phi_{(k)}^{(m)}, \end{aligned} \tag{1.10}$$

where $T_f = 2\pi/\omega_o$ and for convenience, we define $a_1^{(m)} = 1/\breve{a}_1^{(m)}$, $d^{(m)} = \breve{d}^{(m)}/\breve{a}_1^{(m)}$ and $\phi_{(k)}^{(m)} = \breve{\phi}_{(k)}^{(m)}/\breve{a}_1^{(m)} = (\breve{\varphi}_{(k)}^{(m)} - \breve{\varphi}_0^{(m)})/(\breve{a}_1^{(m)}\omega_o)$ where $\breve{\varphi}_{(k)}^{(m)}$ is the sampled phase noise associated with time $t_{(k)}^{(m)} = a_1^{(m)}kT_f + d^{(m)}$. The pulse/frame repetition rate of the transceiver is $a_1^{(m)}T_f$.

Let $a_1^{(m)} = 1 \pm \eta$ and the formulations in the rest of this work do not place any restrictions on the values of η. However, nodes in the network share the same wireless channel based on TDMA. Like any other TDMA system, it is assumed that UWB monocycles transmitted by transmitter m at pre-assign time slots, after propagating through the wireless channel, will arrive within designated time slots at the receiver. If the differences in pulse repetition rate and initial offset between m and s are "too large" to begin with, this will cause monocycles to arrive at the receiver outside the designated time slots. As a result, the proposed time-transfer scheme, to be introduced in Chapter 3, will not perform as required.

Therefore there exist bounds on the maximum allowable differences in initial offset and drift among all pairs of nodes in the network such that the proposed time-transfer scheme will perform as desired. The maximum allowable differences in initial offset and drift are function of the number of nodes in the network, signal propagation delays between nodes and the number of frames to be used for time synchronization.

Thus, we assume that nodes in the network are already in some form of "coarse" time synchronization, for example by factory setting, before deployment. Then, as stated in section 1.2.2, the proposed synchronization scheme is applied periodically to align the timing functions of nodes in the network or to improve the initial coarse timing synchronization to the desired accuracy.

The objective of time synchronization is illustrated in Fig. 2.

Further, with values of oscillator aging ranging from 10^{-9} to 10^{-10} per day [42] [49], for most practical purposes, it is reasonable to assume that $|\eta| \leq 10^{-6}$.

In the subsequent analysis, it is assumed that a correlative timing detector at receiver s is used to measure the time-of-arrival (ToA) of the received UWB monocycles. This requires a reference signal to be generated at the receiver. Defining oscillator parameters as in (1.10), the reference monocycles are assumed to be generated at times

$$t_{(k)}^{(s)} = a_1^{(s)} k T_f + d^{(s)} + \phi_{(k)}^{(s)} . \tag{1.11}$$

The variables $t_{(k)}^{(m)}$ and $t_{(k)}^{(s)}$, measured on the standard time scale, are the kth positive-going zero-crossing of the sinusoid generated by nodes m and s oscillators respectively. Therefore the received and reference signals are modeled as

$$\begin{aligned} y^{(s)}(t) &= A_w \sum_k w\left(t - t_{(k)}^{(m)} - \tau_{m,s} - \rho_{m,s}\right) + n(t) \\ &= A_w \sum_k w\left(t - a_1^{(m)} k T_f - d^{(m)} - \phi_{(k)}^{(m)} - \tau_{m,s} - \rho_{m,s}\right) + n(t) , \end{aligned} \tag{1.12a}$$

$$\begin{aligned} f^{(s)}(t) &= A_r \sum_k r\left(t - t_{(k)}^{(s)}\right) \\ &= A_r \sum_k r\left(t - a_1^{(s)} k T_f - d^{(s)} - \phi_{(k)}^{(s)}\right), \end{aligned} \tag{1.12b}$$

where $k \in \{0,1,2,3,4,...\}$ assuming one monocycle $w(\circ)$ per frame time T_f. The reference signal $f^{(s)}(t)$ is correlated with the received signal to derive the timing difference between the transmitter and receiver. The random variable $n(t)$ is the additive noise in the channel with one-sided power density N_o, A is the amplitude of the respective signals, $w(t)$, $r(t)$ are the received and the

reference monocycle waveforms at the receiver, both with unit energy, and $\tau_{m,s}$ is used to denote the line-of-sight (LoS) propagation delay from transceiver m to transceiver s. The additional propagation delay (excess-delays) if signals transmitted by m arrived at s via a NLoS propagation path is described by the non-negative variable $\rho_{m,s}$.

The drift of an oscillator is characterized by $\breve{a}_v^{(m)}$, $v=1$ to V. In this research, we are interested only in the first order drift term $a_1^{(m)}$ where $a_1^{(m)}T_f$ is the pulse/frame repetition rate of the frame-rate oscillator. The parameter $a_1^{(m)}$, as defined in (1.10), is not the frequency skew defined in [1]. Here, we follow closely discussions in other recent works [55] [56] and called $a_1^{(m)}$ the first order drift (denoting the rate of the clock) of the clock at network node m.

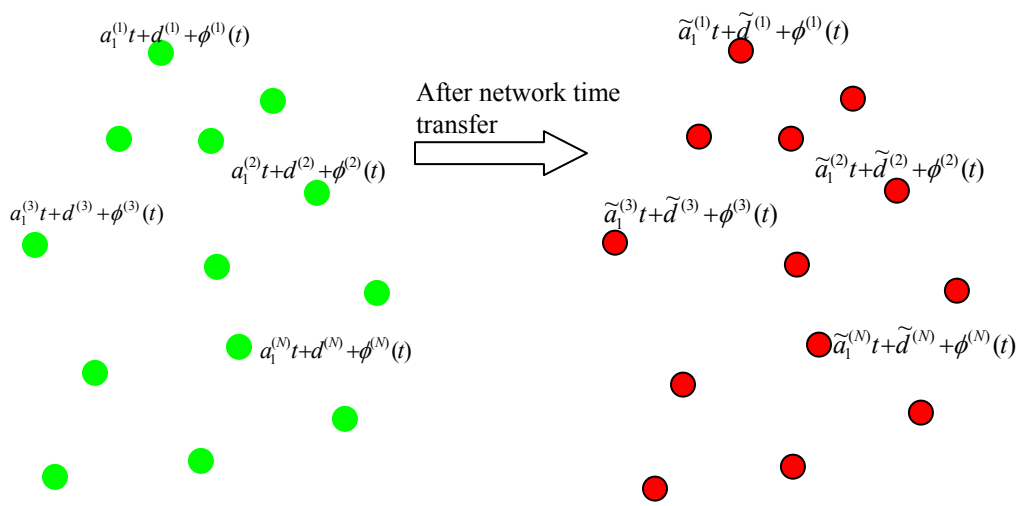

Figure 2: Illustration of the objective of synchronizing a network of wireless nodes. The objective of the network time-transfer is to align the parameters of each node such that $|\tilde{a}_1^{(i)}-\tilde{a}_1^{(j)}|<\varepsilon_a$ and $|\tilde{d}^{(i)}-\tilde{d}^{(j)}|<\varepsilon_d$, $\forall i,j$ and $i\neq j$ where ε_a and ε_d are small numbers that define the timing precision after time transfer.

1.2.5 UWB Monocycle Waveform

In most instances, in order to analyze the performance of the system quantitatively, we have to use a specific model for the received UWB monocycle. Here, the received UWB monocycle $w(t)$ is modelled using the nth order (n>0) derivative $w_n(t)$ of the Gaussian function.

Many authors use the second derivative of a Gaussian curve to model a received UWB pulse when evaluating radio system performance [37] [54] [70]. In this work a general formula for an nth order derivative Gaussian monocycle is presented. The order n is taken as a design parameter and [11] shows that the appropriate choice of n will indeed have impact on the performance of a correlative timing detector measuring the ToA of UWB signals at the receiver.

Equations (1.13a) and (1.13b) give the time and frequency domain representations of the UWB monocycle derived from the nth order derivative of a Gaussian curve. Here σ_w is a scaling factor that has unit of time (e.g., seconds) and is directly proportional to the width of the monocycle.

$$w_n(t) = (-1)^{\lfloor (3n+1)/2 \rfloor} n!\,\pi^{-1/4} e^{-pt^2} \cdot \sum_{k=0}^{\lfloor n/2 \rfloor} \frac{(-1)^k 2^{n+1/4-2k} p^{n/2+1/4-k} t^{n-2k}}{(n-2k)!\,k!\sqrt{(2n-1)!!}} \tag{1.13a}$$

$$W_n(f) = \frac{(-1)^n \cdot i_c^{n^2} \cdot (2\pi)^{n+\frac{1}{4}} p^{-\left(\frac{n}{2}+\frac{1}{4}\right)}}{\sqrt{(2n-1)!!}} f^n e^{-\pi^2 f^2/p} . \tag{1.13b}$$

In (1.13a) and (1.13b), $i_c = \sqrt{-1}$, $p = 1/(2\sigma_w^2)$ and $(2n-1)!! = (2n-1)\cdot(2n-3)...5\cdot3\cdot1$. The monocycle waveform $w_n(t)$ has the following properties:

(a) For $n = even$, the maximum amplitude is at t=0 and positive.

(b) For n=*odd*, the slope at t=0 is positive.

(c) The monocycle has unit energy, i.e., $\int_{-\infty}^{\infty} w_n^2(t)dt = 1$, and satisfies $w_n(t) \approx 0$ for $|t| >> \sigma_w$.

The width of the monocycle is approximated by the width of the main lobe of (1.13a). If n=8, the width of $w_n(t)$ is approximately σ_w.

The proposed monocycle model is a function of the order of the derivative n and a scaling factor σ_w. Increasing the order of derivative of the Gaussian curve has the effect of shifting the spectrum of the monocycle waveform to occupy a somewhat higher frequency range. Maintaining the same energy per pulse, a larger scaling factor stretches the monocycle pulse wider in time and causes a more gradual rise of the main lobe of the waveform.

CHAPTER II

MEASURING TIME-OF-ARRIVAL (ToA)

The time-of-arrival (ToA) of a UWB monocycle at the receiver is defined to be the time difference between the arrivals of the UWB monocycle at the receiver relative to the start of the receiver's frame boundary.

The proposed measurement system to measure the received signal ToA is shown in Fig. 3. It consists of a slope reversal estimator/detector [8] embedded in a feedforward Automatic Gain Control (AGC) loop shown in Fig. 4 respectively.

During measurement, it is assumed that the receiver's local oscillator is free running and the output of the correlative timing detector gives the ToA of the received UWB monocycle. The local oscillator is updated as per the time-transfer scheme to be introduced in Chapter 3.

The major sources of impairments to the measurement of the ToA considered in this research are additive noise (e.g. receiver noise), oscillator phase noise, multipath self-interference and received signal that arrived via NLoS propagation path that give a positive bias to the ToA readings [31]. For UWB impulses fully utilizing the FCC indoor spectral mask, which it is assumed herewith, the bias on the ToA measurements attributed to multipath self interference is assumed negligible [12].

This Chapter is devoted to analyzing the timing jitter at the output of the timing detector. The results will be used later to quantify the performance of the time transfer scheme.

2.1 Acquiring UWB Monocycles

The first task involved in estimating the ToA is to coarsely measure the arrival of the monocycle at the receiver. Reference [11] pointed out that the output of the correlative timing detector is a function of the input signal amplitude and proposed a modified slope-reversal amplitude estimator

from [8] to first estimate and stabilize the amplitude of the received UWB monocycles. This task is performed by an AGC preceding the timing detector.

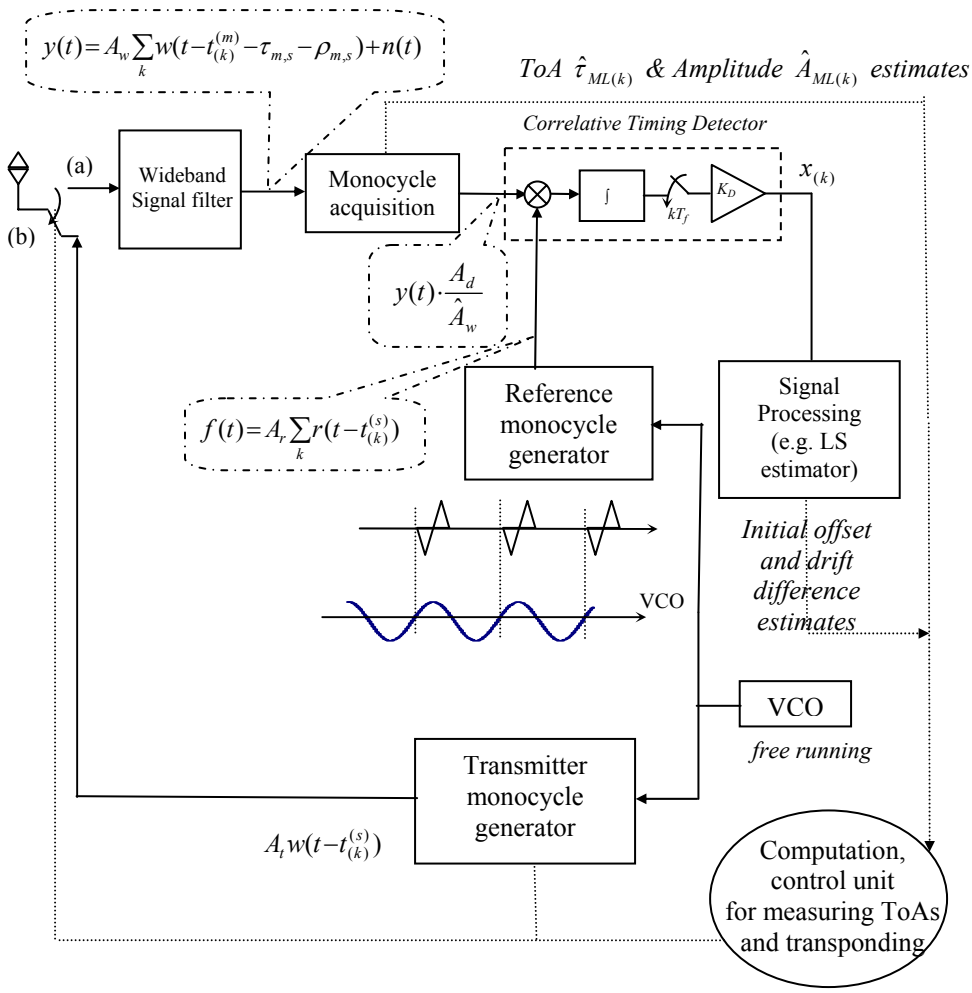

Figure 3: System block diagram of UWB monocycle ToA measurement unit. By closing the appropriate switches, this unit is used to receive (a) UWB monocycles from other nodes in the network, and (b) transmit UWB monocycles when it acts as a transmitter. The solid lines are used to denote signal paths while dotted lines the control/information paths. Note that the zero-crossings of the VCO sinusoid will trigger transmission of UWB pulses (reference and transmit). The "monocycle acquisition" sub-system is illustrated in Fig. 4. The wideband signal filter is used to remove out-of-band noise from the received signal.

(a) AGC with slope -reversal estimator

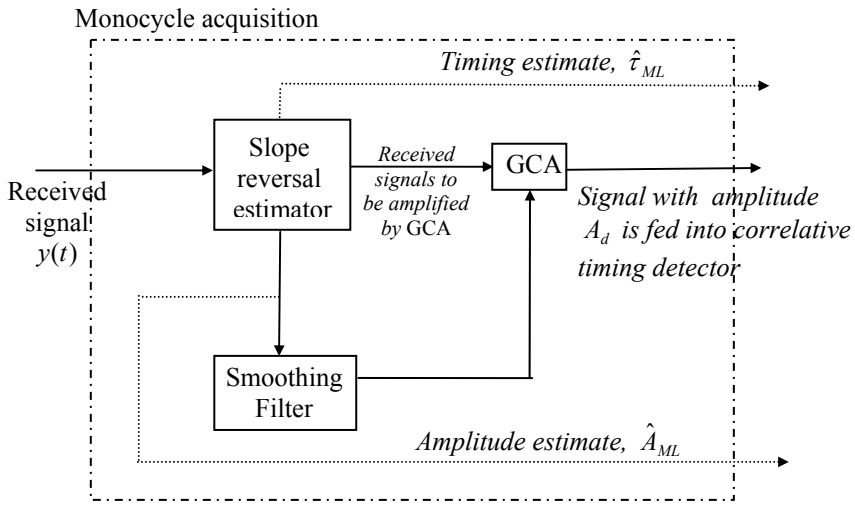

(b) Slope-reversal estimator

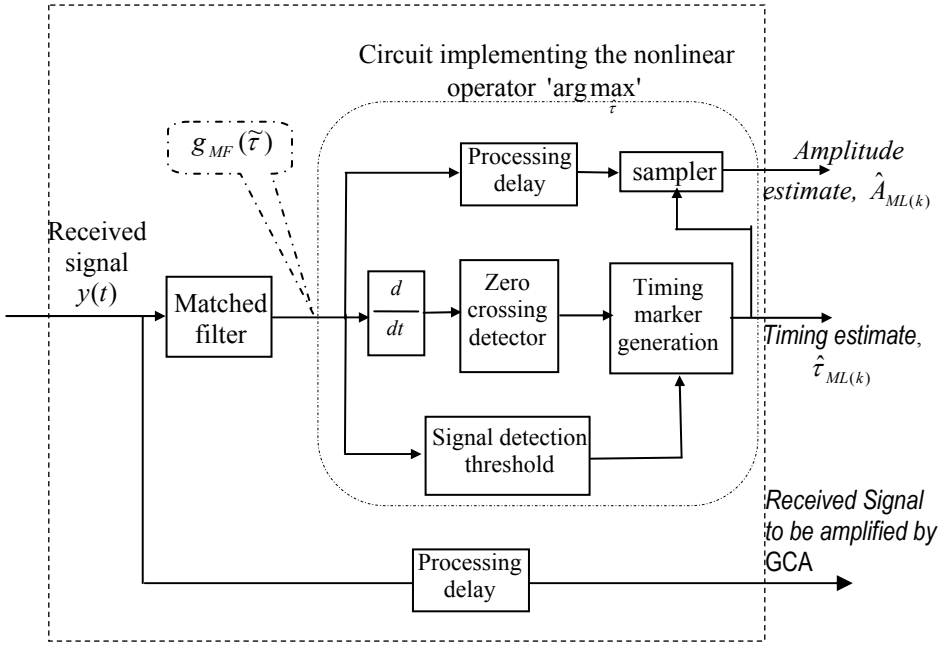

Figure 4: Illustration of the Automatic Gain Control (AGC) loop with the modified "linear filter (slope-reversal) estimator" [8] to estimate the time delay and amplitude of received UWB monocycle. The AGC is indicated as the monocycle acquisition unit in Fig. 3. In (a), the "GCA" is the Gain Control Amplifier and the smoothing filter is used to average out fluctuations in the amplitude estimate $\hat{A}_{ML}$. The details of the slope reversal estimator are shown in (b).

The coarse timing and amplitude estimators are derived from the maximum likelihood (ML) estimates of the ToA and amplitude of the received UWB monocycle. To formulate the ML detector, the first step involves finding the log likelihood ratio[4]. For the system model presented in Chapter 1, an appropriate log likelihood ratio is

$$\ln\Lambda(A,\tilde{\tau})=\frac{2A}{N_o}\int_{-T_D}^{T_D} y(t)w(t-\tilde{\tau})dt \; - \; \frac{A^2}{N_o}, \tag{2.1}$$

where $\tilde{\tau}$ is the receiver timing offset from the received signal and the range of integration T_D is assumed to be much longer than the width of the monocycle. Following the derivations given in [62], which assumed an AWGN channel with constant signal amplitude and known received waveform, the ML estimators are

$$\hat{\tau}_{ML}=\arg\max_{\tilde{\tau}}\int_{-T_D}^{T_D} y(t)w(t-\tilde{\tau})dt\,. \tag{2.2a}$$

$$\hat{A}_{ML}=\max_{\tilde{\tau}}\int_{-T_D+\tilde{\tau}}^{T_D+\tilde{\tau}} y(t)w(t-\tilde{\tau})dt\,. \tag{2.2b}$$

Thus the Cramer-Rao lower bounds on the ToA/delay and amplitude estimates are

$$\mathbf{V}\{\hat{\tau}_{ML}-\tau\}\geq\frac{N_o}{2A^2\overline{\omega^2}}\,, \tag{2.3a}$$

$$\mathbf{V}\{\hat{A}_{ML}-A\}\geq\frac{N_o}{2}\,. \tag{2.3b}$$

The parameter $\overline{\omega^2}$ denotes the effective squared bandwidth [63] of the monocycle and is given by

$$\overline{\omega^2}=\frac{1}{2\pi}\int_{-\infty}^{\infty}\omega^2|F\{w(t)\}|^2\,d\omega\,, \tag{2.3c}$$

where $F\{w(t)\}$ is the Fourier transform of the monocycle $w(t)$.

---

[4] The log-likelihood ratio is $\ln p_{y|H_1}(y(t)|H_1)\big/p_{y|H_o}(y(t)|H_o)$, where hypothesis H_1 is true when signal is present and H_o when received signal is just additive channel noise.

The proposed acquisition system, motivated by (2.2a) and (2.2b), is shown in Fig. 4. It consists of a slope reversal estimator/detector [8] embedded in a feedforward AGC loop. This is concatenated with a correlative timing detector. Together they form the basic building block of the ToA measurement system.

Assuming that there is no inter-frame interference, and considering the kth frame, the output of the matched filter detector depicted in Fig. 4b is

$$\begin{aligned} g_{MF}(\tilde{\tau}) &= A_w A_r \int_{-T_D+t_{(k)}^{(s)}}^{T_D+t_{(k)}^{(s)}} w(t-t_{(k)}^{(m)}-\tau_{m,s}-\rho_{m,s})\cdot w(t-t_{(k)}^{(s)}-\tilde{\tau})dt \\ &\quad + n_{(k)}^{/} \\ &= A_w A_r \int_{-T_D+t_{(k)}^{(s)}}^{T_D+t_{(k)}^{(s)}} w(t-a_1^{(m)}kT_f-d^{(m)}-\phi_{(k)}^{(m)}-\tau_{m,s}-\rho_{m,s})w(t-a_1^{(s)}kT_f-d^{(s)}-\phi_{(k)}^{(s)}-\tilde{\tau})dt \\ &\quad + n_{(k)}^{/} \ , \end{aligned} \tag{2.4}$$

where A_r is the amplitude of the reference monocycle at the receiver and

$$n_{(k)}^{/} = A_r \int_{-T_D+t_{(k)}^{(s)}}^{T_D+t_{(k)}^{(s)}} n(t)\cdot w(t-a_1^{(s)}kT_f-d^{(s)}-\phi_{(k)}^{(s)}-\tilde{\tau})dt \ . \tag{2.5}$$

From (2.2a) and (2.4), the estimated ToA of the UWB monocycle transmitted by transmitter m at its kth frame and received at receiver s, and measured with respect to the start of the kth frame of the receiver is

$$\begin{aligned} \hat{\tau}_{ML(k)} &= \arg\max_{\tilde{\tau}} \ g_{MF}(\tilde{\tau}) \\ &= t_{(k)}^{(m)} - t_{(k)}^{(s)} + \tau_{m,s} + \rho_{m,s} + \xi_{(k)} \\ &= (a_1^{(m)} - a_1^{(s)})kT_f + d^{(m)} - d^{(s)} + \phi_{(k)}^{(m)} - \phi_{(k)}^{(s)} + \tau_{m,s} + \rho_{m,s} + \xi_{(k)} \ , \end{aligned} \tag{2.6}$$

where $\xi_{(k)}$ is the measurement error incorporating the random effect of $n_{(k)}^{/}$ on $\hat{\tau}_{ML(k)}$. Note that the operation "arg max" is a nonlinear operator and $\xi_{(k)} \neq n_{(k)}^{/}$. The amplitude estimate is obtained by replacing $\tilde{\tau}$ with $\hat{\tau}_{ML(k)}$ in (2.4) and without loss of generality, let $A_r = 1$, then

$$\begin{aligned}
\hat{A}_{ML(k)} &= \max_{\tilde{\tau}} \; g_{MF}(\tilde{\tau}) = g_{MF}(\hat{\tau}_{ML(k)}) \\
&= A_w \int_{-T_D+t_{(k)}^{(s)}}^{T_D+t_{(k)}^{(s)}} w(t-t_{(k)}^{(m)}-\tau_{m,s}-\rho_{m,s})\, w(t-t_{(k)}^{(s)}-\hat{\tau}_{ML(k)})dt \; + \; n_{(k)}^{/} \\
&= A_w \int_{-T_D+t_{(k)}^{(s)}}^{T_D+t_{(k)}^{(s)}} w(t-a_1^{(m)}kT_f-d^{(m)}-\phi_{(k)}^{(m)}-\tau_{m,s}-\rho_{m,s})\, w(t-a_1^{(s)}kT_f-d^{(s)}-\phi_{(k)}^{(s)}-\hat{\tau}_{ML(k)})dt \\
&\quad + n_{(k)}^{/} \\
&= A_w \int_{-T_D+t_{(k)}^{(s)}-t_{(k)}^{(m)}-\tau_{m,s}-\rho_{m,s}}^{T_D+t_{(k)}^{(s)}-t_{(k)}^{(m)}-\tau_{m,s}-\rho_{m,s}} w(t)\, w(t-\xi_{(k)})dt \quad + \; n_{(k)}^{/} \; .
\end{aligned} \tag{2.7}$$

Equations (2.4) to (2.7) assume that there is only one monocycle per frame. Also, the monocycle transmitted at the kth frame of transmitter m is received at the kth frame of receiver s.

2.2 Automatic Gain Control Loop

A feedforward AGC is chosen for its stability with minimum time lag between its input and output. For the purpose of this analysis, the AGC of Fig. 4a is represented in Fig. 5 using its equivalent model. From (2.7), the output of the amplitude detector is denoted by $\hat{A}_{ML(k)}$. Following the derivations given in [42], the amplitude suppression factor of the detector is defined as the ratio of the estimated amplitude to the input signal amplitude and denoted by $\Lambda_{SF}(\xi_{(k)})$. It is assumed that the amplitude of the received monocycle remains stable during measurement, then

$$\begin{aligned}
\Lambda_{SF}(\xi_{(k)}) &= \frac{\mathbf{E}\{\hat{A}_{ML(k)} \,|\, \xi_{(k)}\}}{A_w} \\
&= \frac{\mathbf{E}\{g_{MF}(\hat{\tau}_{ML(k)}) \,|\, \xi_{(k)}\}}{A_w} \\
&= \Psi(\xi_{(k)}),
\end{aligned} \tag{2.8a}$$

where

$$\Psi(\xi_{(k)}) = \int_{-T_D+t_{(k)}^{(s)}-t_{(k)}^{(m)}-\tau_{m,s}}^{T_D+t_{(k)}^{(s)}-t_{(k)}^{(m)}-\tau_{m,s}} w(t)\, w(t-\xi_{(k)})dt \; , \tag{2.8b}$$

which is the auto-correlation function of the UWB monocycle pulse $w(t)$. This allows us to express the output of the amplitude detector $\hat{A}_{ML(k)}$ as

$$\hat{A}_{ML(k)} = A_w \cdot \Lambda_{SF}(\xi_{(k)}) + n'_{(k)} . \tag{2.9}$$

The random variables $\xi_{(k)}$ and $n'_{(k)}$ are not independent, and in general $\xi_{(k)}$ is a function of signal-to-noise-ratio (SNR, defined as $A^2/(N_o/2)$). In this work, no further attempt is make to examine the statistical properties of $\hat{A}_{ML(k)}$ analytically.

The Gain Control Amplifier (AGC) depicted in Fig. 5 is a device that amplifies the signal at its input. From [42], we know that there are various possible characterizations of the GCA depending on the actual devices that are being utilized. Here it is assumed that a GCA with a hyperbolic gain is used. The characteristic function of the hyperbolic GCA is

$$G(A_d, \hat{A}_{ML(k)}) = \frac{A_d}{A_{ML(k)}} , \tag{2.10}$$

where A_d is the desired signal amplitude. Thus, the amplitude of the signal at the output of the feedforward AGC becomes

$$\begin{aligned} A_{o(k)} &= G(A_d, \hat{A}_{ML(k)}) \cdot A_w \\ &= \frac{A_d A_w}{\hat{A}_{ML(k)}} \\ &= \frac{A_d A_w}{\Lambda_{SF}(\xi_{(k)}) \cdot A_w + n'_{(k)}} \quad . \end{aligned} \tag{2.11}$$

If $n'_{(k)} \to 0$, $\xi_{(k)} \to 0 \Rightarrow \Lambda_{SF}(\xi_{(k)}) \to 1$, $\hat{A}_{ML(k)} \approx A_w$ and $A_o = A_d$. Some form of averaging can be implemented at the output of the AGC to average out fluctuations in $A_{o(k)}$.

The linear slope reversal amplitude estimator depicted in Fig. 4b is simulated and the results plotted in Figs. 6 and 7 for received SNR ($A_w^2/(N_o/2)$) from 10 to 30 dB. In the simulation, to find $\hat{A}_{ML(k)}$, the matched filter output $g_{MF}(\tilde{\tau})$ is searched over a range of -2000T_s to 2000T_s centered at

the actual ToA position, where T_s is the sampling period of the simulation. The error in estimating the signal amplitude is negligible for most practical purposes for received SNR above 15 dB.

The estimated delay $\hat{\tau}_{ML(k)}$ from the matched filter and the received UWB monocycle at the output of the AGC are then processed by the correlative timing detector.

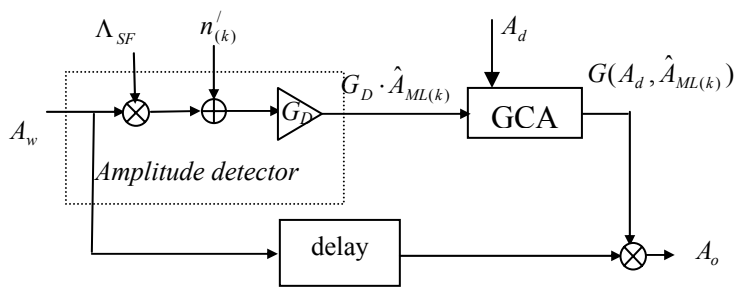

Figure 5: Equivalent representation of the Automatic Gain Control loop. The parameter G_D is the gain of the amplitude detector. Without loss of generality, G_D is set to 1.

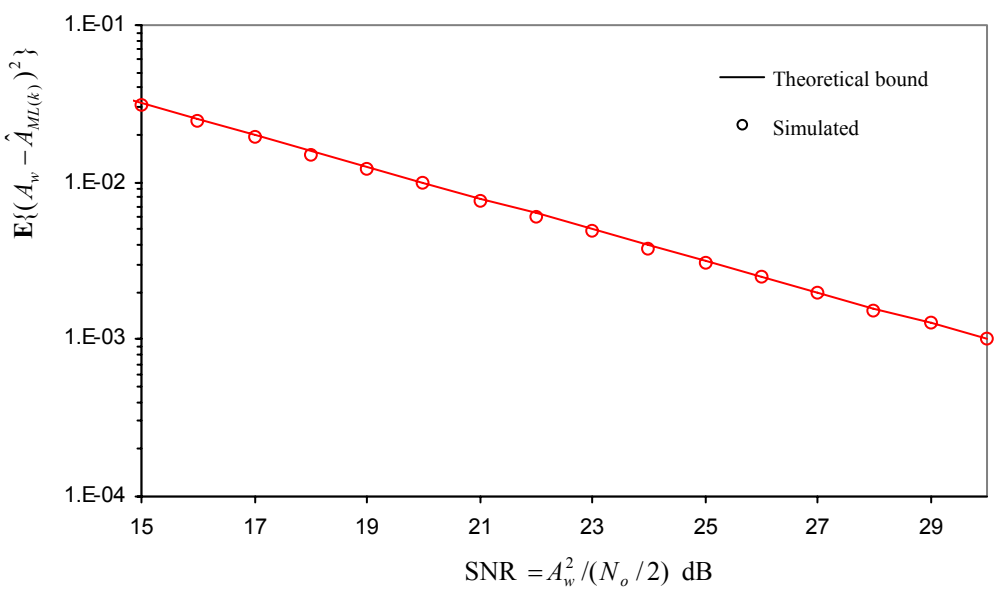

Figure 6: The variance of the amplitude estimate at the output of the matched filter estimator for effective squared bandwidth of $\overline{\omega^2} \in 8.5/\sigma_w^2$ where $\overline{\omega^2} = (2n+1)/(2\sigma_w^2)$ and $n = 8$. The sampling period is 0.01 σ_w and $A_w = 1$. The theoretical bound is given by (2.3b).

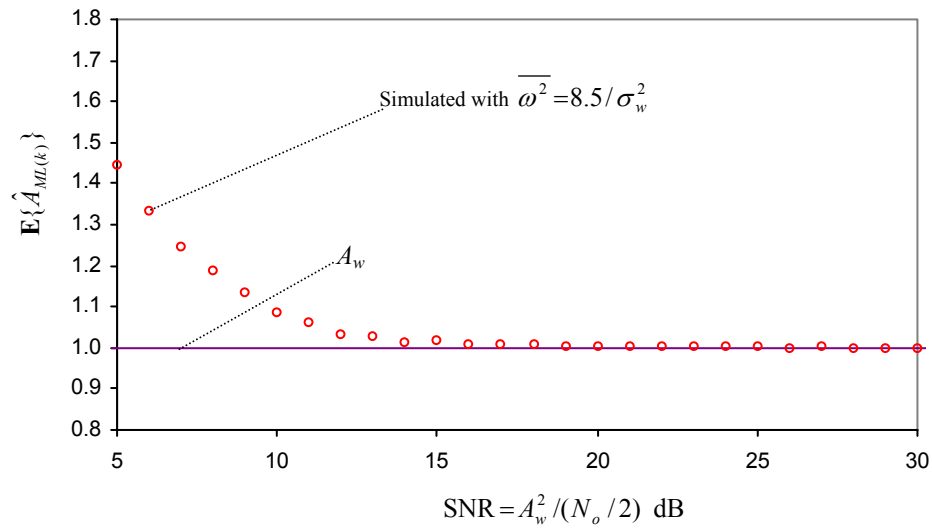

Figure 7: The mean of the amplitude detector output with $A_w = 1$ for a 8th order derivative Gaussian monocycle waveform and effective squared bandwidth $\overline{\omega^2} = 8.5/\sigma_w^2$.

The slope reversal estimator described above, which consists of a matched filter followed by zero-crossing detector, produces estimates of the ToA and the amplitude of the received UWB monocycle. The ToA coarse estimate $\hat{A}_{ML(k)}$ is used as a first attempt to align the reference signal at the receiver with the received signal. This is to ensure that the timing detector following the AGC will operate in the linear region of its characteristic function (S-curve).

The AGC estimates the amplitude of the received monocycle, and with other circuitry shown in Fig. 3, regulates the amplitude of the received monocycle. This is necessary because the gain of the timing detector is a function of the input signal amplitude [11]. From system perspective, it is desirable to control and stabilize the gain of the timing detector so that the system operates at a pre-determined operating point.

In this work, it is assumed that transceivers operate at high signal-to-noise ratio (SNR) such that the AGC described in [10] and above is able to clamp the amplitude of the monocycle to the desired value without significant fluctuations that affect performance of the system. As a result,

$\hat{A}_{ML(k)} \approx A_w$ and $A_{o(k)} = A_d$, and the correlative timing detector that follows the AGC will be able to lock onto the received UWB monocycle. Otherwise, considerably more complicated analysis is needed to analyze the performance of the system considering phenomenon such as detector mean-time-to-lose-lock or detector operates on the nonlinear region of its characteristic function.

2.3 Correlative Timing Detector

The characteristic function (S-curve) of the correlative timing detector is given by [11]

$$g(\varsigma) = A_{o(k)} A_r \int_{-\infty}^{\infty} w(t) r(t+\varsigma) dt \,, \tag{2.12}$$

where $r(t)$ is the reference monocycle generated at the receiver and ς is the timing error between the received and reference signal.

The estimate $\hat{\tau}_{ML(k)}$ is used to bring the reference signal near to the peak of the received monocycle so that ς, assuming ς has a small magnitude, fluctuates about the stable equilibrium point at $\varsigma = 0$. This allows us to approximate[5] $g(\varsigma)$ by $g(\varsigma) = \varsigma \cdot \left((dg(\varsigma)/d\varsigma)|_{\varsigma=0} \right)$ around $\varsigma = 0$. Thus $\hat{\tau}_{ML(k)}$ adjusts the correlative timing detector so that it operates within the linear region of its characteristic function.

From Fig. 3, at the kth frame, the output of the correlative timing detector is

$$x_{(k)} = K_D \cdot g(\varsigma_{(k)}) + K_D \cdot n^{//}_{(k)} \,, \tag{2.13}$$

where

$$g(\varsigma_{(k)}) = A_{o(k)} A_r \int_{-T_D + t^{(s)}_{(k)}}^{T_D + t^{(s)}_{(k)}} w(t) r(t+\varsigma_{(k)}) dt \,, \tag{2.14a}$$

[5] This approximation is widely known as the tracking/linearity assumption.

$$n_{(k)}^{//} = \frac{A_d A_r}{\hat{A}_{ML(k)}} n_{(k)} , \tag{2.14b}$$

$$n_{(k)} = \int_{-\infty}^{\infty} n(t) r(t + \varsigma_{(k)}) dt . \tag{2.14c}$$

and the factor K_D is the detector gain. The coefficient in front of $n_{(k)}$ in $n_{(k)}^{//}$ of (2.14b) arises from multiplying the received signal $y(t)$ by $A_d / \hat{A}_{ML(k)}$ after passing the received signal through the AGC. Let $\breve{g}_{TD}$ be the slope of the characteristic function of the timing detector evaluated at $\varsigma = 0$, i.e.,

$$\begin{aligned} \breve{g}_{TD} &= \left. \frac{dg(\varsigma)}{d\varsigma} \right|_{\varsigma=0} \\ &= \left. \frac{d}{d\varsigma} \int_{-\infty}^{\infty} w(t) r(t+\varsigma) dt \right|_{\varsigma=0} . \end{aligned} \tag{2.14d}$$

Applying the linearity/tracking assumption, the characteristic function becomes

$$g(\varsigma_{(k)}) = A_{o(k)} A_r \cdot \breve{g}_{TD} \cdot \varsigma_{(k)} . \tag{2.15}$$

In the subsequent analysis, the reference monocycle amplitude is set to unity, i.e., $A_r = 1$. Without loss of generality, K_D is chosen to make the slope of the detector characteristic to be 1. However in the absence of perfect knowledge of the received signal amplitude, the receiver assumes that it is A_d, i.e., the desired signal amplitude. Therefore, the detector gain is set at

$$K_D = \frac{1}{\breve{g}_{TD} A_d} . \tag{2.16}$$

As illustrated earlier, for SNR above 15dB, the amplitude detector is able to estimate the amplitude of the received signal accurately, i.e., $\hat{A}_{ML(k)} \approx A_w$.

In this work, we assumed that the received SNR is above 15 dB. As a result, the amplitude of the received signal after passing through the AGC is approximated by $A_{o(k)} = A_d$. Moreover, the noise term $n_{(k)}^{//}$ reduces to $A_d n_{(k)} / A_w$ and the output of the timing detector can now be written as

$$
\begin{aligned}
x_{(k)} &= K_D \cdot g(\varsigma_{(k)}) + K_D \frac{A_d n_{(k)}}{A_w} \\
&= K_D \cdot A_d \cdot \breve{g}_{TD} \cdot \varsigma_{(k)} + K_D \cdot \frac{A_d n_{(k)}}{A_w} \\
&= \varsigma_{(k)} + \frac{1}{A_d \cdot \breve{g}_{TD}} \cdot \frac{A_d n_{(k)}}{A_w} \\
&= \varsigma_{(k)} + \frac{n_{(k)}}{\breve{g}_{TD} \cdot A_w} \quad . \qquad (2.17)
\end{aligned}
$$

The variable $\varsigma_{(k)}$ is the timing difference between the received UWB signals and the locally generated reference signals. From the system model presented in Chapter 1, equations (1.12a) and (1.12b), $\varsigma_{(k)}$ is corrupted by the transmitter and receiver oscillators' phase noise $\phi_{(k)}$.

In Fig. 8, examples of received UWB monocycles measured in an indoor environment are shown. In subsequent sections, we deal with the effect of individual impairments on the output of the timing detector when the detector is measuring the ToA of UWB monocycles.

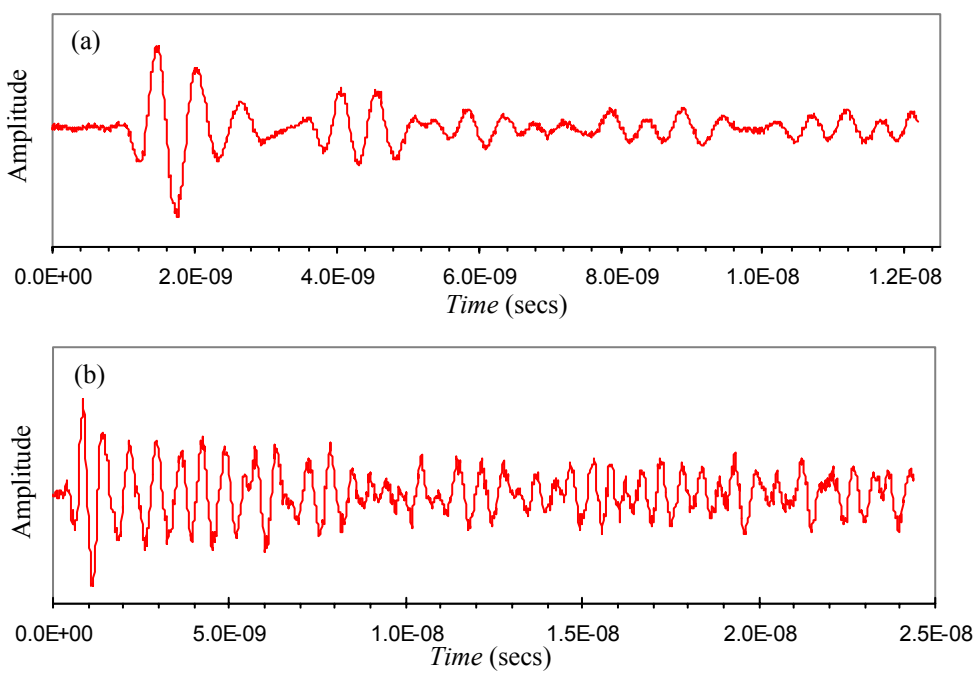

Figure 8: UWB monocycles obtained in an indoor environment. (a) Transmitter and receiver are facing each other (LoS signal). (b) The transmitted signal propagates through a wall before reaching the receiver. (The measurements were taken in a UWB reciprocity experiment conducted with Robert Wilson of CSI, USC.)

2.3.1 Effect of Additive Channel Noise

The AWGN in the channel contributes to timing jitter at the output of the timing detector. In (2.17), given $\varsigma_{(k)}$, i.e., ignoring the effect of oscillators' phase noise and treating $\varsigma_{(k)}$ as a deterministic variable, the variance of the timing detector output is given by

$$\mathbf{V}\{x_{(k)}|\varsigma_{(k)}\}=\mathbf{E}\left\{\frac{n_{(k)}^2}{(A_w\breve{g}_{TD})^2}\right\}, \tag{2.18}$$

where $\mathbf{E}\{n_{(k)}^2\}=N_o/2$ and $\breve{g}_{TD}$ is given by (2.14d).

The slope $\breve{g}_{TD}$ contains all dependence of $\mathbf{V}\{x_{(k)}^2|\varsigma_{(k)}\}$ on $w(t)$ and $r(t)$ and is a measure of the magnitude of the slope of the S-curve at $\varsigma=0$. Clearly, to minimize the effect of the input noise on the timing error variance, the task is to maximize the ratio $A_w^2\breve{g}_{TD}^2/\mathbf{E}\{n_{(k)}^2\}$. However, given the received signal amplitude A_w and the noise variance in the channel $\mathbf{E}\{n_{(k)}^2\}$, it is equivalent to maximizing $\breve{g}_{TD}^2$ subject to the constraints that $w(t)$ and $r(t)$ of (2.14d) are both of unit energy, i.e., $\int_{-\infty}^{\infty} r^2(t)dt=1$ and $\int_{-\infty}^{\infty} w^2(t)dt=1$.

To place a bound on $\mathbf{V}\{x_{(k)}\}$, the quantity $\breve{g}_{TD}^2$ is expressed as

$$\frac{d}{d\varsigma}\int_{-\infty}^{\infty} w(t)r(t+\varsigma)dt\bigg|_{\varsigma=0}=\int_{-\infty}^{\infty} F_w(f)\left[i_c\,2\pi f F_r(f)\right]^C df\,, \tag{2.19}$$

where $[R(f)]^C$ denotes the complex conjugate of $R(f)$ and $F_r(f)$ the Fourier transform of $r(t)$. Let $\langle x,y\rangle=\int x(t)\cdot[y(t)]^C\,dt$ be the usual inner product space in $L_2(-\infty,\infty)$. We denote a bounded linear operator on a Hilbert space as K and its adjoint K^* such that $<x,\mathrm{K}^*y>=<\mathrm{K}x,y>$. Here, these linear operators on $F_r(f)$ can be written as[6]

[6] The operator K^* is shown to be unique in [47].

$$\begin{cases} \mathrm{K}: F_x(f) \rightarrow [i_c 2\pi f]^C \cdot F_x(f) \\ \mathrm{K}^*: F_x(f) \rightarrow i_c 2\pi f F_x(f) \end{cases}. \tag{2.20}$$

Applying the Schwartz inequality to (2.19), we obtain

$$\begin{aligned} \breve{g}_{TD}^2 &= \langle F_w(f), \mathrm{K}^* F_r(f) \rangle^2 \\ &= \langle \mathrm{K} F_w(f), F_r(f) \rangle^2 \\ &\leq \| \mathrm{K} F_w(f) \|^2 \| F_r(f) \|^2 . \end{aligned} \tag{2.21a}$$

Equality occurs when $F_r(f) \propto -i_c 2\pi f F_w(f)$ or $r(t) \propto -dw(t)/dt$. Thus the optimal reference signal is the time derivative of the received monocycle waveform. In [11], it is derived that

$$\breve{g}_{TD}^2 = \overline{\omega^2} , \tag{2.21b}$$

when $r(t) = dw(t)/dt$. Since $\breve{g}_{TD}^2$ is upper bounded by $\overline{\omega^2}$ (2.21a), $\mathbf{V}\{x_{(k)}\}$ of (2.18) is lower bounded by[7]

$$\mathbf{V}\{x_{(k)} | \varsigma_{(k)}\} \geq \frac{1}{\Theta_{m,s} \overline{\omega^2}} , \tag{2.22}$$

where $\Theta_{m,s} = 2A_w^2 / N_o$ is defined as the received SNR at the receiver. It can be shown that $(\mathbf{E}\{x_{(k)}\})^2 = K_D^2 \cdot A_w^2 \cdot A_r^2 \cdot (\int_{-\infty}^{\infty} w(t) \cdot r(t+\varsigma) dt)^2$ and $\mathbf{V}\{x_{(k)} | \varsigma) = K_D^2 \cdot A_r^2 \cdot (N_o/2) \cdot \int_{-\infty}^{\infty} r^2(t+\varsigma) dt$. If $\varsigma = 0$, $r(t) = w(t)$, since $\int_{-\infty}^{\infty} w^2(t) dt = 1$, then the ratio $(\mathbf{E}\{x_{(k)}\})^2 / \mathbf{V}\{x_{(k)} | \varsigma\} = 2A_w^2 / N_o = \Theta_{m,s}$. For simplicity in notation, the term $\int_{-\infty}^{\infty} w^2(t) dt$ is not carried around in subsequent analysis and $\Theta_{m,s}$ should be understood as a unit-less quantity.

The lower bound in (2.22) is known as the Cramer-Rao bound on estimating the non-random delay of a signal distorted by additive noise in the channel [43] [63]. This bound is derived with no restriction on the bandwidth of the signal. We note that this bound is optimistic because matched filter UWB receivers are hard to build.

[7] This result has been arrived at using different techniques in different contexts [48] [50] [68].

Utilizing the monocycle waveform (derivative of a Gaussian curve) defined in Chapter 1, equations (1.13a) and (1.13b), if $w(t)=w_n(t)$ and $r(t)=w_{n'}(t)$ are substituted into (2.19), the slope at $\varsigma=0$ is [11]

$$\frac{d}{d\varsigma}\int_{-\infty}^{\infty} w_n(t)w_{n'}(t+\varsigma)dt\Big|_{\varsigma=0} = \begin{cases} (-1)^n\sqrt{p}\,\dfrac{(n+n')!!}{\sqrt{(2n-1)!!(2n'-1)!!}} & if\ n+n'+1=even \\ 0 & otherwise \end{cases}. \tag{2.23}$$

It can be shown that in the optimal case when $n'=n+1$, we have for n even [11],

$$\begin{aligned}\overline{\omega^2} &= \left(\frac{d}{d\varsigma}\int_{-\infty}^{\infty} w_n(t)w_{n'}(t+\varsigma)dt\Big|_{\varsigma=0}\right)^2 \\ &= (2n+1)p\,, \end{aligned} \tag{2.24}$$

with unit sec^{-2}. In table 1, $1/\breve{g}_{TD}^2$ is tabulated for various values of n and n'. It indicates that a UWB monocycle waveform that is of a higher order derivative of the Gaussian curve is desirable if the objective is to reduce the timing error variance due to AWGN at the input of the detector. The improvement when raising the order from (n=2,n'=3) to (n=10,n'=11) is as high as 6.23 dB. It seems that a higher order Gaussian monocycle has a main lobe that rises faster than a lower order pulse which contributes to this gain.

Table 1: The ratio $(1/\breve{g}_{TD}^2)$ for various values of n and n' ($w(t)=w_n(t), r(t)=w_{n'}(t)$)

	n'=2	3	4	5	6	7	8	9
n=2	-	$1/(5p)$	-	$9/(35p)$	-	$143/(315p)$	-	$221/(231p)$
3	$0.20/p$	-	$1/(7p)$	-	$11/(63p)$	-	$65/(231p)$	-
4	-	$\approx 0.14/p$	-	$1/(9p)$	-	$13/(99p)$	-	$85/(429p)$
5	$\approx 0.26/p$	-	$\approx 0.11/p$	-	$1/(11p)$	-	$15/(143p)$	-
6	-	$\approx 0.17/p$	-	$\approx 0.09/p$	-	$1/(13p)$	-	$17/(195p)$
7	$\approx 0.45/p$	-	$\approx 0.13/p$	-	$\approx 0.08/p$	-	$1/(15p)$	-
8	-	$\approx 0.28/p$	-	$\approx 0.10/p$	-	$\approx 0.06/p$	-	$1/(17p)$
9	$\approx 0.957/p$	-	$\approx 0.198/p$	-	$\approx 0.087/p$	-	$\approx 0.059/p$	-

2.3.2 Effect of Oscillator Phase Noise

In this work, it is assumed that there is no movement of the network nodes during time transfer, then the short-term fluctuations in $x_{(k)}$ of (2.17) are only due to randomness in $\varsigma_{(k)}$ and additive noise in the channel. The random variable $\varsigma_{(k)}$ is the timing difference between the received UWB signal and the locally generated reference signal. From the system model presented in Chapter 1, randomness in $\varsigma_{(k)}$ is caused by the random variables $\phi_{(k)}^{(m)}$ and $\phi_{(k)}^{(s)}$, which are related to the oscillator phase noise $\varphi(t)$ through (1.2d).

From [42], the oscillator phase noise $\varphi(t)$ with power spectral density $S_{\varphi}(\omega)$ can be quantified using the first structure function $D_{\varphi}^{1}(\Delta)$ of the phase noise process

$$\begin{aligned} D_{\varphi}^{1}(\Delta) &= \mathbf{E}\{|\varphi(t+\Delta)-\varphi(t)|^{2}\} \\ &= (2/\pi)\int_{-\infty}^{\infty}\sin^{2}(\omega\Delta/2)S_{\varphi}(\omega)\,d\omega \;\le\; (2/\pi)\int_{-\infty}^{\infty}S_{\varphi}(\omega)\,d\omega, \end{aligned} \tag{2.25a}$$

where Δ is the time interval of interest, e.g., the nominal pulse repetition period T_f. In (2.25a), we have made used of the fact that $\sin^{2}(\omega\Delta/2)\le 1$. Further, the timing jitter due to $\phi_{(k)}$ is defined as

$$\sigma_{\phi}^{2} = D_{\varphi}^{1}(\Delta)/\omega_{o}^{2}. \tag{2.25b}$$

More details on characterizing the oscillator phase instabilities using structure functions can be found in [35]. Reference [35] points out that the first structure function $D_{\varphi}^{1}(\Delta)$ of the phase noise characterizes the stability of the oscillator phase. As put forth in [35], $\varphi(t)$ is not stationary (increments of $\varphi(t)$ can be stationary) and thus does not possess a power spectral density (PSD) in the usual sense. To circumstance this difficulty, [35] defined $S_{\varphi}(\omega)=S_{\dot{\varphi}}(\omega)/\omega^{2}$ where $\dot{\varphi}(t)=d\varphi(t)/dt$ and $\dot{\varphi}(t)$ is a stationary, zero mean random process. The same definition is adopted herein.

2.3.3 Effect of Multipath Self-Interference

(a) *Multi-path Channel Model*

The UWB multi-path channel model is adopted from the modified Saleh-Valenzuela (SV) model described by the IEEE 802.15 working group [19]. It describes a UWB multipath channel consisting of clusters of "rays" arriving at the receiver. The channel impulse response consists of Dirac delta functions spaced according to the inter-rays arrival time within the cluster. In addition, the amplitude of the transmitted signal is attenuated by an exponential factor. This discrete time channel impulse response is of the form

$$h(t)=\chi\sum_{l_h=0}^{L_h}\sum_{k_h=0}^{K_h}\widetilde{\alpha}_{k_h,l_h}\cdot\delta(t-\widetilde{T}_{l_h}-\widetilde{\tau}_{k_h,l_h}), \tag{2.26}$$

where χ represents log-normal shadowing, $\widetilde{\alpha}_{k_h,l_h}$ is the multipath gain coefficient, $\widetilde{T}_{l_h}$ is the delay of the $(l_h)^{\mathbf{th}}$ cluster and $\widetilde{\tau}_{k_h,l_h}$ the delay of the $(k_h)^{\mathbf{th}}$ multipath component relative to the $(l_h)^{\mathbf{th}}$ cluster arrival time. The cluster and ray arrival rate are $\widetilde{\Lambda}$ and $\widetilde{\lambda}$ respectively. The inter-arrival times of the cluster and rays within each cluster are modelled using exponential distributions. Specifically, the conditional probability density function (p.d.f.) on $\widetilde{\tau}_{k_h,l_h}$ is

$$\mathbf{P}(\widetilde{\tau}_{k_h,l_h}|\widetilde{\tau}_{k_h-1,l_h})=\widetilde{\lambda}\cdot e^{-\lambda(\widetilde{\tau}_{k_h,l_h}-\widetilde{\tau}_{k_h-1,l_h})},\qquad k_h>0. \tag{2.27a}$$

If $k_h=0$, by definition, $\widetilde{\tau}_{0,l_h}=0$. The channel coefficients in (2.26) are given by

$$\widetilde{\alpha}_{k_h,l_h}=\widetilde{\upsilon}_{k_h,l_h}\cdot\widetilde{\xi}_{l_h}\cdot\widetilde{\beta}_{k_h,l_h}. \tag{2.27b}$$

Signal inversion due to reflections is modelled via $\widetilde{\upsilon}_{k_h,l_h}$, which is distributed equi-probably over ±1. The factors $\widetilde{\xi}_{l_h}$ and $\widetilde{\beta}_{k_h,l_h}$ denotes fading associated with the $(l_h)^{\text{th}}$ cluster and the $(k_h)^{\text{th}}$ ray of the $(l_h)^{\text{th}}$ cluster respectively. It is further assumed in [19] that

$$\mathbf{E}\left\{\left|\tilde{\xi}_{l_h}\tilde{\beta}_{k_h,l_h}\right|^2\right\}=\tilde{\Omega}_o e^{-\tilde{T}_{l_h}/\tilde{\Gamma}} e^{-\tilde{\tau}_{k_h,l_h}/\tilde{\gamma}} , \tag{2.27c}$$

where $\tilde{\Omega}_o$ is the mean energy of the first path of the first cluster. The cluster and ray attenuation factors are denoted by $\tilde{\Gamma}$ and $\tilde{\gamma}$ respectively.

(b) *Variance of Multipath Self-interference*

In this section, the effect of multipath self-interference on the performance of the open loop timing detector is analyzed. The received signal at the input to the timing detector is written as

$$\tilde{y}(t)=A_t\chi\sum_{l_h}\sum_{k_h}\tilde{\alpha}_{k_h,l_h}w(t-\tilde{T}_{l_h}-\tilde{\tau}_{k_h,l_h})+n(t) , \tag{2.28}$$

where $n(t)$ is the additive noise in the channel with one-sided PSD of N_o and A_t is the amplitude of the transmitted monocycle. The output of the detector, in the absence of noise, becomes

$$K_D\cdot g(\varsigma)=K_D\chi A_w A_r\sum_{l_h}\cdot\sum_{k_h}\tilde{\alpha}_{k_h,l_h}\int_{-\infty}^{\infty}w(t-\tilde{T}_{l_h}-\tilde{\tau}_{k_h,l_h})r(t+\varsigma)dt \ . \tag{2.29a}$$

Equation (2.29a) indicates that the output of the correlative timing detector is corrupted by multipaths in the channel.

In this work, it is assumed that the ToA is derived from the first ray of the first multipath cluster, i.e., in subsequent analysis, $l_h=1$. Further, while tracking the first ray of the $l_h=1$ multipath cluster, the contributions to the timing detector output from multipath rays originated from other clusters are ignored. The timing detector output reduces to

$$K_D\cdot g(\varsigma)=K_D\chi A_w A_r\sum_{k_h}\tilde{\alpha}_{k_h,l_h}\int_{-\infty}^{\infty}w(t-\tilde{T}_1-\tilde{\tau}_{k_h,1})r(t+\varsigma)dt \ . \tag{2.29b}$$

As pointed out in section 2.3, the gain of the timing detector is a function of the received signal amplitude and an Automatic Gain Controller (AGC) is placed before the correlative timing detector to ensure constant detector gain. From (2.17), the output of the timing detector is

$$x_{(k)} = K_D \cdot g(\varsigma_{(k)}) + \frac{n_{(k)}}{\breve{g}_{TD} \cdot A_w}. \tag{2.30a}$$

where $K_D = 1/(\breve{g}_{TD} \cdot A_d)$ and $A_w = A_t \cdot \chi \cdot \widetilde{\alpha}_{0,1}$ is the amplitude of the first ray of the first multipath cluster. Assuming that there is enough SNR such that the amplitude of the monocycles at the output of the AGC is $A_{o(k)} = A_d$ and $\hat{A}_{ML(k)} = A_w$. The output of the timing detector becomes

$$\begin{aligned} x_{(k)} &= \frac{1}{A_d \cdot \breve{g}_{TD}} \cdot \frac{A_d}{\widetilde{\alpha}_{0,l_h}} \cdot \left(\widetilde{\alpha}_{0,l_h} \int_{-\infty}^{\infty} w(t-\widetilde{T}_1) r(t+\varsigma) dt + \sum_{k_h \neq 1} \widetilde{\alpha}_{k_h,1} \cdot \int_{-\infty}^{\infty} w(t-\widetilde{T}_1 - \widetilde{\tau}_{k_h,1}) r(t+\varsigma) dt \right) + \frac{n_{(k)}}{\breve{g}_{TD} \cdot A_w} \\ &= \frac{1}{\breve{g}_{TD}} \cdot \left(\int_{-\infty}^{\infty} w(t) r(t+\widetilde{T}_1+\varsigma) dt + \sum_{k_h \neq 1} \frac{\widetilde{\alpha}_{k_h,1}}{\widetilde{\alpha}_{0,1}} \cdot \int_{-\infty}^{\infty} w(t-\widetilde{\tau}_{k_h,1}) r(t+\widetilde{T}_1+\varsigma) dt \right) + \frac{n_{(k)}}{\breve{g}_{TD} \cdot A_w} \\ &= \frac{1}{\breve{g}_{TD}} \cdot \left(\int_{-\infty}^{\infty} w(t) r(t+\varsigma') dt + \sum_{k_h \neq 1} \frac{\widetilde{\alpha}_{k_h,1}}{\widetilde{\alpha}_{0,1}} \cdot \int_{-\infty}^{\infty} w(t-\widetilde{\tau}_{k_h,1}) r(t+\varsigma') dt \right) + \frac{n_{(k)}}{\breve{g}_{TD} \cdot A_w} \ , \end{aligned} \tag{2.30b}$$

where $\varsigma' = \varsigma + \widetilde{T}_1$.

In the modified SV channel model for UWB systems [19], the signal inversion coefficient $\widetilde{\upsilon}_{k_h,l_h}$ is statistically independent and has zero mean. As a result, $\mathbf{E}\{\widetilde{\alpha}_{k_h,l_h}\} = 0$ and

$$\mathbf{E}\{K_D \cdot g(\varsigma)\} = 0 \ . \tag{2.31}$$

In (2.31), $g(\varsigma)$ is a function of the channel coefficients, and is described statistically by (2.27b) and (2.27c). Assuming that the multipath components have independent random amplitudes, the variance of the sum of (2.30b) is the sum of the variances. Therefore the variance of the detector output, conditioned on $\widetilde{T}_1$ and $\widetilde{\tau}_{k_h,1}$, is computed as

$$\begin{aligned} \mathbf{E}\{x_{(k)}^2\} = &\frac{1}{\breve{g}_{TD}^2} \cdot \left[\left(\int_{-\infty}^{\infty} w(t) r(t+\varsigma') dt \right)^2 + \frac{e^{\widetilde{T}_1/\widetilde{\Gamma}}}{A_t^2 \cdot \mathbf{E}\{\chi^2\} \cdot \widetilde{\Omega}_o} \cdot \frac{N_o}{2} \right] \\ &+ \frac{1}{\breve{g}_{TD}^2} \sum_{k_h \neq 0} e^{-\widetilde{\tau}_{k_h,1}/\widetilde{\gamma}} \left(\int_{-\infty}^{\infty} w(t-\widetilde{\tau}_{k_h,1}) r(t+\varsigma') dt \right)^2 \ . \end{aligned} \tag{2.32}$$

The variance expressed by (2.32) consists of two separate parts: variance of the first ray corrupted by AWGN and the variance attributed to self-interference from the multipath components.

In the presence of additive noise, measuring the first ray of the cluster requires sufficient received signal energy for tolerable timing error jitter. This is described by the Cramer-Rao (CR) lower bound of (2.22).

To justify ignoring multipath rays from other clusters, considered a signal arrives via a NLoS path 10 nanoseconds after the first ray of the $(l_h)^{\text{th}}$ cluster, i.e., $\widetilde{T}_{l_h+1} \approx 10$ nano-secs, which represents a difference in signal propagation distance of 3 meters, and if $\widetilde{\Gamma} = 7.1$ as in IEEE 802.15.3a report, $e^{-\widetilde{T}_{l_h+1}/\widetilde{\Gamma}}$ represents a reduction in power of 6.1 dB $(= 10\log(e^{-10/7.1}))$ compared to the first ray of the $(l_h)^{\text{th}}$ cluster. The effect of a multipath component from another cluster therefore, on average, is of 6.1 dB less power than the signal to be tracked. With this 6.1dB reduction of power, it is assumed that multipaths from other clusters contribute negligibly to the timing detector output.

In subsequent analysis, let $w(t) = w_n(t)$ and $r(t) = w_{n'}(t)$. Making use of the Parseval's relationship and the integral solutions in ([2], equation 7.3.1) ([21], equation 3.462), we arrive at

$$\int_{-\infty}^{\infty} w_n(t-\widetilde{\tau}_{k_h,1}) w_{n'}(t+\varsigma')dt = \frac{(-1)^{n+n'}(n+n')!\,p^{(n+n')/2} e^{-\widetilde{\zeta}^2 p/2}}{\sqrt{(2n-1)!!(2n'-1)!!}} \sum_{k=0}^{\lfloor (n+n')/2 \rfloor} \frac{(-1)^k \widetilde{\zeta}^{\,n+n'-2k}}{(n+n'-2k)!k!(2p)^k}, \tag{2.33}$$

where $\widetilde{\zeta} = \varsigma' + \widetilde{\tau}_{k_h,1}$. If there is no multipath components and no timing error between the received signal and the reference signal at the receiver, i.e., $\widetilde{\tau}_{k_h,1} = 0$ and $\varsigma = 0$, because $(n+n')$ is designed to be odd, (2.33) is identically zero.

Let $\widetilde{V}$ be the right-hand-side of (2.33), then

$$\widetilde{V}^2 = \frac{p^{n+n'} \cdot \left((n+n')!\right)^2}{(2n-1)!!(2n'-1)!!} \cdot \left\{ e^{-\tau^2 p} \sum_{v_1=0}^{\lfloor (n+m)/2 \rfloor} \frac{(-1)^{v_1} \tau^{n+m-2v_1}}{(n+m-2v_1)!v_1!(2p)^{v_1}} \sum_{v_2=0}^{\lfloor (n+n')/2 \rfloor} \frac{(-1)^{v_2} \tau^{n+n'-2v_2}}{(n+n'-2v_2)!v_2!(2p)^{v_2}} \right\}. \tag{2.34}$$

An analytical expression for the variance due to the second ray in the cluster is presented next. We postulate that, because of the narrow pulse width of UWB impulses, it is sufficient for most applications to consider only the additional variance caused by the second ray of the cluster if the objective of the timing detector is to measure the ToA of the first ray of the cluster. The conditional

p.d.f. of the second ray of the cluster is $\mathbf{P}(\tilde{\tau}_{1,1}|\tilde{\tau}_{0,.1}=0)=\tilde{\lambda}\cdot e^{-\tilde{\lambda}\cdot\tilde{\tau}_{1,1}}$. Therefore the variance at the output of the timing detector due to the second ray in the first cluster is

$$\sigma_{MP}^2=(1/\breve{g}_{TD}^2)\cdot\mathbf{E}\left\{\tilde{V}^2 e^{-\tilde{\tau}_{1,1}/\tilde{\gamma}}\right\}. \tag{2.35a}$$

Substituting (2.34) into (2.35a), leads to

$$\begin{aligned}\sigma_{MP}^2=&\frac{(1/\breve{g}_{TD}^2)\cdot\tilde{\lambda}\cdot p^{-1/2}\left((n+n')!\right)^2}{2^{n+n'+1}(2n-1)!!(2n'-1)!!}\\ &\times\sum_{v_1=0}^{\lfloor(n+n')/2\rfloor}\sum_{v_2=0}^{\lfloor(n+n')/2\rfloor}(-1)^{v_1+v_2}\cdot\exp\left\{\frac{3(\tilde{\lambda}+1/\tilde{\gamma})^2}{32p}\right\}\\ &\frac{(2(n+n')-2(v_1+v_2))!}{(n+n'-2v_1)!v_1!(n+n'-2v_2)v_2!}\\ &\times\left\{\frac{\sqrt{\pi}}{\Gamma[(n+n')-(v_1+v_2)+1]}\cdot{}_1F_1\left((n+n')-(v_1+v_2)+1/2;1/2;\frac{\left(\tilde{\lambda}+1/\tilde{\gamma}\right)^2}{16p}\right)\right.\\ &\left.-\frac{\left(\sqrt{\pi/p}\right)\cdot\left(\tilde{\lambda}+1/\tilde{\gamma}\right)/2}{\Gamma[(n+n')-(v_1+v_2)+1/2]}\cdot{}_1F_1\left((n+n')-(v_1+v_2)+1;3/2;\frac{\left(\tilde{\lambda}+1/\tilde{\gamma}\right)^2}{16p}\right)\right\},\end{aligned} \tag{2.35b}$$

where ${}_1F_1(\alpha;\gamma;z)$ is the confluent hypergeometric function and $\Gamma[\circ]$ is the Gamma function ([21], section 6.4). In (2.35b), $\breve{g}_{TD}^2=(2n+1)/(2\sigma_w^2)$. Note that (2.35b) is a function of $(n,n',\tilde{\lambda},\tilde{\gamma},p)$ where $p=1/(2\sigma_w^2)$.

In Fig. 9, we plotted σ_{MP}^2 as a function of $\tilde{\lambda}\sigma_w$ and $\tilde{\gamma}/\sigma_w$. The variance σ_{MP}^2 can be interpreted as the timing error variance attributed to multipath in the channel. This is in additional to timing jitter contributed by other disturbances in the system such as AWGN and oscillator instabilities. It is evident that (2.35b) correctly predicts that when $\tilde{\lambda}=0$, $\sigma_{MP}^2=0$ and as $\tilde{\gamma}\to 0$, $\sigma_{MP}^2\to 0$.

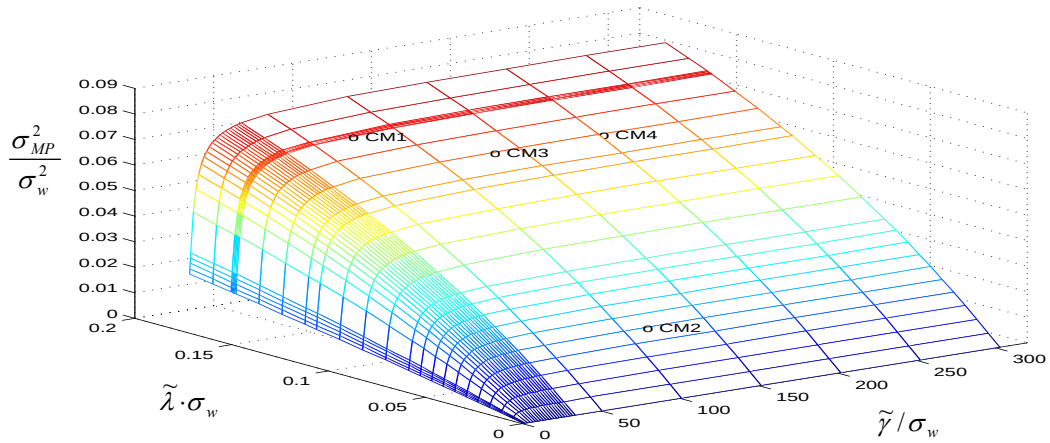

Figure 9: Additional variance σ_{MP}^2 due to the 2nd ray of the cluster in a multipath propagation environment as a function of normalized quantities $\tilde{\lambda}\sigma_w$ and $\tilde{\gamma}/\sigma_w$. Here, $\breve{g}_{TD}^2=(2n+1)/(2\sigma_w^2)$, *n=8, n′=9* and $\sigma_w=0.05948\ ns$. The points CM1, CM2, CM3 and CM4 indicated on the surface of the plot are obtained with channel parameters specified in IEEE 802.15.3a [19].

In Fig. 9, for channel environments CM1, CM2, CM3 and CM4 proposed in [19] the ratio $\sigma_w/(1/\tilde{\lambda})=\sigma_w\tilde{\lambda}$ is a small quantity while $\tilde{\gamma}/\sigma_w$ is relatively large. A large $\tilde{\gamma}/\sigma_w$ puts these channel environments on the "saturation" part of the σ_{MP}^2 plot where σ_{MP}^2 is not sensitive to variations in $\tilde{\gamma}$. As $1/\tilde{\lambda}$ is a measure of the temporal spacing of the multipaths and σ_w a measure of the width of the monocycles, a small $\sigma_w\tilde{\lambda}$ therefore indicates that the multipaths are likely to be resolved.

For the channels identified as CM1, CM2, CM3 and CM4 in [19], the ratio σ_{MP}^2/σ_w^2 are 0.0744, 0.0202, 0.0671 and 0.0675 respectively.

Denoting the starting and stopping times of the integrator of the correlative timing detector as $-T_D+t_{(k)}^{(s)}$ and $T_D+t_{(k)}^{(s)}$ respectively where $t_{(k)}^{(s)}$ is the timing of the receiver oscillator, σ_{MP}^2 is derived assuming $T_D\to\infty$. During implementation, T_D can be designed to be close to the pulse width of the monocycle and thus the effect of multipath self-interferences would be even smaller.

However it is noted in [28] that there exists a "region" in the UWB power delay profile located beyond the arrival of the LoS signal where the power delay profile 'exhibits a single diffuse multipath cluster caused by superposition of a large number of un-resolved paths'. There are also 'limitations imposed on resolvability imposed by the UWB antennas' [28]. If the timing detector is tracking a NLoS component in this diffuse multipath region of the power delay profile, the analysis performed in this section which assumes a channel with discrete impose response is no longer valid. As a result, there will be timing error at the output of the detector due to multipath self-interferences.

In subsequent analysis, the effect of multipath self-interference on the output of the timing detector is ignored.

2.3.4 Effect of Non-Line-of-Sight (NLoS) Signal Propagation

A NLoS signal refers to transmitted signal that arrived at the receiver after being scattered from scattering centers distributed around the transceivers or signals that have blockages in their signal propagation paths.

It is assumed for convenience, and lacking definitive results on UWB signal propagating through materials in the literature, that retardation of the LoS signal passing through blockages is negligible compared with additional propagation time via scattering[8]. This assertion needs further scrutiny when more propagation data for typical environments becomes available in the open literature. Discussion on the behavior of UWB signals passing through material can be found in [38]. In the absent of blockages, it is assumed that the first arrival is the LoS path.

In this work, the propagation delay of a signal transmitted by node m and received at node s is modeled by

[8] The distribution of scatters around transmitter has been modeled with scatter models such as ring, uniform, Gaussian, circular and elliptical [25]. However, these models are developed primarily for narrowband signals and may not be applicable for UWB signals.

$$\tau = \tau_{m,s} + \rho_{m,s} \ , \tag{2.36}$$

and the distance traveled by the signal is $D_{m,s} = (\tau_{m,s} + \rho_{m,s})/c$ where c is the speed of light. The propagation delay, as illustrated in Fig. 10, along the LoS path is given by $\tau_{m,s}$ and by definition $\tau_{m,s} = \tau_{s,m}$. If the propagation path of a LoS signal is being blocked resulting in low SNR at the receiver and ignored, the ToA measurement is derived from scattered NLoS signals. In this case, the receiver locks onto the NLoS path and the excess-delay $\rho_{m,s} > 0$. A quantity that is useful for subsequent analysis is $\tilde{\rho}_{m,s}$, which is defined as

$$\begin{aligned} \tilde{\rho}_{m,s} &= \frac{\tau_{m,s} + \rho_{m,s} - \tau_{s,m} - \rho_{s,m}}{2} \\ &= \frac{\rho_{m,s} - \rho_{s,m}}{2} \ . \end{aligned} \tag{2.37}$$

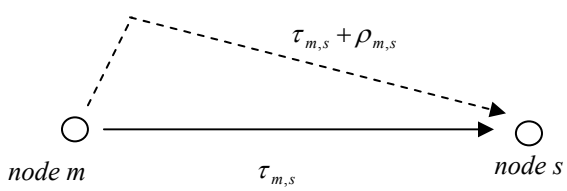

Figure 10: Illustration of signal propagation paths between two nodes.

In this work, a matched filter embedded in the AGC is used to provide a coarse estimation of the ToA of the received UWB monocycle at the receiver. If the NLoS signal is stronger than the LoS component, the threshold detector in the AGC (Fig. 4b) may miss the LoS component and lock onto the NLoS signal instead. A two-way ranging scheme is also being utilized to measure the round-trip propagation delay between the transmitter and receiver and the estimated round-trip delay is used in computing/estimating the difference in initial offset between the oscillators of the two nodes.

When measuring the ToAs of the received signals, it is possible that:

(a) Both nodes m and s lock to the same LoS path. As a result, $\rho_{m,s} = \rho_{s,m} = 0$ and $\tilde{\rho}_{m,s} = 0$.

(b) Both nodes m and s lock to the same path, which however is not the LoS path. As a result, $\rho_{m,s} > 0$ and $\rho_{s,m} > 0$. From the reciprocity relationships between receiving and radiating properties of antenna systems [59], it can be deduced that the same propagation channel is presented to transceivers m and s. Further, if the receiver operations are identical in m and s, the principle of reciprocity[9] implies that $\tau_{m,s} + \rho_{m,s} = \tau_{s,m} + \rho_{s,m}$, therefore $\rho_{m,s} = \rho_{s,m}$ and $\tilde{\rho}_{m,s} = 0$.

(c) Transceivers m and s lock onto different NLoS paths. This can be due to changes in the scattering environment. It is also possible that the receiver in individual node makes a measurement that is different from the other node when tracking the NLoS signal (an example of a NLoS signal is shown in Fig. 8). An algorithm (in each receiver) that attempts to avoid locking onto different paths and find the earliest path is described in [31]. Further, due to manufacturing tolerance, the matched filter at each node may differ.

If scatters that cause the excess delay $\rho_{m,s}$ "re-orientates" itself with respect to the positions of nodes m and s before node s transmits the return-pulse, then it is likely that $\rho_{m,s} \neq \rho_{s,m}$ and $|\rho_{m,s}| > 0$. This is plausible when nodes access the channel in separate time slots which are temporally "far" apart that the scattering environment is no longer stationary. For example, consider a TDMA scheme with $T_f = 10^{-4}$ seconds and one pulse per frame, $K = 1000$ pulses per time slot and N nodes in the network. If each node is to transmit during one time slot and wait for other nodes in the network to finish their transmission in their respective time slots before transmitting again, the temporal spacing between the first pulse of one transmission to another transmission by the same node is $N \cdot K \cdot T_f = N \times 10^{-1}$ seconds.

[9] Exception includes short-wave transmission over long distance [59] and HF systems on long propagation path [18].

Nevertheless, NLoS propagation is undesirable because NLoS signals traveled a longer distance with larger excess delay than LoS propagation. A longer propagation delay will lead to lower SNR at the receiver and hence higher timing jitter.

The variable $\widetilde{\rho}_{m,s}$ will be referred to as the receiver processing error in subsequent discussion and models the asymmetry in the uplink and downlink propagation paths.

2.4 Estimating Differences in Initial Offset and Frame Repetition Rate

We assume transceivers are stationary during measurements. There are at least two different approaches to estimate the differences in oscillator frame repetition rate and initial offset.

One possible approach is to employ a second order delay-locked loop [10] [42] at the receiver to track the UWB pulses from the transmitter. That is, a second order tracking loop is used to correct the difference in frame repetition rate between the transmitter and the receiver. The transmitter will transmit a sequence of monocycles of length K to be pulled-in and tracked by the tracking loop at the receiver, which will then estimate the difference in frame repetition rate $(a_1^{(m)} - a_1^{(s)}) \cdot T_f$ and the ToA of the UWB monocycles at the receiver.

The other possible approach is to process the output of the timing detector using a least squares (LS) estimator without placing the detector in a tracking loop [10]. In this work, we assume that the open loop approach is implemented to estimate the fame frequency differences.

If the timing detector is not embedded in a tracking loop, from (2.17) and $K_D = 1/\breve{g}_{TD} A_w$, the ToA of UWB monocycles at the receiver is the output of the correlative timing detector given by

$$\begin{aligned} x_{(k)} &= K_D A_w \breve{g}_{TD} \cdot (t_{(k)}^{(m)} - t_{(k)}^{(s)} + \tau_{m,s} + \rho_{m,s}) + K_D n_{(k)}^{(s)} \\ &= t_{(k)}^{(m)} - t_{(k)}^{(s)} + \tau_{m,s} + \rho_{m,s} + n_{(k)}^{(s)} / (A_w \breve{g}_{TD}) \\ &= (a_1^{(m)} - a_1^{(s)}) k T_f + d^{(m)} - d^{(s)} + \tau_{m,s} + \rho_{m,s} + \phi_{(k)}^{(m)} - \phi_{(k)}^{(s)} + n_{(k)}^{(s)} / (A_w \breve{g}_{TD}) \ , \end{aligned} \tag{2.38}$$

where $\varsigma_{(k)} = t_{(k)}^{(m)} - t_{(k)}^{(s)} + \tau_{m,s} + \rho_{m,s}$.

Let the difference in frame repetition rate be

$$\begin{aligned}\gamma^{(m,s)} &= (a_1^{(m)} - a_1^{(s)}) \cdot T_f \\ &= a_\delta^{(m,s)} T_f \,,\end{aligned} \tag{2.39a}$$

where $a_\delta^{(m,s)} = a_1^{(m)} - a_1^{(s)}$ and let the propagation delay from m to s plus difference in initial offset be

$$\begin{aligned}\zeta^{(m,s)} &= d^{(m)} - d^{(s)} + \tau_{m,s} + \rho_{m,s} \\ &= d_\delta^{(m,s)} + \tau_{m,s} + \rho_{m,s} \,,\end{aligned} \tag{2.39b}$$

where $d_\delta^{(m,s)} = d^{(m)} - d^{(s)}$. Further, let

$$\varepsilon_{x(k)}^{(m,s)} = \phi_{(k)}^{(m)} - \phi_{(k)}^{(s)} + n_{(k)}^{(s)} / (A_w \breve{g}_{TD}) \,. \tag{2.39c}$$

where $\mathbf{E}\{\varepsilon_{x(k)}^{(m,s)}\} = 0$. The timing detector output given by (2.38) can be expressed as

$$x_{(k)} = \gamma^{(m,s)} \cdot k + \zeta^{(m,s)} + \varepsilon_{x(k)}^{(m,s)} \,. \tag{2.40}$$

Denoting the variance of $x_{(k)}$ by $\sigma_x^2(m,s)$, we have

$$\begin{aligned}\sigma_x^2(m,s) &= \mathbf{V}\{x_{(k)}\} \\ &= \mathbf{E}\{(\varepsilon_{x(k)}^{(m,s)})^2\} \\ &= \mathbf{E}\{(n_{(k)}^{(s)} / (A_w \breve{g}_{TD}))^2\} + \mathbf{E}\{(\phi_{(k)}^{(m)})^2\} + \mathbf{E}\{(\phi_{(k)}^{(s)})^2\} \\ &= \sigma_n^2(m,s) + 2\sigma_\phi^2 \,.\end{aligned} \tag{2.41}$$

Equation (2.41) makes use of (2.22), that is,

$$\sigma_n^2(m,s) = \mathbf{E}\{(n_{(k)}^{(s)} / (A_w \breve{g}_{TD}))^2\} \geq \frac{1}{\Theta_{m,s} \overline{\omega^2}} \,, \tag{2.42a}$$

and from (2.25b),

$$\begin{aligned}\sigma_\phi^2 &= \frac{D_\varphi^1(\Delta)}{\omega_o^2} \\ &\leq \frac{2}{\pi} \int_{-\infty}^{\infty} S_\varphi(\omega) d\omega \,.\end{aligned} \tag{2.42b}$$

A recursive implementation of the LS estimator can be found in [41]. However, the simplicity of the LS estimator in this application leads to a simple batch processing without computing any matrix inverses.

To formulate the LS estimator, consider a more general case when the output of the timing detector is described by

$$x_{(k)} = a_{\delta}^{(m,s)} \cdot T_f \cdot \Delta_{LS} \cdot k + \zeta^{(m,s)} + \varepsilon_{x(k)}^{(m,s)}, \tag{2.43a}$$

where $x_{(k)}$ is obtained at the output of the detector at regular temporal spacing of $\Delta_{LS} \cdot k \cdot T_f$ for $\Delta_{LS} \geq 1$. Equation (2.43a) can be written in vector form with K measurements, such that

$$\begin{bmatrix} x_{(K+K_{ST}-1)} \\ x_{(K+K_{ST}-2)} \\ \vdots \\ x_{(K_{ST}+1)} \\ x_{(K_{ST})} \end{bmatrix} = \mathbf{H} \cdot \begin{bmatrix} \gamma^{(m,s)} \\ \zeta^{(m,s)} \end{bmatrix} + \begin{bmatrix} \varepsilon_{x(K+K_{ST}-1)}^{(m,s)} \\ \varepsilon_{x(K+K_{ST}-2)}^{(m,s)} \\ \vdots \\ \varepsilon_{x(K_{ST}+1)}^{(m,s)} \\ \varepsilon_{x(K_{ST})}^{(m,s)} \end{bmatrix}, \tag{2.43b}$$

where

$$\mathbf{H}^{\mathbf{T}} = \begin{bmatrix} \Delta_{LS} \cdot (K+K_{ST}-1) & \Delta_{LS} \cdot (K+K_{ST}-2) & \cdots & K_{ST} \\ 1 & 1 & \cdots & 1 \end{bmatrix}. \tag{2.43c}$$

It can be shown that the LS estimates of $\gamma^{(m,s)}$ and $\zeta^{(m,s)}$ are [41]

$$\begin{bmatrix} \hat{\gamma}_{LS}^{(m,s)} \\ \hat{\zeta}_{LS}^{(m,s)} \end{bmatrix} = (\mathbf{H}^{\mathbf{T}}\mathbf{H})^{-1}\mathbf{H}^{\mathbf{T}} \cdot \begin{bmatrix} x_{(K+K_{ST}-1)} \\ x_{(K+K_{ST}-2)} \\ \vdots \\ x_{(K_{ST})} \end{bmatrix}. \tag{2.43d}$$

From (2.43d), the LS estimators are [10]

$$\hat{\gamma}_{LS}^{(m,s)} = \frac{12 \sum_{k=K_{ST}}^{K+K_{ST}-1} k \cdot x_{(k)}}{K \cdot (K^2-1) \cdot \Delta_{LS}} - \frac{6 \cdot (K+2K_{ST}-1) \sum_{k=K_{ST}}^{K+K_{ST}-1} x_{(k)}}{K \cdot (K^2-1) \cdot \Delta_{LS}}, \tag{2.43e}$$

$$\hat{\zeta}_{LS}^{(m,s)} = \frac{2 \cdot ((K-1)(2K-1)+6K_{ST}(K+K_{ST}-1)) \sum_{k=K_{ST}}^{K+K_{ST}-1} x_{(k)}}{K \cdot (K^2-1)} - \frac{6 \cdot (K+2K_{ST}-1) \sum_{k=K_{ST}}^{K+K_{ST}-1} k \cdot x_{(k)}}{K \cdot (K^2-1)}, \tag{2.43f}$$

where $k \in \{K_{ST}, ..., K_{ST}+K-1\}$ if K frames are used and $K_{ST} \geq 0$ denotes the time index of the first received pulse.

Substituting (2.43a) into (2.43e), we arrive at

$$\begin{aligned}\hat{\gamma}_{LS}^{(m,s)} =& \frac{12}{K(K^2-1)\cdot\Delta_{LS}}\sum_{k=K_{ST}}^{K+K_{ST}-1}\gamma^{(m,s)}\cdot\Delta_{LS}\cdot k^2 - \frac{6(K+2K_{ST}-1)}{K(K^2-1)\cdot\Delta_{LS}}\sum_{k=K_{ST}}^{K+K_{ST}-1}\gamma^{(m,s)}\cdot\Delta_{LS}\cdot k \\ &+\frac{12}{K(K^2-1)\cdot\Delta_{LS}}\sum_{k=K_{ST}}^{K+K_{ST}-1}k\zeta^{(m,s)} - \frac{6(K+2K_{ST}-1)}{K(K^2-1)\cdot\Delta_{LS}}\sum_{k=K_{ST}}^{K+K_{ST}-1}\zeta^{(m,s)} \\ &+\frac{12}{K(K^2-1)\cdot\Delta_{LS}}\sum_{k=K_{ST}}^{K+K_{ST}-1}k\cdot\varepsilon_{x(k)}^{(m,s)} - \frac{6(K+2K_{ST}-1)}{K(K^2-1)\cdot\Delta_{LS}}\sum_{k=K_{ST}}^{K+K_{ST}-1}\varepsilon_{x(k)}^{(m,s)} \quad . \end{aligned} \tag{2.44}$$

The first two terms of (2.44) evaluate to

$$\begin{aligned}&\frac{12}{K(K^2-1)}\sum_{k=K_{ST}}^{K+K_{ST}-1}\gamma^{(m,s)}k^2 - \frac{6(K+2K_{ST}-1)}{K(K^2-1)}\sum_{k=K_{ST}}^{K+K_{ST}-1}\gamma^{(m,s)}k \\ &=\frac{\gamma^{(m,s)}}{K(K^2-1)}\left(12\sum_{k=K_{ST}}^{K+K_{ST}-1}k^2 - 6(K+2K_{ST}-1)(K_{ST}+K+K_{ST}-1)\frac{K}{2}\right) \\ &=\frac{\gamma^{(m,s)}}{K(K^2-1)}\left(\frac{12K}{6}((K-1)(2K+2K_{ST}-2-2K_{ST}+1))\right. \\ &\quad\left.+\ 6K_{ST}(K+K_{ST}-1))-3(K+2K_{ST}-1)(K+2K_{ST}-1)\cdot K\right) \\ &=\frac{\gamma^{(m,s)}}{K(K^2-1)}\left(K^3-K\right)=\gamma^{(m,s)} \quad . \end{aligned} \tag{2.45a}$$

The second line of (2.44) reduces to

$$\begin{aligned}&\frac{12}{K(K^2-1)\cdot\Delta_{LS}}\sum_{k=K_{ST}}^{K+K_{ST}-1}k\zeta^{(m,s)} - \frac{6(K+2K_{ST}-1)}{K(K^2-1)\cdot\Delta_{LS}}\sum_{k=K_{ST}}^{K+K_{ST}-1}\zeta^{(m,s)} \\ &=\frac{12\zeta^{(m,s)}}{K(K^2-1)\cdot\Delta_{LS}}\cdot\frac{K}{2}(K_{ST}+K+K_{ST}-1) - \frac{6(K+2K_{ST}-1)}{K(K^2-1)\cdot\Delta_{LS}}\cdot K\cdot\zeta^{(m,s)} \\ &=0. \end{aligned} \tag{2.45b}$$

Therefore, $\hat{\gamma}_{LS}^{(m,s)} = \gamma^{(m,s)} + \varepsilon_{\gamma_{LS}}^{(m,s)}$ where the estimation error $\varepsilon_{\gamma_{LS}}^{(m,s)}$ is indicated by the third line of (2.44)

$$\varepsilon_{\gamma_{LS}}^{(m,s)} = \frac{12}{K(K^2-1)\cdot\Delta_{LS}}\sum_{k=K_{ST}}^{K+K_{ST}-1}k\cdot\varepsilon_{x(k)}^{(m,s)} - \frac{6(K+2K_{ST}-1)}{K(K^2-1)\cdot\Delta_{LS}}\sum_{k=K_{ST}}^{K+K_{ST}-1}\varepsilon_{x(k)}^{(m,s)} \quad . \tag{2.45c}$$

From (2.43e) and (2.43f), it can be shown that the estimators are unbiased, i.e.,

$$\mathbf{E}\{\gamma^{(m,s)} - \hat{\gamma}_{LS}^{(m,s)}\} = 0 \,, \tag{2.46a}$$

$$\mathbf{E}\{\zeta^{(m,s)} - \hat{\zeta}_{LS}^{(m,s)}\} = 0 \,, \tag{2.46b}$$

and the LS estimation variances $\sigma^2_{\hat{\gamma}^{(m,s)}_{LS}}$ and $\sigma^2_{\hat{\zeta}^{(m,s)}_{LS}}$ are bounded as follows

$$\begin{aligned}\sigma^2_{\hat{\gamma}^{(m,s)}_{LS}} &= \mathbf{E}\{|\gamma^{(m,s)} - \hat{\gamma}^{(m,s)}_{LS}|^2\} \\ &\geq \frac{12\cdot\mathbf{V}\{\varepsilon^{(m,s)}_{x(k)}\}}{K(K^2-1)\cdot(\Delta_{LS})^2} \xrightarrow{K\ \textbf{large}} 12\frac{\sigma^2_x(m,s)}{K^3\cdot(\Delta_{LS})^2} \ .\end{aligned} \tag{2.47}$$

$$\begin{aligned}\sigma^2_{\hat{\zeta}^{(m,s)}_{LS}} &= \mathbf{E}\{|\zeta^{(m,s)} - \hat{\zeta}^{(m,s)}_{LS}|^2\} \\ &\geq \frac{2\big((K-1)(2K-1)+6K_{ST}(K+K_{ST}-1)\big)\cdot\mathbf{V}\{\varepsilon^{(m,s)}_{x(k)}\}}{K(K^2-1)} \\ &\xrightarrow{K\ \textbf{large}} \frac{2\big(2K^2+6K\cdot K_{ST}+6K^2_{ST}\big)\cdot\sigma^2_x(m,s)}{K^3} \ .\end{aligned} \tag{2.48}$$

From (2.41), $\mathbf{V}\{\varepsilon^{(m,s)}_{x(k)}\} = \mathbf{V}\{x_{(k)}\} = \sigma^2_x(m,s)$. It is illustrated in Fig. 11 that the variance $\sigma^2_{\hat{\zeta}^{(m,s)}_{LS}}$ depends on the starting index K_{ST}.

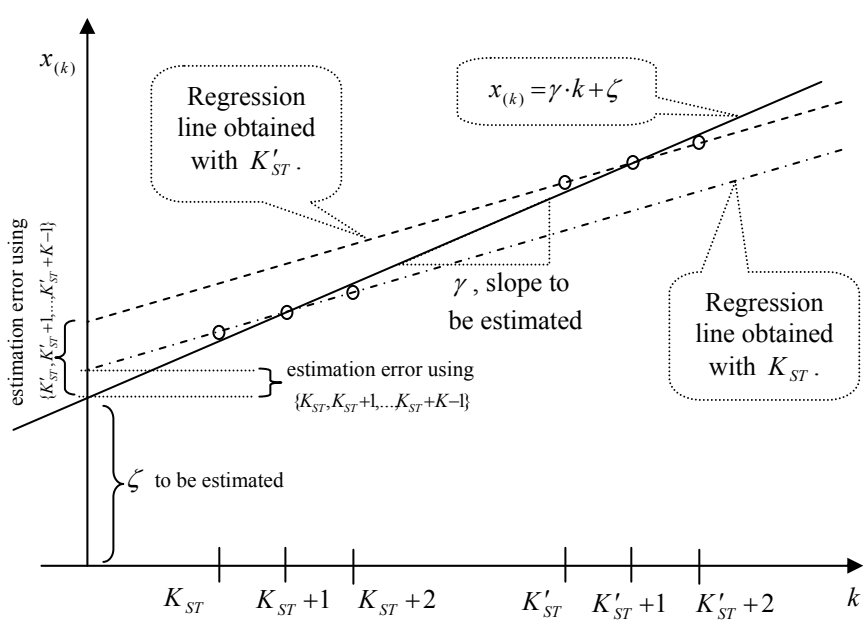

Figure 11: Illustration of estimation error by applying LS on two sets of data with different starting index K_{ST} and K'_{ST} where $K'_{ST} > K_{ST}$. It illustrates that a larger starting index will lead to a larger error in estimating ζ even though error in estimating the slope γ is the same. Note that the error in estimating γ is independent of K_{ST}.

The Cramer-Rao bound of (2.22) is the lower bound on the timing jitter of the open-loop correlative timing detector when the disturbances are caused by AWGN in the channel. The LS estimator is estimating the parameters $\gamma^{(m,s)}$ and $\zeta^{(m,s)}$ given the ToAs' measurement. Using the LS estimator, the variance in estimating $a_{\delta}^{(m,s)}T_f$ and the variance of the estimation error $(\zeta^{(m,s)} - \hat{\zeta}_{LS}^{(m,s)})$ are asymptotically inversely proportional to K^3 and K respectively where K is the number of frames used in the estimation.

According to ([41], pg.112), since

(a) the mean of the measurement error $\varepsilon_{x(k)}^{(m,s)}$ is zero,

(b) $\varepsilon_{x(k)}^{(m,s)}$ are independently identically distributed and

(c) $\mathbf{H}$ is deterministic,

then the LS estimator is unbiased and an efficient estimator within the class of linear estimators. Reference [13] has derived a Cramer-Rao bound on estimating the difference in oscillator frame repetition rate between a pair of transceivers by digitally sampling the received monocycles and applying the least squares technique. If the sampling rate is allowed to go to infinity to generate the continuous time bound, the bound given by [13] reduces to (2.47). Here the bound on the initial offset is obtained as well.

In Fig. 12, the theoretical lower bounds on $\sigma_{\hat{\gamma}_{LS}}^2$ and $\sigma_{\zeta_{LS}^{(m,s)}}^2$ at different K given by (2.47) and (2.48) for $K_{ST}=0$ are plotted alongside their ensemble averages (over 3000 realizations) obtained via simulation implementing equations (2.43e) and (2.43f). In the simulation, the received SNR is $\Theta_{m,s}=30\,dB$, $\overline{\omega^2}=8.5/\sigma_w^2$, $\mathbf{V}\{\varepsilon_{\gamma_{LS}}^{(m,s)}\}=1.176T_s$, $(a_1^{(m)}-a_1^{(s)})\cdot T_f=10T_s$, $\tau_{m,s}+d^{(m)}-d^{(s)}=20T_s$ where T_s is the sampling interval.

It should be noted that either performing LS estimation on the output of the open loop timing detector or embedding the correlative timing detector in an error tracking loop will not be able to

separate the propagation delay $\tau_{m,s}$ from $d^{(m)} - d^{(s)}$ in $\zeta^{(m,s)}$. Other techniques as described in [9] and subsequent chapters are needed to obtain an estimate of the difference in initial offset between transceivers' oscillators.

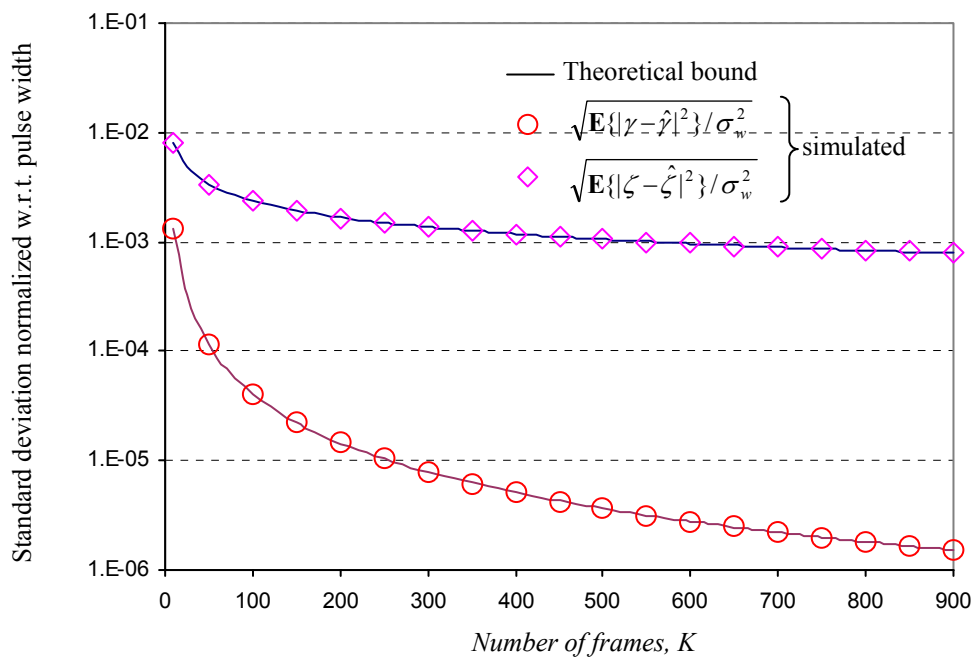

Figure 12: Normalized standard deviation of Least Squares estimates for $\gamma^{(m,s)}$ and $\zeta^{(m,s)}$. The standard deviation of the measurement error is $\sigma_x^2(m,s) = 1.176T_s$ sec at received SNR of $\Theta_{m,s} = 30$ dB where T_s is the sampling interval and K is the number of frames used in the LS estimation.

CHAPTER III

TIME-TRANSFER SCHEME

This Chapter describes the proposed time-transfer scheme to implement a synchronous impulse network. The proposed time-transfer scheme consists of frame-synchronization pulses transmitted from the master node to slave nodes to align the pulse/frame repetition rate of the slaves' oscillator to that of the master. This is followed by two-way ranging to mitigate the unknown signal propagation delay. The measurement system presented in Chapter 2 is utilized to measure the relative ToA of UWB monocycles at the receiver in the presence of additive noise, oscillator phase noise, and NLoS propagation. The estimation technique presented in Chapter 2 is also used to estimate differences in the frame repetition rate and the initial offset between network nodes' oscillator.

Three different arrangements of the frame-synchronization, uplink and downlink frames are presented in this Chapter. They represent three variations of the proposed time-transfer scheme.

3.1 TDMA Time-Transfer Scheme

In Fig. 13, the time-transfer scheme for two nodes (master and slave) in the network is illustrated. The first-step of the proposed time-transfer scheme involves the master node broadcasting frame-synchronization pulses to slave nodes to align the pulse/frame repetition rate of the slaves' oscillator to that of the master. This is followed by two-way ranging to mitigate the unknown signal propagation delay. The initial timing offset between the master m and slave s with timing functions $T^{(m)}(t)$ and $T^{(s)}(t)$ respectively is $d^{(m)} - d^{(s)}$. The signal propagation delay from m to s is $\tau_{m,s} + \rho_{m,s}$ where $\rho_{m,s}$ is the excess-delay. The difference $\widetilde{\rho}_{m,s} = (\rho_{m,s} - \rho_{s,m})/2$ is used to model receiver processing error resulting from non-symmetry of the uplink and downlink ToAs measured by the receiver. More details on $\widetilde{\rho}_{m,s}$ are given in section 2.3.4.

Let the ToAs of the frame-synchronization and downlink pulses transmitted from master to slave and measured with respect to the receiver oscillator timing be Ω_{SY} and Ω_{DN} respectively. Similarly, Ω_{UP} with subscript *'UP'*, denotes the ToA of the uplink pulses transmitted from slave to the master and measured with respect to the master's oscillator. In the following equations, the subscript in parenthesis $(\circ)_{(z)}$ is used to indicate dependency on time of measurement. The integer indices v, u and z will be defined later and direction of the transmission is indicated as subscript without parenthesis, e.g. master to slave as 'm,s'.

Let $n_{(v)}^{(s)}$, $n_{(u)}^{(m)}$ and $n_{(z)}^{(s)}$ be the additive channel noise at the output of the timing detector of node m or s (indicated by the superscript in parenthesis) present at time vT_f, uT_f and zT_f respectively and described by (2.14c). The amplitude of the received UWB monocycle at nodes m and s are denoted by $A_w^{(m)}$ and $A_w^{(s)}$ respectively.

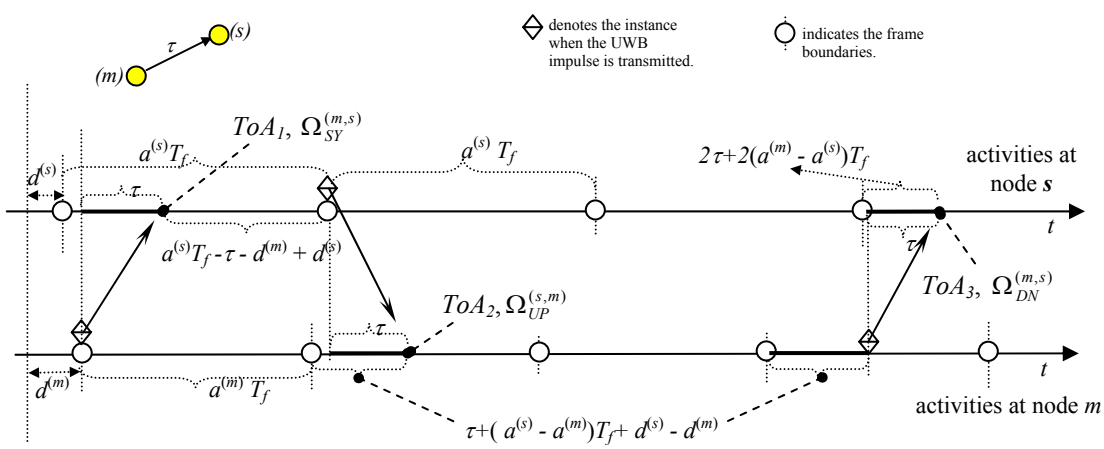

Figure 13: A jitter-free diagram illustrating the parameters used to compute the timing offset. Timings generated by transceivers oscillators are scaled by their respective drift rate $a_1^{(s)}$ while all annotated parameters such as τ, $d^{(m)}$ and $d^{(s)}$ are timed by the ideal oscillator ("true time"). It is assumed that the width of the impulses, which is stretched by the transmitter drift rate, does not affect determination of its ToA at the receiver.

The synchronizing scheme, illustrated in Fig. 13, works as follows. The master starts by broadcasting frame-synchronization pulses at $t_{(v)}^{(m)}$ for $v = K_{ST} + k$ and values of k in $\{0,1,2,3,...,K_s - 1\}$ to all other transceivers in the network. The variable $K_{ST} \geq 0$ is the starting index of the transmitted pulses. The start of the time-transfer process is indicated by $K_{ST} = 0$. The slave transceiver measures the relative ToA $\Omega_{SY(v)}^{(m,s)}(k)$ of the vth frame-synchronization pulse with respect to the start of its vth frame. The relative ToA, $\Omega_{SY(v)}^{(m,s)}(k)$ is the output of the correlative timing detector when the receiver (at node s) is tracking the UWB monocycles transmitted from node m. Therefore from (2.38), $\Omega_{SY(v)}^{(m,s)}(k) = x_{(k)}$ and

$$\begin{aligned}\Omega_{SY(v)}^{(m,s)}(k) &= \tau_{m,s} + t_{(v)}^{(m)} - t_{(v)}^{(s)} + \rho_{m,s} + n_{(v)}^{(s)} / (A_w^{(s)} \breve{g}_{TD}) \\ &= \zeta_{SY}^{(m,s)} + \gamma^{(m,s)} \cdot (k + K_{ST}) + \varepsilon_{SY}^{(m,s)} .\end{aligned} \tag{3.1}$$

where $d_\delta^{(m,s)} = d^{(m)} - d^{(s)}$, $a_\delta^{(m,s)} = a_1^{(m)} - a_1^{(s)}$, $\zeta_{SY}^{(m,s)} = \tau_{m,s} + d_\delta^{(m,s)} + \rho_{m,s}$, $\gamma^{(m,s)} = a_\delta^{(m,s)} T_f$ and $\varepsilon_{SY}^{(m,s)} = \mu_{(v)} + n_{(v)}^{(s)} / (A_w^{(s)} \breve{g}_{TD})$. We have defined the random variable $\mu_{(v)}$ as

$$\mu_{(v)} = \phi_{(v)}^{(m)} - \phi_{(v)}^{(s)} . \tag{3.2}$$

If there are N transceivers in the network, then in its assigned time slot, e.g., time slot j, $j \in \{2,...,N\}$ (the index '1' is reserved for the first master node that starts the time-transfer process), each slave transceiver will transmit K_r up-link ranging pulses in contiguous frames to the master. These pulses will arrive at the jth slot of the master node. The ToA measured with respect to the frame boundaries of the master node is

$$\begin{aligned}\Omega_{UP(u)}^{(s,m)}(k) &= \tau_{s,m} + t_{(u)}^{(s)} - t_{(u)}^{(m)} + \rho_{s,m} + n_{(u)}^{(m)} / (A_w^{(m)} \breve{g}_{TD}) \\ &= \zeta_{UP}^{(s,m)} + \gamma^{(s,m)} \cdot u + \varepsilon_{UP(u)}^{(s,m)} .\end{aligned} \tag{3.3a}$$

The frame index u is measured with respect to the start of the time-transfer process. It indicates the frame at which the uplink pulse is transmitted and is given by

$$u = K_s + (j-2)K_r + k + K_{ST} , \tag{3.3b}$$

and $k \in \{0,1,2,3,4,...,K_r-2,K_r-1\}$, $d_\delta^{(m,s)} = d^{(m)} - d^{(s)}$, $\gamma^{(s,m)} = -a_\delta^{(m,s)} T_f$, $a_\delta^{(m,s)} = a_1^{(m)} - a_1^{(s)}$, $\zeta_{UP}^{(s,m)} = \tau_{s,m} - d_\delta^{(m,s)} + \rho_{s,m}$, and $\varepsilon_{UP(u)}^{(s,m)} = -\mu_{(u)} + n_{(u)}^{(m)} / (A_w^{(m)} \breve{g}_{TD})$.

The master will 'transpond' the received ranging pulse from individual slaves to the designated downlink time slot and re-transmit it as the return ranging pulse. The result of transponding is to transmit downlink pulses from m to s at time instances

$$\Omega_{UP(u)}^{(s,m)}(k) + t_{(z)}^{(m)},$$

where z is the frame index of the downlink transmission given by

$$z = K_s + (N-1)K_r + (i-2)K_r + k + K_{ST}, \tag{3.4a}$$

and i, $i \in \{2,..,N\}$, i not necessary equal to j, identifies the downlink time slot. Therefore the ToA of the return pulse at the slave is

$$\begin{aligned}\Omega_{DN(z)}^{(m,s)}(k) &= \tau_{m,s} + \Omega_{UP(u)}^{(s,m)}(k) + t_{(z)}^{(m)} + \rho_{m,s} + n_{(z)}^{(s)} / (A_w^{(s)} \breve{g}_{TD}) - t_{(z)}^{(s)} \\ &= 2\tau_{m,s} + t_{(z)}^{(m)} - t_{(u)}^{(m)} - t_{(z)}^{(s)} + t_{(u)}^{(s)} + \rho_{m,s} + \rho_{s,m} \\ &\quad + n_{(u)}^{(m)} / (A_w^{(m)} \breve{g}_{TD}) + n_{(z)}^{(s)} / (A_w^{(s)} \breve{g}_{TD}) \\ &= \zeta_{DN}^{(m,s)} + \gamma^{(m,s)} \cdot (z-u) + \varepsilon_{DN(z)}^{(m,s)},\end{aligned} \tag{3.4b}$$

where $\zeta_{DN}^{(m,s)} = \tau_{s,m} + \tau_{m,s} + \rho_{m,s} + \rho_{s,m}$ and $\varepsilon_{DN(z)}^{(m,s)} = \mu_{(z)} - \mu_{(u)} + \dfrac{n_{(z)}^{(s)}}{A_w^{(s)} \breve{g}_{TD}} + \dfrac{n_{(u)}^{(m)}}{A_w^{(m)} \breve{g}_{TD}}$.

It is assumed that there is no inter-frame interference. The timing-offset equation derived at the slave transceiver after the master has broadcast K_s frame-synchronization pulses during the first time slot, and completion of K two-way ranging pulses/frames at the jth uplink and i^{th} downlink time slot is defined as

$$\vartheta^{(m,s)}(k) = \Omega_{DN(z)}^{(m,s)}(k)/2 - \Omega_{SY(v)}^{(m,s)}(k). \tag{3.5a}$$

The timing-offset equation given in (3.5a) gives an estimate of the difference in initial offset between nodes m and s. In Fig. 14, the ToAs, $\Omega_{SY(v)}^{(m,s)}(k)$, $\Omega_{UP(u)}^{(s,m)}(k)$ and $\Omega_{DN(z)}^{(m,s)}(k)$ are illustrated together with the frame indices.

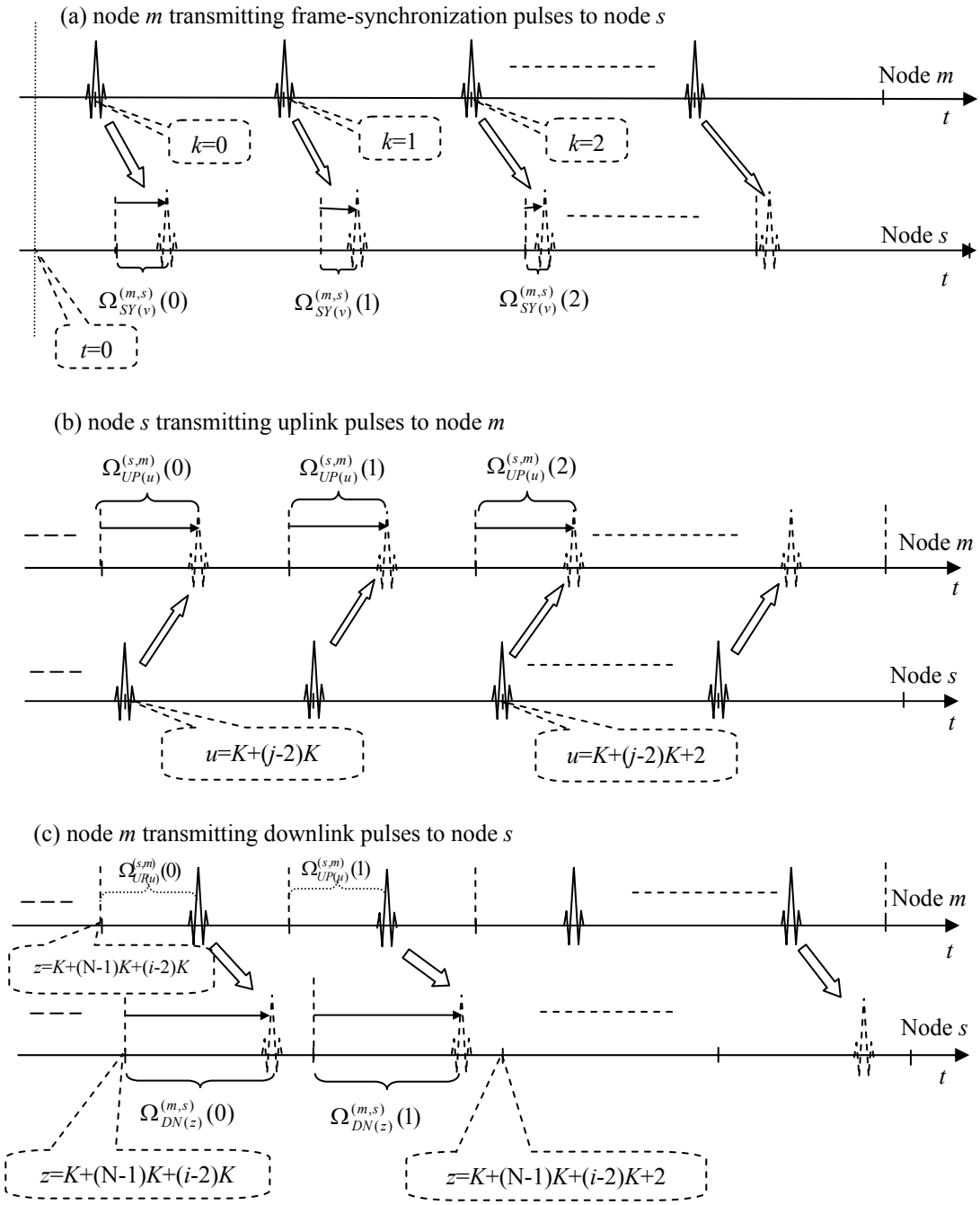

Figure 14: Illustration of the time indices when transmitting the frame-synchronization, uplink and downlink ranging pulses for time-transfer scheme A. In this example, it is assumed that $K_{ST}=0$, the uplink slot is j and the downlink slot is i.

For simplicity, in subsequent analysis, we consider the case in which $K = K_s = K_r$ and $i = j$. If there are K measurements of $\vartheta^{(m,s)}(k)$, $k \in \{0,1,2,...,K-1\}$, then collecting these K measurements, (3.5a) can be expressed in vector form as

$$\begin{bmatrix} \vartheta^{(m,s)}(K-1) \\ \vdots \\ \vartheta^{(m,s)}(2) \\ \vartheta^{(m,s)}(1) \\ \vartheta^{(m,s)}(0) \end{bmatrix} = \frac{1}{2} \begin{bmatrix} \Omega_{DN(z)}^{(m,s)}(K-1) \\ \vdots \\ \Omega_{DN(z)}^{(m,s)}(2) \\ \Omega_{DN(z)}^{(m,s)}(1) \\ \Omega_{DN(z)}^{(m,s)}(0) \end{bmatrix} - \begin{bmatrix} \Omega_{SY(v)}^{(m,s)}(K-1) \\ \vdots \\ \Omega_{SY(v)}^{(m,s)}(2) \\ \Omega_{SY(v)}^{(m,s)}(1) \\ \Omega_{SY(v)}^{(m,s)}(0) \end{bmatrix}. \tag{3.5b}$$

That is,

$$\vec{\vartheta}^{(m,s)} = \frac{1}{2} \cdot \vec{\Omega}_{DN(z)}^{(m,s)} - \vec{\Omega}_{SY(v)}^{(m,s)}, \tag{3.5c}$$

where

$$\vec{\Omega}_{DN(z)}^{(m,s)} = \begin{bmatrix} \Omega_{DN(z)}^{(m,s)}(K-1) \\ \vdots \\ \Omega_{DN(z)}^{(m,s)}(2) \\ \Omega_{DN(z)}^{(m,s)}(1) \\ \Omega_{DN(z)}^{(m,s)}(0) \end{bmatrix}, \ \vec{\Omega}_{SY}^{(m,s)} = \begin{bmatrix} \Omega_{SY(v)}^{(m,s)}(K-1) \\ \vdots \\ \Omega_{SY(v)}^{(m,s)}(2) \\ \Omega_{SY(v)}^{(m,s)}(1) \\ \Omega_{SY(v)}^{(m,s)}(0) \end{bmatrix} \text{ and } \vec{\vartheta}^{(m,s)} = \begin{bmatrix} \vartheta^{(m,s)}(K-1) \\ \vdots \\ \vartheta^{(m,s)}(2) \\ \vartheta^{(m,s)}(1) \\ \vartheta^{(m,s)}(0) \end{bmatrix}.$$

Substituting (3.1) and (3.4b) into (3.5a) gives

$$\begin{aligned} \vartheta^{(m,s)}(k) = & \frac{t_{(z)}^{(m)} - t_{(u)}^{(m)} - t_{(z)}^{(s)} + t_{(u)}^{(s)}}{2} - t_{(v)}^{(m)} + t_{(v)}^{(s)} \\ & + \frac{1}{2}\left(\frac{n_{(u)}^{(m)}}{A_w^{(m)} \breve{g}_{TD}} + \frac{n_{(z)}^{(s)}}{A_w^{(s)} \breve{g}_{TD}} \right) - \frac{n_{(v)}^{(s)}}{A_w^{(s)} \breve{g}_{TD}} \\ & + \frac{\rho_{s,m} - \rho_{m,s}}{2} \\ = & \frac{a_1^{(s)} u T_f - a_1^{(m)} u T_f + a_1^{(m)} z T_f - a_1^{(s)} z T_f}{2} \\ & - a_1^{(m)} \cdot (k + K_{ST}) \cdot T_f + a_1^{(s)} \cdot (k + K_{ST}) \cdot T_f + d^{(s)} - d^{(m)} + \frac{\rho_{s,m} - \rho_{m,s}}{2} + \varepsilon_{\vartheta}^{(m,s)} \\ = & \frac{(a_1^{(m)} - a_1^{(s)}) \cdot (z - u - 2v) \cdot T_f}{2} + d^{(s)} - d^{(m)} + \frac{\rho_{s,m} - \rho_{m,s}}{2} + \varepsilon_{\vartheta}^{(m,s)}, \end{aligned} \tag{3.6a}$$

where $\varepsilon_{\vartheta}^{(m,s)}$ is the random fluctuation with zero mean given by

$$\begin{aligned}\varepsilon_{\vartheta}^{(m,s)} &= \frac{\phi_{(u)}^{(s)} - \phi_{(u)}^{(m)} + \phi_{(z)}^{(m)} - \phi_{(z)}^{(s)}}{2} - \phi_{(v)}^{(m)} + \phi_{(v)}^{(s)} - \frac{n_{(v)}^{(s)}}{A_w^{(s)} \breve{g}_{TD}} + \frac{n_{(u)}^{(m)} / (A_w^{(m)} \breve{g}_{TD}) + n_{(z)}^{(s)} / (A_w^{(s)} \breve{g}_{TD})}{2} \\ &= \frac{\mu_{(z)} - \mu_{(u)}}{2} - \mu_{(v)} - \frac{n_{(v)}^{(s)}}{A_w^{(s)} \breve{g}_{TD}} + \frac{n_{(u)}^{(m)} / (A_w^{(m)} \breve{g}_{TD}) + n_{(z)}^{(s)} / (A_w^{(s)} \breve{g}_{TD})}{2} . \end{aligned} \tag{3.6b}$$

It is assumed that the oscillator phase noise, $\phi_{(k)}^{(m)}$ and $\phi_{(k)}^{(s)}$, $k \in \{v,u,z\}$ are i.i.d., therefore

$$\mathbf{E}\{\mu_{(z)}^2\} = \mathbf{E}\{\mu_{(u)}^2\} = \mathbf{E}\{\mu_{(v)}^2\} . \tag{3.7a}$$

From (2.25a) and (2.25b),

$$\mathbf{E}\{\mu_{(v)}^2\} = \mathbf{E}\{(\phi_{(v)}^{(m)} - \phi_{(v)}^{(s)})^2\} = 2\sigma_{\phi}^2 . \tag{3.7b}$$

The noise variances are

$$\mathbf{E}\left\{\frac{n_{(v)}^{(s)}}{A_w^{(s)} \mu_{TD}}\right\} = \mathbf{E}\left\{\frac{n_{(z)}^{(s)}}{A_w^{(s)} \mu_{TD}}\right\} = \sigma_n^2(m,s) , \tag{3.8a}$$

$$\mathbf{E}\left\{\frac{n_{(u)}^{(m)}}{A_w^{(m)} \mu_{TD}}\right\} = \sigma_n^2(s,m) . \tag{3.8b}$$

Therefore the variance of $\varepsilon_{\vartheta}^{(m,s)}$ is

$$\begin{aligned}\mathbf{V}\{\varepsilon_{\vartheta}^{(m,s)}\} &= \frac{3}{2} \cdot (2\sigma_{\phi}^2) + \frac{5}{4} \cdot \sigma_n^2(m,s) + \frac{1}{4} \cdot \sigma_n^2(s,m) \\ &= \frac{5 \cdot \sigma_x^2(m,s) + \sigma_x^2(s,m)}{4} , \end{aligned} \tag{3.9}$$

where $\sigma_x^2(m,s) = 2\sigma_{\phi}^2 + \sigma_n^2(m,s)$. In (3.6a), $\vartheta^{(m,s)}(k)$ is a function of the initial offset and is independent of the propagation delay between nodes m and s if $\rho_{m,s} - \rho_{s.m} = 0$. The short-term variations in (3.6b) are assumed to have zero means.

Note that for the time-transfer scheme illustrated in Fig. 14, the difference in the downlink and uplink frame index is

$$\begin{aligned} z - u &= (N - 1 + i - j) K_r \\ &= (N-1) K . \end{aligned} \tag{3.10}$$

From (3.6a), it is observed that if $a_1^{(m)} = a_1^{(s)}$, then $|\vartheta^{(m,s)}(k)|$ is not a function of time index k.

Since $\tilde{\rho}_{m,s} = (\rho_{m,s} - \rho_{s,m})/2$, $d_\delta^{(m,s)} = d^{(m)} - d^{(s)}$, $a_\delta^{(m,s)} = a_1^{(m)} - a_1^{(s)}$ and for $i = j$, let

$$\begin{aligned}\theta(k) &= \frac{z-u-2k}{2} \\ &= \frac{(N-1+i-j)K_r - 2k}{2} \\ &= \frac{(N-1)K-2k}{2} \quad . \end{aligned} \tag{3.11}$$

The quantity $\theta(k)$ is a function of the transmission index of the frame-synchronization, uplink and downlink pulses and is specific to the time-transfer scheme shown in Fig. 14. The function $\theta(k)$ will be called the characteristics function of the time-transfer scheme in subsequent analysis. Replacing $(z-u-2k)/2$ in (3.6a) with $\theta(k)$, the initial-offset equation becomes

$$\begin{aligned}\vartheta^{(m,s)}(k) &= \frac{\Omega_{DN(z)}^{(m,s)}(k)}{2} - \Omega_{SY}^{(m,s)}(k) \\ &= -d_\delta^{(m,s)} - \tilde{\rho}_{m,s} + \varepsilon_\vartheta^{(m,s)} + (\theta(k) - K_{ST}) \cdot a_\delta^{(m,s)} T_f \quad . \end{aligned} \tag{3.12}$$

3.2 Bounds on Number of Network Nodes

As mentioned earlier, the proposed time-transfer scheme assumed that monocycles arrived at the receiver at its designated frame within specific time slots. In the absence of noise and interference, the differences in the frame repetition rate $a_\delta^{(m,s)} T_f = (a_1^{(m)} - a_1^{(s)}) \cdot T_f$ and initial offset $d_\delta^{(m,s)} = (d^{(m)} - d^{(s)})$ between master and slaves determine the number of nodes N we can place in the network such that UWB impulses would arrive at the designated time slots and the TDMA scheme is not violated. Further, to avoid inter-frame interference, let τ' includes the delay spread of the channel[10].

[10] In IEEE 802.15.3a UWB channel model [19], the channel models CM1, CM2, CM3 and CM4 specifies root-mean-squares delay spread of 5, 8, 14 and 26 nanoseconds respectively.

Although nodes access the channel by time division multiplexing, nodes in the network have different initial offsets, frame repetition rates and transmitted pulses travelled different distances before arriving at, for example, the master node. As a result, as illustrated in Fig. 15, it is not always possible that there is only one received monocycle (corresponds to each transmitter) per frame, being received at the master node. In order for the master node to perform transponding and transfer its timing to the slave nodes, the master node must be able to associate the received monocycles with the transmitter. And hence there are bounds on the number of network nodes given the maximum differences in oscillator parameters among pair of network nodes.

The first bound on N can be deduced from the requirement that ToA_1, $\Omega_{SY(v)}^{(m,s)}(k)$ (illustrated in Figs. 13 and 14) needs to be within the designated receiving time slot of the slave transceiver, and for the last transmitted pulse in the time slot, $0<\Omega_{SY(v)}^{(m,s)}(K_s-1)<a_1^{(s)}T_f$. With $K_{ST}=0$, this leads to the inequalities

$$a_\delta^{(m,s)}\cdot(K_s-1)\cdot T_f+\tau'>d^{(s)}-d^{(m)}, \tag{3.13a}$$

$$d^{(s)}-d^{(m)}>a_\delta^{(m,s)}\cdot(K_s-1)\cdot T_f+\tau'-a_1^{(s)}T_f. \tag{3.13b}$$

Applying a similar restriction on ToA_2, $\Omega_{UP(u)}^{(s,m)}(k)$ for $a_\delta^{(m,s)}K_rT_f>0$ and analyzing the typical case when $j=N$, $k=K_r-1$ in (3.3a), produces the inequalities

$$N>\frac{-d_\delta^{(m,s)}+\tau'-a_1^{(m)}T_f-a_\delta^{(m,s)}T_f(K_s-K_r-1)}{a_\delta^{(m,s)}K_rT_f}, \tag{3.14a}$$

$$N<\frac{-d_\delta^{(m,s)}+\tau'-a_\delta^{(m,s)}T_f\cdot(K_s-K_r-1)}{a_\delta^{(m,s)}K_rT_f}. \tag{3.14b}$$

For $a_\delta^{(m,s)}K_rT_f>0$, the bound on ToA_3, $\Omega_{DN(z)}^{(m,s)}(k)$ and for $k=K_r-1$ is $0<\Omega_{DN(z)}^{(m,s)}(K_r-1)<a_1^{(s)}T_f$. This leads to

$$N>\frac{2\tau'}{-a_\delta^{(m,s)}K_rT_f}-i+j+1, \tag{3.15a}$$

$$N < \frac{a_1^{(s)} T_f - 2\tau'}{a_\delta^{(m,s)} K_r T_f} - i + j + 1 . \tag{3.15b}$$

The corresponding inequalities on N if $a_\delta^{(m,s)} K_r T_f < 0$ can be derived similarly. The upper bound on N for master-slave time-transfer is obtained by combining the inequalities (3.13), (3.14) and (3.15) and their dual when $a_\delta^{(m,s)} K T_f < 0$.

To obtain numerical values on N, the communicating range of the UWB transceiver is assumed to be between 1 and 10 m, therefore the LoS propagation delay between two nodes m and s, denoted by $\tau_{m,s}$, is in the order of $3\text{x}10^{-8}$ sec. In Fig. 16, we plotted the upperbound on N with $\tau' \in \{10^{-8}, 2\text{x}10^{-8}, 3\text{x}10^{-8}\}$ sec, ignoring NLoS measurement error, considering $T_f \in \{10^{-3}, 10^{-4}, 10^{-6}\}$ sec and $N > 0$, $d^{(m)} = d^{(s)}$, $a_1^{(m)} = 1$ and $a_1^{(s)} = a_1^{(m)} \pm \eta$ where η is a small number that represents the largest difference in drift between pair of oscillators in the network. We have arbitrarily let $K = K_s = K_r = 512$ and $i = j$ in Fig. 16. It illustrates that at $\eta = 10^{-9}$, $\tau' = 3\times10^{-8}$ and $T_f = 10^{-3}$, $N < 120$.

For a fixed number of frames, a longer T_f implies that for the same drift difference $|\eta|$, the oscillator in each node would have drifted further apart than when T_f is small for the same elapsed "true" time (the time measured by the standard source). Thus a UWB monocycle transmitted in the last frame of the ranging time slot and propagates to the receiver with a finite propagation delay would not arrive within its designated time slot if $|\eta|$ is not sufficiently small. Thus fewer nodes can be supported when frame times T_f are longer.

For a given T_f and $T_f >> \tau'$, if the propagation delay τ' is short, because of difference in frame repetition rate, a transmitted pulse would arrive at the receiver before its designated time slot as the transmitter and receiver oscillators drift further apart.

The situations mentioned in the previous two paragraphs (illustrated in Fig. 17) will lead to multiple or no received monocycle at the receiver.

The requirement that pulses arrived at their respective time slot can be "relaxed" if some form of coding is applied onto the transmitted pulses to differentiate transmission of one node from the other nodes in the network. Then, instead of lock-onto a single pulse, the receiver has to lock-onto a coded train of pulses (also known as spreading codes). For simplicity in discussion, the following analysis does not incorporate a spreading code. However the transmitted monocycle in the following analysis can be spread using a chip sequence and the matched filter described in Chapter 2 matched to the chip sequence of individual nodes so as to measure the ToAs of pulses at the receiver. Then the measured ToAs will not be affected by the application of a spreading code sequence. However, pulses from different transceivers may interfere with each other at the receiver as illustrated in Fig. 15 resulting in multiple-access-interference (MAI).

From Figs. 15 and 16, it can be inferred that nodes in the network should be in some form of coarse synchronization via UWB acquisition or factory setting to ensure $d^{(m)} \approx d^{(s)}$ and $a_1^{(m)} \approx a_1^{(s)}$ before the start of the SIN synchronization process.

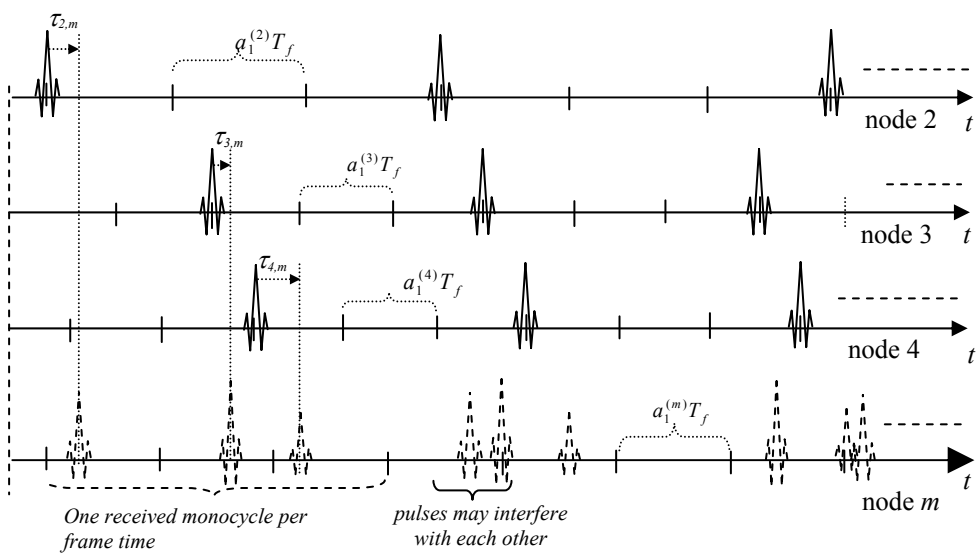

Figure 15: Illustration of the effect of differences in initial offsets and frame repetition rates between the master and slave nodes in the network. The master node may receive multiple or no monocycles per frame time as illustrated in this figure. Moreover, pulses may interfere with each other at the receiver resulting in multiple-access-interference (MAI).

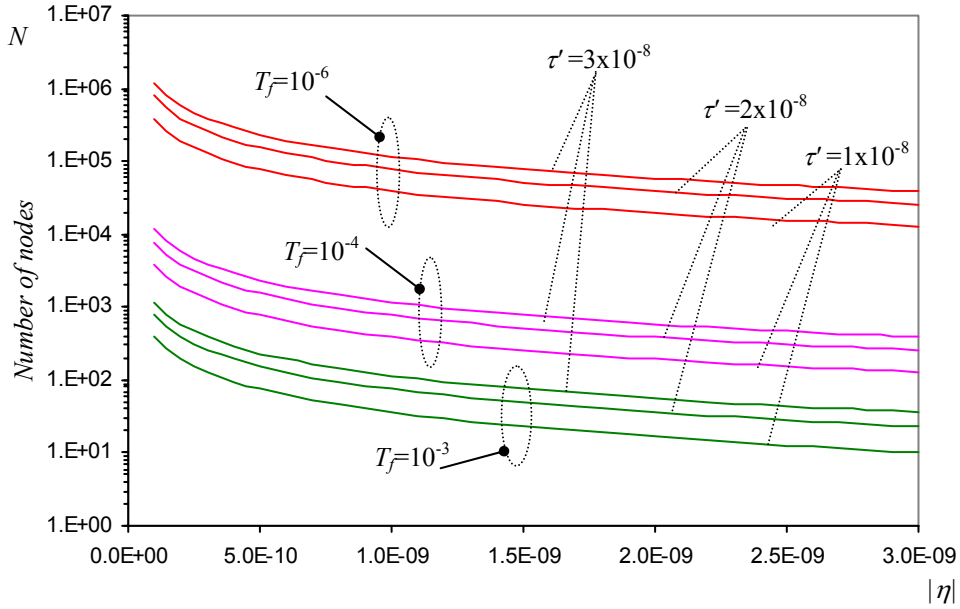

Figure 16: Upper bound on the number of nodes in the network N when the difference in oscillator drift η is allows to vary assuming there is no jitter or measurement errors and K=512. The y-axis is in log scale.

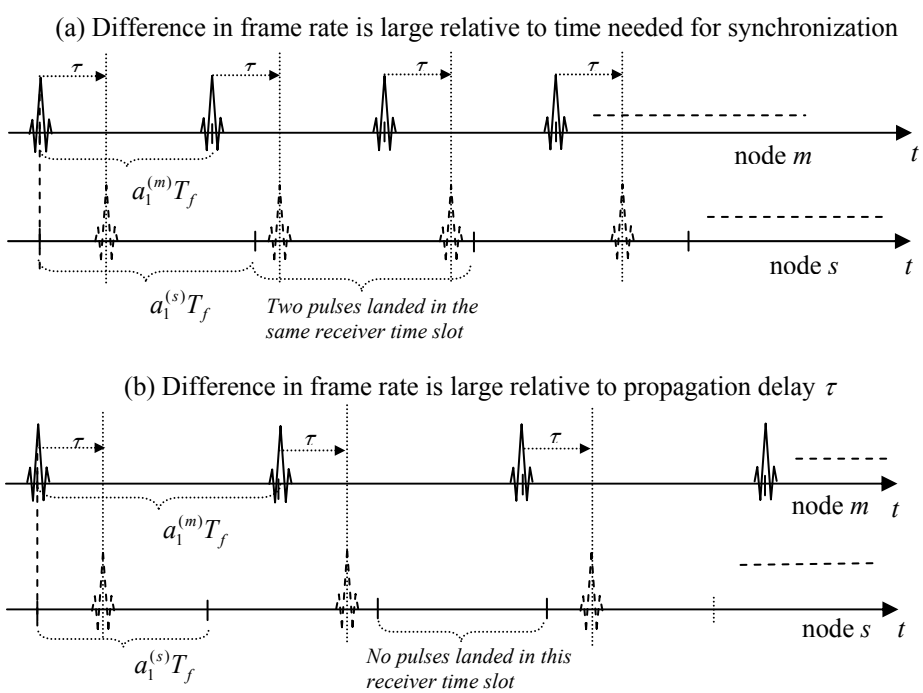

Figure 17: Illustration of cases when there is no or multiple received monocycles per frame time at the receiver.

3.3 Oscillator Timing Adjustment

Timing is said to have transferred from one node to another if both oscillators are ticking at the same time after synchronization. This entails that both nodes, after time-transfer, have the same initial offset $d^{(m)}$ with respect to the true time t and the same drift $a_1^{(m)}$. If nothing is done to effect the time-transfer, the timing of both nodes will drift further apart as "t" progresses. For example, for a length of time equivalent to the duration needed to perform time transfer using the synchronization scheme proposed in section 3.1, the timing difference between a pair of nodes m and s would have been (ignoring all the zero mean random variables/disturbances)

$$t_{((2N-1)K)}^{(m)} - t_{((2N-1)K)}^{(s)} = a_{\delta}^{(m,s)} T_f \cdot 2(N-1)K + d_{\delta}^{(m,s)} . \tag{3.16}$$

Thus $d_{\delta}^{(m,s)} = d^{(m)} - d^{(s)}$ and $a_{\delta}^{(m,s)} = a_1^{(m)} - a_1^{(s)}$ have to be estimated from the ToA measurements $\{\Omega_{SY(v)}^{(m,s)}(k)\}_{k=0}^{K-1}$, $\{\Omega_{UP(u)}^{(s,m)}(k)\}_{k=0}^{K-1}$ and $\{\Omega_{DN(z)}^{(m,s)}(k)\}_{k=0}^{K-1}$ to correct for the accumulated timing error. There are various ways to derive an estimate of $d_{\delta}^{(m,s)}$ and $a_{\delta}^{(m,s)}$ from the ToA measurements depending on the design criteria.

The bounds, shown in Fig. 16, on the number of network nodes that can be synchronized with the proposed time transfer scheme are derived without taking into considerations the effects of the oscillator phase noise and additive noise in the channel. No processing is performed on the measured ToAs to estimate and correct for the initial offset and frame repetition rate differences until possibly at the end of the two-way ranging. These bounds indicate that in order to maximize the number of nodes in the network, the difference in frame repetition rate must be as small as possible.

In this work, we set off to design a synchronous impulse network that is capable of synchronizing as many nodes as possible for applications such as implementing a time-synchronous sensor network. Thus the first task of the proposed synchronization scheme is to synchronize the frame repetition rate of all nodes in the network.

In the following, an approach that is based on the LS estimation techniques described in Chapter 2 will be presented.

For the time-transfer scheme described in section 3.1, from (2.47), the LS estimates of $\gamma^{(m,s)} = (a_1^{(m)} - a_1^{(s)}) \cdot T_f$, denoted as $\hat{\gamma}_{LS}^{(m,s)}$, obtained from $\Omega_{SY(v)}^{(m,s)}(k)$, has estimation error variance

$$\begin{aligned}\sigma^2_{\hat{\gamma}_{LS}^{(m,s)}} &= \mathbf{E}\{|\gamma^{(m,s)} - \hat{\gamma}_{LS}^{(m,s)}|^2\} \\ &= \mathbf{V}\{\varepsilon_{\gamma_{LS}}^{(m,s)}\} \\ &\geq 12 \cdot \sigma_x^2(m,s)/K^3 . \end{aligned} \tag{3.17}$$

Note that the relative ToAs $\{\Omega_{SY(v)}^{(m,s)}(k)\}_{k=0}^{K-1}$ at the output of the timing detector is obtained at the frame-repetition rate $a_1^{(s)} T_f$ of node s if node s received the transmitted monocycles from m. After determining $\hat{\gamma}_{LS}^{(m,s)}$, the node s's oscillator is updated and $\Omega_{SY(v)}^{(m,s)}(k)$ is recomputed/estimated to be

$$\begin{aligned}\hat{\Omega}_{SY(v)}^{(m,s)}(k) &= \Omega_{SY(v)}^{(m,s)}(k) - \hat{\gamma}_{LS}^{(m,s)} \cdot (k + K_{ST}) \\ &= \zeta_{SY}^{(m,s)} + \gamma^{(m,s)} \cdot (k + K_{ST}) + \varepsilon_{SY}^{(m,s)} - \hat{\gamma}_{LS}^{(m,s)} \cdot (k + K_{ST}) \\ &= \zeta_{SY}^{(m,s)} + \varepsilon_{SY}^{(m,s)} + (\gamma^{(m,s)} - \hat{\gamma}_{LS}^{(m,s)}) \cdot (k + K_{ST}) \\ &= \zeta_{SY}^{(m,s)} + \varepsilon_{SY}^{(m,s)} - \varepsilon_{\gamma_{LS}}^{(m,s)} \cdot (k + K_{ST}) , \end{aligned} \tag{3.18}$$

where $\varepsilon_{\gamma_{LS}}^{(m,s)}$ is the error in estimating $\gamma^{(m,s)}$ with variance $\sigma^2_{\hat{\gamma}_{LS}^{(m,s)}}$ given by (3.17) and from (2.45c), $\hat{\gamma}_{LS}^{(m,s)} = \gamma^{(m,s)} + \varepsilon_{\gamma_{LS}}^{(m,s)}$. After the slave's frame repetition rate is updated, the new frame repetition rate, denoted by $\hat{a}_1^{(s)} T_f$, is

$$\begin{aligned}\hat{a}_1^{(s)} T_f &= a_1^{(s)} T_f + \hat{\gamma}_{LS}^{(m,s)} \\ &= a_1^{(s)} T_f + a_1^{(m)} T_f - a_1^{(s)} T_f + \varepsilon_{\gamma_{LS}}^{(m,s)} \\ &= a_1^{(m)} T_f + \varepsilon_{\gamma_{LS}}^{(m,s)} . \end{aligned} \tag{3.19}$$

Similarly, the uplink and downlink ToAs are

$$\begin{aligned}\hat{\Omega}_{UP(u)}^{(s,m)}(k) &= \zeta_{UP}^{(s,m)} + (\hat{a}_1^{(s)} T_f - a_1^{(m)} T_f) \cdot u + \varepsilon_{UP(u)}^{(s,m)} \\ &= \zeta_{UP}^{(s,m)} + (a_1^{(m)} T_f + \varepsilon_{\gamma_{LS}}^{(m,s)} - a_1^{(m)} T_f) \cdot u + \varepsilon_{UP(u)}^{(s,m)} \\ &= \zeta_{UP}^{(s,m)} + \varepsilon_{\gamma_{LS}}^{(m,s)} \cdot u + \varepsilon_{UP(u)}^{(s,m)} . \end{aligned} \tag{3.20}$$

$$\begin{aligned}\hat{\Omega}_{DN(z)}^{(m,s)} &= \zeta_{DN}^{(m,s)} + (a_1^{(m)}T_f - \hat{a}_1^{(s)}T_f)\cdot(z-u) + \varepsilon_{DN(z)}^{(m,s)} \\ &= \zeta_{DN}^{(m,s)} + (a_1^{(m)}T_f - a_1^{(m)}T_f - \varepsilon_{\gamma_{LS}}^{(m,s)})\cdot(z-u) + \varepsilon_{DN(z)}^{(m,s)} \\ &= \zeta_{DN}^{(m,s)} - \varepsilon_{\gamma_{LS}}^{(m,s)}\cdot(z-u) + \varepsilon_{DN(z)}^{(m,s)} \ . \end{aligned} \tag{3.21}$$

Substituting (3.18) and (3.21) into (3.5a), the initial-offset equation obtained at the end of the synchronization process becomes

$$\begin{aligned}\vartheta^{(m,s)}(k) &= \frac{1}{2}\hat{\Omega}_{DN(z)}^{(m,s)}(k) - \hat{\Omega}_{SY(v)}^{(m,s)}(k) \\ &= \frac{\zeta_{DN}^{(m,s)} - \varepsilon_{\gamma_{LS}}^{(m,s)}\cdot(z-u) + \varepsilon_{DN(z)}^{(m,s)}}{2} - \zeta_{SY}^{(m,s)} - \varepsilon_{SY}^{(m,s)} + \varepsilon_{\gamma_{LS}}^{(m,s)}\cdot(k+K_{ST}) \\ &= \frac{\zeta_{DN}^{(m,s)} - 2\zeta_{SY}^{(m,s)} - \varepsilon_{\gamma_{LS}}^{(m,s)}\cdot(z-u-2\cdot v) + \varepsilon_{DN(z)}^{(m,s)} - 2\varepsilon_{SY}^{(m,s)}}{2} \ , \end{aligned} \tag{3.22}$$

which is equivalent to

$$\vartheta^{(m,s)}(k) = -d_\delta^{(m,s)} - \tilde{\rho}_{m,s} + (\theta(k) - K_{ST})\cdot(a_\delta^{(m,s)}T_f - \hat{\gamma}_{LS}^{(m,s)}) + \varepsilon_\vartheta^{(m,s)} , \tag{3.23}$$

where $\varepsilon_\vartheta^{(m,s)}$ and $\theta(k)$ are given by (3.6b) and (3.11) respectively. Note that the main difference between (3.12) and (3.23) is the incorporation of the frame repetition rate correction term $(a_\delta^{(m,s)}T_f - \hat{\gamma}_{LS}^{(m,s)})$, which is a random variable, in (3.23).

To estimate the initial offset difference $d_\delta^{(m,s)}$ between master and slave, the slave transceiver may take the sample mean or apply the LS estimator on $\vartheta^{(m,s)}(k)$ as $\theta(k)$ varies linearly with k. Here $d_\delta^{(m,s)}$ is estimated by taking the sample mean of $\{\vartheta^{(m,s)}(k)\}_{k=0}^{K-1}$. There are no additional advantages gained from using the LS estimator. This is because, from Chapter 2, it can be deduced that the LS estimation error for estimating initial offset differences decreases asymptotically in the order of K, which is equivalent to using the sample mean.

Assuming $K = K_s = K_r >> 1$ and for most practical purposes, the uplink and downlink pulses during two-way ranging are designed to occupy the same relative time slots, that is, $i = j$ such that $\theta(k) = (N-1)K/2 - k$, then an estimate $\hat{d}_\delta^{(m,s)}$ of the difference in initial offset $d_\delta^{(m,s)}$ between nodes m and s can be derived from the sample mean of $\vartheta^{(m,s)}(k)$ for k ranges from $k=0$ to

$k = K-1$. This estimate is

$$\hat{d}_{\delta}^{(m,s)} = -\frac{\sum_{k=0}^{K-1} \vartheta^{(m,s)}(k)}{K}$$
$$= d_{\delta}^{(m,s)} + \tilde{\rho}_{m,s} + \varepsilon_{\hat{d}}^{(m,s)} \quad , \tag{3.24a}$$

where $\varepsilon_{\hat{d}}^{(m,s)}$ is the estimation error with zero mean. The estimate $\hat{d}_{\delta}^{(m,s)}$ has mean

$$\mathbf{E}\{\hat{d}_{\delta}^{(m,s)}\} = d^{(m)} - d^{(s)} + (\rho_{m,s} - \rho_{s,m})/2 \,, \tag{3.24b}$$

which is corrupted by the receiver processing error $\tilde{\rho}_{m,s}$. The variance of (3.24a) is

$$\mathbf{V}\{\hat{d}_{\delta}^{(m,s)}\} = \mathbf{V}\{\varepsilon_{\hat{d}}^{(m,s)}\}$$
$$= \frac{\left(\sum_{k=0}^{K-1}(\theta(k) - K_{ST})\right)^2}{K^2} \cdot \mathbf{V}\{\varepsilon_{\gamma_{LS}}^{(m,s)}\} + \mathbf{V}\{\varepsilon_{\vartheta}^{(m,s)}\} \quad . \tag{3.24c}$$

Equation (3.24c) is derived in Appendix A. Substituting the characteristic function (3.11) into (3.24c), the variance in estimating the initial offset difference for the time-transfer scheme described in section 3.1 is given by

$$\mathbf{V}\{\hat{d}_{\delta}^{(m,s)}\} = \frac{3 \cdot \sigma_x^2(m,s)}{K} \cdot \left((N-1)^2 + \frac{(K + 2K_{ST} - 1) \cdot (2K_{ST} - 1 - 2NK + 3K)}{K^2} \right)$$
$$+ \frac{5 \cdot \sigma_x^2(m,s) + \sigma_x^2(s,m)}{4} \quad . \tag{3.24d}$$

This particular arrangement of frame-synchronization, uplink and downlink pulses as illustrated in Figs. 13 and 14 with $\theta(k)$ given by (3.11) will be referred to as time-transfer scheme A in subsequent analysis. A feature of this time-transfer scheme is the fact that frame-rate synchronization is first performed without waiting for the completion of the transmission of the uplink and downlink ranging pulses.

In Fig. 18, the ToAs $\Omega_{SY(v)}^{(m,s)}(k)$, $\Omega_{UP(u)}^{(s,m)}(k)$ and $\Omega_{DN(z)}^{(m,s)}(k)$ after frame-rate difference estimation are illustrated.

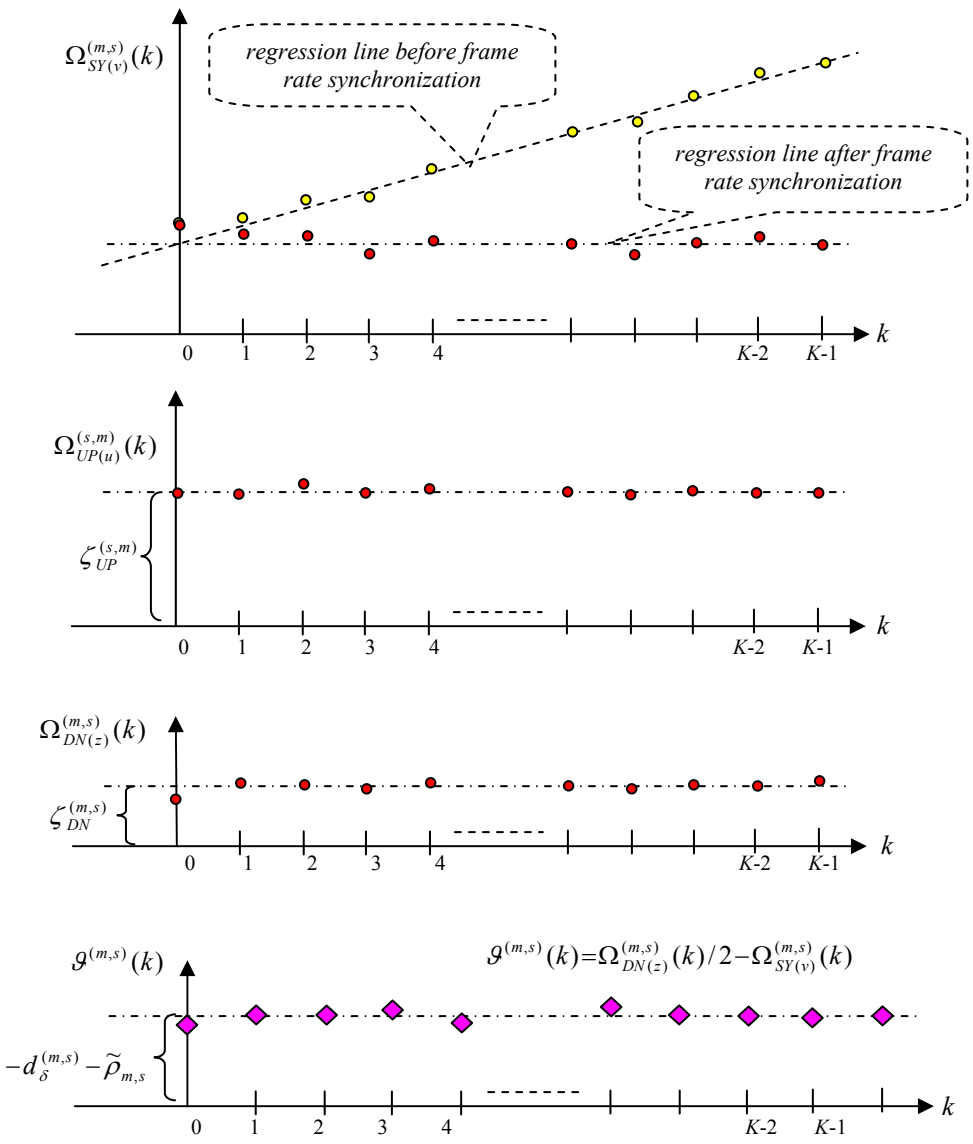

Figure 18: Illustration of the ToAs measured during the frame-synchronization, uplink and downlink time slots. In this example $K=K_s=K_r$.

3.4 Interleaved Time-Transfer Schemes

Instead of transmitting the frame-synchronization, uplink and downlink pulses in contiguous frames within a time slot, it is possible to transmit these pulses in adjacent frames and repeat the process K times. In this case, the pulses are "interleaved" instead of being transmitted in contiguous frames.

One possible interleaved scheme, to be referred to as time-transfer scheme B, is shown in Fig. 19. In this time-transfer scheme, the frame-synchronization pulses are spaced $(2N-1)\cdot T_f$ apart. As a result, we can deduce from (2.47) that the variance of estimating the difference in frame repetition rate between two nodes is reduced by a factor of $(2N-1)^2$. The uplink and downlink pulses of each node are also spaced $(2N-1)\cdot T_f$ apart.

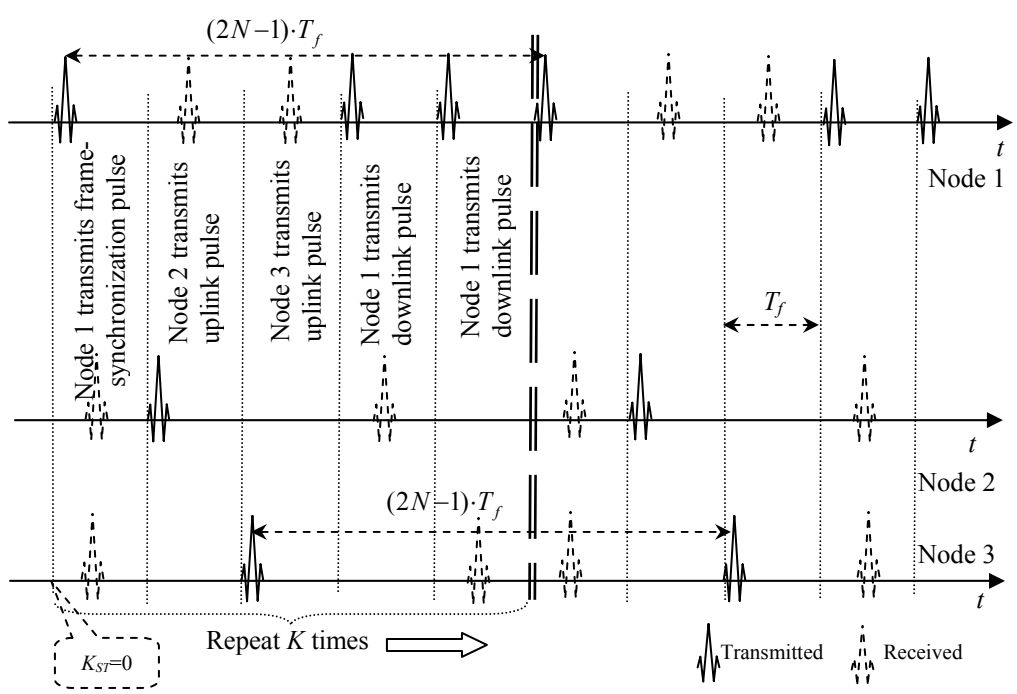

Figure 19: Illustration of the time-transfer scheme B. In this example N=3.

For this time-transfer scheme to be feasible, it is assumed that the receiver can discern the pulses transmitted from different nodes in the network and there is no or minimum collision of pulses, i.e., minimum MAI. In order to update the timing of the nodes correctly, the receiver must at least be able to associate the received pulses with the transmitter that it is engaged in time-transfer. A more detail discussion on separating the pulses at the receiver is given in section 3.2.

In this scheme, the ToAs measured with respect to the receiver's oscillator frame boundaries are

$$\begin{aligned}\Omega_{SY(v)}^{(m,s)}(k) &= \zeta_{SY}^{(m,s)} + a_{\delta}^{(m,s)} \cdot T_f \cdot v + \varepsilon_{SY}^{(m,s)} \\ &= \zeta_{SY}^{(m,s)} + a_{\delta}^{(m,s)} \cdot T_f \cdot ((2N-1)\cdot k + K_{ST}) + \varepsilon_{SY}^{(m,s)} \quad .\end{aligned} \tag{3.25}$$

where $v = (2N-1)\cdot k + K_{ST}$ and $k \in \{0,...,K_r - 1\}$. The measured uplink ToAs are given by

$$\Omega_{UP(u)}^{(s,m)}(k) = \zeta_{UP}^{(s,m)} + a_{\delta}^{(m,s)} \cdot T_f \cdot u + \varepsilon_{UP(u)}^{(s,m)}, \tag{3.26a}$$

where the uplink frame index is

$$u = 1 + (j-2) + k\cdot(2N-1) + K_{ST}, \tag{3.26b}$$

and $j \in \{2,3,4,5,...,N\}$ indicates the slot occupy by individual node. The measured downlink ToAs are

$$\Omega_{DN(z)}^{(m,s)}(k) = \zeta_{DN}^{(m,s)} + a_{\delta}^{(m,s)} \cdot T_f \cdot (z-u) + \varepsilon_{DN(z)}^{(m,s)}, \tag{3.27a}$$

where the downlink pulses are transmitted at frames

$$z = N + (i-2) + k\cdot(2N-1) + K_{ST}, \tag{3.27b}$$

with i (i not necessary equal to j), $i \in \{2,..,N\}$, identifies the downlink time slot. In subsequent analysis, the case $i = j$ is analyzed.

Since $z - u = N - 1$, equation (3.27a) reduces to

$$\Omega_{DN(z)}^{(m,s)}(k) = \zeta_{DN}^{(m,s)} + a_{\delta}^{(m,s)} \cdot T_f \cdot (N-1) + \varepsilon_{DN(z)}^{(m,s)}, \tag{3.27c}$$

and the timing-offset equation derived at node s is

$$\begin{aligned}\vartheta^{(m,s)}(k) &= \Omega_{DN(z)}^{(m,s)}(k)/2 - \Omega_{SY}^{(m,s)}(k) \\ &= \frac{\zeta_{DN}^{(m,s)}}{2} - \zeta_{SY}^{(m,s)} + a_{\delta}^{(m,s)} \cdot T_f \cdot (\theta(k) - K_{ST}) + \frac{\varepsilon_{DN(z)}^{(m,s)}}{2} - \varepsilon_{SY}^{(m,s)}.\end{aligned} \tag{3.28a}$$

The characteristic function of this time-transfer scheme is

$$\theta(k)=\frac{N-1}{2} \; - \; (2N-1)\cdot k \; . \tag{3.28b}$$

Using the LS estimator described in section 2.4, the variance in estimating $\gamma^{(m,s)}$ is given by equation (2.47), however now the frame-repetition pulses are spaced $(2N-1)\cdot T_f$ apart rather than T_f compared to time-transfer scheme A, therefore

$$\sigma^2_{\hat{\gamma}^{(m,s)}_{LS}} = \mathbf{V}\{\varepsilon^{(m,s)}_{\gamma_{LS}}\} \geq \frac{12\cdot\sigma^2_x(m,s)}{K^3\cdot(2N-1)^2} \; . \tag{3.29}$$

For the time-transfer scheme depicted in Fig. 19, substituting (3.28b) into (3.28a), the variance in estimating the initial offset difference between node m and s is

$$\begin{aligned}\mathbf{V}\{\hat{d}^{(m,s)}_{\delta}\} &= \frac{\left(\sum_{k=0}^{K-1}(\theta(k)-K_{ST})\right)^2}{K^2}\cdot\mathbf{V}\{\varepsilon^{(m,s)}_{\gamma_{LS}}\}+\mathbf{V}\{\varepsilon^{(m,s)}_{\vartheta}\} \\ &= \frac{1}{4}\cdot\left((N-1)^2-(2N-1)\cdot(K-1)-2\cdot K_{ST}\right)^2\cdot\mathbf{V}\{\varepsilon^{(m,s)}_{\gamma_{LS}}\} \\ &\quad + \frac{5\cdot\sigma^2_x(m,s)+\sigma^2_x(s,m)}{4K} \; .\end{aligned} \tag{3.30}$$

where $\mathbf{V}\{\varepsilon^{(m,s)}_{\gamma_{LS}}\}$ is given by (3.29).

An alternative interleaved scheme, to be referred to as time-transfer scheme C, is illustrated in Fig. 20. In this time-transfer scheme, the frame-synchronization pulses are spaced $(2N-1)\cdot T_f$ apart while the uplink and downlink pulses of each node are spaced T_f in time.

In both time-transfer schemes B and C, unlike time-transfer scheme A, the synchronization of the frame repetition rate between m and s is performed after the transmission of the uplink and downlink ranging pulses. That is, the slave node s collects all the necessary relative ToA measurements and performs post-processing on the measurements to estimate the initial offset and frame repetition rate differences.

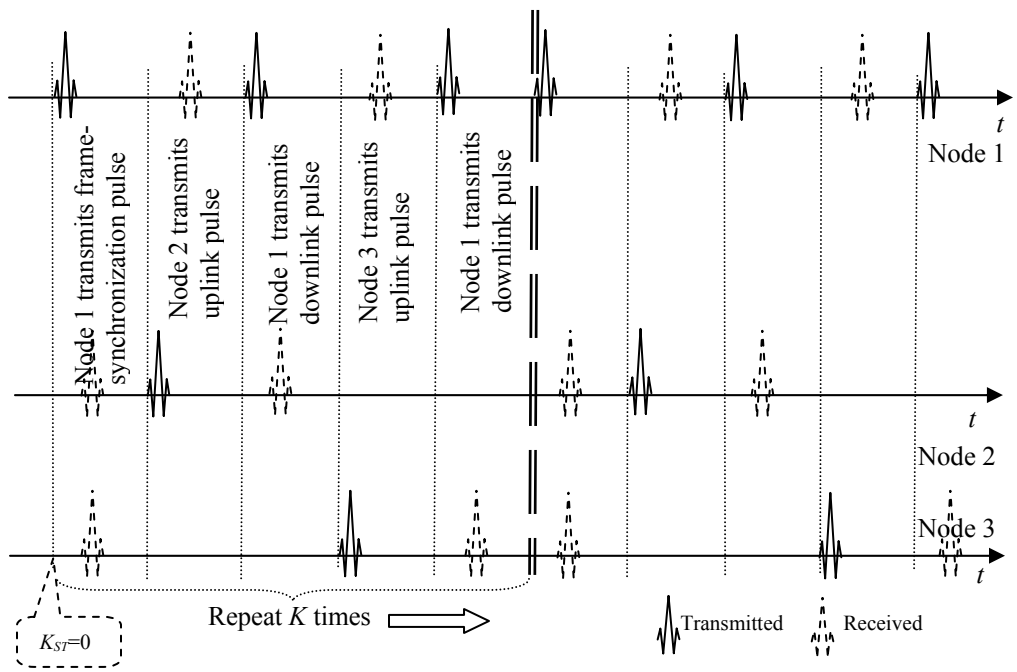

Figure 20: Illustration of the time-transfer scheme C. In this example, N=3.

In time-transfer scheme C, the ToAs measured with respect to the receiver's oscillator frame boundaries are

$$\Omega_{SY(v)}^{(m,s)}(k)=\zeta_{SY}^{(m,s)} + a_{\delta}^{(m,s)}\cdot T_f\cdot v + \varepsilon_{SY}^{(m,s)}, \tag{3.31a}$$

$$\Omega_{UP(u)}^{(s,m)}(k)= \zeta_{UP}^{(s,m)} + a_{\delta}^{(m,s)}\cdot T_f\cdot u + \varepsilon_{UP(u)}^{(s,m)}, \tag{3.31b}$$

$$\Omega_{DN(z)}^{(m,s)}(k)= \zeta_{DN}^{(m,s)} + a_{\delta}^{(m,s)}\cdot T_f\cdot (z-u) + \varepsilon_{DN(z)}^{(m,s)}, \tag{3.31c}$$

where $v=(2N-1)\cdot k+K_{ST}$, $k\in\{0,...,K_r-1\}$, $u=1+(j-2)\cdot 2+k\cdot(2N-1)+K_{ST}$, $j\in\{2,3,4,5,...,N\}$, $z=2+(i-2)\cdot 2+k\cdot(2N-1)+K_{ST}$ and $i\in\{2,..,N\}$.

Since $z-u=1$, the characteristic function of the time-transfer scheme is

$$\theta(k)=\frac{1}{2}\ -\ (2N-1)\cdot k\ , \tag{3.32a}$$

and the timing-offset equation derived at node s is

$$\begin{aligned}\vartheta^{(m,s)}(k)&=\Omega_{DN(z)}^{(m,s)}(k)/2-\Omega_{SY(v)}^{(m,s)}(k)\\&=\frac{\zeta_{DN}^{(m,s)}}{2}-\zeta_{SY}^{(m,s)}+a_{\delta}^{(m,s)}\cdot T_f\cdot\left(\theta(k)-K_{ST}\right)+\frac{\varepsilon_{DN(z)}^{(m,s)}}{2}-\varepsilon_{SY}^{(m,s)}\\&=\frac{\zeta_{DN}^{(m,s)}}{2}-\zeta_{SY}^{(m,s)}+a_{\delta}^{(m,s)}\cdot T_f\cdot\left(\frac{1}{2}-(2N-1)\cdot k-K_{ST}\right)+\frac{\varepsilon_{DN(z)}^{(m,s)}}{2}-\varepsilon_{SY}^{(m,s)}\ .\end{aligned} \tag{3.32b}$$

The variance in estimating the frame-repetition rate is

$$\sigma^2_{\hat{\gamma}_{LS}^{(m,s)}}=\mathbf{V}\{\varepsilon_{\gamma_{LS}}^{(m,s)}\}\geq\frac{12\cdot\sigma_x^2(m,s)}{K^3\cdot(2N-1)^2}\ . \tag{3.33}$$

Substituting (3.32a) into (3.32b), the variance in estimating the initial offset is

$$\begin{aligned}\mathbf{V}\{\hat{d}_{\delta}^{(m,s)}\}&=\frac{\left(\sum_{k=0}^{K-1}(\theta(k)-K_{ST})\right)^2}{K^2}\cdot\mathbf{V}\{\varepsilon_{\gamma_{LS}}^{(m,s)}\}+\frac{5\cdot\sigma_x^2(m,s)+\sigma_x^2(s,m)}{4K}\\&=\frac{1}{K^2}\cdot\frac{K^2}{4}\cdot\left(1-(2N-1)\cdot(K-1)-2\cdot K_{ST}\right)^2\cdot\mathbf{V}\{\varepsilon_{\gamma_{LS}}^{(m,s)}\}\\&\quad+\frac{5\cdot\sigma_x^2(m,s)+\sigma_x^2(s,m)}{4K}\\&=\frac{1}{4}\cdot\left(2N+K-2NK-2\cdot K_{ST}\right)^2\cdot\mathbf{V}\{\varepsilon_{\gamma_{LS}}^{(m,s)}\}+\frac{5\cdot\sigma_x^2(m,s)+\sigma_x^2(s,m)}{4K}\ .\end{aligned} \tag{3.34}$$

In Figs. 21 and 22, the variance in estimating the difference in initial offset and frame repetition rate utilizing the three different time-transfer schemes are plotted. It indicates that time-transfer scheme C has the lowest estimation error variances for estimating both the initial offset and frame repetition rate. However in time-transfer schemes B and C, differences in frame rate between nodes are corrected only after the completion of the two-ray ranging. Thus it is likely that, as illustrated in Fig. 15, there will be multiple-access-interference which degrades the quality of the ToA measurements. In this work, the effect of MAI is not considered.

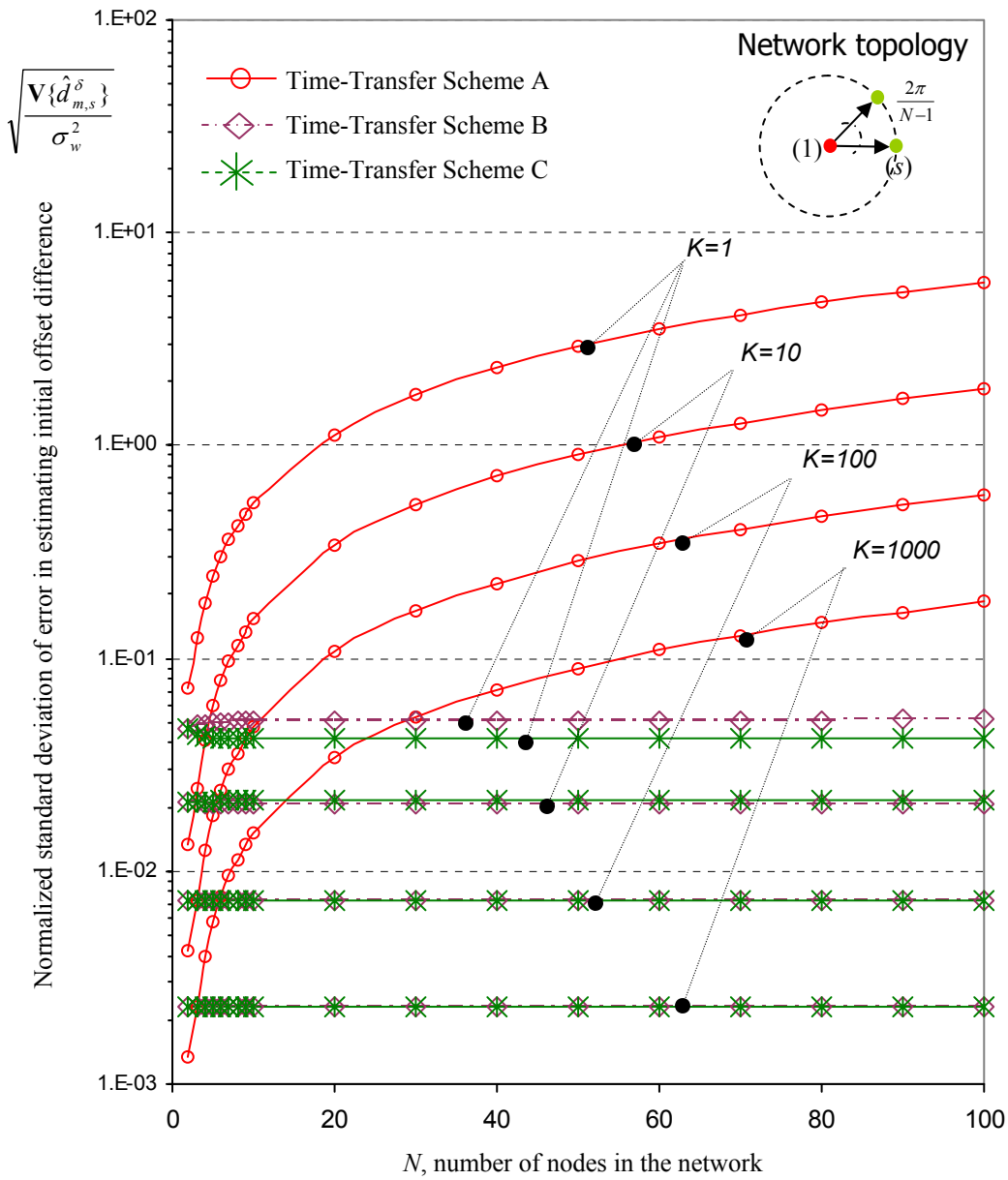

Figure 21: Performance of the different time-transfer schemes described in sections 3.1 and 3.4 in estimating initial offset differences. In this plot, $\Theta_{m,s} = 20$ dB, $K_{ST} = 0$, $\sigma_\phi = 0$ and $\tilde{\rho}_{m,s} = 0$. (Note: K=1 is included for the purpose of comparison.)

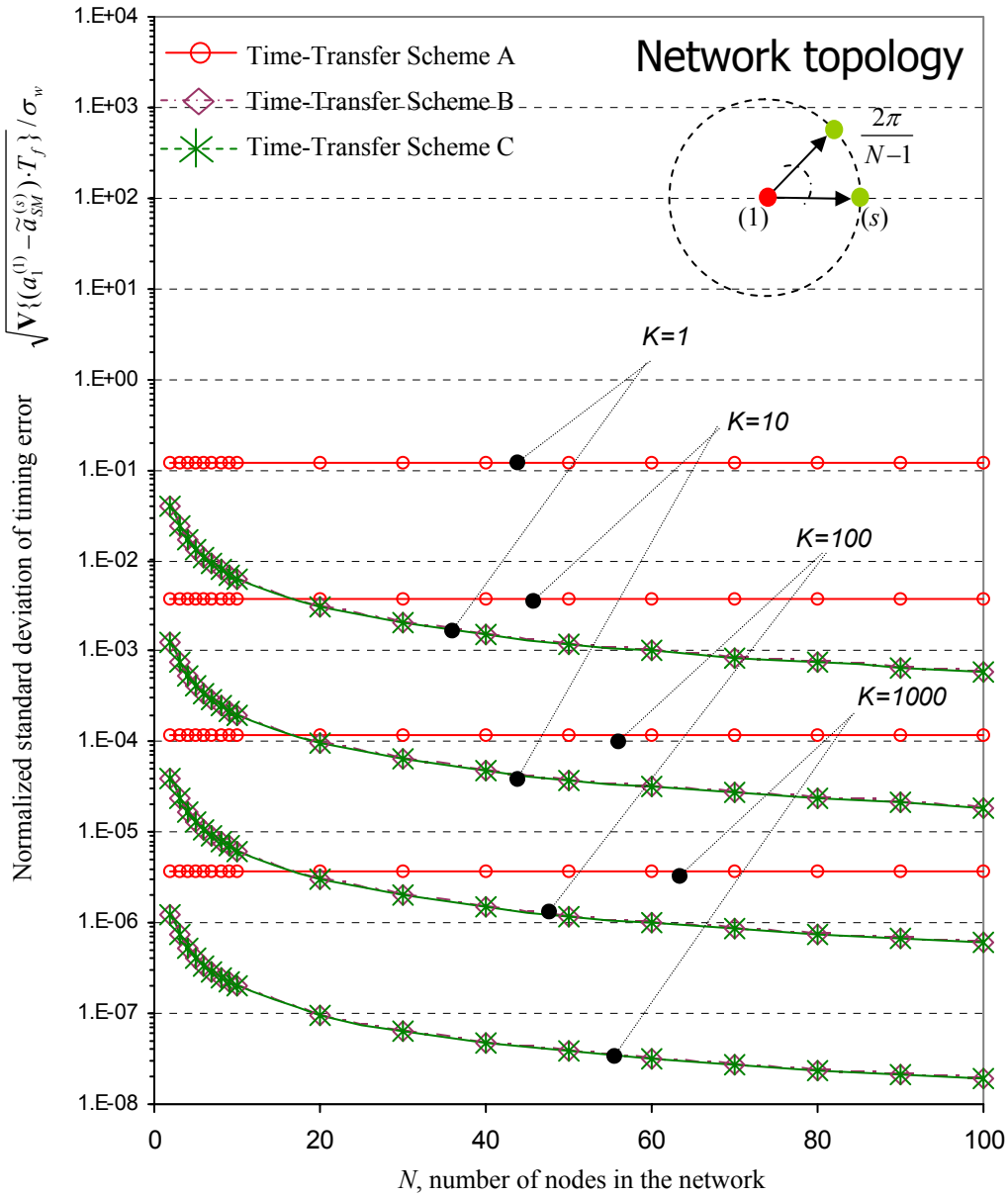

Figure 22: Performance of different time-transfer schemes described in sections 3.1 and 3.4 in estimating frame-repetition-rate differences. In this plot, $\Theta_{m,s}=20$ dB, $K_{ST}=0$, $\sigma_\phi=0$ and $\tilde{\rho}_{m,s}=0$.

(Note: K=1 is included for the purpose of comparison.)

3.5 Other Approaches

3.5.1 Two-way Time Transfer

Some readers may noticed that $\Omega_{SY(v)}^{(m,s)}(k)$ and $\Omega_{UP(u)}^{(s,m)}(k)$ constitute two equations with three unknowns. The unknowns are the differences in frame repetition rates $a_{\delta}^{(m,s)}T_f$, signal propagation delay $\tau_{m,s}$ and initial offset $d_{\delta}^{(m,s)}$ differences between nodes m and s. After estimating $a_{\delta}^{(m,s)}T_f$ using the frame frequency differences estimation techniques described in Chapter 2, and the frame repetition rate of the slave node is corrected such that $\gamma^{(m,s)} - \hat{\gamma}_{LS}^{(m,s)} \approx 0$, then with two unknowns, $d_{\delta}^{(m,s)}$ can be estimated by solving the two equations:

$$\Omega_{SY(v)}^{(m,s)}(k) = \tau_{m,s} + \rho_{m,s} + d_{\delta}^{(m,s)} + \varepsilon_{SY}^{(m,s)}$$

$$\Omega_{UP(u)}^{(s,m)}(k) = \tau_{s,m} - d_{\delta}^{(m,s)} + \rho_{s,m} + \varepsilon_{UP(u)}^{(s,m)}$$

where it is assumed that $\gamma^{(m,s)} - \hat{\gamma}_{LS}^{(m,s)} \approx 0$. That is, the differences in oscillator's initial offset and propagation delay can be determined separately without obtaining $\Omega_{DN(z)}^{(m,s)}(k)$. However, $\Omega_{SY(v)}^{(m,s)}(k)$ and $\Omega_{UP(u)}^{(s,m)}(k)$ are measured at the slave and master transceivers separately. This information about ToAs therefore must be encoded and exchanged via the wireless link to determine the timing offset. In fact, this is performed in known synchronization scheme of two-way time-transfer [58]. Assuming that this has being performed, (measurement results $\Omega_{UP(u)}^{(s,m)}(k)$ are encoded at the master, send to the slave at where it is decoded) the timing equation at the slave transceiver becomes

$$\begin{aligned}\tilde{\vartheta}^{(m,s)}(k) &= (\Omega_{SY(v)}^{(m,s)}(k) - \Omega_{UP(u)}^{(s,m)}(k))/2 \\ &= d^{(m)} - d^{(s)} + \frac{\rho_{m,s} - \rho_{s,m} + \mu_{(v)} + \mu_{(u)} + \dfrac{n_{(v)}^{(s)}}{A_w^{(s)}\breve{g}_{TD}} - \dfrac{n_{(u)}^{(m)}}{A_w^{(m)}\breve{g}_{TD}}}{2} .\end{aligned} \tag{3.35}$$

The process described in the previous paragraph, commonly known as two-way time transfer [58], can clearly be used to perform time-transfer as well and potentially supports more nodes in the network with smaller timing jitter. The exchange of ToA measurement results could possibly be provided by separate a communication channel (data channel) apart from the UWB channel dedicated to time-transfer. If a narrowband channel is used, this entails additional hardware and power requirement on the transceivers. If the information exchange is time division multiplexed into the UWB channels, more time is needed than for transmitting downlink ranging pulses from the master to slave nodes. In addition, if information is exchanged between transceivers using the TDMA UWB channel, this would introduce additional latency that involves higher layer network protocol (encoding and decoding of messages) that is hard to characterize for precision time-transfer.

The intention of this research is not to exchange encoded measurement results (time stamps) for reasons cited in the previous paragraph. Nevertheless, the discussions on various time-transfer architectures to follow are sufficiently generic to encompass (3.35). Ignoring the requirement of an additional data channel, when compared to the two-way time-transfer, the proposed scheme described earlier in section 3.1 has higher timing jitter. This is because the proposed scheme transmits an additional slot of K_r return timing pulses.

3.5.2 Returnable Timing System

If the oscillators in the network are coupled, instead of using explicit ToA measurement to effect time-transfer, as described in [6], [34] and many earlier works, the performance analysis will be different. For example, ignoring propagation delay and additive noise, the quantity investigated in [6] is the oscillator timing process (denoted as 'Θ_k' in [6]), which corresponds to $(T^{(s)}(kT_f)+\hat{\tau}_k)$ of Chapter 1. The variable $\hat{\tau}_k$ is introduced to represent the adjustment made by the receiver when the detector is placed inside a tracking loop. Using the principle of superposition

$$Z\{T^{(s)}(kT_f)+\hat{\tau}_k\}=H(\mathbf{z})\cdot\sum_{m=1,m\neq s}^{N}\alpha_{m,s}Z\{T^{(m)}(kT_f)\}+(1-H(\mathbf{z}))Z\{\phi^{(s)}(kT_f)\}, \tag{3.36}$$

where $Z\{\circ\}$ denotes the Z-transform, $H(\mathbf{z})$ is the transfer function of the phase locked loop and $\alpha_{m,s}$ is the gain of the system. Equation (3.36) is presented here for completeness and will not be pursued further. Note that (3.36) illustrates the difference between the time synchronization techniques described in [6] [34] and the proposed scheme in this research. In [6] and [34], a phase locked loop is used to acquire the phase of the received narrowband signals with delay compensation to transfer time from one node to another. In this case, $T^{(m)}(t)$ and $T^{(s)}(t)$ are manipulated directly. Further, in [34], it is assumed that the drift of any individual oscillator is close to unity such that $T^{(m)}(t+\tau_{m,s})\approx T^{(m)}(t)+\tau_{m,s}$.

In the proposed SIN synchronization scheme, ToAs of the UWB monocycles are measured directly. Then, for a network of nodes, it is more convenient mathematically to project $T^{(m)}(t)$ and $T^{(s)}(t)$ onto t (the standard time scale, section 1.2). Hence the inverse mapping $t_{(k)}^{(m)}$ and $t_{(k)}^{(s)}$ of $T^{(m)}(t_{(k)}^{(m)})=kT_f$ and $T^{(s)}(t_{(k)}^{(s)})=kT_f$ are utilized. The objective of time-transfer remains the same.

In this Chapter, the synchronization scheme for the SIN was presented. When compared with two-way time-transfer [58], the TDMA time-transfer schemes proposed in section 3.1 and 3.3 (time-transfer schemes A, B and C) do not require additional resources to exchange measurement results between pair of nodes (no separate data channel is needed). They are well suited for applications when it is advantageous to perform synchronization on the physical layer with little or no involvement from higher layer protocols.

CHAPTER IV

TIME-TRANSFER ARCHITECTURES

In a network of wireless nodes, the timing of one node can be transferred to another using different time-transfer structures/architectures [7] [34] [45].

In this Chapter, the master-slave (SM) architecture, with a designated master node and other nodes in the network are slave nodes, is first introduced and analyzed. It is followed by description of the hierarchical master-slave (HM) and the mutually synchronous (MU) time-transfer architectures. The proposed MU and HM time-transfer networks are realized based on the "roving master" concept. In the roving master concept, each node in the network takes its turn as the master node. To start the time transfer, a node in the network is designated as the lead master node. The lead master node will be the first node to start transferring its timing to other nodes in the network. The purpose of roving the master duties is to avoid NLoS network signal propagation between nodes. In this research, nodes in the network are assumed to be stationary during time transfer.

To analyze the performance of a SIN implemented with different time-transfer architectures, we select to analyze only the case in which ToA measurements are obtained from an open loop timing detector, i.e., the timing detector is not embedded in a tracking loop and the oscillator is free running during synchronization. We will make use of the results presented earlier in Chapter 3 to analyze the performance of the SIN.

In Chapter 3, sections 3.1 and 3.4, three different time-transfer schemes are presented. They are time-transfer schemes A, B and C. In this Chapter, the estimation errors of individual nodes in a network of N nodes after time-transfer are expressed as a function of $\hat{d}_{\delta}^{(m,s)}$, $\varepsilon_{\hat{d}}^{(m,s)}$ and $\varepsilon_{\gamma_{LS}}^{(m,s)}$ given in Chapter 3. Thus, by substituting time-transfer characteristic functions $\theta(k)$ of different time-transfer schemes, the performance of the SIN for different time-transfer architectures utilizing different time-transfer schemes can be readily obtained.

4.1 Master-Slave Time-Transfer Architecture

The time-transfer schemes described in Chapter 3 seek to transfer the initial offset and frame repetition rate of the master node's oscillator to a slave node. If node 1 in a network of N nodes is the sole master node, and time transfer occurs pair-wise between node 1 with other nodes in the network using different time slots, a master-slave time-transfer architecture using time division multiple access (TDMA) is realized. The necessity of a TDMA instead of a FDMA (Frequency Divisional Multiple Access) scheme arises from the fact that we assume UWB impulse signal occupies all the available bandwidth. It is well known that the timing resolution of a signal is inversely proportional to the signal bandwidth.

A flow chart illustrating the single-master-to-multiple-slaves (SM) time-transfer architecture is shown in Fig. 23. The objective of this architecture is to align the timing of slaves to that of the designated master node.

Equations in section 3.3 express the variances in estimating the differences in initial offset and frame repetition rate between the master and each slave node in the network. The subscripts in these equations indicate that these measurements are obtained from the $v^{\mathbf{th}}$ frame-synchronization pulse, the $u^{\mathbf{th}}$ pulse in uplink slot j and the $z^{\mathbf{th}}$ pulse in down-link slot i of the slave transceiver. That is, the slave node uses up-link slot j to transmit to the master and the master uses down-link slot i to transmit to the slave during two-way ranging. The superscript (m,s) is used to indicate that the measured ToAs are a function of the communication channel between the master m and slave node s participating in the time-transfer.

In this research, we restrict ourselves to analyzing only the case when ToA measurements are obtained from an open loop timing detector, i.e., it is assumed that the timing detector is not embedded in a tracking loop and the oscillator is free running during time-transfer.

After the master node broadcast synchronization pulses to the slave nodes during the frame-synchronization time slot, each slave node, using LS estimator, estimates the difference in pulse repetition rate between its clock and the master node's clock, and adjusts its frame repetition rate to that of the master. The difference in its initial offset is estimated by taking the sample mean of the timing differences obtained after two-way ranging.

The variance in estimating the difference in oscillator frame repetition rate is given by (2.47) while variance in estimating difference in initial offset is given by (3.24c). For ease of reference, they are reproduced here

$$\sigma^2_{\hat{\gamma}_{LS}^{(m,s)}} = \mathbf{E}\{|\gamma^{(m,s)} - \hat{\gamma}_{LS}^{(m,s)}|^2\} = \mathbf{V}\{\varepsilon_{\gamma_{LS}}^{(m,s)}\},$$

$$\mathbf{V}\{\hat{d}_{\delta}^{(m,s)}\} = \frac{\left(\sum_{k=0}^{K-1}(\theta(k) - K_{ST})\right)^2}{K^2} \cdot \mathbf{V}\{\varepsilon_{\gamma_{LS}}^{(m,s)}\} + \mathbf{V}\{\varepsilon_{\vartheta}^{(m,s)}\} .$$

Denoting the "settled" estimate of the initial offset and drift at node s, $s \neq 1$, after time transfer by $\tilde{d}_{SM}^{(s)}$ and $\tilde{a}_{SM}^{(s)}$ respectively, we have

$$\tilde{a}_{SM}^{(s)} \cdot T_f = \hat{\gamma}_{LS}^{(1,s)} + a_1^{(s)} T_f , \tag{4.1a}$$

$$\begin{aligned} \tilde{d}_{SM}^{(s)} &= \hat{d}_{\delta}^{(1,s)} + d^{(s)} \\ &= d^{(1)} + \tilde{\rho}_{1,s} + \varepsilon_{\hat{d}}^{(1,s)} . \end{aligned} \tag{4.1b}$$

Therefore the variances of the estimation errors $(a_1^{(1)} - \tilde{a}_{SM}^{(s)})$ and $(d^{(1)} - \tilde{d}_{SM}^{(s)})$ are given by

$$\mathbf{V}\{a_1^{(1)} - \tilde{a}_{SM}^{(s)}\} = \mathbf{V}\{\varepsilon_{\gamma_{LS}}^{(1,s)}\} , \tag{4.2a}$$

$$\mathbf{V}\{d^{(1)} - \tilde{d}_{SM}^{(s)}\} = \mathbf{V}\{\hat{d}_{\delta}^{(1,s)}\} . \tag{4.2b}$$

The expectation of the square of the difference in initial offset is

$$\mathbf{E}\{(d^{(1)} - \tilde{d}_{SM}^{(s)})^2\} = \mathbf{V}\{d^{(1)} - \tilde{d}_{SM}^{(s)}\} + \tilde{\rho}_{1,s}^2 . \tag{4.3}$$

The LS estimate $\hat{\gamma}_{LS}^{(1,s)}$ of the difference in frame repetition rate between node 1 and node s is not affected by $\tilde{\rho}_{m,s}$.

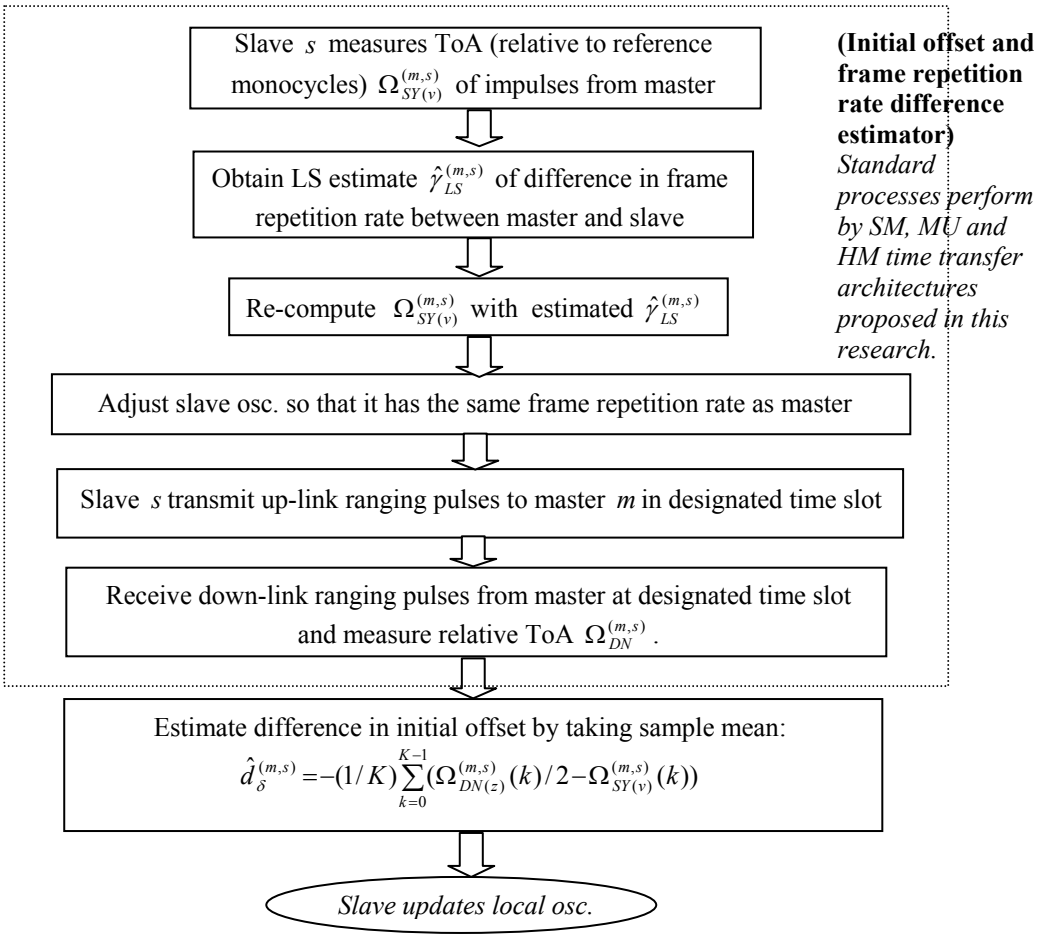

Figure 23: Flow chart illustrating the various steps taken at the slave transceiver to obtain the timing of master in the single-master time-transfer architecture. The processes enclosed in dotted lines are common to SM, HM and MU architectures proposed in this research.

It is mentioned in [66] that oscillator phase noise $\varphi(t)$ depends on the choice of the oscillator, and the power spectral density of $\varphi(t)$ ($S_{\varphi}(\omega)$) is usually specified as single-side-band noise in unit of dBc/Hz (dB relative to the oscillator carrier power in a 1 Hz bandwidth) and denoted as £(f).

A quick survey of the frequency control literature reveals that there exist various models to characterize the timing jitter of oscillator [14] [36] [42] [51]. The model presented in [36] [42] is adopted in this work. From [42], the first order structure function and hence the oscillator phase noise can be obtained from £(f). A technique is given in [44] to calculate the RMS (root-mean-squares) timing jitter from £(f). Applying the technique shown in [44] to the values of £(f) tabulated in [49], a FTS9500 (1993) precision oscillator operating at nominal oscillation frequency of 5 MHz has a RMS timing jitter of 72.1 fs (this calculation is illustrated in Fig. 24). This is better than the "good" crystal oscillator mentioned in [44] which has a RMS timing jitter of 6 ps. The 5 MHz oscillator is chosen because it is mentioned in [65] that 5 MHz is one of the standard frequencies for military communication and synchronization subsystems. Further, a study on enhancing the performance of a CMOS LC oscillator is presented in [40]. The "period jitter"[11] of the various enhanced CMOS LC oscillator ranges from 491 fs to 51 fs. Thus it is reasonable to assume, at current oscillator manufacture technology, oscillator timing jitter σ_{ϕ} ranges from 10^{-11} (for a cheap oscillator) to 10^{-15} (for an expansive oscillator).

The variances expressed by (4.2a) and (4.2b) are plotted in Figs. 25, 26 and 27 for various values of K and N. The received UWB monocycle is modeled using the nth order derivative of a Gaussian curve described in section 1.2.5 and [11] [12] , and we choose monocycle waveform $w_n(t)$, $n=8$, which has a spectrum that fits into the FCC indoor mask. In our analysis, the pulse width

[11] In [40], "period jitter" is defined as $\sqrt{\mathbf{V}\{t_{k+1}-t_k\}}$ where t_k is the absolute instant in time of the kth positive voltage transition of the oscillator output and $\mathbf{E}\{t_{k+1}-t_k\}=1/f_o$.

(approximated by the width of the main lobe of the UWB monocycle) of $w_8(t)$ is approximately σ_w =0.067 nsecs.

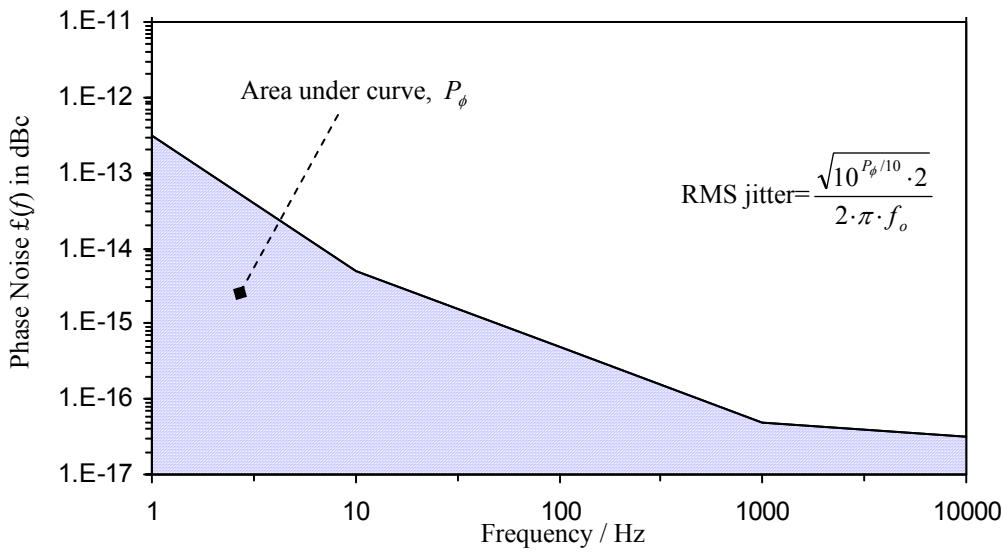

Figure 24: Estimating the phase noise of the FTS9500 oscillator operating at 5 MHz.

In Fig. 25, the theoretical lower bound of $\sqrt{\mathbf{V}\{\gamma^{(1,s)}-\hat{\gamma}_{LS}^{(1,s)}\}}$ is plotted. The variance in estimating the frame frequency difference decreases asymptotically as K^3 while estimating initial offset difference decreases only with K. At 10 dB, plots of $\sigma_\phi = 10^{-12}$ sec, $\sigma_\phi = 10^{-13}$ sec and $\sigma_\phi = 10^{-14}$ sec are close. Plots of $\sigma_\phi = 10^{-13}$ sec and $\sigma_\phi = 10^{-14}$ sec are very close to each other at 30 dB and are not distinguishable in the figure.

In Fig. 26, at received SNR $\Theta_{m,s}$ of 10 dB and 30 dB, the normalized standard deviation $\sqrt{\mathbf{V}\{d^{(1)}-\tilde{d}_{SM}^{(s)}\}}/\sigma_w$ vs. K, is plotted for various σ_ϕ^2. Figure 26 excluded receiver measurement error $\tilde{\rho}_{m,s}$. Note that $\sigma_\phi = 10^{-12}$ sec is 1/1000 of a nanosecond. It is observed that there is hardly any lowering of timing jitter for σ_ϕ better than 10^{-13} sec at $\Theta_{m,s}$ =30 dB. It illustrates that for a specific

$\Theta_{m,s}$, when additive channel noise increases until $\sigma_n^2(m,s) >> 2\sigma_\phi^2$, then the detector output variance becomes $\sigma_x^2(m,s) = \sigma_n^2(m,s) + 2\sigma_\phi^2 \approx \sigma_n^2(m,s)$, and an oscillator with even smaller phase noise would not reduce the timing jitter significantly. That is, there is a threshold beyond which the variance in estimating difference in initial offset is SNR limited. Conversely, when the oscillator phase noise is much larger than additive channel noise, the variance in estimating difference in initial offset is limited by oscillator timing jitter.

In Fig. 27, $\sqrt{\mathbf{V}\{d^{(1)} - \widetilde{d}_{SM}^{(s)}\}}/\sigma_w$ is plotted against number of nodes N in the network at $\Theta_{m,s}$ =10 dB and $\Theta_{m,s}$ =30 dB.

As illustrated in Figures 25, 26 and 27, the SM architecture is able to bring the standard deviation of the difference in initial offset estimation to within one monocycle pulse width.

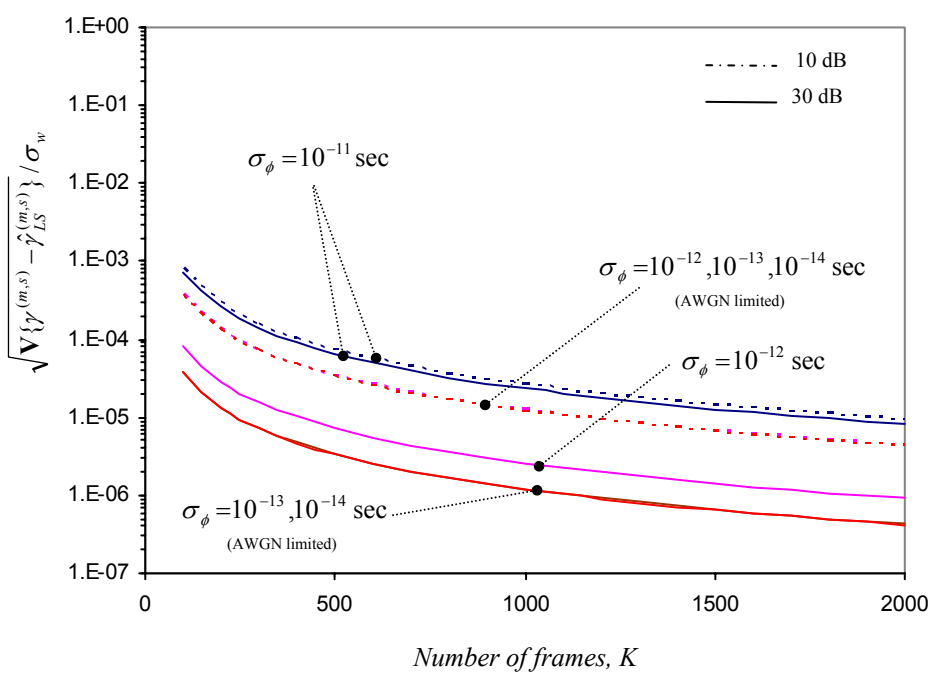

Figure 25: Theoretical lower bound on the standard deviation in estimating frame frequency difference between a pair of transceivers (N=2) as a function of K for various values of σ_ϕ at received SNR of $\Theta_{m,s}$=10 dB and $\Theta_{m,s}$=30 dB. Results obtained using time-transfer scheme A. The width of the UWB monocycle is approximately σ_w =0.067 nsec.

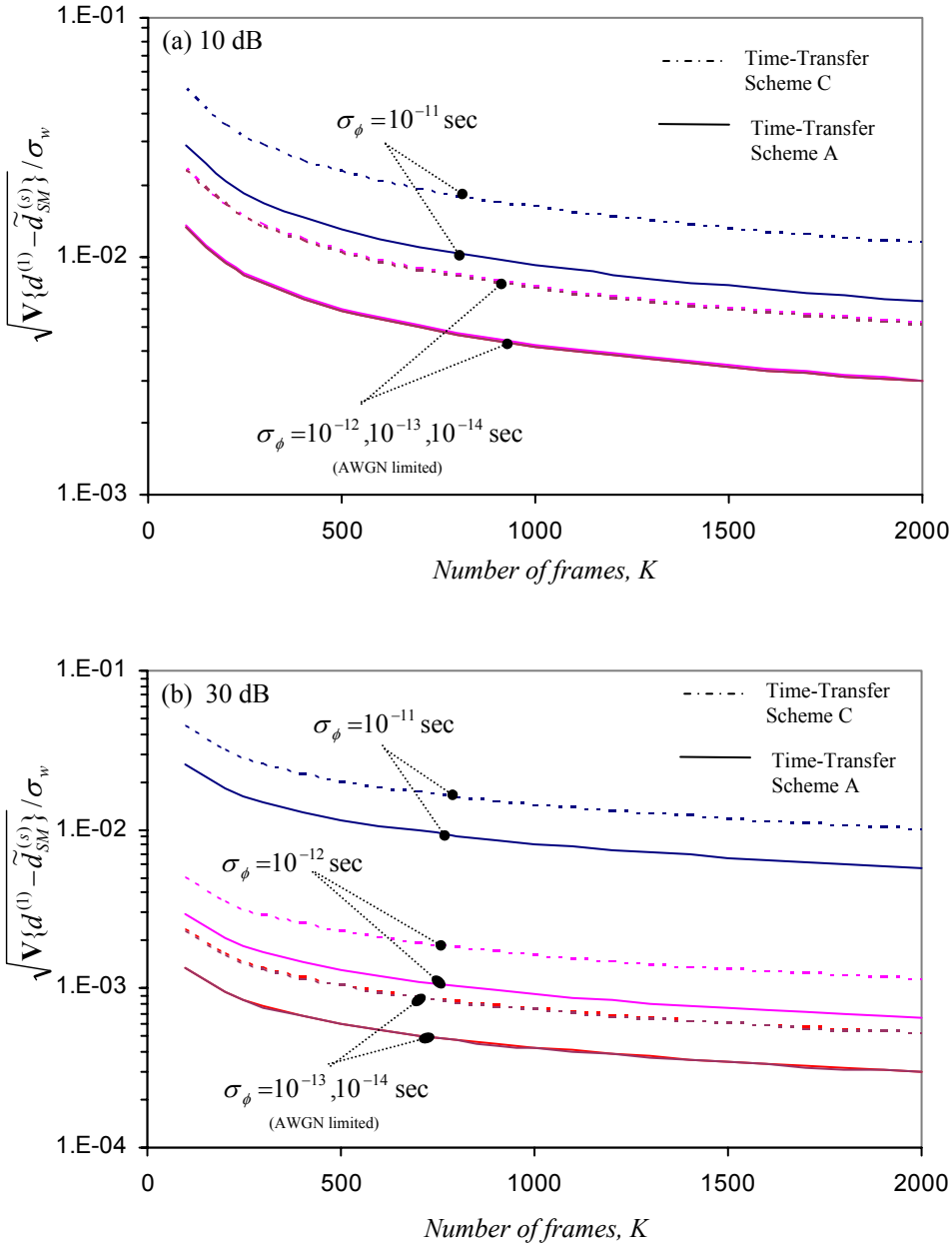

Figure 26: Theoretical lower bound on the standard deviation in estimating difference in initial offset between a pair of transceivers (N=2) due to AWGN and oscillators' phase noise as a function of K for various values of σ_ϕ at received SNR of (a) $\Theta_{m,s}$=10 dB and (b) $\Theta_{m,s}$=30 dB. The width of the UWB monocycle is approximately σ_w=0.067 nsec.

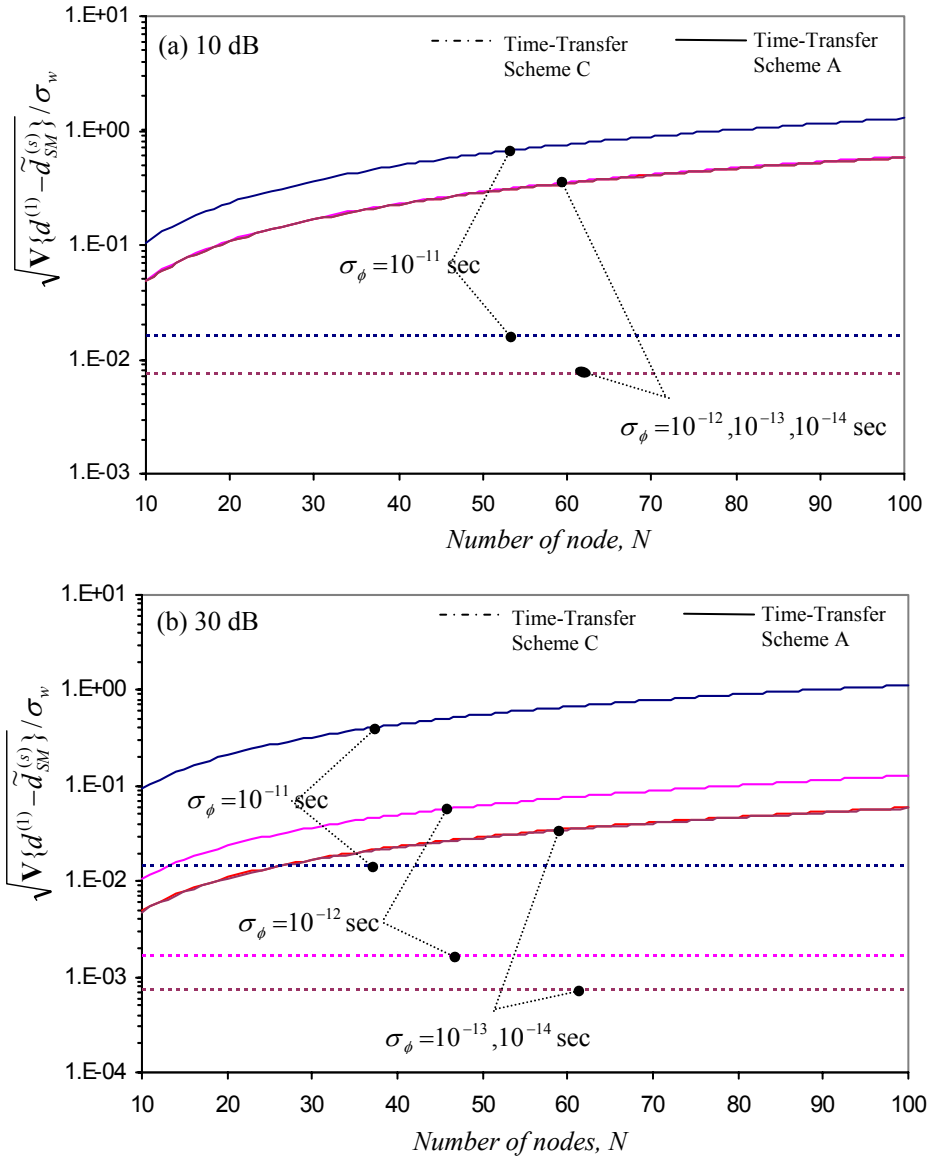

Figure 27: Theoretical lower bound on the standard deviation in estimating difference in initial offset between a pair of transceivers due to AWGN and oscillators' phase noise as a function of N for various values of σ_ϕ at received SNR of (a) $\Theta_{m,s}$=10 dB and (b) $\Theta_{m,s}$=30 dB, $K = 1000$. A 8th order derivative of the Gaussian curve is used to model the received UWB monocycle. The width of the monocycle is approximately 0.067 nsecs. Plots with $\sigma_\phi = 10^{-13}$ sec and $\sigma_\phi = 10^{-14}$ sec are very close to each other at 30 dB and are not distinguishable in the figure.

4.2 Roving Masters

The concept of a "roving" master, which is builds upon the master-slave time-transfer, is to let each transceiver in the network take a turn as the master node. The purpose of this approach is to extend the geographical coverage (Fig. 28a) of the synchronous network and to overcome blockages in signal propagation paths (Fig. 28b).

In wireless sensor networks, the wireless nodes are usually of small form factor with limited power. Therefore the transmission range of each node is likely to be limited due to power constraint. The roving master concept works much like a terrestrial cellular system with numerous fixed base stations each covering a small local area. Each node in the SIN is capable of being the master (base station) to communicate its timing to other nodes (slaves ≡ mobile terminals) that are in close proximity with it. It first synchronized itself to the timing of a designated lead-master node, i.e., the node that is tasked to start the synchronization process as the first master node. When it becomes the master, it propagates this timing to other nodes that the lead-master on its own cannot reach. Thus roving the master increases the coverage of the network. The synchronous network's coverage, accumulated timing jitter in individual nodes and accuracy of time-transfer, depends very much on the scheduling scheme of the roving masters and the geographical layout of nodes in the network (network topology) as will be illustrated in the following sections.

As pointed out earlier, the proposed synchronization scheme, like other wireless systems that rely on measuring the ToA of signals, its performance is limited by the present of NLoS measurements error that can significantly degrade the accuracy of the time-transfer. The roving master concept introduces diversity by exploiting the redundancy inherent in the network. As illustrated in Fig. 28b, node 'C' can choose from either node 'A' or 'B' or a soft combination of timing information from both nodes to establish synchronization with the network. The possibility that a clear LoS exists, which the nodes rely on for accurate time-transfer, between any pair of nodes (one of them is the

roving master) is reasonably assumed to be much higher than when a single master node trying to transfer timing to all other nodes in the network.

The hierarchical master-slave and mutually synchronous SIN are possible realizations of the roving master concept. The different time-transfer architectures are illustrated in Fig. 29. In Figs. 30 and 31, the roving master concept is illustrated with time-transfer schemes A and C proposed in Chapter 3.

Hereinafter, the transmitter SNR is defined as $\Theta_t = A_t^2 / (N_o / 2)$ where A_t^2 is the transmitted monocycle energy, assuming constant for all nodes. If $D_{m,s}$ is the signal propagation distance in meters from node m to s, the received monocycle energy is $A_w^2 = A_t^2 \cdot D_{m,s}^{-2}$. Unless otherwise specified, the path-loss exponent is kept at 2 as in free space [19]. This allows us to write $\sigma_n^2(m,s)$ of (3.8a) as $\sigma_n^2(m,s) \geq D_{m,s}^2 / \left(\Theta_t \overline{\omega^2}\right)$.

(a) 'Roving' the master to extend the geographical coverage

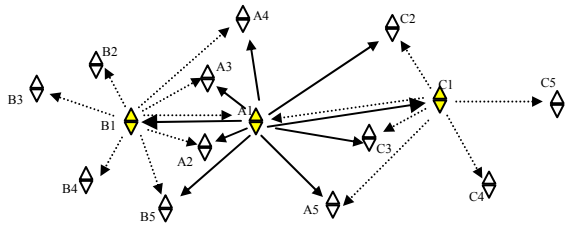

(b) 'Roving' the master to overcome blockages in signal propagation paths

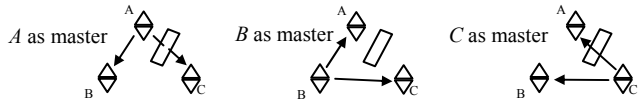

Figure 28: Illustration of the "roving" master concept. In (a), node 'A1' will not be able to reach nodes 'C5', 'B3' on its own. However, when 'C1' and 'B1' are the roving master nodes, 'C5' and 'B3' will be able to synchronize with node 'A1'. In (b), the blockages between A and C is circumvent by C synchronized with B, and B synchronized with A. The 'arrows' depicts the master sending out synchronizing pulses to the slaves.

(a) MS time-transfer architecture with one master node

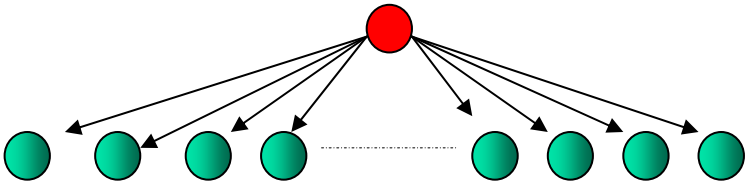

(b) HM time-transfer architecture whereby timings are transferred from one tier of nodes to the next

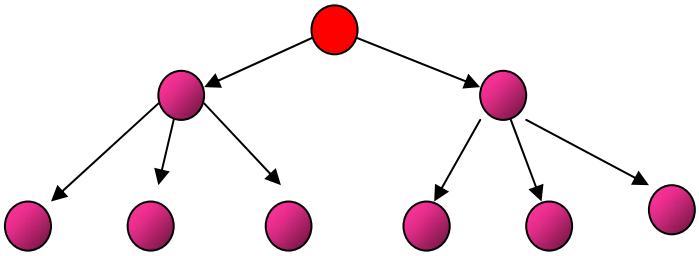

(c) MU time-transfer architecture whereby there is no preferred nodes in the network for the purpose of time synchronization

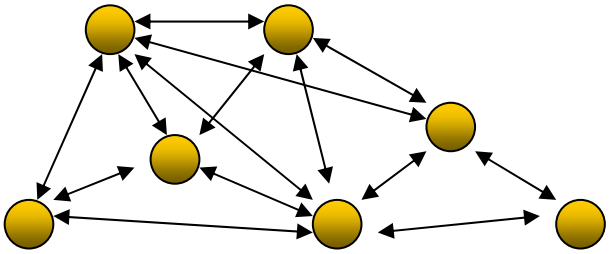

Figure 29: Illustration of the (a) SM, (b) HM and (c) MU time-transfer architectures.

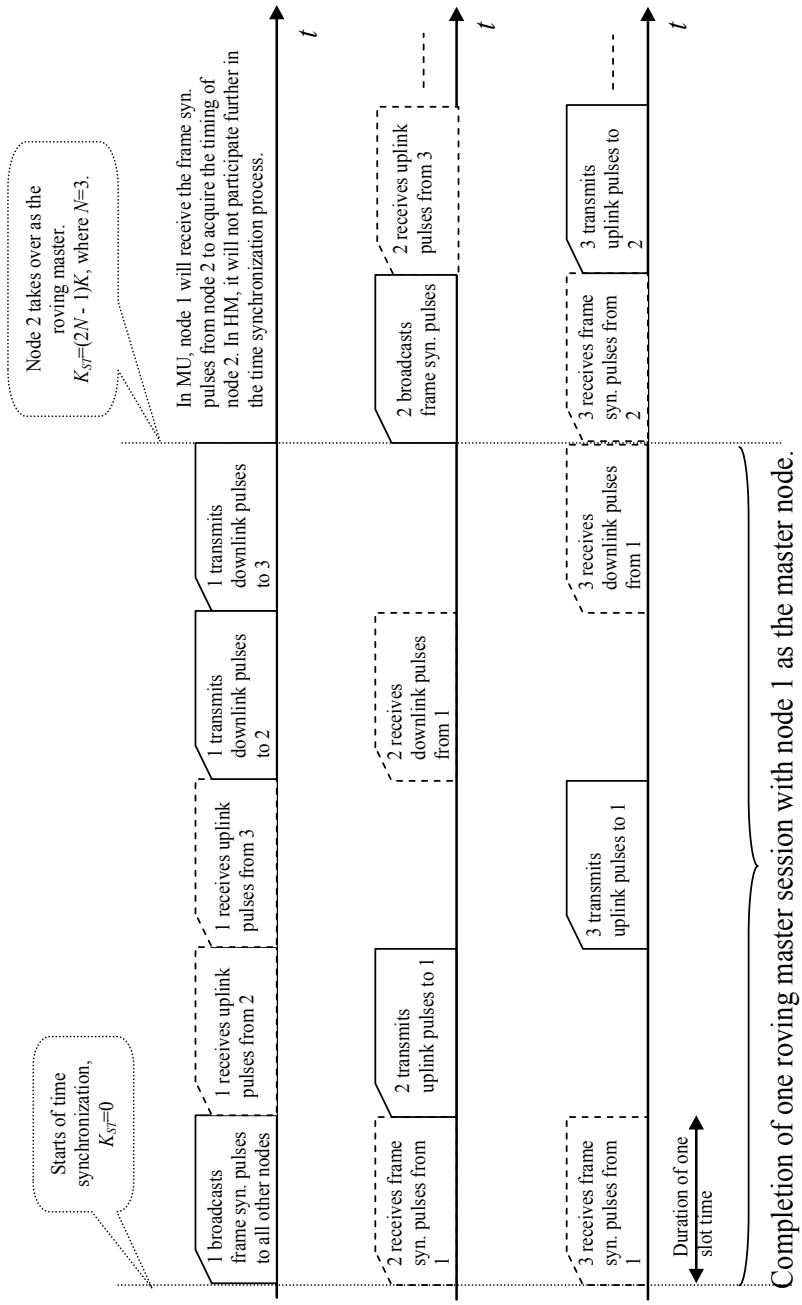

Figure 30: Illustration of the time transfer activities at each node utilizing the roving master concept with time-transfer scheme A. In this example, there are N=3 nodes in the network and node 2 is the roving master node after node 1 has transferred its timing to nodes 2 and 3. There are K frames per time slot. For the purpose of illustration, the durations of all slot time are equal. In practice, due to difference in initial offset and frame repetition rate, the slot times of each node are of slightly different lengths.

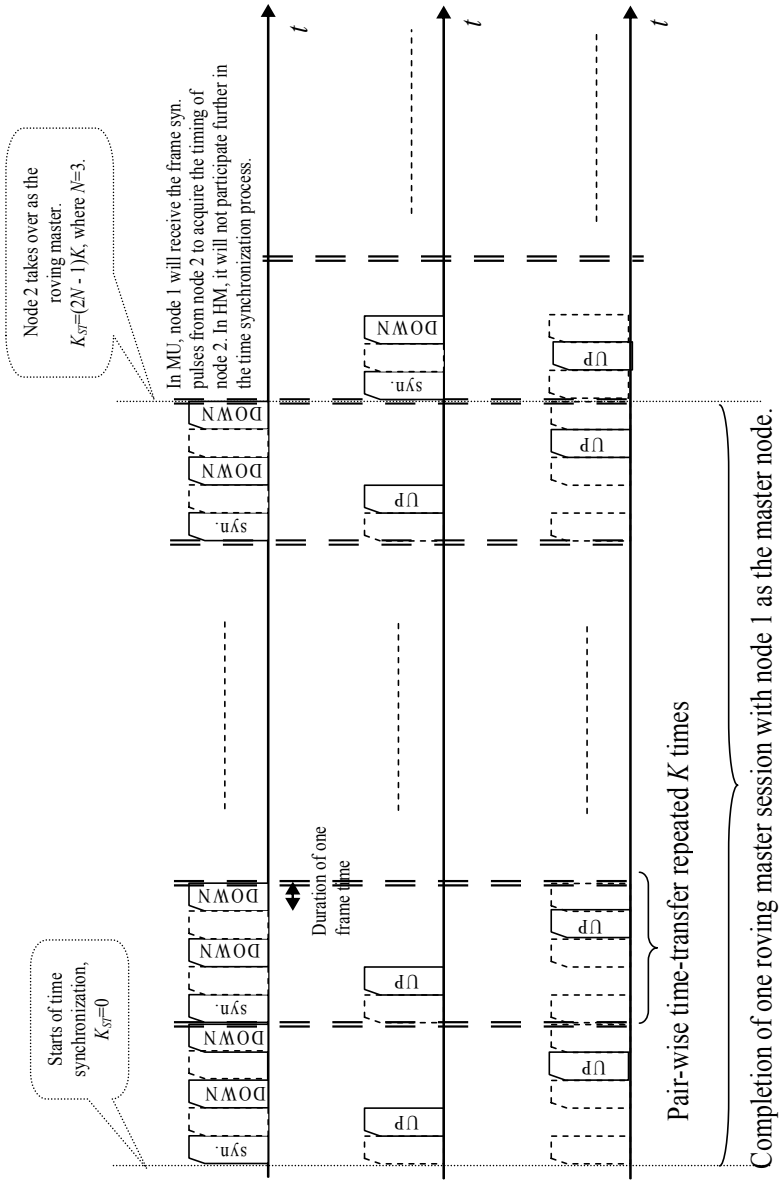

Figure 31: Illustration of the time transfer activities at each node utilizing the roving master concept with time-transfer scheme C. In this example, there are N=3 nodes in the network and node 2 is the roving master node after node 1 has transferred its timing to nodes 2 and 3. The pair-wise time-transfer is performed K times before next node take over as the roving master.

4.3 Hierarchical Master-Slave Time-Transfer Architecture

If nodes in the network are allowed to adjust and synchronize their timing to a roving master node before another node takes over as the roving master, a hierarchical master-slave (HM) time-transfer architecture is formulated. In this time-transfer architecture, all nodes in the network strive to align themselves with the timing of the lead master. This is different from the traditional hierarchical master-slave scheme in the sense that there is no fixed master at each tier of the network. Each roving master looks for the "best" nodes, e.g., the one whereby the communication link between them has the highest SNR (detected by measuring the up-link ranging pulses), to be the next roving master.

In Fig. 32, master A_1 assigns nodes B_1 and C_1 that it can communicate with to be the next tier of master nodes. Other nodes that have received timings from the master node, and assumed they are confident of the timings transferred from A_1, will then not response to the synchronization signals from B_1 and C_1 when B_1 and C_1 act as the master nodes. Other variations of this scheme are possible.

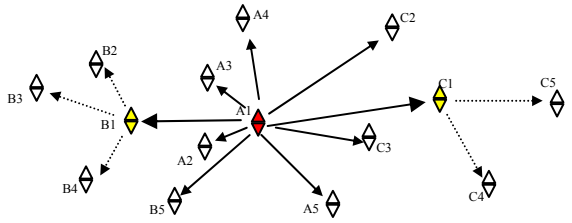

Figure 32: Hierarchical master-slave time-transfer architecture. The roving master nodes are A_1, B_1 and C_1.

It is assumed that a higher layer network protocol is utilized to co-ordinate the assignment of the next roving master node in the HM time-transfer architecture. For simplicity in presentation, the following analysis assumed that there is only one roving master node per time-transfer session. However, the analysis presented subsequently is still valid when there are multiple roving master nodes per time-transfer session.

A feasible HM network works as follows. Assuming $\hat{\gamma}_{LS}^{(m,s)} \approx \gamma^{(m,s)}$, so that $\Omega_{UP(u)}^{(s,m)}(k)$ and $\Omega_{DN(z)}^{(m,s)}(k)$ are approximately independent of time index k, the current roving master m chooses the next roving master m' so that

$$m' = \arg \min_{s} \sqrt{\mathbf{V}\{\Omega_{UP(u)}^{(s,m)}(k)\}}\,, \tag{4.4a}$$

where

$$\mathbf{V}\{\Omega_{UP(u)}^{(s,m)}(k)\} = \mathbf{V}\{\varepsilon_{UP(u)}^{(s,m)}(k)\} + \mathbf{V}\{\varepsilon_{\gamma_{LS}}^{(m,s)}\} \cdot u^2\,, \tag{4.4b}$$

and m' acquires the timing of the previous roving master m.

At the end of synchronization, slave s has measurements of $\Omega_{DN(z)}^{(m',s)}(k)$ from all roving master nodes m', the cardinality of m' not necessary equals $N-1$. The slave s, not one of the roving masters, will use the corresponding $\hat{d}_{\delta}^{(m,s)}$, $\hat{\gamma}_{LS}^{(m,s)}$ computed from the roving master m where,

$$m = \arg \min_{m'} \sqrt{\mathbf{V}\{\Omega_{DN(z)}^{(m',s)}(k)\}}\,, \tag{4.5a}$$

to correct its transceiver oscillator. The variance $\mathbf{V}\{\Omega_{DN(z)}^{(m',s)}(k)\}$, which is the variance of the ToA of the downlink ranging pulse, is

$$\mathbf{V}\{\Omega_{DN(z)}^{(m,s)}(k)\} = \mathbf{V}\{\varepsilon_{DN(z)}^{(m,s)}\} + \mathbf{V}\{\varepsilon_{\gamma_{LS}}^{(m,s)}\} \cdot (z-u)^2\,. \tag{4.5b}$$

In arriving at (4.4b) and (4.5b), we have make use of the fact that,

$$\begin{aligned}\mathbf{E}\{\varepsilon_{UP(u)}^{(m,s)} \cdot \varepsilon_{\gamma_{LS}}^{(m,s)}\} &= \mathbf{E}\{\varepsilon_{UP(u)}^{(m,s)}\} \cdot \mathbf{E}\{\varepsilon_{\gamma_{LS}}^{(m,s)}\} \\ &= 0.\end{aligned} \tag{4.5c}$$

$$\begin{aligned}\mathbf{E}\{\varepsilon_{DN(z)}^{(m,s)} \cdot \varepsilon_{\gamma_{LS}}^{(m,s)}\} &= \mathbf{E}\{\varepsilon_{DN(z)}^{(m,s)}\} \cdot \mathbf{E}\{\varepsilon_{\gamma_{LS}}^{(m,s)}\} \\ &= 0.\end{aligned} \tag{4.5d}$$

This is because the zero mean noise processes $\varepsilon_{UP(u)}^{(m,s)}$, $\varepsilon_{DN(z)}^{(m,s)}$ and $\varepsilon_{\gamma_{LS}}^{(m,s)}$ are present at different time frames and therefore can be assumed to be statistically independent. Moreover noise processes present during transmission between different pair of nodes (nodes are spatially distributed) can be assumed to be independent too.

If σ_ϕ is negligible, for reasonable number of monocycles K used to approximate $\mathbf{V}\{\Omega_{UP(u)}^{(s,m)}(k)\}$, the selection of roving masters based on (4.4a) is governed by the shortest propagation delay between pair of nodes assuming there is no excess attenuation along the shortest path. Likewise, $\mathbf{V}\{\Omega_{DN(z)}^{(m,s)}(k)\}$ is a measure proportional to the signal propagation delay.

The above synchronization architecture suggests that the jitter at a particular node is the jitter accumulated from multiple hops of the shortest possible delays. Then given a network topology and $D_{m,s}$ (including any NLoS paths), the timing jitter at any node in the network can be predicted.

Let $\mathbf{M}$ be an ordered set with cardinality denoted by $|\mathbf{M}|$, and the elements of $\mathbf{M}$ are the roving masters including the lead master node. The order of the elements in $\mathbf{M}$ is the order at which nodes become the roving master. The lead master node is the first element in $\mathbf{M}$, i.e., $\mathbf{M}(0)=1$. If Q is the number of hops from the lead master to the roving master m' from which node s acquires its timing then $\mathbf{M}(Q)=m'$. For example, for the network topology shown in Fig. 33, if $\mathbf{V}\{d^{(1)}-\tilde{d}_{HM}^{(9)}\}$ is to be computed for node 9 when there are 5 roving masters, therefore $\mathbf{M}\in\{1,8,12,4,2\}$, $Q=4$ and $m'=2$ where node 2 is the roving master nearest to node 9.

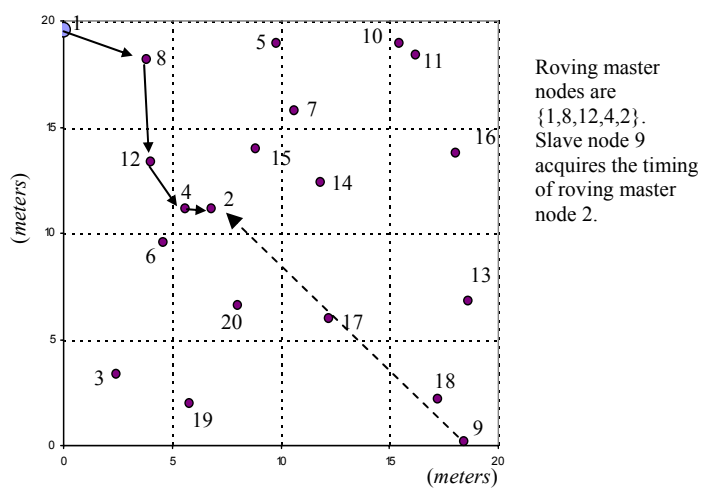

Figure 33: Illustration of the HM time-transfer architecture for a given network topology. The lead master node is node 1 and there are five roving master nodes, namely nodes 1, 8, 12, 4 and 2.

If $\widetilde{d}_{HM}^{(s)}$ and $\widetilde{a}_{HM}^{(s)}$ denote the settled initial offset and drift at node s after hierarchical master-slave time-transfer, we have

$$\begin{aligned}\widetilde{d}_{HM}^{(s)} &= d^{(s)} + \hat{d}_{\delta}^{(m',s)} \\ &= d^{(s)} + d^{(m')} - d^{(s)} + \widetilde{\rho}_{m',s} + \varepsilon_{\hat{d}}^{(m',s)} \\ &= d^{(m')} + \widetilde{\rho}_{m',s} + \varepsilon_{\hat{d}}^{(m',s)} \\ &= d^{(1)} + \varepsilon_{\hat{d}}^{(\mathbf{M}(Q),s)} + \widetilde{\rho}_{(\mathbf{M}(Q),s)} + \sum_{\substack{q=1 \\ \mathbf{M}(q)\neq s}}^{Q} \varepsilon_{\hat{d}}^{(\mathbf{M}(q-1),\mathbf{M}(q))} + \widetilde{\rho}_{(\mathbf{M}(q-1),\mathbf{M}(q))} \quad , \end{aligned} \tag{4.6a}$$

$$\begin{aligned}\widetilde{a}_{HM}^{(s)} T_f &= a_1^{(s)} T_f + \hat{\gamma}_{\delta}^{(m',s)} \\ &= a_1^{(s)} T_f + \gamma^{(m',s)} + \varepsilon_{\gamma_{LS}}^{(m',s)} \\ &= a_1^{(m')} T_f + \varepsilon_{\gamma_{LS}}^{(m',s)} \\ &= a_1^{(1)} T_f + \varepsilon_{\gamma_{LS}}^{(\mathbf{M}(Q),s)} + \sum_{\substack{q=1, \\ \mathbf{M}(q)\neq s}}^{Q} \varepsilon_{\gamma_{LS}}^{(\mathbf{M}(q-1),\mathbf{M}(q))} . \end{aligned} \tag{4.6b}$$

This allows us to express the variance of the difference $(d^{(1)} - \widetilde{d}_{HM}^{(s)})$ as

$$\begin{aligned}\mathbf{V}\{d^{(1)} - \widetilde{d}_{HM}^{(s)}\} &= \mathbf{V}\{\varepsilon_{\hat{d}}^{(M(Q),s)}\} + \sum_{\substack{q=1, \\ M(q)\neq s}}^{Q} \mathbf{V}\{\varepsilon_{\hat{d}}^{(M(q-1),M(q))}\} \\ &= \mathbf{V}\{\hat{d}_{\delta}^{(\mathbf{M}(Q),s)}\} + \sum_{\substack{q=1, \\ M(q)\neq s}}^{Q} \mathbf{V}\{\hat{d}_{\delta}^{(\mathbf{M}(q-1),\mathbf{M}(q))}\} \\ &= \frac{\left(\sum_{k=0}^{K-1}(\theta(k) - (2N-1)\cdot K\cdot Q)\right)^2}{K^2} \cdot \mathbf{V}\{\varepsilon_{\gamma_{LS}}^{(\mathbf{M}(Q),s)}\} + \mathbf{V}\{\varepsilon_{\vartheta}^{(\mathbf{M}(Q),s)}\} \\ &\quad + \sum_{\substack{q=1, \\ M(q)\neq s}}^{Q} \left(\frac{\left(\sum_{k=0}^{K-1}(\theta(k) - K_{ST})\right)^2}{K^2} \cdot \mathbf{V}\{\varepsilon_{\gamma_{LS}}^{(\mathbf{M}(q-1),\mathbf{M}(q))}\} + \mathbf{V}\{\varepsilon_{\vartheta}^{(\mathbf{M}(q),\mathbf{M}(q))}\} \right) \quad , \text{ for } Q>0 \end{aligned} \tag{4.7a}$$

where $K_{ST} = (2N-1)\cdot K\cdot(q-1)$ and

$$\begin{aligned}\mathbf{V}\{d^{(1)} - \widetilde{d}_{HM}^{(s)}\} &= \mathbf{V}\{\varepsilon_{\hat{d}}^{(1,s)}\} \\ &= \left(\sum_{k=0}^{K-1}\theta(k)\right)^2 \cdot \mathbf{V}\{\varepsilon_{\gamma_{LS}}^{(1,s)}\}/K^2 + \mathbf{V}\{\varepsilon_{\vartheta}^{(1,s)}\} \quad , \qquad \text{for } Q=0 \end{aligned} \tag{4.7b}$$

where $\mathbf{V}\{\varepsilon_{\vartheta}^{(m,s)}\} = \dfrac{5\cdot\sigma_x^2(m,s) + \sigma_x^2(s,m)}{4K}$ and $\sigma_x^2(m,s) = D_{m,s}^2/\Theta_t\,\overline{\omega^2} + 2\sigma_{\phi}^2$.

The expectation of the squared of the estimation error is

$$\mathbf{E}\{(d^{(1)}-d_{SM}^{(s)})^2\}=\mathbf{V}\{(d^{(1)}-d_{SM}^{(s)})\}+\left(\widetilde{\rho}_{\mathbf{M}(Q),s}+\sum_{\substack{q=1,\\ \mathbf{M}(q)\neq s}}^{Q}\widetilde{\rho}_{\mathbf{M}(q-1),\mathbf{M}(q)}\right)^2 . \tag{4.7c}$$

The variance of estimating the difference in drift is not a function of K_{ST} and is given by

$$\mathbf{V}\{a_1^{(1)}-\widetilde{a}_{HM}^{(s)}\}=\begin{cases}\mathbf{V}\{\varepsilon_{\gamma_{LS}}^{(\mathbf{M}(Q),s)}\}+\sum_{\substack{q=1\\ \mathbf{M}(q)\neq s}}^{Q}\mathbf{V}\{\varepsilon_{\gamma_{LS}}^{(\mathbf{M}(q-1),\mathbf{M}(q))}\}\ , & Q>0.\\ \mathbf{V}\{\varepsilon_{\gamma_{LS}}^{(\mathbf{M}(0),s)}\}\ , & Q=0.\end{cases} \tag{4.8}$$

If $\sigma_\phi=0$, the standard deviations of the measured uplink and downlink ToAs, $\sqrt{\mathbf{V}\{\Omega_{UP(u)}^{(s,m)}(k)\}_{k=0}^{K-1}}$ and $\sqrt{\mathbf{V}\{\Omega_{DN(z)}^{(m,s)}(k)\}_{k=0}^{K-1}}$, are proportional to signal propagation distances, $D_{m,s}$. On the contrary, if $\sigma_\phi\neq 0$, the distance dependency of the standard deviations will be affected by the randomness in the oscillator phase noise. This introduces randomness both in the selection of the next roving master and transfer of timing from the roving master node to slave nodes.

A flow chart depicting the hierarchical master-slave time-transfer architecture is shown in Fig. 34. The variances of the measured up-link and down-link ToAs can be approximated by their sample variances [32], i.e.,

$$\mathbf{V}\{\Omega_{DN(z)}^{(m',s)}\}=\mathbf{V}\{\Omega_{DN(z)}^{(m',s)}(k)\}\approx\frac{1}{K-1}\sum_{k=K_{ST}}^{K+K_{ST}-1}\left(\Omega_{DN(z)}^{(m',s)}(k)-\left(\sum_{k=K_{ST}}^{K+K_{ST}-1}\Omega_{DN(z)}^{(m',s)}(k)/K\right)\right)^2 , \tag{4.9a}$$

$$\mathbf{V}\{\Omega_{UP(u)}^{(s,m)}\}=\mathbf{V}\{\Omega_{UP(u)}^{(s,m)}(k)\}\approx\frac{1}{K-1}\sum_{z=K_{ST}}^{K+K_{ST}-1}\left(\Omega_{UP(u)}^{(s,m)}(k)-\left(\sum_{z=K_{ST}}^{K+K_{ST}-1}\Omega_{UP(u)}^{(s,m)}(k)/K\right)\right)^2 . \tag{4.9b}$$

Since it is assumed that the oscillator phase noise and additive channel noise are i.i.d. in the rest of the discussion, the index k is omitted and the variances of the downlink and uplink ToAs are expressed as $\mathbf{V}\{\Omega_{DN(z)}^{(m,s)}\}$ and $\mathbf{V}\{\Omega_{UP(u)}^{(s,m)}\}$ respectively.

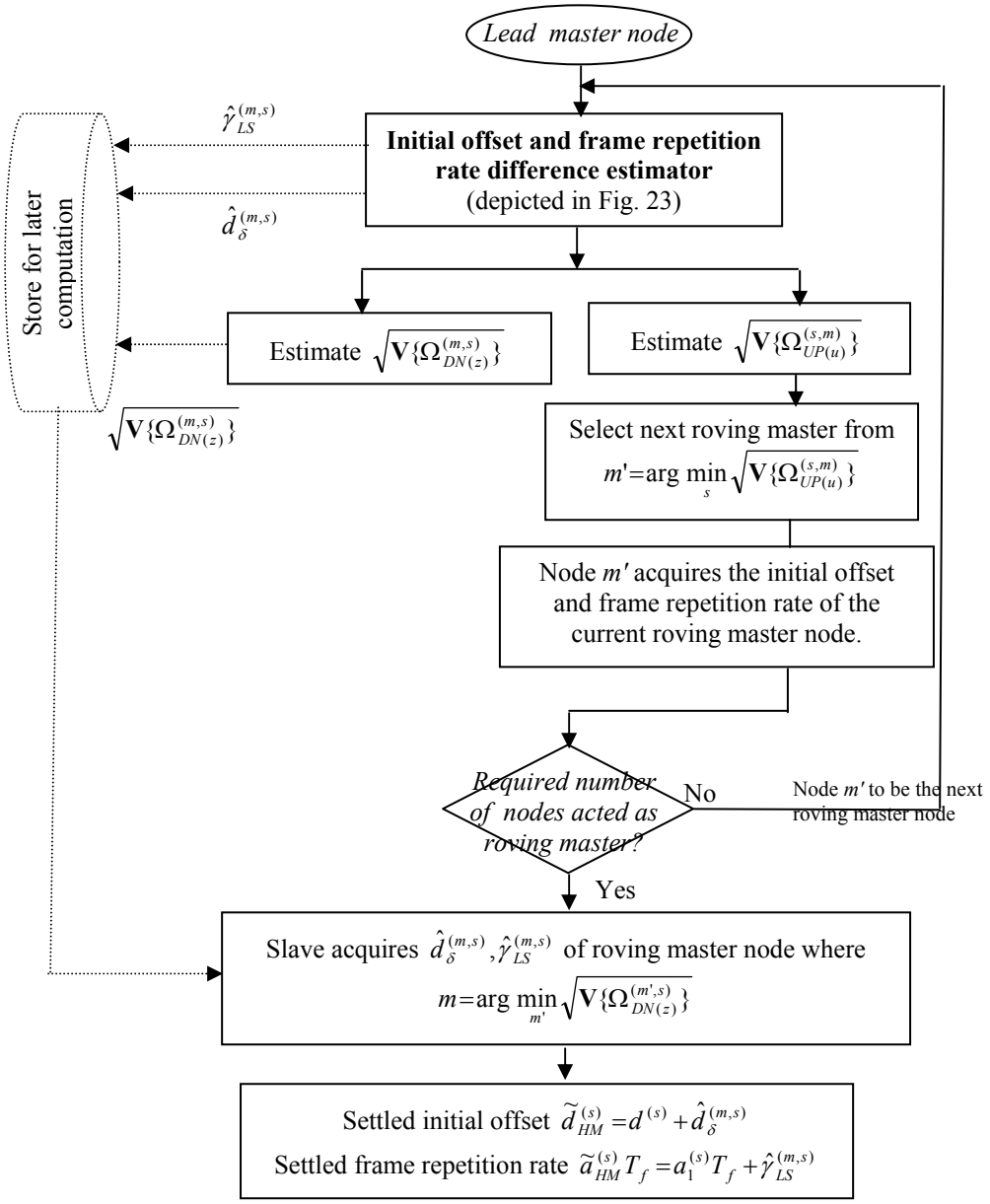

Figure 34: Flow chart illustrating the various processes to implement a hierarchical master slave time-transfer architecture.

4.4 Mutually Synchronous Time-Transfer Architecture

The synchronous networks describe in sections 4.1 and 4.3 employ a master-slave synchronization scheme where nodes in the network align their timings to a designated master node. In this section, the mutually synchronous time-transfer architecture is introduced.

If there are N nodes in a network, a single synchronization session of master-slave will take $(2(N-1)K_r + K_s)$ time frames. A complete roving of all N transceivers in the network will take $(2N-1)NK$ time frames if $K_s = K_r = K$. More importantly, at the end of one roving cycle, each transceiver in the network would have obtained $(N-1)$ measurements of $\{\Omega_{SY(v)}^{(m,s)}(k)\}_{k=0}^{K-1}$, $\{\Omega_{DN(z)}^{(m,s)}(k)\}_{k=0}^{K-1}$ and $\{\Omega_{UP(u)}^{(s,m)}(k)\}_{k=0}^{K-1}$. If appropriate ToA measurement is weighted [34] according to some criteria such as received signal strength, the timing adjustments at each node can be obtained using a weighted combination of inputs from all other nodes in the network. Thus we have a MU network, which is characterized by every oscillator in the network contributing to the settled timing of the network.

If the approaches described in section 3.3 are used to estimate $d_{\delta}^{(m,s)}$ (3.24a) and $\gamma^{(m,s)}$ is estimated using the LS estimator described by (2.43e), a MU scheme maybe implemented as follows.

Assuming nodes act as master in a natural order, i.e., node 1 is the first roving master node, follows by node 2, node 3, …etc. Whenever a node s is not a roving master, it computes $\mathbf{V}\{\Omega_{DN(z)}^{(m',s)}\}$, acquires the frame repetition rate of m' and estimates $\hat{d}_{\delta}^{(m',s)}$. For example, if there are 3 nodes $\{1,2,3\}$ in the network, when node 1 is the master, 2 and 3 acquire 1's frame repetition rate. When 2 becomes the roving master, 1 has to acquire the frame repetition rate of 2, which is a noisy copy of its original frame repetition rate. When 3 is the roving master, it transfers its frame repetition rate, which 3 has earlier acquired from 2, to 1. Preceding initial offset estimation with pair-wise frame repetition rate estimation is to minimize $\mathbf{V}\{\hat{d}_{\delta}^{(m',s)}\}$. Thus all nodes in the network will have a noisy copy of the

original frame repetition rate of 1. If on the contrary, e.g., 1's frame repetition rate is transferred to 2 and 3, and the pair of nodes 2, 3 estimate their differences in initial offset without further estimating each other's frame repetition rates, the resulting $\mathbf{V}\{\hat{d}_{\delta}^{(2,3)}\}$ will be higher than the approach described earlier. This is because, due to channel impairments, 2 and 3 only acquire a noisy copy of 1's frame repetition rate, i.e., there is a residue error between 2 and 3 frame repetition rates that leads to higher $\mathbf{V}\{\hat{d}_{\delta}^{(m,s)}\}$. The process flow of the MU time-transfer architecture is illustrated in Fig. 35.

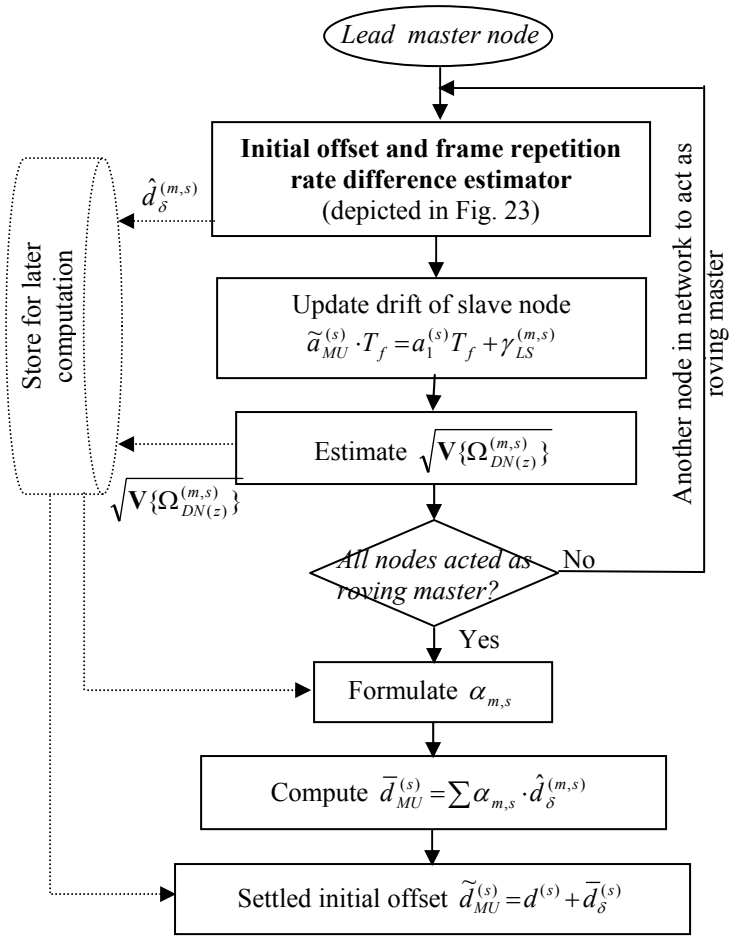

Figure 35: Flow chart illustrating the various processes to implement mutually synchronous time-transfer architecture.

Let the settled drift of node s be $\widetilde{a}_{MU}^{(s)}$. From the description of pair-wise time transfer presented in the previous paragraphs, $\widetilde{a}_{MU}^{(s)}$ is given by

$$\begin{aligned}\widetilde{a}_{MU}^{(s)}T_f &= a_1^{(1)}T_f + \varepsilon_{\gamma_{LS}}^{(1,2)} + \varepsilon_{\gamma_{LS}}^{(2,3)} + \varepsilon_{\gamma_{LS}}^{(3,4)} + \varepsilon_{\gamma_{LS}}^{(4,5)} + \varepsilon_{\gamma_{LS}}^{(5,6)} + \cdots + \varepsilon_{\gamma_{LS}}^{(N-1,N)} + \varepsilon_{\gamma_{LS}}^{(N,s)} \\ &= a_1^{(1)}T_f + \sum_{n=1}^{N\text{-}1}\varepsilon_{\gamma_{LS}}^{(n,n+1)} + \varepsilon_{\gamma_{LS}}^{(N,s)},\end{aligned} \tag{4.10}$$

where the random variable $\varepsilon_{\gamma_{LS}}^{(m,s)}$ is the LS estimation error when estimating $\gamma^{(m,s)}$. Further, the square of (4.10) is

$$\left(\widetilde{a}_{MU}^{(s)}\right)^2 = \left(a_1^{(1)} + \sum_{n=1}^{N\text{-}1}\varepsilon_{\gamma_{LS}}^{(n,n+1)}/T_f\right)^2 + \left(\varepsilon_{\gamma_{LS}}^{(N,s)}/T_f\right)^2 + 2\cdot\left(\varepsilon_{\gamma_{LS}}^{(N,s)}/T_f\right)\left(a_1^{(1)} + \sum_{n=1}^{N\text{-}1}\varepsilon_{\gamma_{LS}}^{(n,n+1)}/T_f\right). \tag{4.11}$$

Therefore

$$\mathbf{E}\{\widetilde{a}_{MU}^{(s)}\} = a_1^{(1)}, \tag{4.12a}$$

and

$$\begin{aligned}\mathbf{E}\left\{\left(\widetilde{a}_{MU}^{(s)}\right)^2\right\} &= \mathbf{E}\left\{\left(a_1^{(1)} + \sum_{n=1}^{N\text{-}1}\mathbf{V}\{\varepsilon_{\gamma_{LS}}^{(n,n+1)}/T_f\}\right)^2\right\} + \mathbf{V}\{\varepsilon_{\gamma_{LS}}^{(N,s)}/T_f\} \\ &= (a_1^{(1)})^2 + \sum_{n=1}^{N\text{-}1}\mathbf{V}\{\varepsilon_{\gamma_{LS}}^{(n,n+1)}/T_f\} + \mathbf{V}\{\varepsilon_{\gamma_{LS}}^{(N,s)}/T_f\},\end{aligned} \tag{4.12b}$$

$$\begin{aligned}\mathbf{V}\{\widetilde{a}_{MU}^{(s)}\} &= \mathbf{E}\left\{\left(\widetilde{a}_{MU}^{(s)}\right)^2\right\} - \left(\mathbf{E}\{\widetilde{a}_{MU}^{(s)}\}\right)^2 \\ &= \sum_{n=1}^{N\text{-}1}\mathbf{V}\{\varepsilon_{\gamma_{LS}}^{(n,n+1)}/T_f\} + \mathbf{V}\{\varepsilon_{\gamma_{LS}}^{(N,s)}/T_f\}.\end{aligned} \tag{4.12c}$$

Here the sample variance of the settled drift estimate across all nodes in the network, denoted by $\mathbf{V}\{\widetilde{a}_{MU}\}$, after time synchronization is of interest. The variance $\mathbf{V}\{\widetilde{a}_{MU}\}$ is defined to be the sample variance [32] of $\widetilde{a}_{MU}^{(s)}$, $s=1,\ldots,N$, and mean of $\mathbf{V}\{\widetilde{a}_{MU}\}$ is defined as

$$\overline{\mathbf{V}\{\widetilde{a}_{MU}\}} = \mathbf{E}\left\{\frac{1}{N-1}\sum_{s=1}^{N}\left(\widetilde{a}_{MU}^{(s)} - \left(\frac{1}{N}\sum_{s=1}^{N}\widetilde{a}_{MU}^{(s)}\right)\right)^2\right\}. \tag{4.13a}$$

The quantity $\sum_{s=1}^{N}\widetilde{a}_{MU}^{(s)}/N$ is known as the sample mean. It is derived in Appendix B that

$$\mathbf{E}\left\{\left(\frac{1}{N}\sum_{s=1}^{N}\tilde{a}_{MU}^{(s)}\right)^2\right\}=(a_1^{(1)})^2+\sum_{n=1}^{N-1}\mathbf{V}\{\varepsilon_{\gamma_{LS}}^{(n,n+1)}/T_f\}+\frac{1}{N^2}\sum_{s=1}^{N}\mathbf{V}\{\varepsilon_{\gamma_{LS}}^{(N,s)}/T_f\}\,, \tag{4.13b}$$

and the mean of the variance across all nodes in the network is

$$\overline{\mathbf{V}\{\tilde{a}_{MU}\}}=\frac{1}{N}\cdot\sum_{s=1}^{N}\mathbf{V}\{\varepsilon_{\gamma_{LS}}^{(N,s)}/T_f\}\,. \tag{4.13c}$$

The weight $\alpha_{m,s}$, where $\sum_{m=1,m\neq s}^{N}\alpha_{m,s}=1$, $\forall s$ and m is the roving master index, is used to weight the various timings acquired by node s from the roving masters. At slave s, assumes $i=j$, for a particular roving master $m'\neq s$, a possible weight function is

$$\alpha_{m',s}=\frac{1\Big/\sqrt{\mathbf{V}\{\Omega_{DN(z)}^{(m',s)}\}}}{\sum_{m=1,m\neq s}^{N}1/\sqrt{\mathbf{V}\{\Omega_{DN(z)}^{(m,s)}\}}}\,, \tag{4.14}$$

where $\mathbf{V}\{\Omega_{DN(z)}^{(m,s)}\}$ is approximated by (4.9a).

The weighted average initial offset difference evaluated at node s is defined as

$$\bar{d}_{\delta}^{(s)}=\sum_{m=1,m\neq s}^{N}\alpha_{m,s}\hat{d}_{\delta}^{(m,s)}\,. \tag{4.15}$$

From section 3.3, equation (3.24a) $\hat{d}_{\delta}^{(m,s)}=d^{(m)}-d^{(s)}+(\rho_{m,s}-\rho_{s,m})/2+\varepsilon_{\hat{d}}^{(m,s)}$ and $\varepsilon_{\hat{d}}^{(m,s)}$ is the zero mean measurement error associated with determining $\hat{d}_{\delta}^{(m,s)}$. The mean of $\hat{d}_{\delta}^{(m,s)}$ is given by

$$\mathbf{E}\{\hat{d}_{\delta}^{(m,s)}\}=d^{(m)}-d^{(s)}+(\rho_{m,s}-\rho_{s,m})/2\,, \tag{4.16a}$$

and using results from Appendix A,

$$\begin{aligned}\mathbf{V}\{\hat{d}_{\delta}^{(m,s)}\}&=\mathbf{E}\{(\varepsilon_{\hat{d}}^{(m,s)})^2\}\\&=\frac{\left(\sum_{k=0}^{K-1}(\theta(k)-K_{ST})\right)^2}{K^2}\cdot\mathbf{V}\{\varepsilon_{\gamma_{LS}}^{(m,s)}\}+\mathbf{V}\{\varepsilon_{\vartheta}^{(m,s)}\}\,,\end{aligned} \tag{4.16b}$$

where $\mathbf{V}\{\varepsilon_{\vartheta}^{(m,s)}\}=(5\sigma_x^2(m,s)+\sigma_x^2(s,m))/(4K)$, $K_{ST}=K\cdot Q\cdot(2N-1)$ and $\sigma_x^2(m,s)=D_{m,s}^2/\Theta_t\overline{\omega^2}+2\sigma_{\phi}^2$. The variable Q, first mentioned in section 4.3, equation (4.6a), is the number of hops from the lead

master to the roving master m' from which s acquires its timing. In the MU time-transfer architecture investigated in this work, $\mathbf{M}\in\{1,2,3,...,N\}$ where $\mathbf{M}(0)=1$ and $|\mathbf{M}|=N$, therefore $K_{ST}=K\cdot(2N-1)\cdot(m-1)$ where $m\in\{1,2,3,...,N\}$. In general, the lead master node is likely to have a larger $\mathbf{V}\{\bar{d}_{MU}^{(s)}\}$ since Q ranges from 1 to $N-1$ in evaluating $\sum_{m=2}^{N}\alpha_{m,1}^{2}\cdot\mathbf{V}\{\hat{d}_{\delta}^{(m,1)}\}$. Conversely, node N will have the smallest $\mathbf{V}\{\bar{d}_{MU}^{(s)}\}$ as Q ranges from 0 to $N-2$. A larger Q implies a larger K_{ST}, which in turns lead to larger $\mathbf{V}\{\hat{d}_{\delta}^{(m,s)}\}$. That is, jitter of individual nodes increases from node 1 to N ignoring the effect of network topology.

The slave node will use $\bar{d}_{\delta}^{(s)}$ to correct its transceiver oscillator such that the updated offset (refered to as "settled" estimate of the initial offset in the rest of the discussion) at the end of the mutually synchronous time-transfer is

$$\begin{aligned}\tilde{d}_{MU}^{(s)} &= d^{(s)}+\bar{d}_{\delta}^{(s)}\\ &= d^{(s)}+\sum_{m=1,m\neq s}^{N}\alpha_{m,s}\cdot\hat{d}_{\delta}^{(m,s)}\\ &= d^{(s)}+\sum_{m=1,m\neq s}^{N}\alpha_{m,s}\cdot\left(d^{(m)}-d^{(s)}+(\rho_{m,s}-\rho_{s,m})/2+\varepsilon_{\hat{d}}^{(m,s)}\right)\\ &= \sum_{m=1,m\neq s}^{N}\alpha_{m,s}\cdot\left(d^{(m)}+(\rho_{m,s}-\rho_{s,m})/2\right)+\sum_{m=1,m\neq s}^{N}\alpha_{m,s}\cdot\varepsilon_{\hat{d}}^{(m,s)}\ .\end{aligned} \tag{4.17}$$

The settled estimated of the initial offset at node s has the following statistics

$$\mathbf{E}\{\tilde{d}_{MU}^{(s)}\}=\sum_{m'=1,m'\neq s}^{N}\alpha_{m',s}\cdot(\mathbf{E}\{d^{(m')}\}+\tilde{\rho}_{m',s})\ , \tag{4.18a}$$

$$\mathbf{V}\{\tilde{d}_{MU}^{(s)}\}=\sum_{m=1,m\neq s}^{N}\alpha_{m,s}^{2}\cdot(\mathbf{V}\{d^{(m)}\}+\mathbf{V}\{\hat{d}_{\delta}^{(m,s)}\})\ . \tag{4.18b}$$

For most practical purposes, and in subsequent analysis, initial offset $d^{(m)}$ for nodes in a given network is treated as a deterministic variable, i.e., $\mathbf{V}\{d^{(m)}\}=0$ and $\mathbf{E}\{d^{(m)}\}=d^{(m)}$. Then (4.18a) and (4.18b) reduce to

$$\mathbf{E}\{\tilde{d}_{MU}^{(s)}\}=\sum_{m'=1,m'\neq s}^{N}\alpha_{m',s}\cdot(d^{(m')}+\tilde{\rho}_{m',s})\ , \tag{4.19a}$$

$$\mathbf{V}\{\widetilde{d}_{MU}^{(s)}\} = \sum_{m=1, m\neq s}^{N} \alpha_{m,s}^{2} \cdot \mathbf{V}\{\hat{d}_{\delta}^{(m,s)}\}\,. \tag{4.19b}$$

In (4.17) through (4.19), the variance $\mathbf{V}\{\hat{d}_{\delta}^{(m,s)}\} = \mathbf{V}\{\varepsilon_{\hat{d}}^{(m,s)}\}$. The mean of the sample variance of $\widetilde{d}_{MU}^{(s)}$, $s = 1,\ldots,N$, after synchronization is defined as

$$\overline{\mathbf{V}\{\widetilde{d}_{MU}\}} = \mathbf{E}\left\{ \frac{1}{N-1} \sum_{s=1}^{N} \left(\widetilde{d}_{MU}^{(s)} - \left(\sum_{s=1}^{N} \widetilde{d}_{MU}^{(s)} / N \right) \right)^{2} \right\}. \tag{4.20a}$$

To evaluate (4.20a), for clarity let $\beta^{(s)} = \sum_{m=1, m\neq s}^{N} \alpha_{m,s} \cdot (d^{(m)} + \widetilde{\rho}_{m,s})$ and $\alpha^{(s)} = \sum_{m=1, m\neq s}^{N} \alpha_{m,s}^{2} \cdot \varepsilon_{\hat{d}}^{(m,s)}$ where $\mathbf{E}\{\alpha^{(s)}\} = 0$. It can be shown that

$$\begin{aligned}
\overline{\mathbf{V}\{\widetilde{d}_{MU}\}} &= \mathbf{E}\left\{ \frac{1}{N-1} \sum_{s=1}^{N} \left(\widetilde{d}_{MU}^{(s)} - \left(\sum_{s=1}^{N} \widetilde{d}_{MU}^{(s)} / N \right) \right)^{2} \right\} \\
&= \mathbf{E}\left\{ \frac{1}{N-1} \sum_{s=1}^{N} \left(\alpha^{(s)} - \left(\sum_{s=1}^{N} \alpha^{(s)} / N \right) \right)^{2} \right\} + \mathbf{E}\left\{ \frac{1}{N-1} \sum_{s=1}^{N} \left(\beta^{(s)} - \left(\sum_{s=1}^{N} \beta^{(s)} / N \right) \right)^{2} \right\},
\end{aligned} \tag{4.20b}$$

which is the sum of the sample variance of the zero-mean disturbances introduced during the wireless time-transfer and the sample variance of the weighted initial offset of nodes before time-transfer. Substituting $\alpha^{(s)}$ and $\beta^{(s)}$ into (4.20b), we have

$$\begin{aligned}
\overline{\mathbf{V}\{\widetilde{d}_{MU}\}} &= \mathbf{E}\left\{ \frac{1}{N-1} \sum_{s=1}^{N} \left(\widetilde{d}_{MU}^{(s)} - \left(\sum_{s=1}^{N} \widetilde{d}_{MU}^{(s)} / N \right) \right)^{2} \right\} \\
&= \frac{1}{N} \sum_{s=1}^{N} \sum_{\substack{m=1 \\ m\neq s}}^{N} \alpha_{m,s}^{2} \mathbf{E}\left\{ \left(\varepsilon_{\hat{d}}^{(m,s)} \right)^{2} \right\} + \frac{1}{N-1} \sum_{s=1}^{N} \left(\sum_{m=1, m\neq s}^{N} \alpha_{m,s} \cdot \left(d^{(m)} + \widetilde{\rho}_{m,s} \right) \right)^{2} \\
&\quad - \frac{1}{N(N-1)} \left(\sum_{s=1}^{N} \sum_{m=1, m\neq s}^{N} \alpha_{m,s} \cdot \left(d^{(m)} + \widetilde{\rho}_{m,s} \right) \right)^{2} \\
&= \frac{1}{N} \sum_{s=1}^{N} \mathbf{V}\{\widetilde{d}_{MU}^{(s)}\} + \frac{1}{N-1} \sum_{s=1}^{N} \left(\sum_{m=1, m\neq s}^{N} \alpha_{m,s} \cdot \left(d^{(m)} + \widetilde{\rho}_{m,s} \right) \right)^{2} \\
&\quad - \frac{1}{N(N-1)} \left(\sum_{s=1}^{N} \sum_{m=1, m\neq s}^{N} \alpha_{m,s} \cdot \left(d^{(m)} + \widetilde{\rho}_{m,s} \right) \right)^{2}.
\end{aligned} \tag{4.20c}$$

The wireless channels between different pairs of transceivers m,s have different noise variances. As a result, $\Omega_{SY}^{(m,s)}$, $\Omega_{UP(u)}^{(s,m)}$ and $\Omega_{DN(z)}^{(m,s)}$ can be vastly different. The weights should be chosen appropriately so that potentially erroneous measurements are de-emphasized while measurements correspond to LoS propagation are enhanced.

A mutually synchronous network is characterized by every oscillator in the network contributing to the settled timing of the network. The timing of the network after time transfer is a weighted contribution of the timings of every node in the network. There are certain advantages of having a mutually synchronous network which are discussed in [7] [34]. The works of [34] has a detail discussion on the individual merits of hierarchical master-slaves and mutually synchronous network.

A possible system implementation of the mutually synchronous TDMA synchronizing scheme for the SIN is shown in Fig. 36. In Fig. 36, the timing detector output $x_{(k)}$ is the relative ToAs' $\Omega_{SY(v)}^{(m,s)}$, $\Omega_{UP(u)}^{(s,m)}$ and $\Omega_{DN(z)}^{(m,s)}$ obtained at the frame-synchronization, uplink and downlink time slots respectively. Note that the VCO is free running during synchronization.

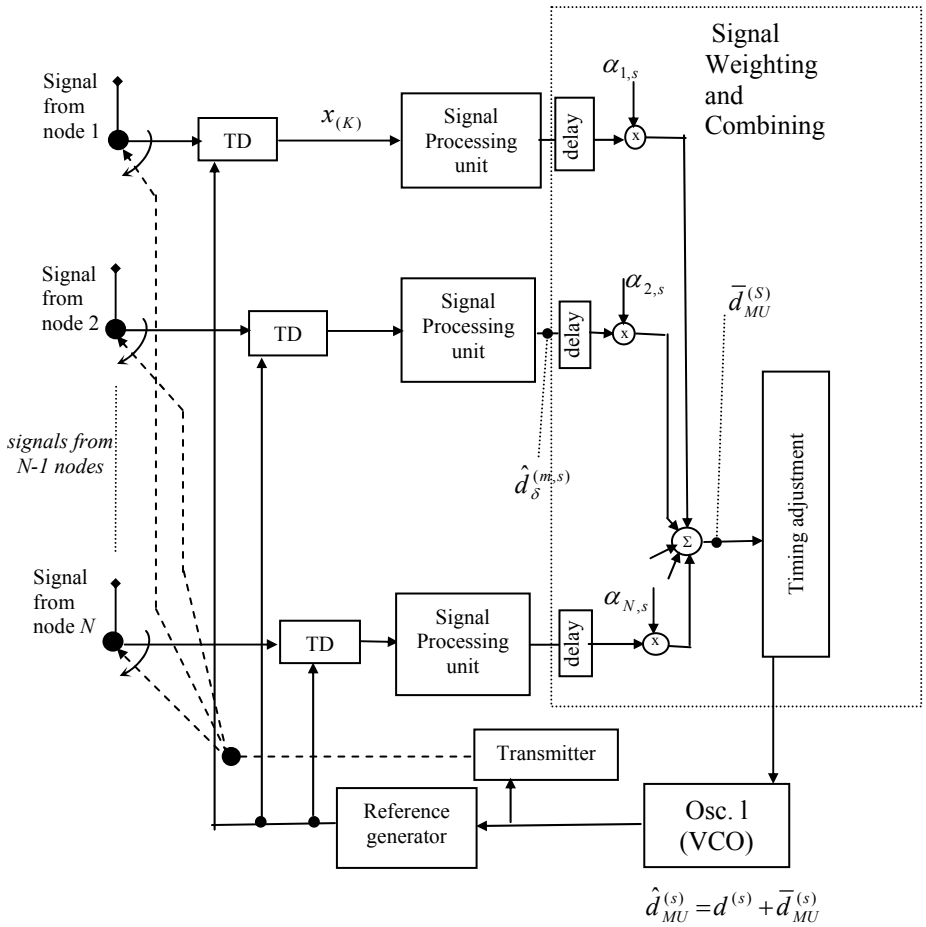

Figure 36: Illustration of the logical channels forming the mutually synchronous SIN. The "signal processing" unit consists of the LS estimator to estimate frame repetition rate differences and the statistical averaging to estimate initial offset differences between transceivers. Antenna switch connects to "dotted" path when transmitting UWB monocycles. The "delay" is to align the estimators output so that they combined at the same time to set the timing of the oscillator after the synchronization process.

CHAPTER V

TIME-TRANSFER ERRORS

From Chapter 1, if $t_{(k')}^{(m)}$ and $t_{(k')}^{(s)}$ are the kth zero crossing of the master and slave nodes m and s respectively, the timing error between nodes m and s after time-transfer at time t' is

$$t_{(k')}^{(m)} - t_{(k')}^{(s)} = a_1^{(m)} t' + d^{(m)} + \phi_{(k')}^{(m)} - a_1^{(s)} t' - d^{(s)} - \phi_{(k')}^{(s)}, \tag{5.1}$$

where $t' = k' T_f$ denotes the time at the end of time-transfer. It is evident from (5.1) that a longer t' will lead to a larger timing error due to mis-match in oscillator drift $(a_1^{(m)} - a_1^{(s)})$.

After time synchronization, the differences in oscillator frame repetition rate and initial offset will both be random variables. This is because time-transfer is performed in the presence of additive channel noise and oscillator phase noise. We assume nodes are stationary during time-transfer.

5.1 Hierarchical Master-slave Time-Transfer Error

For single-master-to-multiple-slaves (SM) and hierarchical master-slave (HM) time-transfer architectures, the variance of the timing error after time transfer is given by

$$\mathbf{V}\{t_{(k')}^{(1)} - \tilde{t}_{HM(k')}^{(s)}\} = \mathbf{V}\{a_1^{(1)} t' + d^{(1)} - \tilde{a}_{HM}^{(s)} t' - \tilde{d}_{HM}^{(s)}\} + 2\sigma_\phi^2, \ \forall s, \ s \neq 1. \tag{5.2}$$

where $\tilde{t}_{HM(k')}^{(s)}$ is the settled timing estimate at node s after time transfer. From Chapters 2 and 3, the difference in initial offset, $d_\delta^{(m,s)}$ between two nodes m and s is estimated by taking the sample mean of $\vartheta^{(m,s)}$ over K frames. From (3.24a), $d_\delta^{(m,s)} = \hat{d}_\delta^{(m,s)} + \tilde{\rho}_{m,s} + \varepsilon_{\hat{d}}^{(m,s)}$, where $\varepsilon_{\hat{d}}^{(m,s)}$ is the zero mean estimation error. The difference in frame repetition rate $\gamma^{(m,s)}$ is estimated via LS estimation from the ToAs of the frame-synchronization pulses, where $\hat{\gamma}_{LS}^{(m,s)} = \gamma^{(m,s)} + \varepsilon_{\gamma_{LS}}^{(m,s)}$ and $\mathbf{E}\{\varepsilon_{\gamma_{LS}}^{(m,s)}\} = 0$.

In Chapter 4, it is defined that $\mathbf{M}$ is an ordered set whose elements are the node label of the roving masters. The elements in the set are arranged according to the order at which node takes turn to be the roving master. The element of $\mathbf{M}$ is denoted as $\mathbf{M}(q)$ where $q=0,...,|\mathbf{M}|-1$ and $\mathbf{M}(0)=1$ is the lead master node. If node s acquires its timing from roving master m' where $\mathbf{M}(Q)=m'$, from section 4.3, the settled initial offset estimate at node s after HM time-transfer is

$$\widetilde{d}_{HM}^{(s)} = d^{(1)} + \varepsilon_{\hat{d}}^{(\mathbf{M}(Q),s)} + \widetilde{\rho}_{\mathbf{M}(Q),s} + \sum_{\substack{q=1 \\ \mathbf{M}(q)\neq s}}^{Q} \varepsilon_{\hat{d}}^{(\mathbf{M}(q-1),\mathbf{M}(q))} + \widetilde{\rho}_{\mathbf{M}(q-1),\mathbf{M}(q)} \ , \ s \neq 1 , \tag{5.3a}$$

and the settled drift estimate is

$$\widetilde{a}_{HM}^{(s)} = a_1^{(1)} + \varepsilon_{\gamma_{LS}}^{(\mathbf{M}(Q),s)} / T_f + \sum_{\substack{q=1 \\ \mathbf{M}(q)\neq s}}^{Q} \varepsilon_{\gamma_{LS}}^{(\mathbf{M}(q-1),\mathbf{M}(q))} / T_f \ , \ s \neq 1 . \tag{5.3b}$$

The variable Q, besides denoting a particular roving master m' in $\mathbf{M}$, i.e., $\mathbf{M}(Q)=m'$, equals the number of hops (time transfers) from the lead master node to the roving master m' from which slave s acquires its timing.

(a) *Hierarchical Master-Slave Timing Jitter*

In Appendix B, it is derived analytically that the timing error variance for HM is given by

$$\begin{aligned}\mathbf{E}\left\{\left(t_{(k')}^{(1)} - \widetilde{t}_{HM(k')}^{(s)}\right)^2\right\} = {} & \mathbf{V}\{a_1^{(1)} - \widetilde{a}_{HM}^{(s)}\}\cdot(t')^2 + \mathbf{V}\{d^{(1)} - \widetilde{d}_{HM}^{(s)}\} + \left(\widetilde{\rho}_{\mathbf{M}(Q),s} + \sum_{\substack{q=1 \\ \mathbf{M}(q)\neq s}}^{Q} \widetilde{\rho}_{\mathbf{M}(q-1),\mathbf{M}(q)}\right)^2 \\ & + 2\cdot\mathbf{E}\{\varepsilon_{\gamma_{LS}}^{(\mathbf{M}(Q),s)}\cdot\varepsilon_{\hat{d}}^{(\mathbf{M}(Q),s)}\}\cdot t'/T_f + 2\cdot\sum_{\substack{q=1 \\ \mathbf{M}(q)\neq s}}^{Q} \mathbf{E}\{\varepsilon_{\gamma_{LS}}^{(\mathbf{M}(q-1),\mathbf{M}(q))}\cdot\varepsilon_{\hat{d}}^{(\mathbf{M}(q-1),\mathbf{M}(q))}\}\cdot t'/T_f \\ & + 2\sigma_{\phi}^2 \ .\end{aligned} \tag{5.4}$$

where $\mathbf{E}\{\varepsilon_{\gamma_{LS}}^{(m,s)}\cdot\varepsilon_{\hat{d}}^{(m,s)}\} = (1/K)\cdot\mathbf{V}\{\varepsilon_{\gamma_{LS}}^{(m,s)}\}\cdot\sum_{k=0}^{K-1}(\theta(k)-K_{ST})$. For HM time-transfer, $t'=k'T_f$ where $k'=(2N-1)\cdot K\cdot|\mathbf{M}|$. In (5.4), when timing is transferred from roving master node $\mathbf{M}(Q)$ to node s,

the starting index is $K_{ST}=(2N-1)\cdot K\cdot Q$. For the accumulated timing error variance from one roving master node ($\mathbf{M}(q-1)$) to another ($\mathbf{M}(q)$), $K_{ST}=(2N-1)\cdot K\cdot(q-1)$, $q\geq 1$.

For time-transfer scheme A described in section 3.1 where each node transmits in contiguous frames, the variance of the timing error is

$$\begin{aligned}\mathbf{E}\left\{\left(t_{(k')}^{(1)}-\tilde{t}_{HM(k')}^{(s)}\right)^2\right\}=&\mathbf{V}\{a_1^{(1)}-\tilde{a}_{HM}^{(s)}\}\cdot(t')^2+\mathbf{V}\{d^{(1)}-\tilde{d}_{HM}^{(s)}\}\\&+\left(\tilde{\rho}_{\mathbf{M}(Q),s}+\sum_{\substack{q=1\\ \mathbf{M}(q)\neq s}}^{Q}\tilde{\rho}_{\mathbf{M}(q-1),\mathbf{M}(q)}\right)^2\\&+2\cdot\frac{12}{K^3}\cdot\left(\frac{NK-2K-2\cdot(2N-1)\cdot K\cdot Q+1}{2}\right)\cdot\sigma_x^2(\mathbf{M}(Q),s)\cdot t'/T_f\\&+2\cdot\sum_{\substack{q=1\\ \mathbf{M}(q)\neq s}}^{Q}\frac{12}{K^3}\cdot\left(\frac{NK-2K-2\cdot(2N-1)\cdot K\cdot(q-1)+1}{2}\right)\cdot\sigma_x^2(\mathbf{M}(q-1),\mathbf{M}(q))\cdot t'/T_f\\&+2\sigma_\phi^2\ .\end{aligned}\tag{5.5}$$

It is interesting to note that the coefficient $(NK-2K-2(2N-1)KQ+1)/2$ of $\sigma_x^2(\mathbf{M}(Q),s)$, resulting from the cross-correlation between drift $(a_1^{(1)}-\tilde{a}_{HM}^{(s)})$ and initial offset $(d^{(1)}-\tilde{d}_{HM}^{(s)})$ errors, is negative if $Q>(NK-2K+1)/(2NK-K)$. For realistic cases considered in this work, the denominator $2NK-K$ is always greater than the numerator $NK-2K+1$. Therefore the cross-correlation term is always negative.

If $\tilde{t}_{SM(k')}^{(s)}$ is the settled timing at node s after master-slaves time-transfer, where $k'=(2N-1)K$, the timing error can be obtained from (5.4) by letting $Q=0$, then

$$\begin{aligned}\mathbf{E}\left\{\left(t_{(k')}^{(1)}-\tilde{t}_{SM(k')}^{(s)}\right)^2\right\}=&\mathbf{V}\{a_1^{(1)}-\tilde{a}_{SM}^{(s)}\}\cdot(t')^2+\mathbf{V}\{d^{(1)}-\tilde{d}_{SM}^{(s)}\}+\tilde{\rho}_{1,s}^2\\&+2\cdot\mathbf{E}\{\varepsilon_{\gamma_{LS}}^{(1,s)}\cdot\varepsilon_{\hat{d}}^{(1,s)}\}\cdot t'/T_f+2\sigma_\phi^2\ ,\end{aligned}\tag{5.6}$$

where $\mathbf{V}\{a_1^{(1)}-\tilde{a}_{SM}^{(s)}\}$ and $\mathbf{V}\{d^{(1)}-\tilde{d}_{SM}^{(s)}\}$ are given by equations (4.2a) and (4.2b) in Chapter 4.

(b) *Effect of Path-Loss Exponent*

From Chapter 4, $\sigma_x^2(m,s)=\left(1/\overline{\omega^2}\cdot\Theta_{m,s}+2\sigma_\phi^2\right)=\left(D_{m,s}^{\rho_L}/\overline{\omega^2}\cdot\Theta_t+2\sigma_\phi^2\right)$, and the path-loss exponent, denoted by ρ_L, is fixed at 2. It is known that because the power required to transmitting from m to s is governed by the path-loss exponent ($\rho_L \geq 2$), it is possible to relay information from m to s via intermediate node/s with less power than to transmit directly from m to s [29] [52].

In Figs. 37, 38 and 39, the effect of path-loss exponent on the timing error variances is investigated.

To investigate the effect of path-loss exponent, we assumed a network topology whereby nodes in the network are arranged in a straight line. This network topology is illustrated in Fig. 37. If SM time-transfer architecture is utilized, the lead master node transfers its timing directly to the last node, distance $D_{m,s}$ away, without relays by intermediate nodes. In HM, each node acts as a roving master (except the last node) and timing is transferred from the lead master to the last node via $N-1$ roving sessions if there are N nodes in the network.

Analytical results shown in Figs. 38 and 39 clearly indicate that the timing error variances of HM approach that of SM if the path-loss exponent, ρ_L is greater than 4.

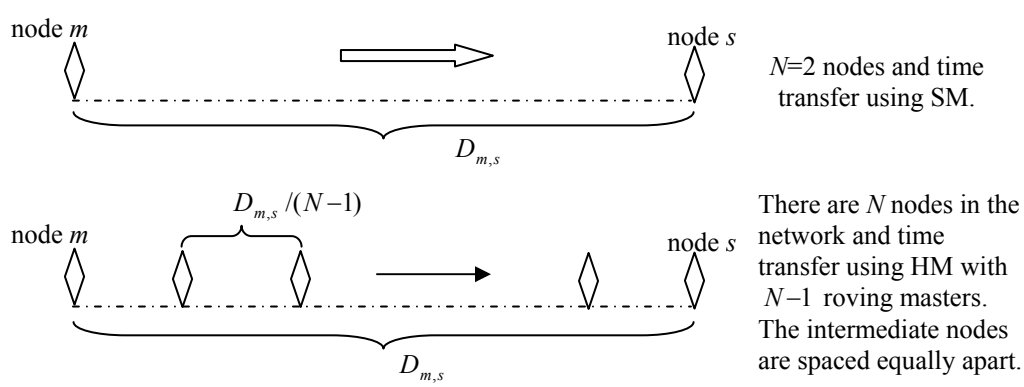

Figure 37: A simplified straight-line network topology to illustrate the effects of path-loss exponent on the timing error variances of SM and HM time-transfer architectures.

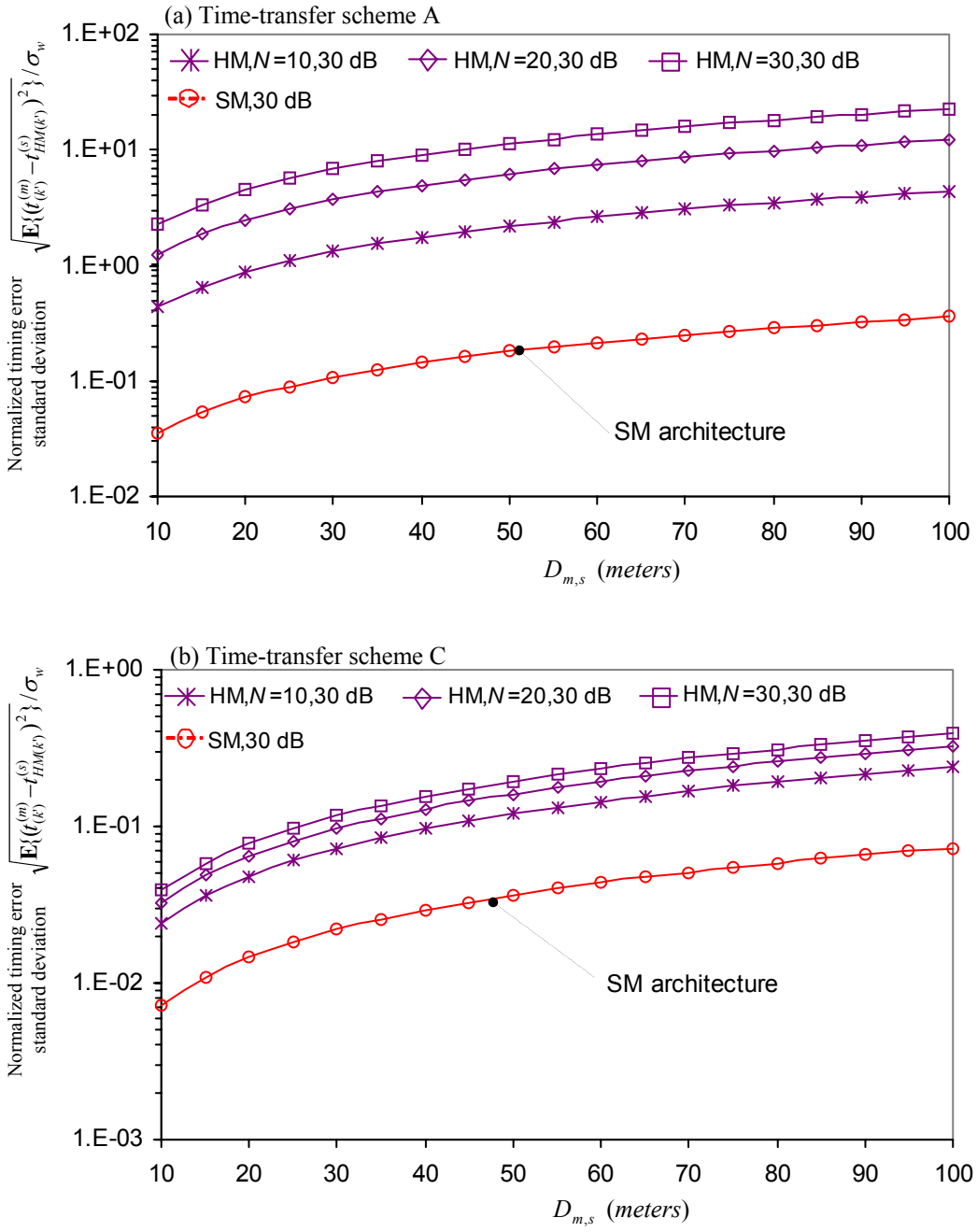

Figure 38: Normalized timing error standard deviation with path-loss exponent $\rho_L = 2$ at $\Theta_t = 30$ dB, $\sigma_\phi = 0$ and $K = 1000$. The network topology is shown in Figure 37. Results obtained using (a) time- transfer scheme A and (b) time-transfer scheme C.

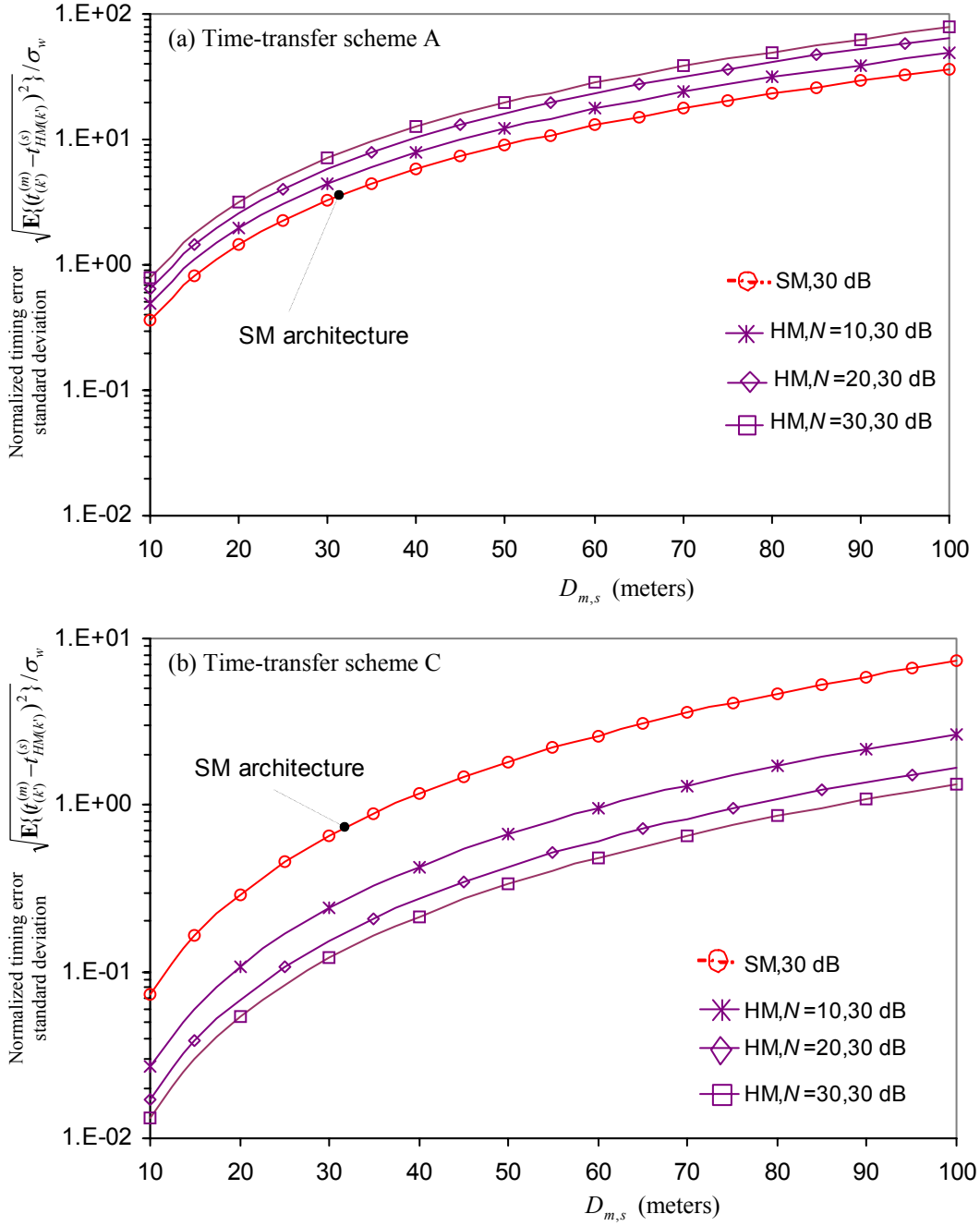

Figure 39: Normalized timing error standard deviation with path-loss exponent $\rho_L = 4$ at $\Theta_t = 30$ dB, $\sigma_\phi = 0$ and $K = 1000$. The network topology is shown in Figure 37. Results obtained using (a) time-transfer scheme A and (b) time-transfer scheme C.

5.2 Mutually Synchronous Time-Transfer Error

(a) *Mutually Synchronous Timing Jitter*

Let the settled timing estimate at node s at the end of mutually synchronous time-transfer be

$$\tilde{t}_{MU(k')}^{(s)} = \tilde{a}_{MU}^{(s)} \cdot t' + \tilde{d}_{MU}^{(s)} + \phi_{(k')}^{(s)} , \tag{5.7}$$

where $t' = k' T_f$ and $k' = (2N-1) \cdot K \cdot N$. The oscillator timing jitter sequence $\phi_{(k')}^{(s)}$ is assumed to be independently identically distributed with zero mean and variance σ_ϕ^2. From Appendix B, the expected value of the squares of (5.7) is

$$\mathbf{E}\left\{\left(\tilde{t}_{MU(k')}^{(s)}\right)^2\right\} = \mathbf{E}\left\{\left(\tilde{a}_{MU}^{(s)}\right)^2\right\} \cdot (t')^2 + \mathbf{E}\left\{\left(\tilde{d}_{MU}^{(s)}\right)^2\right\} + 2 \cdot \mathbf{E}\left\{\tilde{a}_{MU}^{(s)} \cdot \tilde{d}_{MU}^{(s)}\right\} \cdot t' + \mathbf{E}\{(\phi_{(k')}^{(s)})^2\} , \tag{5.8}$$

where

$$\mathbf{E}\left\{\left(\tilde{a}_{MU}^{(s)}\right)^2\right\} = \left(a_1^{(1)}\right)^2 + \sum_{n=1}^{N-1} \mathbf{E}\left\{\left(\varepsilon_{\gamma_{LS}}^{(n,n+1)}\right)^2\right\} / T_f^2 + \mathbf{E}\left\{\left(\varepsilon_{\gamma_{LS}}^{(N,s)}\right)^2\right\} / T_f^2 , \tag{5.9a}$$

$$\mathbf{E}\left\{\left(\tilde{d}_{MU}^{(s)}\right)^2\right\} = \left(\sum_{\substack{m=1,\\ m \neq s}}^{N} \alpha_{m,s} \cdot (d^{(m)} + \tilde{\rho}_{m,s}) \right)^2 + \sum_{\substack{m=1,\\ m \neq s}}^{N} \alpha_{m,s}^2 \cdot \mathbf{E}\left\{\left(\varepsilon_{\hat{d}}^{(m,s)}\right)^2\right\} , \tag{5.9b}$$

and

$$\mathbf{E}\left\{\tilde{a}_{MU}^{(s)} \cdot \tilde{d}_{MU}^{(s)}\right\} = a_1^{(1)} \sum_{\substack{m=1,\\ m \neq s}}^{N} \alpha_{m,s} \cdot d^{(m)} + a_1^{(1)} \sum_{\substack{m=1,\\ m \neq s}}^{N} \alpha_{m,s} \cdot \rho_{m,s} + \sum_{n=1}^{N-1} \sum_{\substack{m=1,\\ m \neq s}}^{N} \frac{\alpha_{m,s}}{T_f} \cdot \mathbf{E}\{\varepsilon_{\gamma_{LS}}^{(n,n+1)} \cdot \varepsilon_{\hat{d}}^{(m,s)}\}$$
$$+ \sum_{\substack{m=1,\\ m \neq s}}^{N} \frac{\alpha_{m,s}}{T_f} \cdot \mathbf{E}\{\varepsilon_{\gamma_{LS}}^{(N,s)} \cdot \varepsilon_{\hat{d}}^{(m,s)}\} . \tag{5.9c}$$

The sample variance of $\tilde{t}_{MU(k')}^{(s)}$ is defined to be

$$\frac{1}{N-1} \sum_{s=1}^{N} \left(\tilde{t}_{MU(k')}^{(s)} - \left(\frac{1}{N} \sum_{s=1}^{N} \tilde{t}_{MU(k')}^{(s)} \right) \right)^2 . \tag{5.10}$$

For a MU time-transfer architecture, unlike HM, there is no "preferred" node in the network. To characterize the performance of the MU time-transfer architecture, we consider the timing variances across all nodes in the network. One appropriate measure is the mean of the sample variance of $\tilde{t}_{MU(k')}^{(s)}$, $\forall s$, at time $t'=k'T_f$ where $k'=(2N-1)\cdot K\cdot N$. The mean of the timing variances across all nodes in the network is defined as

$$\overline{\mathbf{V}\{\tilde{t}_{MU(k')}\}}=\mathbf{E}\left\{\frac{1}{N-1}\sum_{s=1}^{N}(\tilde{t}_{MU(k')}^{(s)})^2-\left(\frac{1}{N}\sum_{s=1}^{N}\tilde{t}_{MU(k')}^{(s)}\right)^2\right\}. \tag{5.11}$$

In Appendix B, it is shown that

$$\overline{\mathbf{V}\{\tilde{t}_{MU(k')}\}}=\overline{\mathbf{V}\{\tilde{a}_{MU}\}}\cdot(t')^2+\overline{\mathbf{V}\{\tilde{d}_{MU}\}}+\frac{2\cdot t'}{N}\sum_{s=1}^{N-1}\frac{\alpha_{N,s}}{T_f}\cdot\mathbf{E}\{\varepsilon_{\gamma_{LS}}^{(N,s)}\cdot\varepsilon_{\hat{d}}^{(N,s)}\}+\sigma_{\phi}^2 \quad , \tag{5.12}$$

where $\mathbf{E}\{\varepsilon_{\gamma_{LS}}^{(m,s)}\cdot\varepsilon_{\hat{d}}^{(m,s)}\}=(1/K)\cdot\mathbf{V}\{\varepsilon_{\gamma_{LS}}^{(m,s)}\}\cdot\sum_{k=0}^{K-1}(\theta(k)-K_{ST})$ and $K_{ST}=(2N-1)\cdot K\cdot(N-1)$. The mean of the sample variances of the settled drift and initial offset estimates for all nodes in the network are derived earlier in Chapter 4, and they are

$$\overline{\mathbf{V}\{\tilde{a}_{MU}\}}=\frac{1}{N}\cdot\sum_{s=1}^{N}\mathbf{V}\{\varepsilon_{\gamma_{LS}}^{(N,s)}/T_f\}\ ,$$

$$\overline{\mathbf{V}\{\tilde{d}_{MU}\}}=\frac{1}{N}\sum_{s=1}^{N}\mathbf{V}\{\tilde{d}_{MU}^{(s)}\}+\frac{1}{N-1}\sum_{s=1}^{N}\left(\sum_{m=1,m\neq s}^{N}\alpha_{m,s}\cdot\left(d^{(m)}+\tilde{\rho}_{m,s}\right)\right)^2-\frac{1}{N\cdot(N-1)}\left(\sum_{s=1}^{N}\sum_{m=1,m\neq s}^{N}\alpha_{m,s}\cdot\left(d^{(m)}+\tilde{\rho}_{m,s}\right)\right)^2.$$

(b) *Effect of Different Weight Functions*

In Fig. 40, the sample timing variances $\overline{\mathbf{V}\{\tilde{t}_{MU(k')}\}}$ obtained via (5.12) for a particular network topology (shown in Fig. 42 of Chapter 6) with $N=20$ at various SNR is presented. The plots in the figure are the timing variances when different weight functions $\alpha_{m,s}$ are substituted into (5.12). For this particular example, the differences in timing variances obtained using the three different weight functions are not significant.

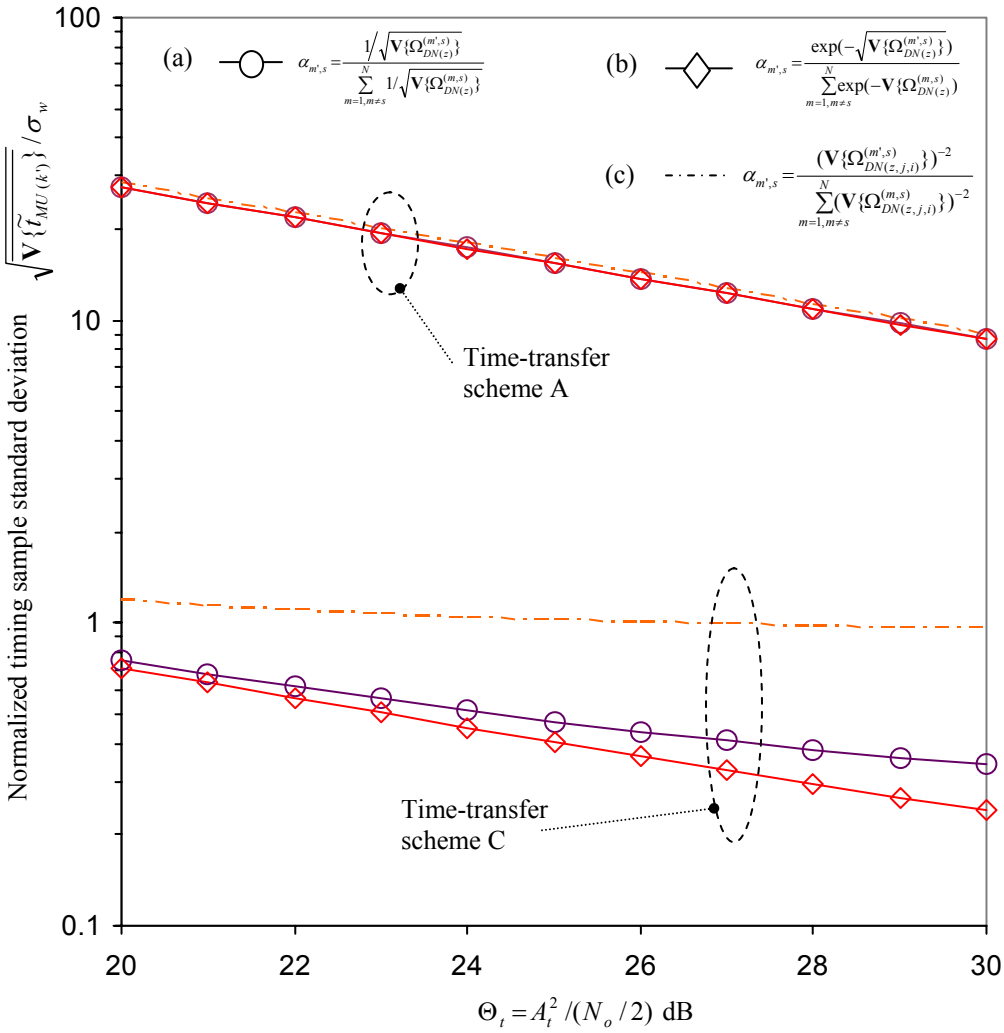

Figure 40: The square-root of the normalized timing sample variances when different weight functions $\alpha_{m,s}$ are used in evaluating (5.12). The weight functions are: (a) the square-root, (b) the exponential, and (c) the square. The results are obtained with $\rho_L = 2$, $\sigma_\phi = 0$, $\tilde{\rho}_{m,s} = 0$, $K = 1000$ and signals propagate along LoS paths between transmitters and receivers. The network topology is shown in Fig. 42.

5.3 Summary of Time-Transfer Equations

For ease of reference, the variances in estimating the differences in frame repetition rate, initial offset and timing errors using the SM, HM and MU time-transfer architectures presented in earlier chapters are tabulated in Tables 2, 3 and 4. The zero mean error of the initial-offset equation is given by

$$\mathbf{V}\{\varepsilon_{\vartheta}^{(m,s)}\}=\frac{5\cdot\sigma_x^2(m,s)+\sigma_x^2(s,m)}{4}\ .$$

The cross-correlation between the LS estimation error and initial offset estimation error is

$$\mathbf{E}\{\varepsilon_{\gamma_{LS}}^{(m,s)}\cdot\varepsilon_{\hat{d}}^{(m,s)}\}=\frac{1}{K}\cdot\mathbf{V}\{\varepsilon_{\gamma_{LS}}^{(m,s)}\}\cdot\sum_{k=0}^{K-1}(\theta(k)-K_{ST})\ .$$

The variance of the initial offset estimation error between nodes m and s is

$$\mathbf{V}\{d_{\delta}^{(m,s)}\}=\frac{\left(\sum_{k=0}^{K-1}(\theta(k)-K_{ST})\right)^2}{K^2}\cdot\mathbf{V}\{\varepsilon_{\gamma_{LS}}^{(m,s)}\}+\mathbf{V}\{\varepsilon_{\vartheta}^{(m,s)}\}\ .$$

The variance of uplink ToAs is

$$\mathbf{V}\{\Omega_{UP(u)}^{(s,m)}\}=\mathbf{V}\{\varepsilon_{\gamma_{LS}}^{(m,s)}\}\cdot u^2+\mathbf{V}\{\varepsilon_{UP(u)}^{(s,m)}\}\ .$$

The variance of downlink ToAs is

$$\mathbf{V}\{\Omega_{DN(z)}^{(s,m)}\}=\mathbf{V}\{\varepsilon_{\gamma_{LS}}^{(m,s)}\}\cdot(z-u)^2+\mathbf{V}\{\varepsilon_{DN(z)}^{(m,s)}\}\ .$$

The variance of the measurement error when measuring uplink ToAs is

$$\mathbf{V}\{\varepsilon_{UP(u)}^{(s,m)}\}=2\cdot\sigma_{\phi}^2+\sigma_n^2(s,m)=\sigma_x^2(s,m)\ .$$

The variance of the measurement error when measuring downlink ToAs is

$$\mathbf{V}\{\varepsilon_{DN(u)}^{(m,s)}\}=\sigma_x^2(s,m)+\sigma_x^2(m,s)\ .$$

The variance of the output of the open-loop timing detector is $\sigma_x^2(m,s)=D_{m,s}^2/(\overline{\omega^2}\cdot\Theta_t)+2\sigma_{\phi}^2$.

Table 2: Equations that defined the various time-transfer schemes

Time-transfer scheme A	$\theta(k)=\frac{(N-1)K}{2} - k$, $k\in\{0,1,...,K-1\}$ $v=k+K_{ST}$, $u=K+(j-2)\cdot K+K_{ST}+k$ and $z-u=(N-1)\cdot K$. $\mathbf{V}\{\varepsilon_{\gamma_{LS}}^{(m,s)}\}=\frac{12\cdot\sigma_x^2(m,s)}{K^3}$ $\mathbf{V}\{\hat{d}_{\delta}^{(m,s)}\}=\frac{3\cdot\sigma_x^2(m,s)}{K}\cdot\left((N-1)^2+\frac{(K+2K_{ST}-1)\cdot(2K_{ST}-1-2NK+3K)}{K^2}\right)+\mathbf{V}\{\varepsilon_{\vartheta}^{(m,s)}\}$ $\mathbf{E}\{\varepsilon_{\gamma_{LS}}^{(m,s)}\cdot\varepsilon_{\hat{d}}^{(m,s)}\}=\frac{12}{K^3}\cdot\sigma_x^2(m,s)\cdot\left(\frac{NK-2K+1}{2} - K_{ST}\right)$
Time-transfer scheme B	$\theta(k)=\frac{N-1}{2} - (2N-1)\cdot k$, $k\in\{0,1,...,K-1\}$ $v=(2N-1)\cdot k+K_{ST}$, $u=1+(j-2)+(2N-1)\cdot k+K_{ST}$ and $z-u=N-1$. $\mathbf{V}\{\varepsilon_{\gamma_{LS}}^{(m,s)}\}=\frac{12\cdot\sigma_x^2(m,s)}{K^3}\cdot\frac{1}{(2N-1)^2}$ $\mathbf{V}\{\hat{d}_{\delta}^{(m,s)}\}=\frac{3\cdot\sigma_x^2(m,s)}{K^3\cdot(2N-1)^2}\cdot\left(N-2K_{ST}-1-(2N-1)\cdot(K-1)\right)^2+\mathbf{V}\{\varepsilon_{\vartheta}^{(m,s)}\}$ $\mathbf{E}\{\varepsilon_{\gamma_{LS}}^{(m,s)}\cdot\varepsilon_{\hat{d}}^{(m,s)}\}=\frac{12\cdot\sigma_x^2(m,s)}{K^3\cdot(2N-1)^2}\cdot\left(\frac{N-1-(2N-1)\cdot(K-1)}{2} - K_{ST}\right)$
Time-transfer scheme C	$\theta(k)=\frac{1}{2} - (2N-1)\cdot k$, $k\in\{0,1,...,K-1\}$ $v=(2N-1)\cdot k+K_{ST}$, $u=1+(j-2)\cdot 2+(2N-1)\cdot k+K_{ST}$ and $z-u=1$. $\mathbf{V}\{\varepsilon_{\gamma_{LS}}^{(m,s)}\}=\frac{12\cdot\sigma_x^2(m,s)}{K^3}\cdot\frac{1}{(2N-1)^2}$ $\mathbf{V}\{\hat{d}_{\delta}^{(m,s)}\}=\frac{3\cdot\sigma_x^2(m,s)}{K^3\cdot(2N-1)^2}\cdot\left(2N+K-2NK-2K_{ST}\right)^2+\mathbf{V}\{\varepsilon_{\vartheta}^{(m,s)}\}$ $\mathbf{E}\{\varepsilon_{\gamma_{LS}}^{(m,s)}\cdot\varepsilon_{\hat{d}}^{(m,s)}\}=\frac{12\cdot\sigma_x^2(m,s)}{K^3\cdot(2N-1)^2}\cdot\left(\frac{1-(2N-1)\cdot(K-1)}{2} - K_{ST}\right)$

Table 3: Variances of the estimation error in estimating the differences in frame repetition rate and initial offset for SM, HM and MU time-transfer architectures

SM	$\mathbf{V}\{a_1^{(1)}-\tilde{a}_{SM}^{(s)}\}\geq\mathbf{V}\{\varepsilon_{\gamma_{LS}}^{(1,s)}\}/T_f^2$, $s\in\{2,...,N\}$.
	$\mathbf{E}\{(d^{(1)}-\tilde{d}_{SM}^{(s)})^2\}=\mathbf{V}\{\hat{d}_{\delta}^{(1,s)}\}+\mathbf{V}\{\varepsilon_{\vartheta}^{(1,s)}\}+\tilde{\rho}_{1,s}^2$, $K_{ST}=0$.
HM	$\mathbf{V}\{a_1^{(1)}-\tilde{a}_{HM}^{(s)}\}=\begin{cases}\mathbf{V}\{\varepsilon_{\gamma_{LS}}^{(1,s)}\}/T_f^2+\sum\limits_{\substack{q=1\\ \mathbf{M}(q)\neq s}}^{Q}\mathbf{V}\{\varepsilon_{\gamma_{LS}}^{(\mathbf{M}(q-1),\mathbf{M}(q))}\}\cdot T_f^2, & Q>0.\\ \mathbf{V}\{\varepsilon_{\gamma_{LS}}^{(1,s)}\}/T_f^2, & Q=0.\end{cases}$
	$\mathbf{E}\{(d^{(1)}-\tilde{d}_{SM}^{(s)})^2\}=\mathbf{V}\{(d^{(1)}-\tilde{d}_{SM}^{(s)})\}+\left(\tilde{\rho}_{\mathbf{M}(Q),s}+\sum\limits_{\substack{q=1,\\ \mathbf{M}(q)\neq s}}^{Q}\tilde{\rho}_{\mathbf{M}(q-1),\mathbf{M}(q)}\right)^2$, where $\mathbf{V}\{d^{(1)}-\tilde{d}_{HM}^{(s)}\}$ $\begin{cases}=\mathbf{V}\{\hat{d}_{\delta}^{(\mathbf{M}(Q),s)}\}+\mathbf{V}\{\varepsilon_{\vartheta}^{(\mathbf{M}(Q),s)}\}+\sum\limits_{\substack{q=1\\ \mathbf{M}(q)\neq s}}^{Q}\mathbf{V}\{\hat{d}_{\delta}^{(\mathbf{M}(q-1),\mathbf{M}(q))}\}+\mathbf{V}\{\varepsilon_{\vartheta}^{(\mathbf{M}(q-1),\mathbf{M}(q))}\}, & Q>0.\\ =\mathbf{V}\{\hat{d}_{\delta}^{(1,s)}\}+\mathbf{V}\{\varepsilon_{\vartheta}^{(1,s)}\}, & Q=0.\end{cases}$ If $Q=0$, $K_{ST}=0$. If $Q>0$, in $\mathbf{V}\{\hat{d}_{\delta}^{(\mathbf{M}(Q),s)}\}$, $K_{ST}=(2N-1)\cdot K\cdot Q$. In $\mathbf{V}\{\hat{d}_{\delta}^{(\mathbf{M}(q-1),\mathbf{M}(q))}\}$, $K_{ST}=(2N-1)\cdot K\cdot(q-1)$, $q\geq 1$.
MU	$\mathbf{V}\{\tilde{a}_{MU}^{(s)}\}=\sum\limits_{n=1}^{N\text{-}1}\mathbf{V}\{\varepsilon_{\gamma_{LS}}^{(n,n+1)}\}/T_f^2+\mathbf{V}\{\varepsilon_{\gamma_{LS}}^{(N,s)}\}/T_f^2$.
	$\mathbf{E}\{(\tilde{d}_{MU}^{(s)})^2\}=\sum\limits_{m=1,m\neq s}^{N}\alpha_{m,s}^2\cdot\mathbf{V}\{\hat{d}_{\delta}^{(m,s)}\}+\left(\sum\limits_{m=1,m\neq s}^{N}\alpha_{m,s}\cdot(d^{(m)}+\tilde{\rho}_{m,s})\right)^2$. Assuming $\mathbf{M}\in\{1,2,...,N\}$, K_{ST} in $\mathbf{V}\{\hat{d}_{\delta}^{(m,s)}\}$ is given by $K_{ST}=(2N-1)\cdot K\cdot(m-1)$.

Table 4: Variances of timing error for SM, HM and MU time-transfer architectures

SM	$\mathbf{E}\left\{\left(t_{(k')}^{(1)}-\tilde{t}_{SM(k')}^{(s)}\right)^2\right\}=\mathbf{V}\{a_1^{(1)}-\tilde{a}_{SM}^{(s)}\}\cdot(t')^2+\mathbf{V}\{d^{(1)}-\tilde{d}_{SM}^{(s)}\}+\tilde{\rho}_{1,s}^2$ $+2\cdot\mathbf{E}\{\varepsilon_{\gamma_{LS}}^{(1,s)}\cdot\varepsilon_{\hat{d}}^{(1,s)}\}\cdot t'/T_f+2\sigma_\phi^2$, where $t'=(2N-1)\cdot K\cdot T_f$, $K_{ST}=0$.
HM	$\mathbf{E}\left\{\left(t_{(k')}^{(1)}-\tilde{t}_{HM(k')}^{(s)}\right)^2\right\}=\mathbf{V}\{a_1^{(1)}-\tilde{a}_{HM}^{(s)}\}\cdot(t')^2+\mathbf{V}\{d^{(1)}-\tilde{d}_{HM}^{(s)}\}+\left(\tilde{\rho}_{\mathbf{M}(Q),s}+\sum_{\substack{q=1\\ \mathbf{M}(q)\neq s}}^{Q}\tilde{\rho}_{\mathbf{M}(q-1),\mathbf{M}(q)}\right)^2$ $+2\cdot\mathbf{E}\{\varepsilon_{\gamma_{LS}}^{(\mathbf{M}(Q),s)}\cdot\varepsilon_{\hat{d}}^{(\mathbf{M}(Q),s)}\}\cdot t'/T_f$ $+2\cdot\sum_{\substack{q=1\\ \mathbf{M}(q)\neq s}}^{Q}\mathbf{E}\{\varepsilon_{\gamma_{LS}}^{(\mathbf{M}(q-1),\mathbf{M}(q))}\cdot\varepsilon_{\hat{d}}^{(\mathbf{M}(q-1),\mathbf{M}(q))}\}\cdot t'/T_f$ $+2\sigma_\phi^2$. Here $t'=(2N-1)\cdot K\cdot T_f\cdot\lvert\mathbf{M}\rvert$. Values of K_{ST} are given in Table 3.
MU	$\overline{\mathbf{V}\{\tilde{t}_{MU(k')}\}}=\overline{\mathbf{V}\{\tilde{a}_{MU}\}}\cdot(t')^2+\overline{\mathbf{V}\{\tilde{d}_{MU}\}}+\frac{2\cdot t'}{N}\sum_{s=1}^{N-1}\frac{\alpha_{N,s}}{T_f}\cdot\mathbf{E}\{\varepsilon_{\gamma_{LS}}^{(N,s)}\cdot\varepsilon_{\hat{d}}^{(N,s)}\}+\sigma_\phi^2$, where $t'=(2N-1)\cdot K\cdot T_f\cdot N$, $\overline{\mathbf{V}\{\tilde{a}_{MU}\}}=\frac{1}{N\cdot T_f^2}\cdot\sum_{s=1}^{N-1}\mathbf{E}\{(\varepsilon_{\gamma_{LS}}^{(N,s)})^2\}$, and $\overline{\mathbf{V}\{\tilde{d}_{MU}\}}=\frac{1}{N}\sum_{s=1}^{N}\mathbf{V}\{\tilde{d}_{MU}^{(s)}\}+\frac{1}{N-1}\sum_{s=1}^{N}\left(\sum_{m=1.m\neq s}^{N}\alpha_{m,s}\cdot\left(d^{(m)}+\tilde{\rho}_{m,s}\right)\right)^2$ $-\frac{1}{N\cdot(N-1)}\left(\sum_{s=1}^{N}\sum_{m=1.m\neq s}^{N}\alpha_{m,s}\cdot\left(d^{(m)}+\tilde{\rho}_{m,s}\right)\right)^2$. Values of K_{ST} are given in Table 3.

Note that $\theta(k)$ is the characteristic function of the time-transfer scheme and K_{ST} is the starting index of the ToA measurements to be used to estimate the initial offset differences. In Fig. 41, the normalized timing error variance computed from Table 4 for a SM time-transfer architecture with a circular network topology is shown.

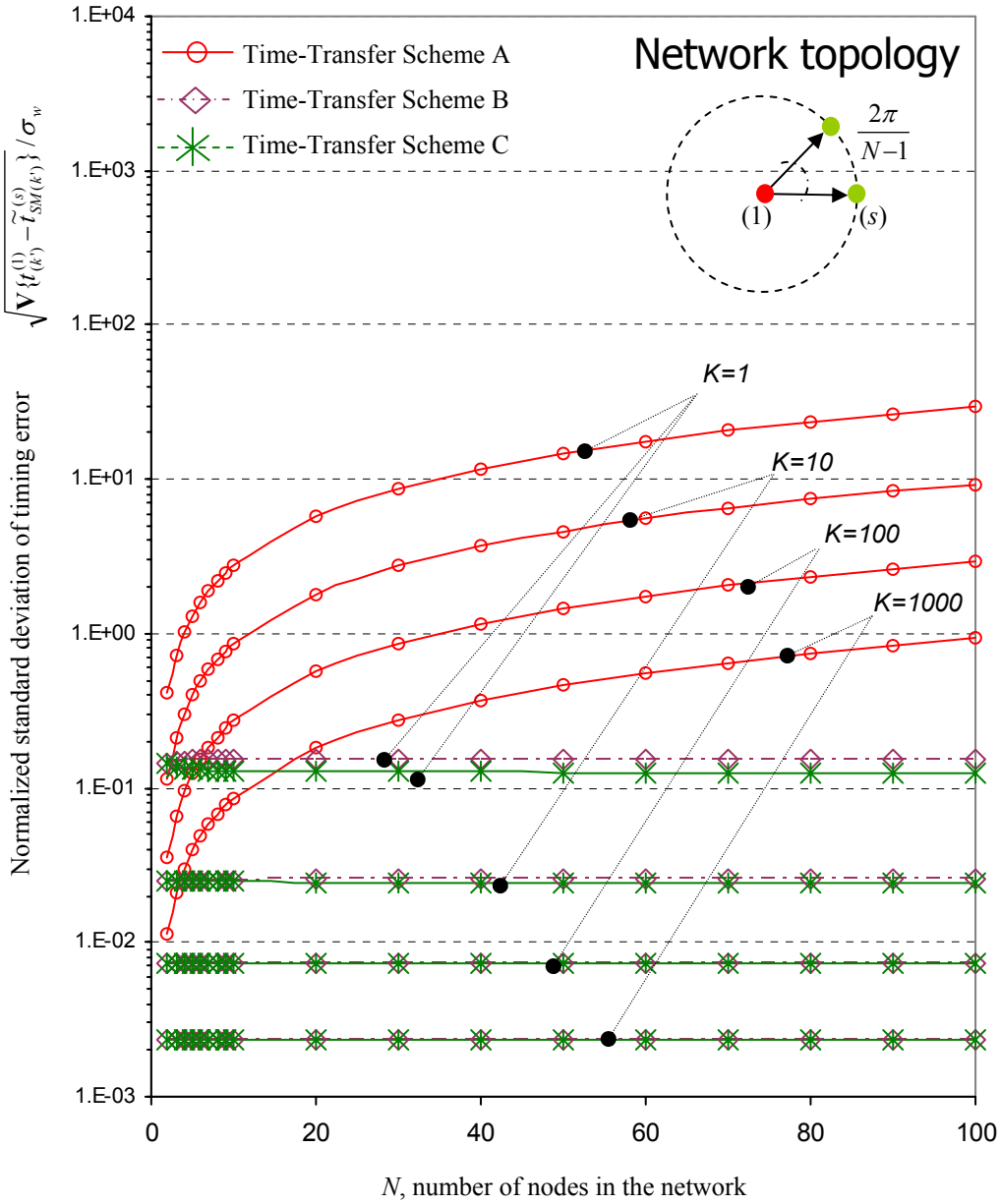

Figure 41: Timing error variance for a circular network topology synchronized with SM. The performance of different time-transfer schemes is first described in sections 3.1 and 3.4. In this plot, $\Theta_{m,s} = 20$ dB, $K_{ST} = 0$, $\sigma_\phi = 0$ and $\tilde{\rho}_{m,s} = 0$.

There exist other possibilities to arrange the frame-synchronization, uplink and downlink pulses. For example, the downlink pulse can be "returned" to the slave in the same frame as the uplink pulse arrives at the master node, that is, the master node acts like a relay to complete the two-way ranging (this is similar to that performed in the RTS). In this case, $z=u$ and the total number of uplink plus downlink frames is reduced by half. Although the time needed for synchronization has now reduced approximately by half, it does not bring about a lower timing jitter for schemes B and C. This is because the variance of estimating the frame-repetition rate difference is now increased by a factor of 2 as the spacing between the frame-synchronization pulses is reduced by half. Further, it can be shown that the characteristic function of this scheme will be $\theta(k)=-(2N-1)\cdot k$ and if $K>>1$, $\mathbf{V}\{\hat{d}_{\delta}^{(m,s)}\}$ for this scheme will be similar to that of time-transfer scheme C. However, by making $z=u$, the timing jitter after time transfer using time-transfer scheme A will be smaller due to a shortening of the time needed to perform synchronization while the spacing between the frame-synchronization pulses remains at T_f.

CHAPTER VI

SIMULATIONS AND OBSERVATIONS

The earlier chapters have presented the theoretical formulations of the proposed time transfer schemes (time-transfer schemes A, B and C) and described the various time-transfer architectures to implement a SIN. This Chapter presents the computer simulations results. It is followed by a discussion of the advantages and disadvantages of the single-master-to-multiple-slaves (SM), hierarchical master-slaves (HM) and mutually synchronous time-transfer (MU) architectures.

When SM and HM are used to perform time synchronization, the timing jitter is defined as the variance of the timing error between the lead master node (node 1) and other nodes in the network. For MU time-transfer architecture, the sample variance of the timings of all nodes in the network is defined to be the timing jitter.

6.1 Simulation of Proposed Time-Transfer Architectures

To verify the theoretical formulations presented in earlier chapters and to gain further insight into the working of the proposed SIN, the various time transfer architectures, namely, the SM, HM and the MU time-transfer architectures are simulated.

The simulations assume that the received SNR is sufficient for the AGC described in Chapter 2 to be effective in controlling the amplitude of the received UWB monocycles and for the timing detector to operate at the linear region of its characteristic function. Therefore equations (3.1), (3.3a) and (3.4b), which describe the measured ToAs, are simulated. The measured ToAs are impaired by additive channel noise, the oscillator's phase noise and network NLoS signal propagations. The additive noise samples are drawn from a Gaussian distribution with zero mean and variance $\sigma_n^2(m,s)$.

The oscillator phase noise samples have a uniform probability density function with zero mean and variance σ_{ϕ}^{2}. Each simulation result is obtained with at least 500 Monte Carlo steps.

The simulations implemented the techniques described in Chapter 3 to estimate the differences in fame repetition rate and initial offset between network nodes. The various time-transfer architectures described in Chapter 4 are also implemented accordingly.

The simulations first performed on a given network topology. With a given network topology, the timing variances at each network node are observed. This is follows by allowing the network nodes to be randomly distributed over a given area and the ensemble averages of the timing variances are observed.

6.1.1 Simulations with a given Network Topology

A SIN is simulated for a given network topology shown in Fig. 42 with $N=20$. In the simulations, time synchronization is performed using the SM, HM and MU time-transfer architectures. The simulation parameters are (unless otherwise specified): $K=K_s=K_r=1000$ frames, $\sigma_{\phi}=0$ sec, effective squared bandwidth $\overline{\omega^2}=1.9\times10^{21}$ sec^{-2}, initial offset of network nodes before time transfer are $d^{(s)}\in$ {-0.15, 0.10, 0.17, 0.07,-0.07,-0.02, 0.05, 0.25, 0.23, 0.09, 0.11, 0.10, 0.28, 0.01, 0.10, 0.12, 0.003, 0.071, 0.271, 0.14} $\times10^{-9}$ sec. And drift of network nodes before time transfer are $a^{(s)}=1+\eta$ where $\eta\in$ { 0, 7,-4, 9, 5, 4,-8,-5, 2,-7, 8, 1, 7,-4, 8, 5, 7, 4, 3,-2}$\times10^{-6}$.

It is discussed in section 2.3.4 that when the scattering environment changes, the uplink and downlink excess-delay may not be equal, as a result, $\tilde{\rho}_{m,s}\neq0$. This is more likely for time-transfer scheme A because nodes transmit the uplink and downlink ranging pulses in time slots that are temporally far apart if number of network nodes is large. In time-transfer scheme C, the uplink and downlink pulses are transmitted in adjacent frames and hence it is least likely that the scattering

environment changes in between transmissions. Further, $\widetilde{\rho}_{m,s}$ is also used to model any receiver processing errors that may arise when the timing detector lock onto a NLoS path.

In this work, it is assumed that $\widetilde{\rho}_{m,s}$ is not random. It will be left to future research to model $\widetilde{\rho}_{m,s}$ as a random variable.

To illustrate the effects of $\widetilde{\rho}_{m,s}$ (to be summarized as receiver processing error), links between selected nodes are replaced with a longer propagation path. The selected links are: $D_{1,15} = (\tau_{1,15} + \rho_{1,15}) \cdot c$, $D_{1,17} = (\tau_{1,17} + \rho_{1,17}) \cdot c$ and $D_{1,20} = (\tau_{1,20} + \rho_{1,20}) \cdot c$ where c is the speed of light. The excess-delays due to NLoS propagation are: $\rho_{1,15} = 0.5 \cdot \tau_{1,15}$, $\rho_{1,17} = 0.5 \cdot \tau_{1,17}$ and $\rho_{1,20} = 0.5 \cdot \tau_{1,20}$. As a result, the receiver measurement errors are: $\widetilde{\rho}_{1,15} = 0.25\tau_{1,15}$, $\widetilde{\rho}_{1,17} = 0.25\tau_{1,17}$ and $\widetilde{\rho}_{1,20} = 0.25\tau_{1,20}$.

The HM network described in section 4.3 is simulated with the network topology shown in Fig. 42. In Figs. 43 to 45, the normalized standard deviation of the estimated differences in initial offset between the lead master and selected nodes 2, 17 and 9 at $\Theta_t = 20$ dB to 30 dB are shown. Node 9 is the furthest node in the network from the lead master. Node 2 is about half-way between lead master and node 9. The transmitted signal propagates from node 1 to node 17 via a NLoS path with $\widetilde{\rho}_{1,17} = 0.25\tau_{1,17}$. In Figs. 46 to 48, the timing error variances $\mathbf{E}\{(t_{(k')}^{(1)} - \widetilde{t}_{HM(k')}^{(s)})^2\}$ for nodes 2, 17 and 9 are plotted. For HM with five roving masters, $t' = (2N-1)KT_f \cdot 5$, while nineteen roving masters require a synchronization time of $t' = (2N-1)KT_f \cdot 19$ to synchronize $N = 20$ nodes in the network. The results shown in Figs. 43 and 48 are obtained using time-transfer scheme A.

Not illustrated in Figs. 43 to 48 is the fact that during simulations when oscillator jitter σ_ϕ^2 is significant compared to jitter due to channel noise, there is increased randomness in the selection of nodes to be the next roving masters. For example, if $\sigma_\phi = 0$, using only 5 roving masters, the order of the roving master is {1,8,12,4,2} in almost all simulation runs, which corresponds to the shortest propagation distances between nodes. In this case, simulation results agree well with the results

obtained from theoretical formulations (the equations of the timing variances are listed in Tables 3 and 4). At $\sigma_\phi = 10^{-11}$ secs, order of roving master can be as different as {1,8,12,7,4} or {1,4,7,2,12} and some other possibilities at various SNR. This causes an increase in timing jitter in some nodes because time-transfer is no longer via the shortest possible hops for these nodes. Similar observations are made when all nodes in the network (except the last node) take turns being the roving master.

The MU network described in section 4.4 is simulated for $N = 20$ with nodes distributed as shown in Fig. 42. The quantity $\mathbf{E}\left\{\left(\tilde{d}_{MU}^{(s)}\right)^2\right\}$ is plotted in Fig. 49 at $\Theta_t = 30$ dB for $\sigma_\phi = 0$. The mean of the timing sample variance of all nodes in the network after MU architecture (utilizing time-transfer scheme A) is indicated as a horizontal line in Fig. 50. In Fig. 51, the timing sample variance $\overline{\mathbf{V}\{\tilde{t}_{MU}\}}$ is plotted when time-transfer between pair of nodes is performed using time-transfer scheme C. The simulation results agree well with the theoretical formulations.

Included in Figs. 49 to 51 are also estimation variances when HM and SM time-transfer architectures are utilized to perform time synchronization at $\Theta_t = 30$ dB. The timing error variances after time transfer with HM and SM are plotted in the same figure together with the network timings sample variance after using MU time-transfer architecture.

It is interesting to note from Fig. 49 and 50 that, for node 8, which is the closest to the lead master, SM and HM produce the same estimation variance for estimating the initial offset difference $\sqrt{\mathbf{E}\{(d^{(1)} - \tilde{d}_{HM}^{(8)})^2\}} \Big/ \sigma_w$. However, the corresponding timing error variance at node 8 given by $\sqrt{\mathbf{E}\{(t_{(k')}^{(1)} - \tilde{t}_{HM(k')}^{(8)})^2\}} \Big/ \sigma_w$ and shown in Fig. 50, no longer coincides. In fact, HM with 19 roving masters has higher timing error variance than HM with 5 roving masters and SM has the lowest variance. This is because the time required to perform time synchronization for HM with 19 roving masters is the longest follows by utilizing 5 roving masters. The longer synchronization time multiplied by drift estimation error leads to higher timing error variances.

In Fig. 52, the timing sample variances for MU time-transfer are plotted for $\sigma_\phi = 0$, $\sigma_\phi = 10^{-11}$ sec and the monocycle pulse width is approximately $\sigma_w = 0.067$ nsec.

The variances $\overline{\mathbf{V}\{\widetilde{d}_{MU}\}}$ and $\overline{\mathbf{V}\{\widetilde{t}_{MU(k')}\}}$ will hit a noise floor if the MU synchronization process is applied repeatedly. This is because $\mathbf{V}\{\widetilde{d}_{MU}^{(s)}\}$ is a function of network topology via $D_{m,s}$, noise density N_o, σ_ϕ, and network parameters N, K. If MU is applied repeatedly, there is a threshold beyond which the reduction effect of the weight $\alpha_{m,s}$ will not be able to reduce the variances further. Also, if MU is applied repeatedly, the variances $\overline{\mathbf{V}\{\widetilde{a}_{MU}\}}$ will increase due to noise accumulation. The results of repeatedly applying the MU time-transfer architecture with the network topology shown in Fig. 42 are plotted in Fig. 53. In this simulation, time-transfer scheme C is utilized. Moreover, to illustrate the effect of repeatedly applying MU, the initial offset before time transfer is 10 times of that used to obtain Figs. 43 to 52.

In estimating the difference in initial offset, the SM architecture achieves the lowest estimation error variance at a given SNR. However it is not capable of mitigating receiver measurement error. The HM architecture has the second lowest estimation error variance and selects propagation paths so as to avoid NLoS measurement. The MU has the highest sample variance after the estimation process. Its strength is its ability to average out the effect of receiver measurement error. The same observations apply to the timing error variances.

The simulation results illustrated the robustness of the MU and HM time-transfer architectures against NLoS measurement error. It is also evident that the topology of a network has a strong influence on individual node's timing jitter.

More simulation results are included in Appendix C, D, E and F.

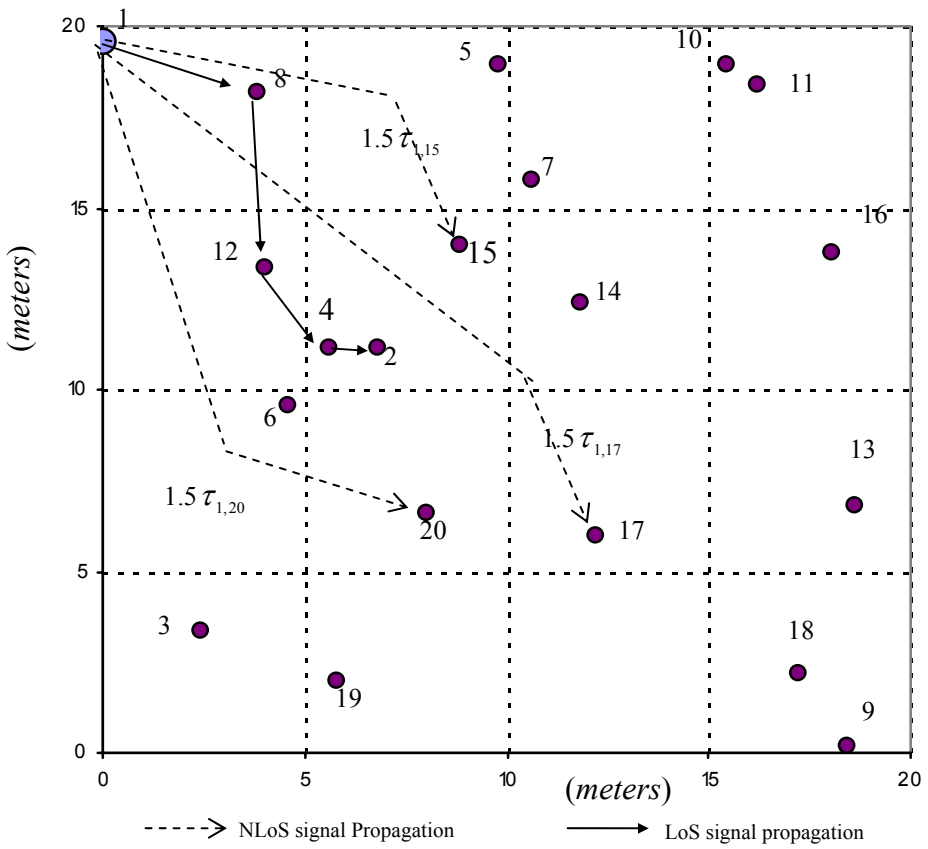

Figure 42: Illustration of the network topology used for time-transfer simulations. Node 1 is the lead master node.

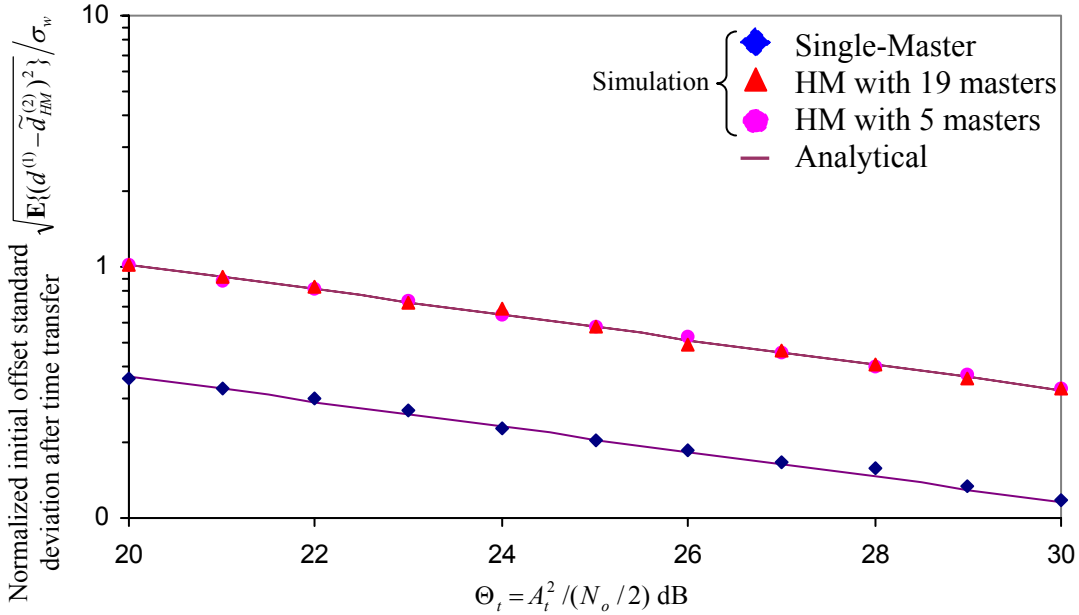

Figure 43: Normalized standard deviation of the settled initial offset estimate for node 2 with respect to lead master node after SM, HM time transfer. The SM, HM with 5 roving masters and 19 roving masters are plotted in the same figure. Results obtained using time-transfer scheme A.

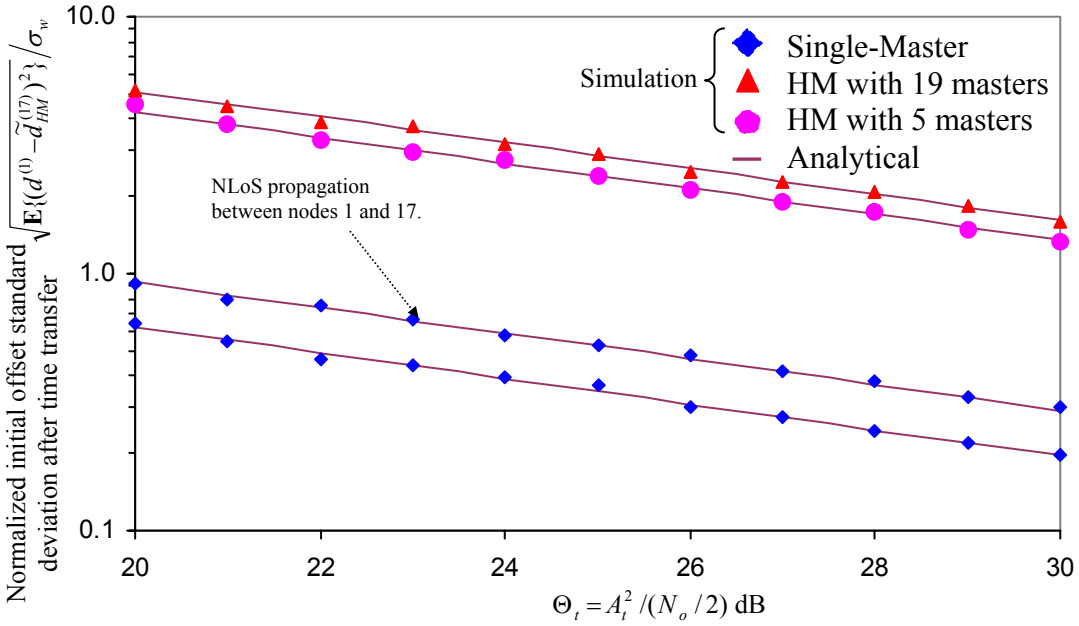

Figure 44: Normalized standard deviation of the settled initial offset estimate for node 17 with respect to lead master node after SM, HM time transfer. The SM, HM with 5 roving masters and 19 roving masters are plotted in the same figure. Results obtained using time-transfer scheme A.

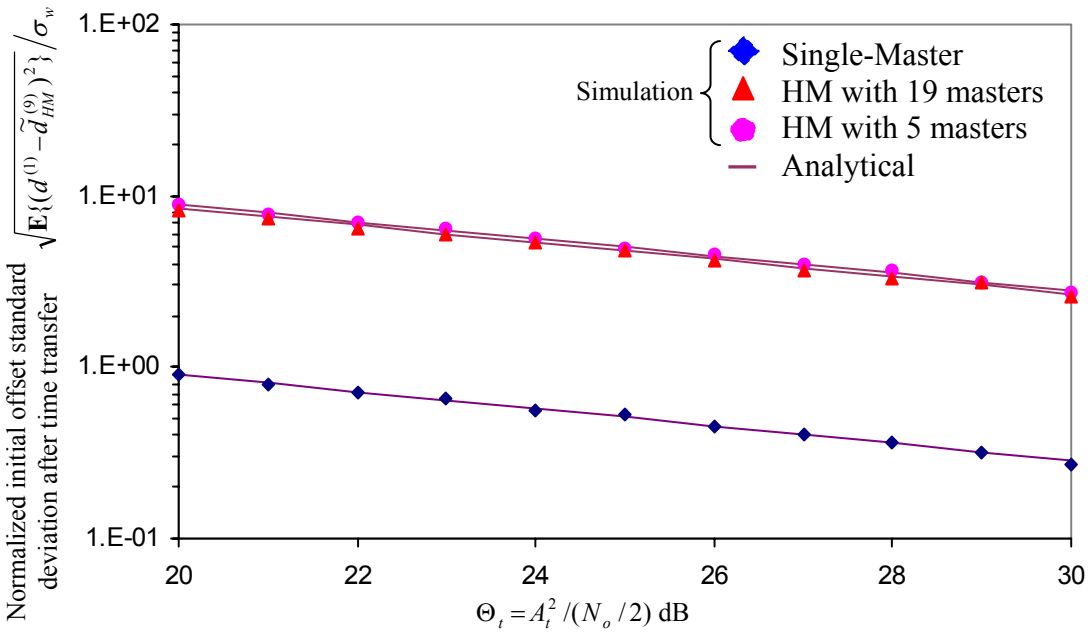

Figure 45: Normalized standard deviation of the settled initial offset estimate for node 9 with respect to lead master node after SM, HM time transfer. The SM, HM with 5 roving masters and 19 roving masters are plotted in the same figure. Results obtained using time-transfer scheme A.

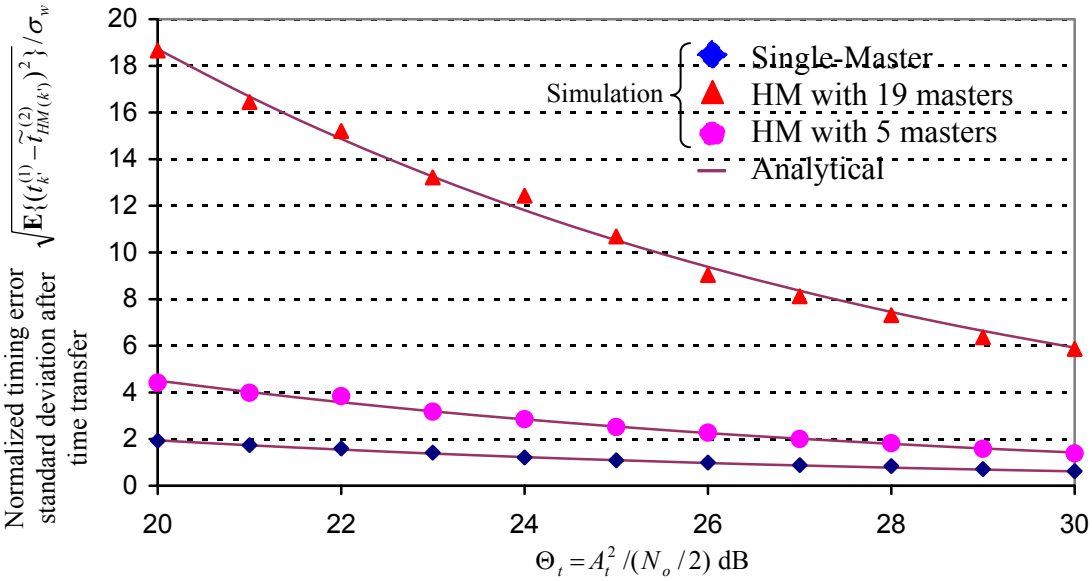

Figure 46: Normalized standard deviation of the settled timing error estimate for node 2 with respect to lead master node after SM, HM time transfer. The SM, HM with 5 roving masters and 19 roving masters respectively are plotted in the same figure. Results obtained using time-transfer scheme A.

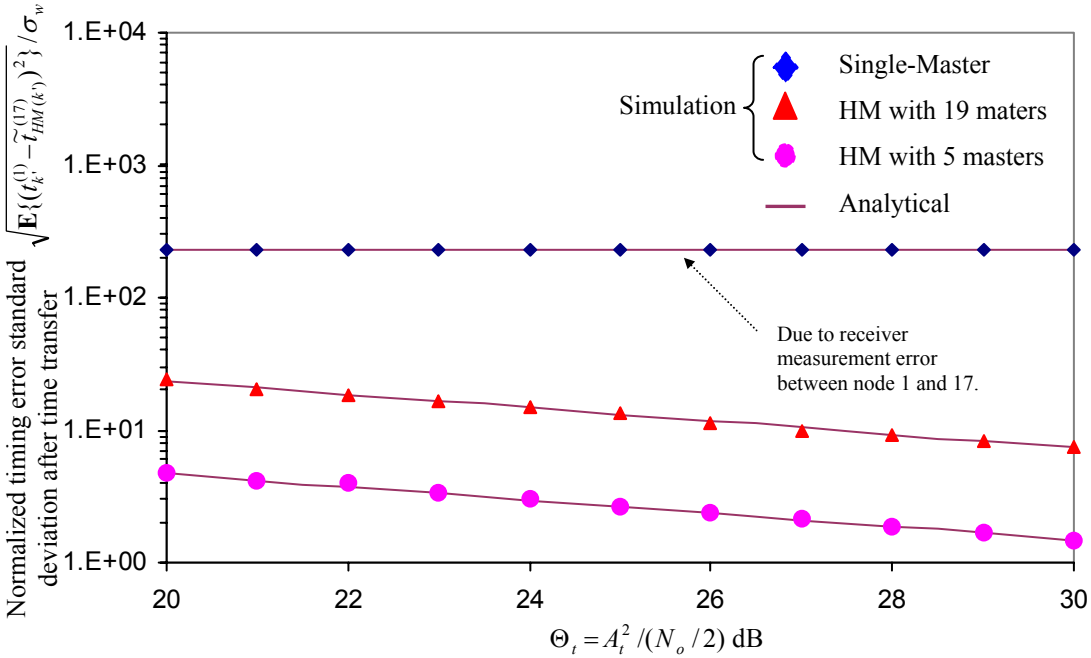

Figure 47: Normalized standard deviation of the settled timing error estimate for node 17 with respect to lead master node after SM, HM time transfer. The SM, HM with 5 roving masters and 19 roving masters are plotted in the same figure. Results obtained using time-transfer scheme A.

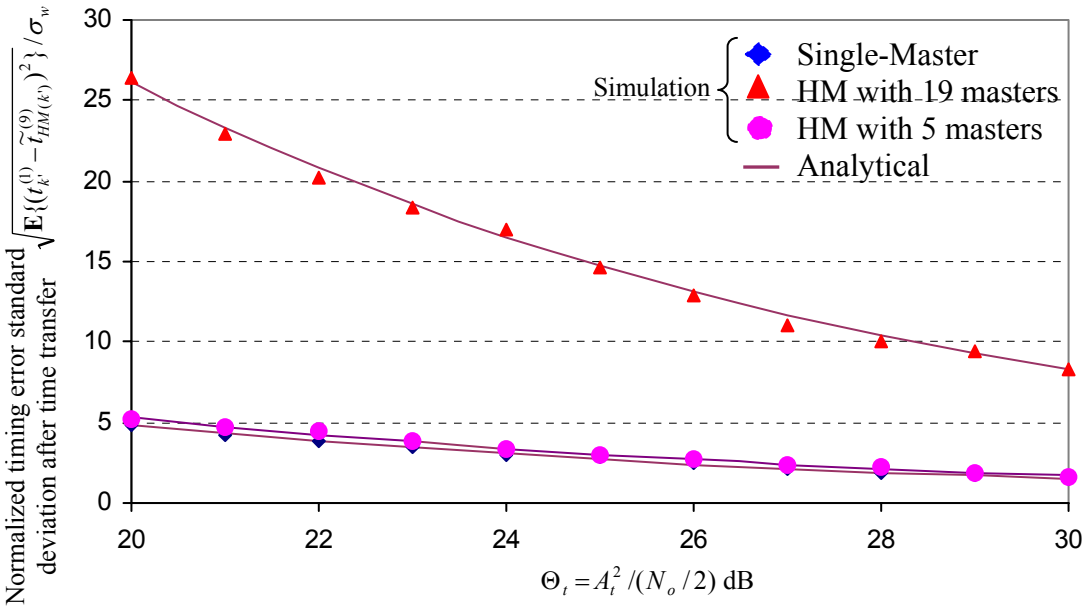

Figure 48: Normalized standard deviation of the settled timing error estimate for node 9 with respect to lead master node after SM, HM time transfer. The SM, HM with 5 roving masters and 19 roving masters are plotted in the same figure. Results obtained using time-transfer scheme A.

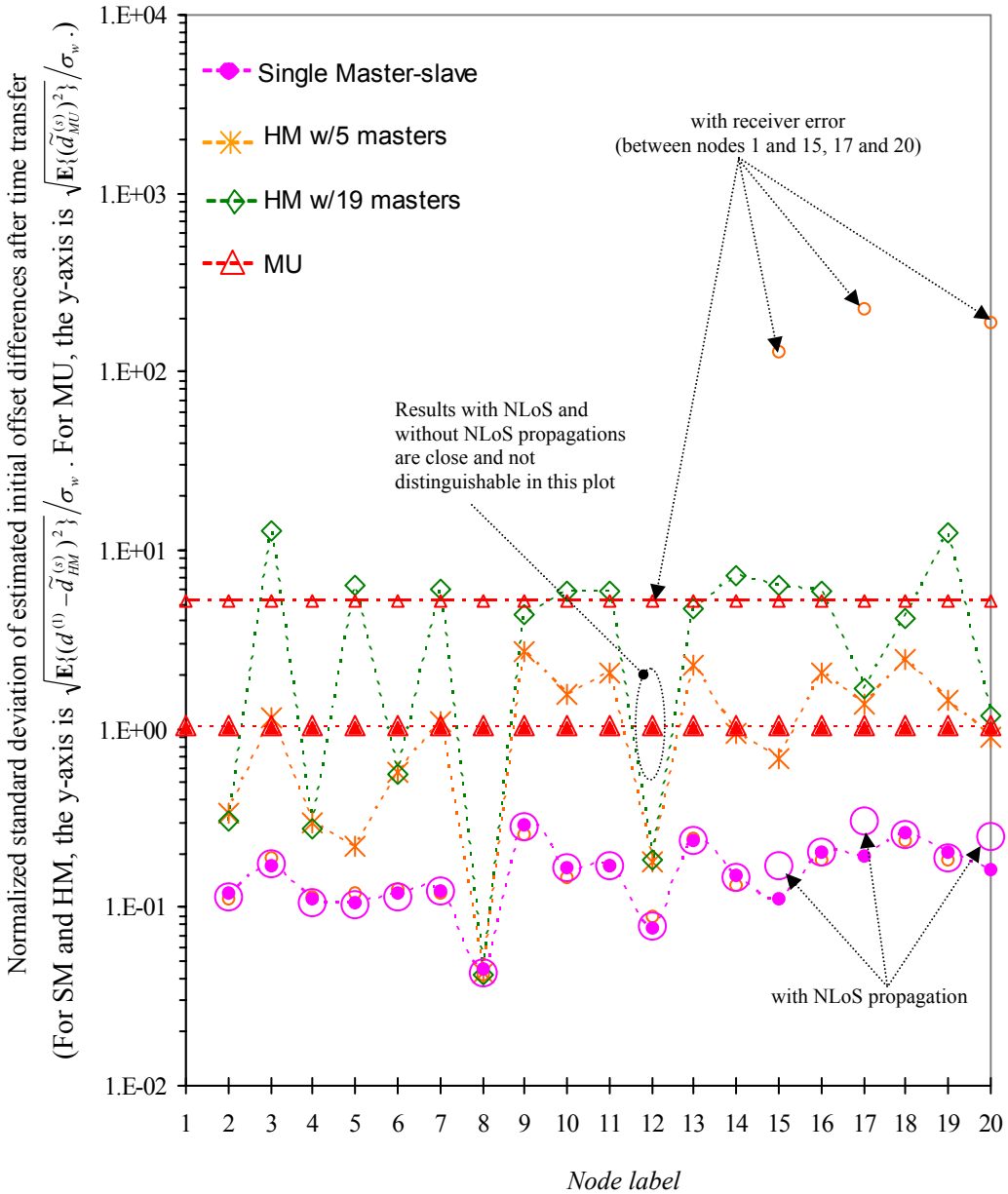

Figure 49: Normalized standard deviation in estimating difference in initial offset after time transfer using SM, HM and MU time-transfer architectures and time-transfer scheme A with $\rho_L = 2$, $\sigma_\phi = 0$ and $\Theta_t = 30$ dB. Results obtained via simulations.

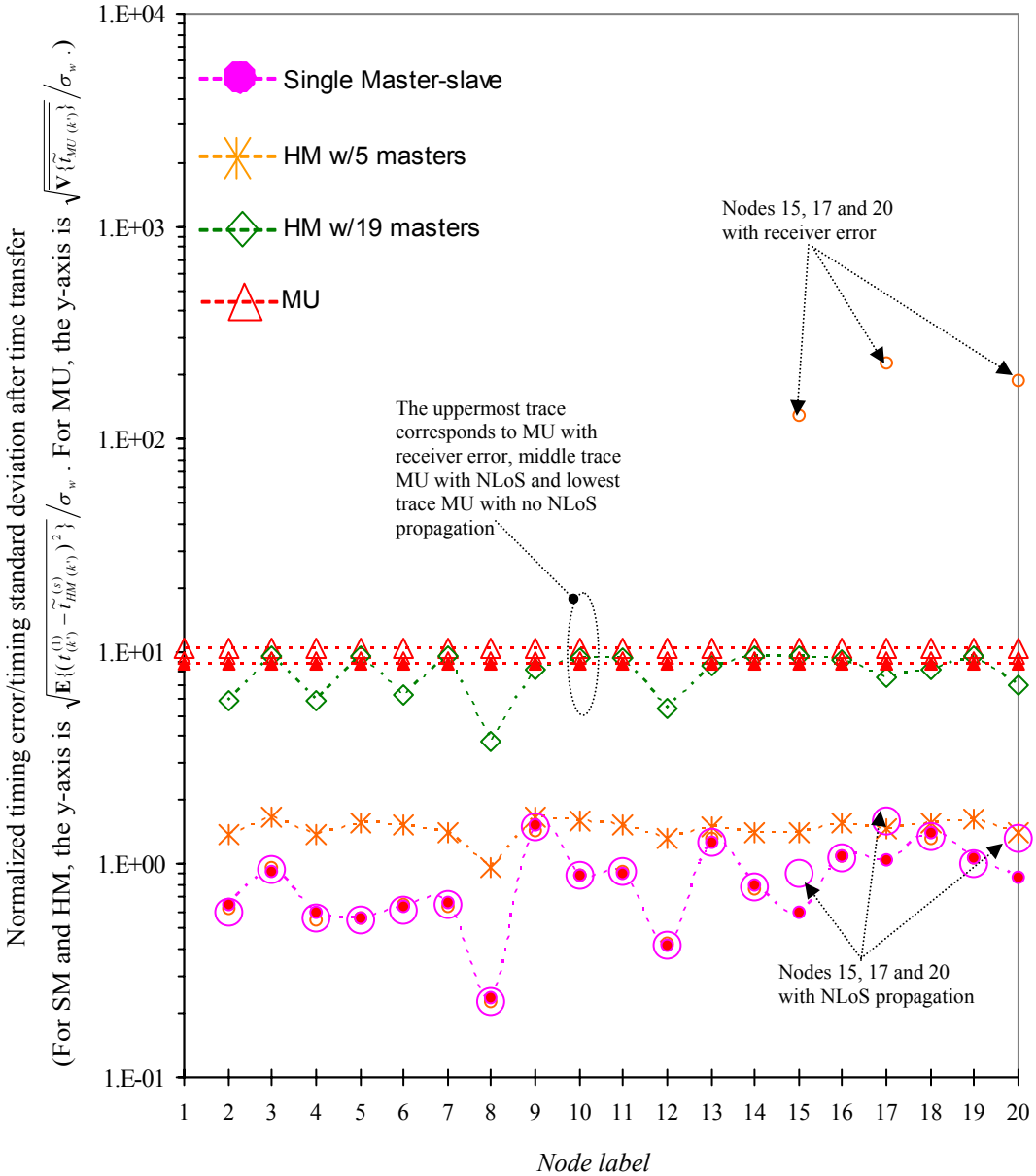

Figure 50: Normalized standard deviation of timing error after time synchronization using SM, HM and MU time-transfer architectures and time-transfer scheme A with $\rho_L = 2$, $\sigma_\phi = 0$ and $\Theta_t = 30$ dB. Results obtained via simulations.

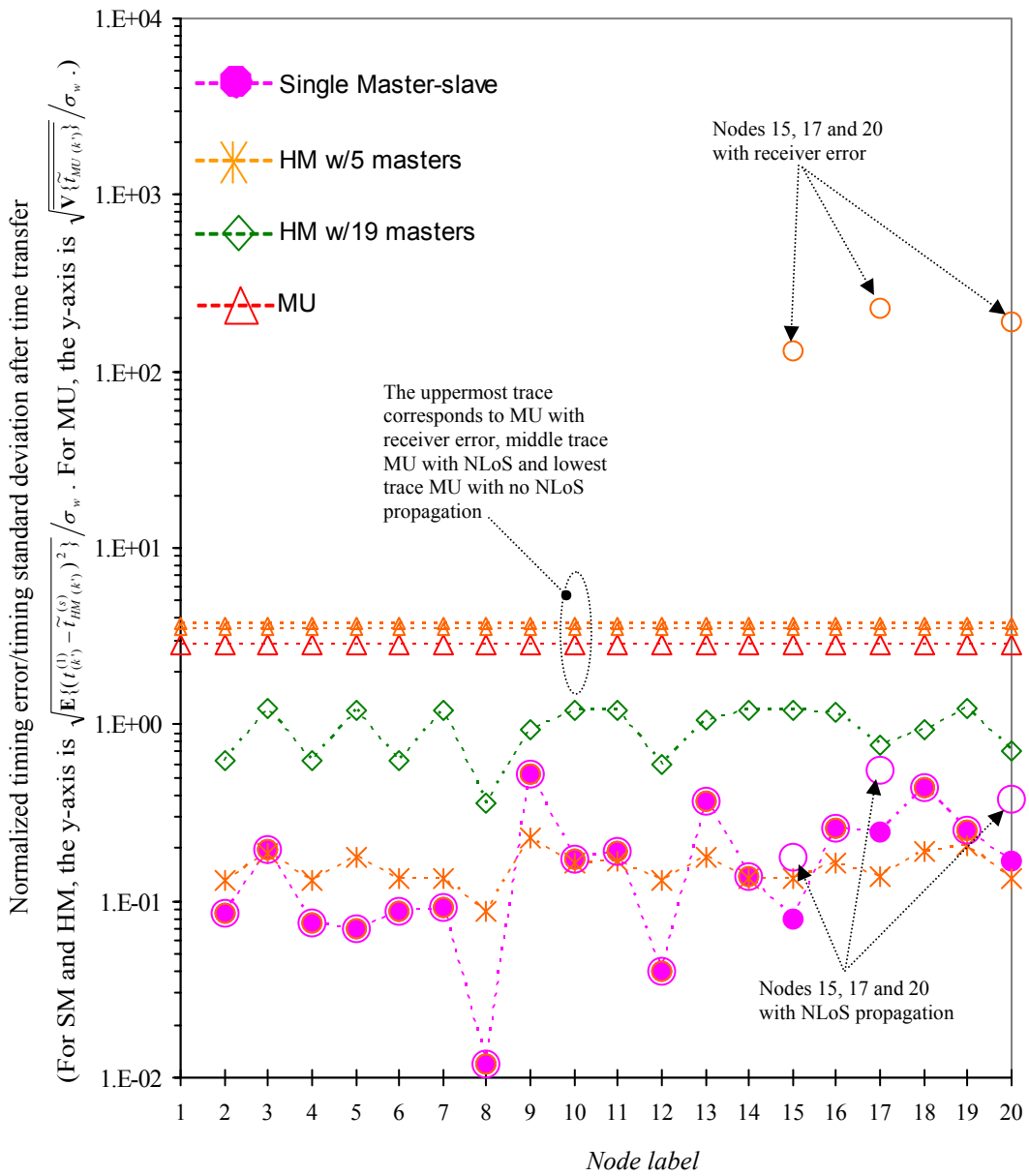

Figure 51: Normalized standard deviation of timing error after time synchronization using SM, HM and MU time-transfer architectures and time-transfer scheme C with $\rho_L = 4$, $\sigma_\phi = 0$ and $\Theta_t = 30$ dB.

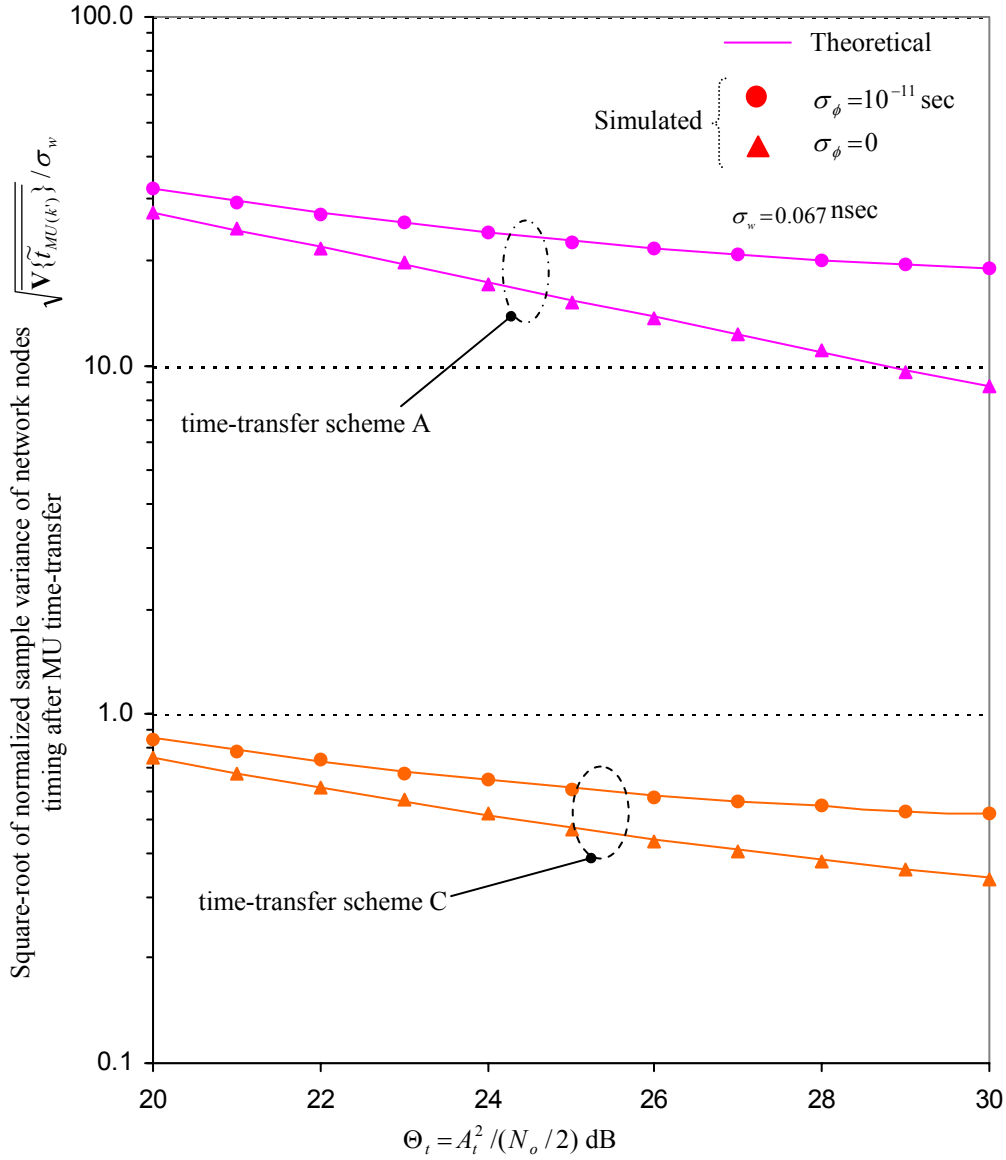

Figure 52: Sample variance of network nodes' timings immediately after time-transfer using MU time-transfer architecture. The time needed for time transfer is $t' = (2N-1) \cdot K \cdot N \cdot T_f$. In this simulation, there is no NLoS propagations and $\rho_L = 2$, $K = 1000$ and $N = 20$. The network topology is shown in Fig. 42.

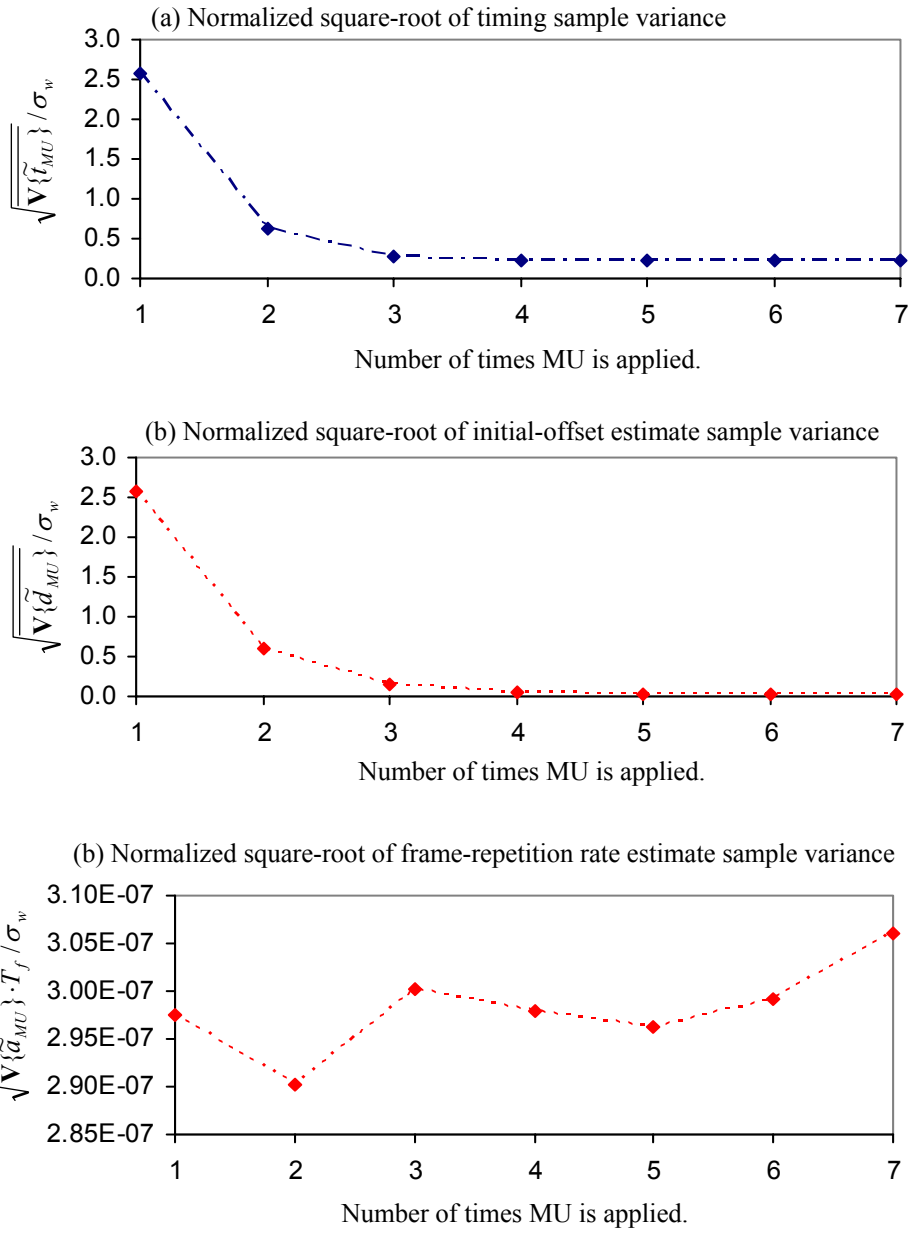

Figure 53: Simulation results from repeatedly applying MU time-transfer to the network shown in Fig. 42 at $\Theta_t = 30$ dB, $\rho_L = 2$ and $\sigma_\phi = 0$. In (a), the square-root of the timing sample variance is plotted. While (b) and (c) are the initial offset and frame-repetition rate sample variance. Results obtained using time-transfer scheme C.

6.1.2 Simulations with Random Network Topology

It is of interest to examine the ensemble average performances of the various time-transfer architectures when the network nodes are randomly distributed in a given area.

We let the x and y co-ordinates of the network nodes to be uniformly distributed between 0 to 20 meters while fixing the lead master node at location (0, 20), i.e., the lead master node is at the upper left-hand-corner of Fig. 42. At each Monte Carlo's step, the network nodes occupied new locations within a square of 20x20 meters and take on new values of initial offset and frame repetition rate. In these simulations, no receiver error is assumed, i.e., $\tilde{\rho}_{m,s} = 0$.

The simulation results are plotted in Figs. 54 to 56. The initial offset and η are uniformly distributed within $\pm 0.5\text{x}10^{-9}$ and between $1\text{x}10^{-6}$ to $10\text{x}10^{-6}$ respectively except the lead master node which has η=0. No NLoS propagation is introduced into the simulation and when HM is employed, the number of roving masters is N-1. The timing error and timing variances are computed using the analytical equations presented in Chapter 5.

Note that when oscillator phase noise is negligible, i.e., $\sigma_\phi = 0$, the sample variance of the timings of all nodes in the network after MU time-transfer is close to the maximum timing error variance obtained via HM time-transfer with $N-1$ roving masters (including the lead master node). The maximum timing error variance for a network of N nodes after HM time-transfer is defined as $\max\{\mathbf{V}\{t_{(k')}^{(1)} - \tilde{t}_{HM(k')}^{(s)}\}\}_{s=2}^{N}$. Similarly the minimum timing error variance is defined as $\min\{\mathbf{V}\{t_{(k')}^{(1)} - \tilde{t}_{HM(k')}^{(s)}\}\}_{s=2}^{N}$.

If $\sigma_\phi = 10^{-11}$ sec, $\sigma_w = 0.067$ nanosecond and at sufficient SNR so that measured ToAs are not overwhelmed by noise, the sample variance after MU time-transfer is close to the minimum timing error variance obtained via HM time-transfer.

The better performance of MU compared to HM when oscillator phase noise is significant can be explained by the fact that timing error variances are accumulated from one roving master to another in the HM time-transfer architecture. The non-zero oscillator's timing jitter is propagated through the network leading to higher timing error variances in individual nodes in the HM time-transfer architecture.

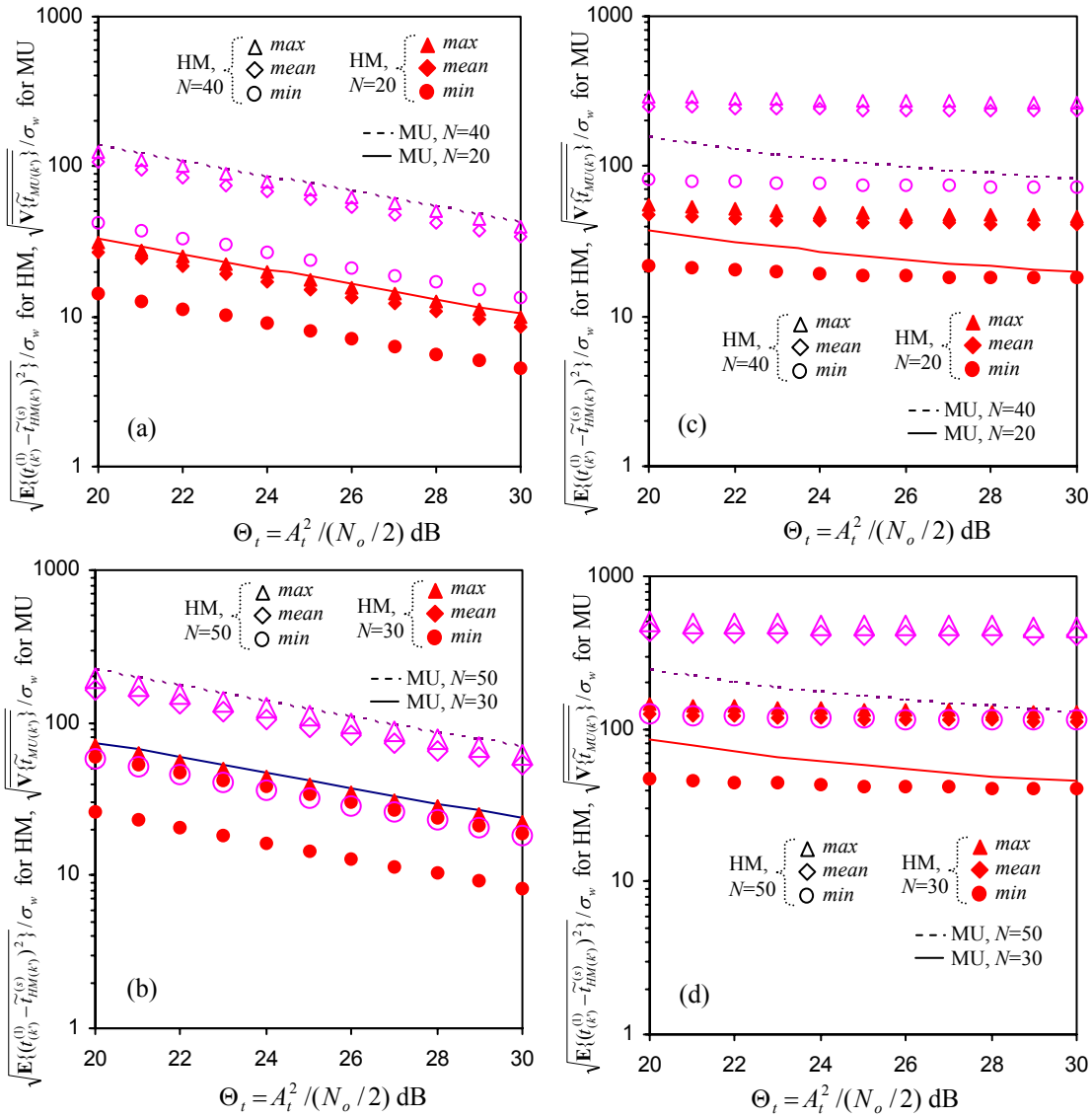

Figure 54: Normalized timing/timing error standard deviation when co-ordinates of the network nodes are uniformly distributed and utilizing time-transfer scheme A for transmitted SNR from 20 dB to 30 dB. In (a) and (b), σ_ϕ=0 while in (c) and (d), σ_ϕ=10^{-11} sec. Here $\sigma_w = 0.067$ nsec.

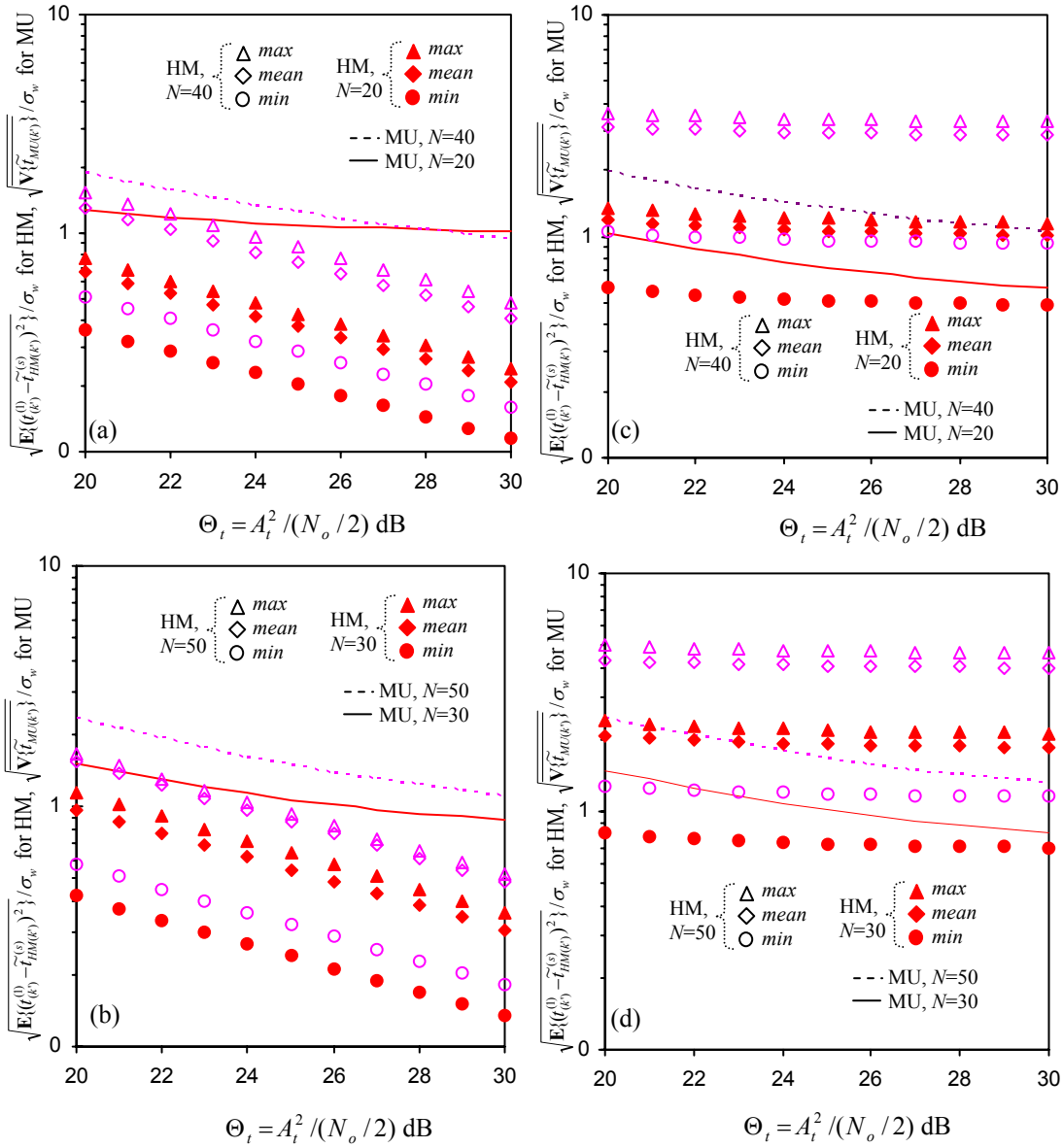

Figure 55: Normalized timing/timing error standard deviation when co-ordinates of the network nodes are uniformly distributed and utilizing time-transfer scheme C for transmitted SNR from 20 dB to 30 dB. In (a) and (b), σ_ϕ=0 while in (c) and (d), σ_ϕ=10^{-11} sec. The pulse width of the UWB monocycle is approximately $\sigma_w = 0.067$ nsec.

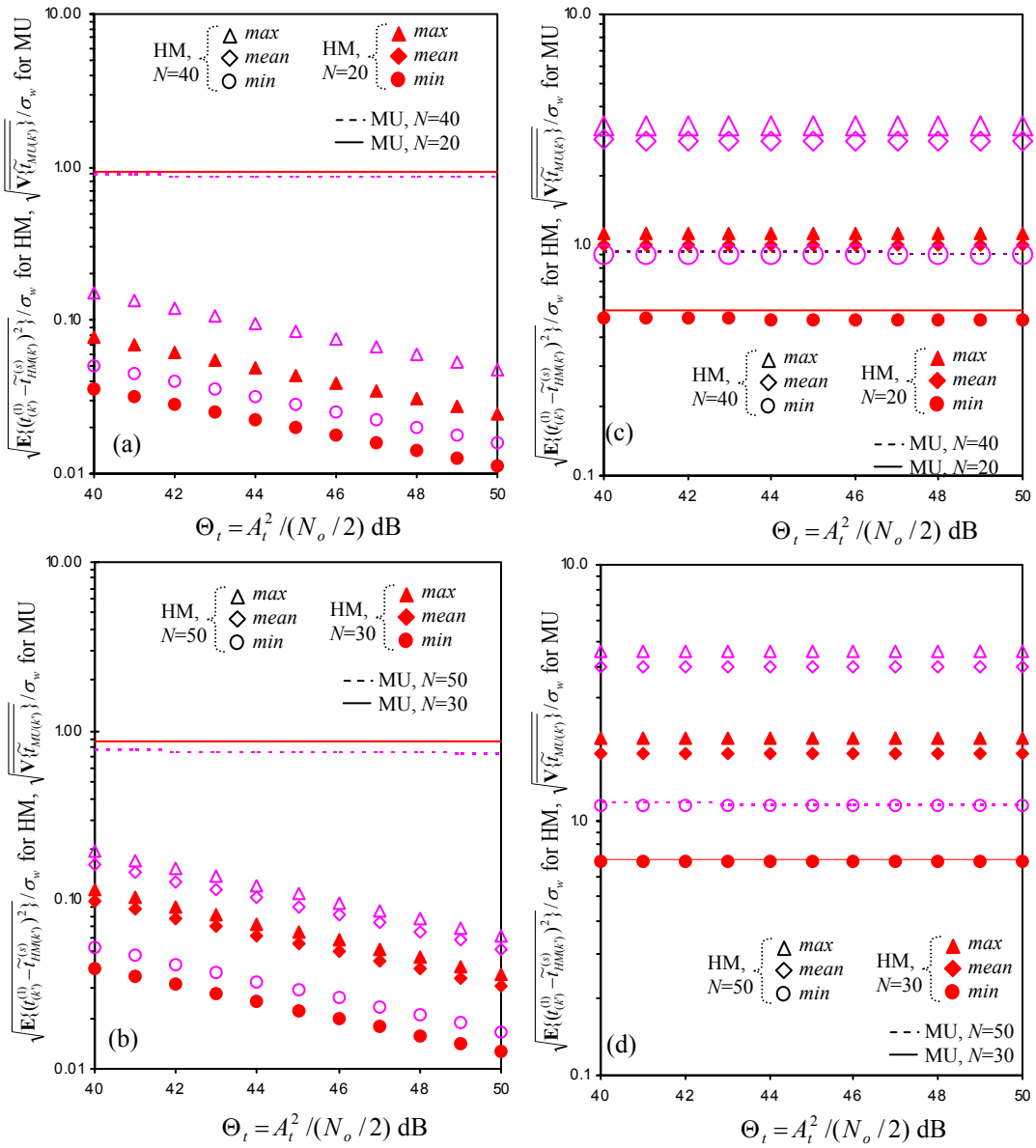

Figure 56: Normalized timing/timing error standard deviation when co-ordinates of the network nodes are uniformly distributed and utilizing time-transfer scheme C for transmitted SNR from 40 dB to 50 dB. In (a) and (b), σ_ϕ=0 while in (c) and (d), σ_ϕ=10^{-11} sec. The pulse width of the UWB monocycle is approximately $\sigma_w = 0.067$ nsec.

6.2 Discussion

In general, the number of nodes N supported by the network is bounded by differences in the oscillator's drift and initial offset as described in section 3.2 regardless of the time-transfer architectures as long as TDMA is used to multiplex the time-transfer among nodes. Therefore, to enable a larger N, it is important that sufficient number of synchronization frames, K_s is transmitted to mitigate the differences in initial offset and oscillator drift between pair of nodes using approaches described in section 2.4.

In HM, there is accumulation of jitter in successive levels/tiers of network nodes. When nodes take a turn to be the roving master, the timing jitter attributed to oscillator phase noise and additive channel noise is passed on to the next tier of nodes. This accumulated jitter is higher than previous tier of nodes however it may be smaller than what it would be if the lead master is to directly communicate its timing to these nodes assuming LoS signal propagation exists between nodes.

In MU, each node in the network based its timing primarily from nodes around it. This is assuming nodes that are nearer traveled shorter distance, likely to be LoS with less additive noise and thus given a larger weight. The lead master only plays the role of starting the time-transfer process and hence there is no accumulation of error in estimating the initial offset. It has the same properties of overcoming signal blockages and extending the geographical coverage of the network as the HM architecture.

In SM architecture, a slave node having larger timing jitter is likely to be a consequence of poor SNR and/or as a result of receiver measurement error. In HM and MU architectures, timing is transferred from the lead master to far-away nodes using multiple hops of shorter distances or emphasizing timings from nearby nodes. The roving master scheme exploits the rich spatial diversity (availability of abundant signal propagation paths) inherent in a dense network. With abundant

alternative network signal propagation paths to propagate timing from one node to another, time transfer can be performed via multiple intermediate nodes for which it is with high probabilities the links between nodes are LoS signal propagation paths. Therefore the SIN with roving masters does not present new algorithms to mitigate timing error arising from NLoS signals between pair of nodes per se. Its intention is to select the propagation path with the smallest measured timing jitter and possibly complement the many works already available in the literature such as [3], [64], [67] and [71] that described how to discern and handle the presence of NLoS signals in a multipath environment.

In [67], where multiple receivers are used to locate the position of a radio frequency source, the fact that the difference between NLoS and LoS propagations are always positive is used to constraint the domain over which mathematical programming is used to find the ML estimate of the source position. A similar technique is used in [64], which estimates are based on a constrained nonlinear optimization problem derived from the topology of the system. A more heuristic approach is used in [71] that discriminates between LoS versus NLoS measurements using the time history of the range measurements and corrects the NLoS ranging error by exploiting apriori knowledge of the statistical characteristics of the system's standard measurement noise. The approach adopted in [3] is to apply the maximum likelihood expectation-maximization and Bayesian estimators to estimate the LoS distance between transmitter and receiver, given the probability density function of the ToA which is derived from a multipath scattering model.

On first inspection, the results presented in Figs. 43 to 51 seem to indicate that SM has the lowest timing jitter among the three different time-transfer architectures for all nodes in the network. The simulations and theoretical analysis are based on the assumption that the measurement system, in particular, the AGC and the timing detector operate at received SNR above 15 dB. However, the transmitted SNR (defined as $\Theta_t = A_t^2/(N_o/2)$) is related to the received SNR by $\Theta_{m,s} = \Theta_t - \rho_L \cdot 10 \cdot \log_{10}(D_{m,s})$. If $\rho_L = 2$ and $\Theta_t = 30$ dB, a node 10 meters away from the lead

master node would have a received SNR of $\Theta_{m,s} = 10$ dB. This violates the earlier assumption that the measurement system operates at $\Theta_{m,s} \geq 15$ dB. As illustrated in Chapter 2, when $\Theta_{m,s} < 15$ dB, the AGC may not be able to regulate the amplitude of the received UWB monocycle and as a result the timing detector may not be operating at the tracking mode (linear portion of its characteristic function). The assumption that $\Theta_{m,s} \geq 15$ dB is easily met for HM and MU since each roving master will be transmitting at Θ_t. Hence, when there is a constraint to the maximum power that the master node can transmit, HM is a better choice than SM. In Fig. 57, the receiver SNR at node s relative to the transmitted SNR of the lead master node is illustrated.

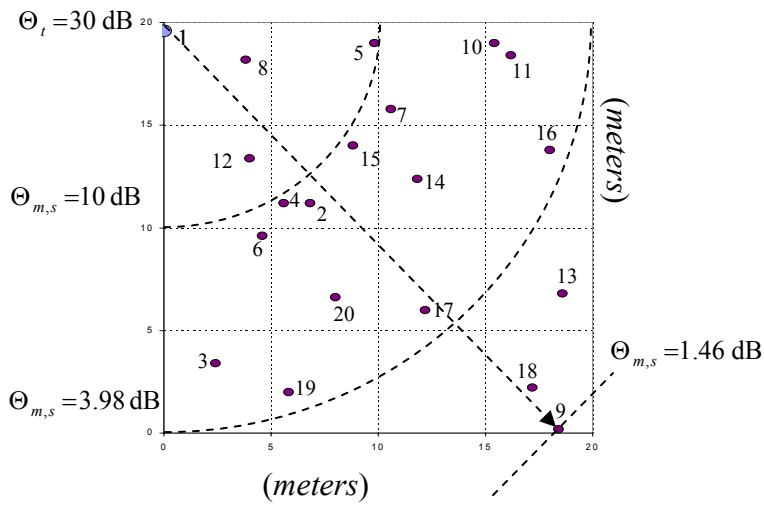

Figure 57: Illustration of the relationship between transmitter and receiver SNR. In order for node 9 to have received SNR of $\Theta_{m,s} = 15$ dB, node 1 needs to transmit at $\Theta_t = 43.5$ dB.

The simulation results on random network demonstrated the characteristic of the MU time-transfer architecture. When $\sigma_\phi = 0$ or is negligible (when a highly stable oscillators are utilized), the HM outperforms the MU. For the range of SNR simulated, the sample timing variance of MU is not better than the node in the HM architecture that has the poorest timing jitter. However, when σ_ϕ is

significant, the sample timing variance of MU is close to the timing jitter of the node in the HM with the smallest timing jitter. This is because when σ_ϕ is significant relative to additive channel noise, nodes in HM are not able to select roving master nodes based on links that have the smallest ToA variances. Further more, the oscillator phase noise propagates and accumulates through the network. The inability to select roving master node based on link quality and accumulation of oscillator phase noise degrades the performance of HM time-transfer architecture significantly especially for nodes that only acquired their timings after multiple roving master sessions.

If only $\Omega_{SY(v)}^{(m,s)}$ and $\Omega_{UP(u)}^{(s,m)}$ are measured at s and m respectively, time-transfer can still be performed via two-way time-transfer [58], noting that $\Omega_{SY(z)}^{(m,s)}$ and $\Omega_{UP(u)}^{(s,m)}$ have smaller measurement noise than $\Omega_{DN(z)}^{(m,s)}$. However, to complete the time-transfer, measurements obtained at s and m have to be encoded into information bits and exchanged using additional wireless resources. When extended to network synchronization, it is likely that the pair-wise two-way time-transfer involves more resources from higher layers (above the physical layer) with timing latency that is harder to predict than the proposed scheme.

The proposed synchronization scheme is similar to the RTS [33] [34] because both use a forward path and two return paths for propagation delay mitigation. However, RTS requires $2N$ phase detectors per node, which may not be practical for UWB signals.

It should also be noted that [39] has used linear regression (LS) to estimate the frame frequency differences and it is also mentioned in [15] as a possible way to correct the frame frequency differences.

Using [34] as a checklist, the proposed SIN exhibits most of the said advantages such as "decentralized timing control" and "each network node has equivalent influence" for MU and "stable" for HM. It should be noted that the objective of HM is different from MU. In HM, it is desired to have the timing of all nodes in the network to follow as closely as possible to the timing of a designated

master node. For MU, one of its objectives is to prevent the failure of network node/s from affecting the performance of the synchronous network severely.

In a SM network, the time needed for synchronization is $2(N-1)KT_f$ seconds. The HM with Q_m roving master (including lead master) needs $2(N-1)KT_f \cdot Q_m$ seconds while MU needs $2(N-1)KT_f N$ seconds to synchronize all nodes in the network. Among the three time-transfer architectures, the HM involves more computation and concerted effort is needed to select, assign and let the other nodes know which node is the next roving master. This involves higher layer network protocol and is not the subject of investigation in this work.

CHAPTER VII

CONCLUSIONS

7.1 Conclusions

In this section, the works accomplished and the performance of SIN and its practical applications are summarized.

(a) *Works Accomplished*

A synchronous impulse network (SIN) realized with the proposed time-division-multiplex synchronizing scheme and its variations are the subject of this research. The nodes in the network are time synchronized using the master-slaves (SM), hierarchical master-slaves (HM) or mutually synchronous (MU) time-transfer architectures.

In Chapter 2, we have comprehensively analyzed the correlative timing detector that is used to measure the ToA of UWB monocycles at the receiver in the presence of additive channel noise, oscillator phase noise, multipath self-interference and NLoS propagations. Chapter 3 presented

(i) the proposed time-transfer schemes (time-transfer schemes A, B and C),

(ii) the LS estimator to estimate the frame frequency differences followed by

(iii) two-way ranging to estimate the differences in initial offset among network nodes, and

(iv) evaluated the number of nodes supported in the network.

Chapter 4 introduces the roving master concept for time-transfer and evaluated the performances of the SM, HM and MU time-transfer architectures in implementing the SIN. The variances of the timing errors are presented in Chapter 5 and Chapter 6 reported the simulation results.

A summary of works accomplished in this research is shown in Fig. 58.

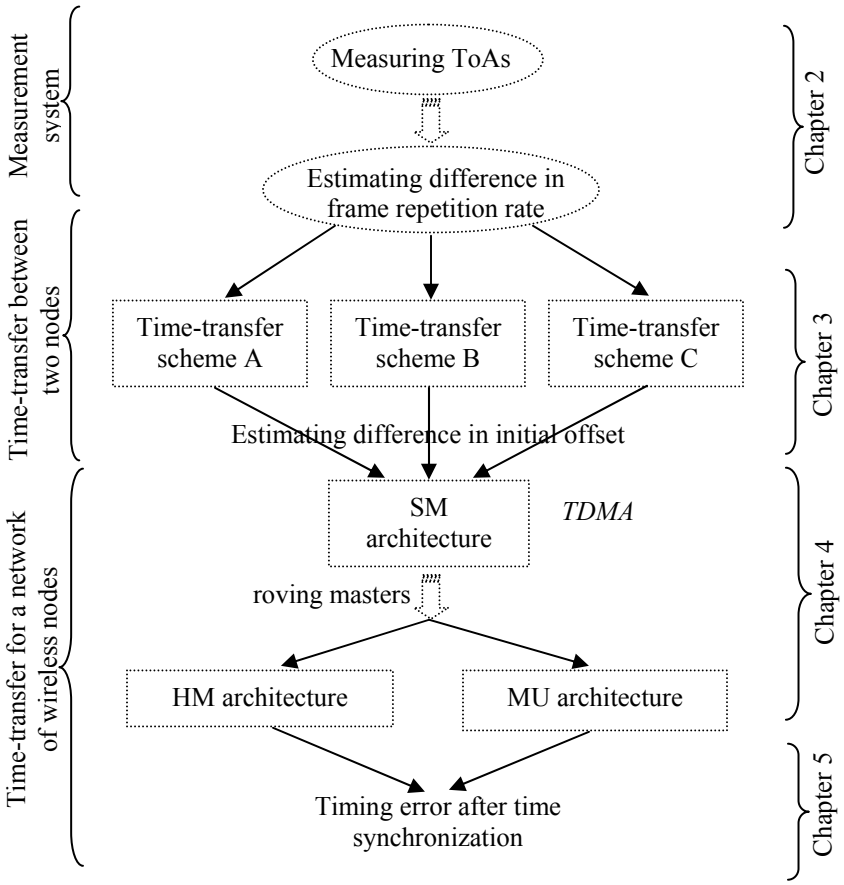

Figure 58: Summary of works performed in this research.

The SM time-transfer architecture implemented using the proposed time transfer schemes is shown to be able to realize a SIN with timing error within one monocycle pulse width at reasonable SNR. The SM time-transfer architecture implemented with time-transfer scheme A is also presented in our earlier work [9]. Chapter 2 summarizes our works published in [10] [11] and [12] on measuring the ToA of received UWB monocycles and incorporating an AGC in the measurement system. The analysis of an AGC for tracking the first arrival of UWB monocycle at the receiver, to be best of our knowledge, has not being previously explored in the communications literature.

The roving master concept for time synchronization is the other contribution of this work. The roving master leads to the HM and MU time-transfer architectures. The HM seeks out alternative network signal propagation paths to perform time transfer and selects the one that is most likely to be

a LoS path. The main objective is to avoid time transfer via NLoS signal propagation paths. A signal received via a NLoS propagation path has lower SNR due to the longer propagation distance compared to a LoS signal. The MU averages the timings of nodes in the network.

(b) *SIN Performance*

For a given path-loss exponent and time-transfer architecture, time-transfer scheme C achieves the lowest timing error variances while time-transfer scheme A has the highest timing error variance. (Fig. 22)

Assuming the received SNR is above 15 dB and employing a specific time-transfer scheme (A, B or C), the relative performance between SM, HM and MU time-transfer architectures depends on the path-loss exponent and the network topology. In general, the timing jitter in HM will be close to that achieves by SM for a channel with larger path-loss exponent or a network covering a larger area with few roving mater nodes. (Figs. 38 and 39)

Assuming a path-loss exponent of $\rho_L = 2$, it is observed that if time-transfer is via LoS propagation and oscillator phase noise is negligible compared to timing jitter introduced by additive channel noise, the SM architecture achieves the lowest timing error variance at a given SNR. The HM architecture has the second lowest timing error variance while the MU has the highest timing sample variance. (Figs. 50 and 51)

The other objective of extending the geographical coverage of the synchronous network using roving masters is hindered by the need to have a TDMA scheme to multiplex time transfer among nodes. The proposed roving master concept requires nodes to take a turn as the master node. This extends the time horizon needed to perform time transfer/synchronization. In the presence of residual error in frame frequency ($\text{drift} \times T_f$) difference estimation, a longer synchronization time multiplied with the frame frequency estimation error leads to larger timing errors and jitter.

This work has demonstrated that, ignoring σ_ϕ, it is possible to achieve a synchronous impulse network with timing jitter in the order of the pulse width of a UWB monocycle, for example, node 8 in Figs. 50 and 51, and the results shown in Fig. 41.

(c) *Applications*

From section 6.2, we observed that if the objective of time synchronization is to ensure minimum timing jitter, then taking into consideration the fact that the measurement system (consisting of AGC and correlative timing detector) is to operate at received SNR above 15 dB, the SM time-transfer architecture should be the appropriate option when there are many nodes in the network occupying a small area (e.g. 10x10 meters and smaller). Possible applications include array-beam forming and reach-back communications if these nodes are deployed in a small localized area.

For a network covering a wider area, HM time-transfer architecture should be utilized. The HM architecture is well-suited for application like geo-locationing. In this application, multiple receivers (nodes that perform the task of locating the emitter/s) are usually placed in fixed known locations. Then a HM roving master scheme can be devised easily to ensure small timing jitter. For example, if the distances between nodes are known a priori, it is possible to pre-determine the order of the roving master node. This minimizes un-certainties in assigning roving master nodes and generally produces lower timing jitter.

If the network nodes need to be in-expensive and are implemented with oscillators that have high phase noise, the MU is a better choice than HM. The MU fits well in application such as sensor networks when the nodes are expected to be cheap, and the nodes formed an ad hoc network with no preferred nodes. Moreover, in most practical situations, the physical phenomenon to be sensed does not require network nodes to have very fine timing resolutions. The need of timing precision in the order of nanoseconds offered by SM and HM architectures described in this work usually does not arise.

If many nodes are deployed in a large geographical area, to avoid the long synchronization time of the roving masters approach, dividing the network into smaller area and employing a mixture of SM, HM and MU time-transfer architectures should be a better engineering solution than trying to deploy a SIN with only one type of time-transfer architecture.

(d) *Research Contributions*

This research has proposed a time-transfer scheme (and its variations) to establish a synchronous impulse network utilizing UWB impulse radio. The ultra-wide bandwidth of UWB signals is exploited to enable a synchronous impulse network achieving timing precision, i.e. timing differences among network nodes, in the order of nanoseconds. This compared favorably with timing precision reported in the review paper [56], which reported various timing synchronization schemes archiving precision in the order of microseconds.

The proposed roving master concept for time-transfer exploited the "richness" (availability) of alternate network signal propagation paths in the HM architecture to avoid time-transfer via NLoS paths, and enable a MU architecture that attempts to average out the effect of NLoS propagation error.

We have derived analytical results for multi-hops time synchronization taking into consideration the effect of frame-repetition rate differences between network nodes. Thus filling the gap mentioned in [56] that there is a 'lack of analytical models for multi-hop synchronization'. However, we should note that [34] has formulated analytically a HM time-transfer architecture for a FDMA scheme that utilizes a closed-loop phase detector for time synchronization. The effect of frame-repetition rate differences is not considered in [34].

The proposed synchronization scheme can be modified to suit some narrowband communication systems. Note that mulitpath self-interference may then have to be taken into account when evaluating the performance of the synchronous system.

7.2 Future Research

This work has not, in its humble length of approximately 100 pages, been able to exhaustively analyze and address all issues involved in establishing a SIN. The following is a list of possible issues that we feel will enhance the usefulness of this work. This list of possible future research topics is broadly grouped into separate headlines, namely: estimation techniques, effect of network topology, ranging, and a summary of restrictive assumptions that are made in this work.

7.2.1 Estimation Techniques

The techniques used to estimate the initial offset and frame repetition rate differences are under the realm of "classical" techniques. The Least Squares estimator used to estimate the differences in frame repetition rate between a pair of nodes can be shown to approach the Cramer Rao lower bound for a stationary AWGN channel [13]. The ToAs are measured at the output of the open loop timing detector, and there is no tracking of timing jitter.

Incorporating a tracking loop will help to deal with variations in the wireless channels and possibly improve the performance of the time-transfer. If the oscillator phase jitter is to be modeled as a Gauss-Markov process, iterative techniques such as those mentioned in [61] to track the phase jitter, are likely to improve the performance of the time-transfer.

Other estimation techniques such as Kalman filtering, expectation-maximization are not investigated in this work.

When the received SNR is below 15 dB, it is shown in Chapter 2 that the AGC may not be able to regulate the amplitude of the received UWB monocycle effectively. As a result, the timing detector may not be operating in the linear portion of its characteristic function. This will degrade the performance of the time-transfer schemes. A more comprehensive analysis of the working of the AGC at lower SNR is left to future work.

There possibly exist other approaches to utilizing the ToA measurements to estimate the differences in initial offset and drift. There are also possible ways to enhance the performance of the proposed time-transfer scheme. For example, at the end of each roving-master session, the slave node can utilize the measured ToAs of the frame-synchronizing pulses, $\Omega_{SY(v)}^{(m,s)}$ and downlink ranging pulses, $\Omega_{DN(z)}^{(m,s)}$ to re-estimate the difference in frame repetition rate between itself and the master node. To avoid exhaustively analyzing all possible alternative approaches, a more efficient analytical technique, such as graph theory, is needed.

7.2.2 Effect of Network Topology

(a) *Graph Theory and Network Topology*

The performances of the various time-transfer architectures depend on the network topology. To aid in choosing the "optimal" time-transfer architecture for a specific application, a statistical description of the performances of the various time-transfer architectures for an arbitrary network topology will be useful. The modeling of an arbitrary network topology with nodes randomly distributed in a given area with links that may or may not be LoS has not been addressed in this work.

A recent work [26], which modeled $\rho_{m,s}$ and $\rho_{s,m}$ as random variables with exponential distribution of mean $\overline{\rho}$, has derived an unbiased ML estimator for $d_{\delta}^{(m,s)} = d^{(m)} - d^{(s)}$. Assuming $a^{(m)} = a^{(s)}$, and ignoring additive channel noise and oscillator phase noise, the ML unbiased estimator for $d_{\delta}^{(m,s)}$ is $\hat{d}_{\delta}^{(m,s)} = \left(\min\{\Omega_{SY(v)}^{(m,s)}(k)\}_{k=0}^{K-1} - \min\{\Omega_{UP(u)}^{(m,s)}(k)\}_{k=0}^{K-1}\right)/2$ with variance $\overline{\rho}/2K^2$. This result may help in devising addition signal processing techniques to further mitigating the bias introduced by NLoS propagation.

To investigate the performance of a network of randomly distributed nodes, graph theory maybe a useful tool. From [30], a simple graph is defined as,

> "a triple $G=(V,E,I)$ where V and E are disjoint finite sets and I is an incidence relation such that every element of E is incident with exactly two distinct elements of V and no two elements of E are incident to the same pair of elements of V ."

Sets V and E are known as the vertex and edge sets of G respectively. Then it is possible to represent nodes in the network as elements of the vertex set, and two nodes are joined by an edge $\in E$ if it is possible for one to communicate with the other.

(b) *Minimum Energy Network*

In [29] and [52], graph theory is used to devise network protocols to establish a 'minimum energy network' for wireless communications. The proposed network protocol finds the minimum-energy path between m and s, assuming a communication link between m and s is feasible. In this context, the minimum energy path is defined as one that allows messages to be transmitted with a minimum use of energy. The protocol is devised making use of the fact that power required to transmit from m to s is governed by the path-loss exponent $\rho_L \geq 2$ in $\left(D_{m,s}\right)^{\rho_L}$ where $D_{m,s}$ is the distance traveled by the signal propagating from m to s in meters. Therefore it is possible to relay information from m to s via intermediate node/s with less power than to transmit directly from m to s. For the protocol to establish a minimum energy network, both [29] and [52] require each node to know its location. This is made possible by assuming that nodes in the network are each equipped with a GPS receiver.

If we view the shortest propagation path as being equivalent to the minimum energy path for communications [29] [52], there seems to be close resemblance between constructing a minimum energy network and establishing a synchronous impulse network with minimum timing error. In fact,

exploiting the properties of the path loss exponent is a feature of the proposed roving-master time-transfer concept. The possibilities of drawing on results reported in [29] [52] to analyze the proposed synchronous impulse network are left to future research. There may be other works in computer/information and networking technologies, such as network scheduling that may be utilized to improve or analyze the performance of the proposed time synchronization schemes.

(c) *Multiple Roving Masters per Time-transfer Session*

This work analyzed the case whereby each node takes a turn as the roving master, i.e., only one node is being assigned as the 'master' while other nodes are slaves at any point in time. It is possible that the current master node estimates the variances of the measured ToA of impulses from other nodes in the network and appoints multiple nodes to be the next tier of roving masters by grouping nodes with similar measured ToA variances. This "tree-like" HM time transfer architecture is illustrated in Figs. 59 and 60. Obviously more could be accomplished with more resources expended at each node to co-ordinate this 'tree-like' architecture instead of the "thread-like" hierarchical master-slave time-transfer architecture investigated in this work.

If the topology of the network is known, the performance of the network depicted in Fig. 59 can be predicted using analytical expressions presented in Chapters 4 and 5.

(d) *Optimality of Time-Transfer Scheme*

The optimality of the proposed time-transfer scheme has not been fully addressed in this work. The design of the proposed time-transfer scheme is guided by implementation considerations, for example, TDMA is the natural choice instead of FDMA because UWB signals occupied very large bandwidth.

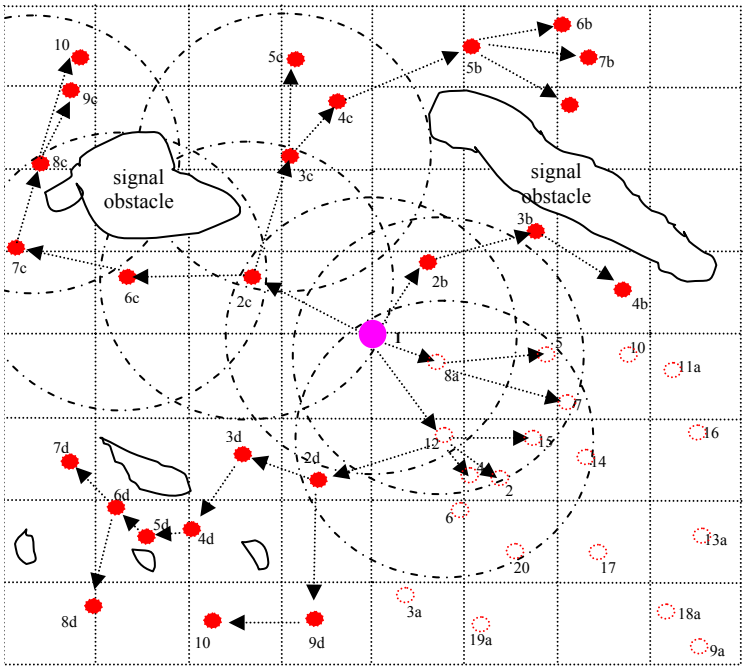

Figure 59: Example of a HM time transfer architecture whereby multiple nodes formed the next tier of the hierarchy. Number of nodes forming the next tier of the time transfer architecture depends on the network topology. Network protocol above physical layer is needed to co-ordinate the assignment of multiple roving masters per time transfer session.

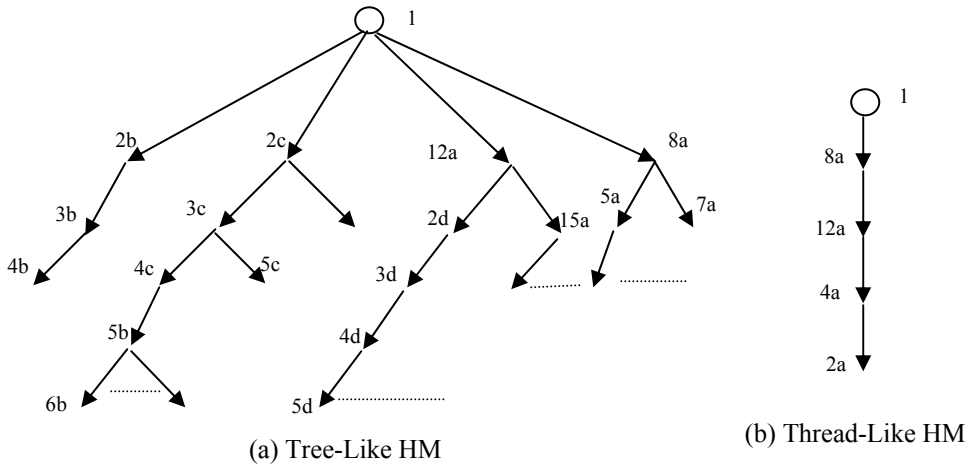

Figure 60: The nodes tree for the HM time transfer architecture shown in Fig. 59.

It is assumed that the first arrival is most probably a LoS path and possibly offers the best signal for measuring the ToA. In practice, the first discernible signal at the receiver may be a signal that arrives via a NLoS propagation path.

In HM time-transfer architecture, the order of time-transfer is dictated by the shortest signal propagation path. The shortest signal propagation path is assumed to correspond to the signal propagation path with measured ToAs that has the smallest variance.

In MU time-transfer architecture, timing information obtained from the shortest path is emphasized (given larger weight). Moreover, it is assumed that nodes take turns being the roving master in the natural order if nodes are labeled as 1,2,3,… . It is likely that for a given network topology, there may exist a preferred way to order the nodes when utilizing MU time-transfer architecture to achieve minimum timing error variance. The optimal order has not being investigated in this work.

Choosing the shortest network signal propagation paths or emphasizing timings associated with these paths has not being proven to bring about a globally optimal system with the smallest timing error for all nodes in the network. Intuitively, choosing the link with the shortest propagation delay for time transfer will likely lead to smaller timing error.

7.2.3 Restrictive Assumptions

In this work, nodes are assumed stationary which considerably simplifies estimating the difference in frame repetition rate between nodes. In a practical application, such as operating on a mobile platform, there is a need to consider the effect of compression and expansion of UWB signals.

After introducing the synchronization scheme, the derivations that followed assume the indices of the uplink i and downlink j time slots is such that $i = j$ for every node in the network. This introduces "regularity" in the network and simplifies the analysis. The regularity refers to the fact that the characteristic function of the time-transfer scheme $\theta(k)$ in (3.12) will then only be a function

of N and K for all nodes in the network. A larger $|i-j|$ will increase the error in estimating the difference in initial offset for the pair of nodes with uplink index i and downlink index j. The existence of an optimal way of assigning the time slots index i and j that will reduce the timing error in the network is not addressed here.

The number of synchronization frames is assumed to be equal to the number of ranging frames. Allocating different numbers of frames for frame repetition rate synchronization and ranging estimation may lead to a more power efficient time-transfer scheme. This is because error variance for frame repetition rate estimation decreases asymptotically in the order of K^3 while initial offset estimation variances decreases only in the order of K.

The path-loss exponent is assumed to be 2 in our performance analysis. A higher path-loss exponent may make HM performs better than the SM time-transfer architecture. In Chapter 5, Figs. 37 to 39, an analysis using a "straight" line topology, i.e., nodes in the network are arranged in a straight line, shows that indeed a higher path-loss exponent will bring the timing error variance of HM closer to that of SM.

In the MU time-transfer architecture simulations, the weight $\alpha_{m,s}$ is constructed via the function $\alpha_{m,s} = 1/\sqrt{\mathbf{V}\{\Omega_{DN(z)}^{(m,s)}\}} \Big/ \sum_{m'=1,m'\neq s}^{N} 1/\sqrt{\mathbf{V}\{\Omega_{DN(z)}^{(m',s)}\}}$. It is not known whether other weight functions, for example, $\alpha_{m,s} = \exp(-\sqrt{\mathbf{V}\{\Omega_{DN(z)}^{(m,s)}\}}) \Big/ \sum_{m'=1,m'\neq s}^{N} \exp(-\sqrt{\mathbf{V}\{\Omega_{DN(z)}^{(m',s)}\}})$, or employing higher order polynomial, would yield a lower timing jitter. In Chapter 5, Fig. 40, the timing variances using 3 different weight functions are evaluated analytically for the network topology shown in Fig. 42. For this example, no significant differences in timing variances using the 3 weight functions defined in Fig. 40 is observed.

Last but not least, no stability analysis is performed in this work. Here, "stability" means timing error does not increase without bound after application of time transfer. Although HM is likely to be stable, as timing information is passed from the lead master to other nodes in the network in one

direction with no feedback. The stability of MU is of concern if it is to be applied repeatedly since timing information is transferred back and forth through the network.

To expand the number of nodes that can be supported by the proposed synchronization scheme, each network of N nodes can be described as a single "cell" and a higher layer network protocol may be used to connect cells together to form an extended network.

An obvious disadvantage of the proposed synchronization scheme is that transceivers in the network are assigned specific time slot, thus it is difficult to dynamically add or remove transceivers from the network. To mitigate this shortcoming, protocols above physical layer may be needed.

7.2.4 Ranging and Geo-locationing

This work is about synchronizing the timing of network nodes. A by-product of the proposed time synchronization scheme is range information between pair of nodes. The range information between pair of nodes can be derived/estimated from the ToA of the downlink ranging pulses. From (3.21),

$$\mathbf{E}\left\{\Omega_{DN(z)}^{(m,s)}\right\} = \tau_{m,s} + \tau_{s,m} + \rho_{m,s} + \rho_{s,m} ,$$

and

$$\mathbf{V}\{\Omega_{DN(z)}^{(m,s)}\} = \mathbf{E}\{(\varepsilon_{\gamma_{LS}}^{(m,s)})^2\} \cdot (z-u)^2 + \mathbf{E}\{(\varepsilon_{DN(z)}^{(m,s)})^2\} .$$

This can be expanded further to geo-locating of network nodes. It will be interesting to examine the performance of ranging and the precision in estimating the co-ordinates of nodes achievable using the proposed time synchronization scheme.

GLOSSARY

Conventions

$\mathbf{V}\{x\}$	variance of random variable x
$\mathbf{E}\{x\}$	expected value of random variable x
$F_x(t)$	$=F\{x(t)\}$, Fourier transform of signal $x(t)$
$f(x,t)$	function of variables x and t
$\mathbf{H}^{\mathbf{T}}$	transpose of matrix $\mathbf{H}$
$\mathbf{P}(x)$	probability density function of random variable x
$Z\{x_{(k)}\}$	denote the Z-transform
$\circ$	denote convolution
$\propto$	proportional to
$[X]^c$	complex conjugate of variable X
$\dot{x}(t)$	time derivative of $x(t)$
i_c	$=\sqrt{-1}$

Specific Terms

Lead master	the first node to start transferring its timings to all other nodes in the network
drift	deviation of oscillator's oscillation frequency from ideal due to oscillator aging plus external environmental factor

List of symbols

Variables and symbols that for clarity are introduced only once in the text are omitted. Symbols are arranged in alphabetical order.

A

$\breve{a}_1^{(m)}$	first order drift of oscillator m
$a_1^{(m)}$	$=1/\breve{a}_1^{(m)}$
$a_\delta^{(m,s)}$	$=a^{(m)}-a^{(s)}$, difference in drift between node m and s before time transfer
$\widetilde{a}_{HM}^{(s)}$	estimated drift of node s after hierarchical master-slave time transfer, also refers to as settled drift estimate after HM time transfer
$\widetilde{a}_{MU}^{(s)}$	estimated drift of node s after mutually synchronous time transfer, also refers to as settled drift estimate after MU time transfer
A_d	desired amplitude at output of automatic gain control loop
A_r	amplitude of reference monocycle waveform
A_t	amplitude of transmitted monocycle waveform
A_w	amplitude of received monocycle waveform
$\alpha_{m,s}$	weight used in mutually synchronous time-transfer architecture
c	$=3\times10^8$ meters/second, speed of light

D

$\breve{d}^{(m)}$	initial offset of oscillator m with respect to true time $t=0$ before time-transfer
$d^{(m)}$	$=\breve{d}^{(m)}/\breve{a}_1^{(m)}$
$d_\delta^{(m,s)}$	$=d^{(m)}-d^{(s)}$, difference in initial offset between node m and s before time transfer
$\hat{d}_\delta^{(m,s)}$	estimate of difference in initial offset $d_\delta^{(m,s)}$ between nodes m and s
$\bar{d}_\delta^{(s)}$	weighted average initial offset differences evaluated at node s
$\tilde{d}_{HM}^{(s)}$	estimated initial offset of node s after hierarchical master-slave time transfer, also refers to as settled initial offset estimate after HM time-transfer
$\tilde{d}_{MU}^{(s)}$	estimated initial offset of node s after mutually synchronous time transfer, also refers to as settled initial offset estimate after MU time-transfer
$\theta(k)$	characteristic function of time-transfer scheme $=(N-1)\cdot K_r/2-k$, time-transfer scheme A $=(N-1)/2-(2N-1)\cdot k$, time-transfer scheme B $=1/2-(2N-1)\cdot k$, time-transfer scheme C
$D_{m,s}$	distance traveled by signal transmitted from node m to receiver s measured in meters
$D_\varphi^1(\Delta)$	first structure function of the phase noise process of oscillator

E

$\varepsilon_a^{(m,s)}$	random variable representing difference in drift between two oscillators *m* and *s* after time-transfer
$\varepsilon_d^{(m,s)}$	random variable representing difference in initial offset between two oscillators *m* and *s* after time-transfer
$\varepsilon_{x(k)}^{(m,s)}$	zero mean random error at output of open loop timing detector
$\varepsilon_{SY}^{(m,s)}$	zero mean random error due to additive channel noise and oscillator phase noise when measuring $\Omega_{SY(v)}^{(m,s)}(k)$
$\varepsilon_{UP(u)}^{(s,m)}$	zero mean random error due to additive channel noise and oscillator phase noise when measuring $\Omega_{UP(u)}^{(s,m)}(k)$
$\varepsilon_{DN(z)}^{(m,s)}$	zero mean random error due to additive channel noise and oscillator phase noise when measuring $\Omega_{DN(z)}^{(m,s)}(k)$
$\varepsilon_\vartheta^{(m,s)}$	zero mean random error of timing equation $\vartheta^{(m,s)}(k)$
$\varepsilon_{\hat{d}}^{(m,s)}$	zero mean error associated with determining the estimate $\hat{d}_\delta^{(m,s)}$ of $d_\delta^{(m,s)}$ by averaging $\vartheta^{(m,s)}(k)$ over *k*
$\varepsilon_{\gamma_{LS}}^{(m,s)}$	zero mean error associated with determining the least squares estimate $\hat{\gamma}_{LS}^{(m,s)}$ of $\gamma^{(m,s)}$
η	$a_1^{(m)}=1+\eta$

F

f frequency in Hertz

f_o nominal frequency of frame clock in transceiver in units of Hertz

$g(\varsigma)$ characteristic function of correlative timing detector

$g_{MF}(\tilde{\tau})$ output of matched filter at $\tilde{\tau}$

$\tilde{g}_{TD}$ $=dg(\varsigma)/d\varsigma\big|_{\varsigma=0}$, slope of the characteristic function of the timing detector evaluated at zero timing error

$\gamma^{(m,s)}$ $=(a_1^{(m)}-a_1^{(s)})\cdot T_f$, difference in frame repetition rate between transmitter m and receiver s before time-transfer

$\hat{\gamma}_{LS}^{(m,s)}$ least squares estimate of $\gamma^{(m,s)}$ obtained from $\{\Omega_{SY(v)}^{(m,s)}(k)\}_{k=0}^{K-1}$

i index of down-link time slot

j index of up-link time slot

K number of frames per time slot

K_D gain of timing detector

K_r number of up-link or down-link ranging frames per time slot

K_s number of synchronization frames per time slot

K_{ST} ≥ 0, starting index of the first transmitted or the first received pulse measured with respect to start of time-transfer at a transceiver with transceivers sharing the channel via time division multiplexing

L

Λ_{SF} amplitude suppression factor of AGC

$\mu_{(k)}$ $=\phi_k^{(m)}-\phi_k^{(s)}$, difference in timing jitter of oscillators *m* and *s*

N number of nodes in network

$n(t)$ additive noise with one-sided power spectral density of N_o

O

ω frequency of oscillation in radians per seconds

ω_o nominal oscillating frequency of frame clock in transceiver

$\overline{\omega^2}$ effective squared bandwidth of UWB monocycle with unit sec^{-2}.

$\Omega_{SY}^{(m,s)}(k)$ relative ToA of monocycles transmitted from master to slave and measured at slave receiver during synchronization time slot

$\Omega_{UP(q)}^{(s,m)}(k)$ relative ToA of up-link ranging monocycles transmitted from slave to master and measured at master node receiver

$\Omega_{DN(z)}^{(m,s)}(k)$ relative ToA of down-link ranging monocycles transmitted from master to slave and measured at slave node receiver

$\Omega_{SY}^{(m,s)}$ to represent $\{\Omega_{SY(v)}^{(m,s)}(k)\}_{k=0}^{K-1}$

$\Omega_{UP}^{(s,m)}$ to represent $\{\Omega_{UP(u)}^{(s,m)}(k)\}_{k=0}^{K-1}$, when $i=j$

$\Omega_{DN}^{(m,s)}$ to represent $\{\Omega_{DN(z)}^{(m,s)}(k)\}_{k=0}^{K-1}$, when $i=j$

p $=1/2\sigma_w^2$, parameter of Gaussian derivative monocycle waveform

$\breve{\varphi}^{(m)}(t)$ random phase jitter of oscillator m

$\breve{\varphi}_{(k)}^{(m)}$ $=\breve{\varphi}^{(m)}(kT_f)$, random phase jitter of oscillator m at $t=kT_f$

$\breve{\phi}^{(m)}(t)$ $=(\breve{\varphi}^{(m)}(t)-\breve{\varphi}^{(m)}(0))/\omega_o$, in units of seconds

$\breve{\phi}_{(k)}^{(m)}$ $=(\breve{\varphi}_{(k)}^{(m)}-\breve{\varphi}_{(0)}^{(m)})/\omega_o$

$\phi_{(k)}^{(m)}$ $=\breve{\phi}_{(k)}^{(m)}/\breve{a}_1^{(m)}$

P

$\Phi(t)$ total phase of oscillator in radians

$\Psi(\varsigma_{(k)})$ auto-correlation function of UWB monocycle waveform evaluated at delay $\varsigma_{(k)}$

Q number of hops from the lead master node to a particular roving master from which a slave node s acquires its timing

$r(t)$ reference monocycle waveform generated at receiver

R

$\rho_{m,s}$ additional propagation delay (excess-delay) from master m to slave s due to NLoS signal propagation

$\tilde{\rho}_{m,s}$ $=(\rho_{m,s}-\rho_{s,m})/2$, difference in excess-delay

ρ_L path-loss exponent of wireless channel between transmitter and receiver, fixed at 2 in this work unless otherwise specified

S

σ_ϕ standard deviation of oscillator phase noise

σ_w parameter of nth derivative of a Gaussian curve, approximating width of main lobe of UWB monocycle

$\sigma_x^2(m,s)=\mathbf{V}\{x_k\}=\sigma_n^2(m,s)+2\sigma_\phi^2(m,s)$, variance of output of open loop timing detector due to zero mean noise and oscillator phase noise

$\sigma_n^2(m,s)$ variance of output of open loop timing detector due to additive white Gaussian noise in the channel between nodes m and s

$\sigma_{\gamma_{LS}^{(m,s)}}^2$ $=\mathbf{E}\{|\gamma^{(m,s)}-\hat{\gamma}_{LS}^{(m,s)}|^2\}$, variance of LS estimate on estimating $\gamma^{(m,s)}$

$\sigma_{\zeta_{LS}^{(m,s)}}^2$ $=\mathbf{E}\{|\zeta^{(m,s)}-\hat{\zeta}_{LS}^{(m,s)}|^2\}$, variance of LS estimate on estimating $\zeta^{(m,s)}$

ς timing error between the received and reference signal at the input of the timing detector

T

t true time (time on standard time scale)

$\tau_{m,s}$ LoS propagation delay from master m to slave s

T_D positive limit of range of integration of timing detector measured from origin

T_f $=2\pi/\omega_o$, nominal frame repetition rate

$T^{(m)}(t)$ time function for transceiver m

$T_{\delta}^{(m,s)}(t)$ timing error between two oscillators m and s at time t

$\vartheta^{(m,s)}(k)$ $=\Omega_{DN(z)}^{(m,s)}(k)/2-\Omega_{SY}^{(m,s)}(k)$, initial-offset equation

$\Theta_{m,s}$ $=A_w^2/(N_o/2)$, received signal-to-noise ratio measured at receiver

Θ_t $=A_t^2/(N_o/2)$, transmit signal-to-noise ratio measured at transmitter

$\tilde{\tau}$ receiver timing offset from the received signal in matched filter detector

U

u time index of uplink ranging pulses

v time index of frame-synchronization pulses

$\mathbf{V}\{\tilde{a}_{MU}\}$ sample variance of settled drift estimate for all nodes in the network after mutual synchronization

$\overline{\mathbf{V}\{\tilde{a}_{MU}\}}$ mean of sample variance of settled drift estimate for all nodes in the network after mutually synchronous time transfer

$\mathbf{V}\{\tilde{d}_{MU}\}$ sample variance of initial offset estimate for all nodes in the network after mutual synchronization

$\overline{\mathbf{V}\{\tilde{d}_{MU}\}}$ mean of sample variance of settled initial offset estimate for all nodes in the network after mutually synchronous time transfer

$w(t)$ received monocycle waveform

$w_n(t)$ n^{th} order derivative of a Gaussian curve

$x_{(k)}$ output of open loop timing detector

Z

z time index of downlink ranging pulses

$\zeta^{(m,s)}$ $=d^{(m)}-d^{(s)}+\tau_{m,s}+\rho_{m,s}$, propagation delay from transmitter m to receiver s plus difference in initial offset

$\zeta_{SY}^{(m,s)}$ $=d^{(m)}-d^{(s)}+\tau_{m,s}+\rho_{m,s}$, propagation delay and difference in initial offset obtained from synchronization pulses

$\zeta_{UP}^{(s,m)}$ $=-d^{(m)}+d^{(s)}+\tau_{s,m}+\rho_{s,m}$, propagation delay and difference in initial offset obtained from uplink ranging pulses

$\zeta_{DN}^{(m,s)}$ $=\tau_{m,s}+\tau_{s,m}+\rho_{m,s}+\rho_{s,m}$, propagation delay obtained from downlink ranging pulses

$\hat{\zeta}_{LS}^{(m,s)}$ Least Squares (LS) estimate of $\zeta^{(m,s)}$

BIBLIOGRAPHY

[1] H. S. Abdel-Ghaffar, "Analysis of Synchronization Algorithms with Time-Out Control over Networks with Exponentially Symmetric Delays", *IEEE Trans. on Commun.*, vol. 50, No. 10, Oct 2002.

[2] M. Abramowitz and I. A. Stegun, *Handbook of Mathematical Functions with Formulas, Graphs, and Mathematical Tables*, Chapter 7, eqn. 7.1.3, National Bureau of Standards (US Department of Commerce)-Applied Mathematics Series 55, 10th printing, Dec 1972.

[3] S. Al-Jazzar and J. Caffery Jr., "ML & Bayesian TOA Location Estimators for NLOS Environments", *Proc. IEEE VTC*, 2002-Fall.

[4] J. A. Barnes, "The Measurement of Linear Frequency Drift in Oscillators", *Proc. 15th annual PTTI meeting*, 1983.

[5] J. C. Bellamy, "Digital Network Synchronization", *IEEE Commun. Mag.*, April 1995.

[6] W. R. Braun, "Short Term Frequency Instability Effects in Networks of Coupled Oscillators", *IEEE Trans. Commun.*, vol. COM-28, No. 8, Aug. 1980.

[7] S. Bregni, "A Historical Perspective on Telecommunications Network Synchronization", *IEEE Commun. Mag.*, June 1998.

[8] E. Brookner (Editor), *Radar Technology*, Artech House, Chapters 6 and 11, 1978.

[9] C. C. Chui and R. A. Scholtz, "A Synchronizing Scheme for an Impulse Network", *Proc. IEEE MILCOM*, 2004.

[10] C. C. Chui and R. A. Scholtz, "Estimating Parameters of Received UWB Monocycles", *Proc. Asilomar Conf. Signals, Systems, and Computers*, 2004.

[11] C. C. Chui and R. A. Scholtz, "Optimizing Tracking Loops for UWB Monocycles", *Proc. IEEE Globecom*, 2003.

[12] C. C. Chui and R. A. Scholtz, "Tracking UWB Monocycles in IEEE 802.15 Multi-path channels", *Proc. Asilomar Conf. Signals, Systems, and Computers*, 2003.

[13] A. A. D'Amico and U. Mengali, "Frame Frequency Estimation in Ultra-Wideband Systems", *IEEE Trans. Wireless Commun.*, in press.

[14] A. Demir, A. Mehrotra and J. Roychowdhury, "Phase Noise in Oscillators: A Unifying Theory and Numerical Methods for Characterization", *IEEE Trans. Circuits and Systems - I:Fundamental Theory and Applications*, vol. 47, No. 5, May 2000.

[15] J. Elson, L. Girod and D. Estrin, "Fine-Grained Network Time Synchronization using Reference Broadcasts", *Proc. of the Fifth Symposium on Operating Systems Design and Implementation* (OSDI 2002), Boston, MA. December 2002.

[16] J. Elson, "Time Synchronization Services for Wireless Sensor Networks", dissertation proposal, UCLA, April 2001.

[17] J. Elson and K. Romer, "Wireless Sensor Networks: A New Regime for Time Synchronization", *Proc. of the First Workshop on Hot Topics in Networks*, Oct. 2002. Available at http://www.circlemud.org/~jelson/.

[18] R. L. Freeman, *Radio System Design for Telecommunications*, 2nd Edition, page 608, Wiley, 1997.

[19] J. Foerster et. al., *Channel Modeling sub-committee Report Final*, IEEE 802.15.3a Wireless Personal Area Networks, Nov. 18, 2002.

[20] R. M. Gagliardi, *Satellite Communications*, USC Custom Publishing, 2nd Edition.

[21] S. Gradshteyn and I. M. Ryzhik, *Table of Integrals, Series, and Products,* Academic Press, 5th edition.

[22] P. Houghton, "Wireless Sensor Networks for Location and Control", *RFIC Symposium*, 2003. Available at http://www.aetherwire.com.

[23] Y. W. Hong and A. Scaglione, "Time Synchronization and Reach-Back Communications with Pulse-coupled Oscillators for UWB Wireless Ad-hoc Network", *Proc. IEEE International Conference on Ultra Wideband Systems and Technologies*, 2003.

[24] Innovative Wireless Technologies, "Innovative Wireless Technologies Wins U.S. Army Contract for Ultra-Wideband Sensor Networks", March 17, 2003. Available at http://www.iwtwireless.com/uwb.htm.

[25] R. Janaswamy, "Angle and Time of Arrival Statistics for the Gaussian Scatter Density Model", *IEEE Trans. Wireless Commun*, vol. 1, No. 3, July 2002.

[26] D. R. Jeske, "On Maximum-Likelihood Estimation of Clock Offset", *IEEE Trans. on Commun.*, vol. 53, No. 1, Jan 2005.

[27] K. Kiasaleh, "Performance of Master-Slave Synchronized Clocks", *Proc. Globecom,* 1988.

[28] J. Kunisch and J. Pamp, "UWB Radio Channel Modeling Considerations". Available at http://www.whyless.org/flies/public/WP5_iceaa2003_jk.pdf.

[29] L. Li and J. Y. Halpern, "Minimum-Energy Mobile Wireless Networks Revisited", *Proc. IEEE ICC*, 2001.

[30] S. C. Locke, "Graph Theory - Index, Brief History, Basic Definitions", Sept. 1, 2000. Available at http://www.math.fau.edu/locke/graphthe.htm.

[31] J. Y. Lee and R. A. Scholtz, "Ranging in a Dense Multipath Environment using an UWB Radio Link", *IEEE J. Select. Areas Commun.*, vol. 20, No. 9, Dec 2002.

[32] A. Leon-Garcia, *Probability and Random Processes for Electrical Engineering*, 2nd Edition, Addison-Wesley, 1994.

[33] W. C. Lindsey, A. V. Kantak and A. Dobrogowski, "Network Synchronization by Means of a Returnable Timing System", *IEEE Trans. on Commun.*, vol. COM-26, No. 6, June 1978.

[34] W. C. Lindsey, F. Ghazvinian, W. C. Hagmann and K. Dessouky, "Network Synchronization", *Proc. IEEE*, vol. 73, No. 10, October 1985.

[35] W. C. Lindsey and C. M. Chie, "Theory of Oscillator Instability Based Upon Structure Functions", *Proc. IEEE*, Dec 1976.

[36] W. C. Lindsey and C. M. Chie, "A Survey of Digital Phase-Locked Loops", *Proc. IEEE*, vol. 69, No. 4, April 1981.

[37] W. M. Lovelace and J. K. Townsend, "The Effects of Timing Jitter on the Performance of Impulse Radio", *Proc. IEEE Conference on Ultra Wideband Systems and Technologies*, 2002.

[38] J. Marshall, "Modeling of Through-Wall Propagation for Ultra-Wideband Signals", *Proc. MILCOM*, 2004.

[39] F. Mazzenga, F. Vatalaro and C. E. Wheatley III, "Performance Evaluation of a Network Synchronization Technique for CDMA Cellular Communications", *IEEE Trans. Wireless Commun.*, vol. 1, No. 2, April 2002.

[40] M. S. McCorquodale, M. K. Ding and R. B. Brown, "Study and Simulation of CMOS LC Oscillator Phase Noise and Jitter", *Proc. ISCAS,* 2003.

[41] J. M. Mendel, *Lessons in Estimation Theory for Signal Processing, Communications, and Control*, Prentice Hall, 1995.

[42] H. Meyr, M. Moeneclaey and S. A. Fechtel, *Digital Communication Receivers – Synchronization, Channel Estimation, and Signal Processing*, Wiley, 1998.

[43] H. Meyr and G. Ascheid, *Synchronization in Digital Communications – Volume 1, Phase-, Frequency-Locked Loops, and Amplitude Control*, Wiley 1990.

[44] MF Electronics, "Offset Filter - The Critical New Spec.". Available at http://www. mfelectronics.com.

[45] M. J. Miller and S. V. Ahamed, *Digital Transmission Systems and Networks*, vol. 2: Applications, Chapter 2.2, Computer Science Press, 1988.

[46] D. L. Mills, "Improved Algorithms for Synchronizing Computer Network Clocks", *IEEE/ACM Trans. on Networking*, vol. 3, No. 3, June 1995.

[47] A. W. Naylor and G. R. Sell, *Linear Operator Theory in Engineering and Science*, page 352 to 360, Springer-Verlag 2000.

[48] R. Sampaio-Neto and R. A. Scholtz, "Precorrelation Filter Design for Spread-Spectrum Code Tracking in Interference", *IEEE J. Select. Areas Commun.*, vol. SAC-3, No. 5, Sept. 85.

[49] J. R. Norton and J. M. Cloeren, "Brief History of the Development of Ultra-Precise Oscillators for Ground and Space Applications", *Proc. IEEE International Frequency Control Symposium*, 1996.

[50] R. L. Peterson, R.E. Ziener and D. E. Broth, *Introduction to Spread Spectrum Communications*, Chapters 4 and 5, Prentice Hall, 1995.

[51] B. Razavi, "A Study of Phase Noise in CMOS Oscillators", *IEEE Journal of Solid-State Circuits*, vol. 30, No. 3, March 1996.

[52] V. Rodoplu and T. H. Meng, "Minimum Energy Mobile Wireless Networks", *IEEE J. Select. Areas Commun.*, vol. 17, No. 8, Aug. 1999.

[53] J. E. Rustad, R. Skaug and A. Aasen, "New Radio Netwroks for Tactical Communication", *IEEE J. Select. Areas Commun*., vol. 8, No. 5, June 1990.

[54] R. A. Scholtz, "Multiple Access with Time-Hoppng Impulse Modulation", *Proc. MILCOM*, 1993.

[55] M. L. Sichitiu and C. Veerarittiphan, "Simple, Accurate Time Synchronization for Wireless Sensor Networks", *Proc. WCNC*, 2003.

[56] F. Sivrikaya and B. Yener, "Time Synchronization in Sensor Networks: A Survey", *IEEE Network*, July/August 2004.

[57] M. I. Skolnik, *Introduction to Radar Systems*, 2nd Edition, McGraw-Hill, Chapters 10 and 11, 1980.

[58] D. B. Sullivan and J. Levine, "Time Generation and Distribution", *Proc. IEEE*, vol. 79, No. 7, July 1991.

[59] F. E. Terman, *Radio Engineers' Handbook*, page 78, 1st Edition, McGraw Hill, 1943.

[60] J. B. Tsui, *Fundamentals of Global Positioning System Receivers*, Wiley, 2nd Edition, 1995.

[61] D. Thirupathi and K. M. Chugg, "Symbol Synchronization in Coded UWB Systems using Adaptive Iterative Detection", *Proc. MILCOM*, 2004.

[62] H. L. Van Trees, *Detection, Estimation, and Modulation Theory - Part I*, Wiley, 1968.

[63] H. L. Van Trees, *Detection, Estimation, and Modulation Theory - Part III*, Wiley, 1968.

[64] S. Venkatraman, J. Caffery Jr. and H-R You, "Location Using LOS Range Estimation in NLOS Environments", *Proc. IEEE VTC*, 2002-Spring.

[65] J. R. Vig, "Introduction to Quartz Frequency Standards", *Technical Report SLCET-TR-92-1*, Army Research Laboratory, Electronics and Power Sources Directorate, October 1992. Available at http://www.ieee-uffc.org/freqcontrol/quartz/vig/vigtoc.htm.

[66] W. F. Walls and F. L. Walls, "Computation of Time-Domain Frequency Stability and Jitter from PM noise Measurement", *Proc. IEEE International Frequency Control Symposium and PDA Exhibition*, 2001.

[67] X. Wang, Z. Wang and B. O' Dea, "A TOA-Based Location Algorithm Reducing the Errors Due to Non-Line-Of-Sight (NLOS) Propagation", *IEEE Trans. on Vehicular Technology*, vol. 52, No. 1, Jan 2003.

[68] X. Wu, C. Ling and H. Xiang, "Despreading Chip Waveform Design for coherent delay-locked tracking in DS/SS systems", *Proc. ICC*, 2002.

[69] M. Z. Win and R. A. Scholtz, "On the Robustness of Ultra-Wide Bandwidth Signals in Dense Multipath Environments", *IEEE Comm. Letters*, vol. 2, No. 2, Feb 1998.

[70] M. Z. Win and R. A. Scholtz, "Ultra-Wide Bandwidth Time-Hopping Spread-Spectrum Impulse Radio for Wireless Multiple-Access Communications", *IEEE Trans. on Commun.*, vol. 48, No. 4, April 2000.

[71] M. P. Wylie and J. Holtzman, "The Non-Line of Sight Problem in Mobile Location Estimation", *Proc. 5th IEEE International Conference on Universal Personal Communications*, 1996.

APPENDIX A

VARIANCE OF ESTIMATED DIFFERENCE IN INITIAL OFFSET BETWEEN MASTER AND SLAVE NODES

In this appendix, the variance of $d_{\delta}^{(m,s)} - \hat{d}_{\delta}^{(m,s)}$ between a pair of node, the master m and slave s, is evaluated for the time-transfer scheme introduced in section 3.1 (time-transfer scheme A). In this time-transfer scheme, each node transmits the frame-synchronization, uplink and downlink ranging pulses in contiguous frames. The error variances for the two other schemes (time-transfer schemes B and C) introduced in section 3.4 can be evaluated similarly.

To evaluate $\hat{d}_{\delta}^{(m,s)} = \sum_{k'=0}^{K-1} -\vartheta^{(m,s)}(k')/K$ of (3.24a), from (3.22)

$$\begin{aligned}\vartheta^{(m,s)}(k') &= \frac{\zeta_{DN}^{(m,s)} - 2\zeta_{SY}^{(m,s)}}{2} - \varepsilon_{\gamma_{LS}}^{(m,s)} \cdot \left(\theta(k') - K_{ST}\right) + \frac{\varepsilon_{DN(z)}^{(m,s)} - 2\varepsilon_{SY}^{(m,s)}}{2} \\ &= \frac{\zeta_{DN}^{(m,s)} - 2\zeta_{SY}^{(m,s)}}{2} - \varepsilon_{\gamma_{LS}}^{(m,s)} \cdot \left(\frac{(N-1)K - 2k'}{2} - K_{ST}\right) + \frac{\varepsilon_{DN(z)}^{(m,s)} - 2\varepsilon_{SY}^{(m,s)}}{2} .\end{aligned}$$

Therefore

$$\begin{aligned}\hat{d}_{\delta}^{(m,s)} &= \frac{1}{K}\sum_{k'=0}^{K-1} \frac{2\zeta_{SY}^{(m,s)} - \zeta_{DN}^{(m,s)}}{2} + \varepsilon_{\gamma_{LS}}^{(m,s)} \cdot \left(\theta(k') - K_{ST}\right) - \frac{\varepsilon_{DN(z)}^{(m,s)} - 2\varepsilon_{SY}^{(m,s)}}{2} \\ &= \frac{1}{K}\sum_{k'=0}^{K-1}\left(\frac{2\zeta_{SY}^{(m,s)} - \zeta_{DN}^{(m,s)}}{2} + \varepsilon_{\gamma_{LS}}^{(m,s)} \cdot \left(\frac{(N-1)K - 2k'}{2} - K_{St}\right) - \frac{\varepsilon_{DN(z)}^{(m,s)} - 2\varepsilon_{SY}^{(m,s)}}{2}\right) ,\end{aligned}$$

where $\theta(k')$, $k' \in \{0,1,...,K-1\}$ is the characteristic function of the time-transfer scheme. For notation simplicity, we let

$$\zeta = -(\zeta_{DN}^{(m,s)}/2 - \zeta_{SY}^{(m,s)}) = d_{\delta}^{(m,s)} + \tilde{\rho}_{m,s} , \tag{A.1}$$

$$\varepsilon_{\gamma} = \varepsilon_{\gamma_{LS}}^{(m,s)} , \tag{A.2}$$

$$\varepsilon_{n} = (2\varepsilon_{SY}^{(m,s)} - \varepsilon_{DN(z)}^{(m,s)})/2 , \tag{A.3}$$

$$\begin{aligned}\theta'(k) &= (z-q-2k')/2-K_{ST}\\ &= ((N-1)K-2k')/2-K_{ST}\\ &= (z-q-2k)/2\end{aligned} \tag{A.4}$$

where ε_γ and ε_n are random variables and K_{ST} indicates the first time index of the K measurements to be used to estimate the difference in initial offset. In (A.4), we have let $k=k'+K_{ST}$ and, by change of variable, the limit of summation becomes $k=K_{ST}$ to $k=K+K_{ST}-1$, then

$$\begin{aligned}\mathbf{V}\{\hat{d}_\delta^{(m,s)}\} &= \mathbf{E}\left\{\left(\frac{\sum_k -\vartheta^{(m,s)}(k)}{K}\right)^2\right\}-\left(\mathbf{E}\left\{\frac{\sum_k -\vartheta^{(m,s)}(k)}{K}\right\}\right)^2\\ &= \mathbf{E}\left\{\left(\frac{\sum_k (\zeta+\varepsilon_\gamma\cdot\theta'(k)+\varepsilon_n)}{K}\right)^2\right\}-\left(\mathbf{E}\left\{\frac{\sum_k (\zeta+\varepsilon_\gamma\cdot\theta'(k)+\varepsilon_n)}{K}\right\}\right)^2.\end{aligned} \tag{A.5}$$

Consider the first term on the right-hand-side of (A.5), noting that $\mathbf{E}\{\varepsilon_n\}=0$, $\mathbf{E}\{\varepsilon_\gamma\}=0$, $\sum_k 1=K$, $\sum_k\sum_z 1=K^2$ and $\sum_{k=K_{ST}}^{K+K_{ST}-1} k=\frac{K}{2}(K+2K_{ST}-1)$, we have

$$\begin{aligned}&\mathbf{E}\left\{\left(\sum_k(\zeta+\varepsilon_\gamma\cdot\theta'(k)+\varepsilon_n)\right)^2\right\}\\ &=\mathbf{E}\left\{\zeta^2\sum_k\sum_z 1+(\varepsilon_\gamma)^2\sum_k\sum_z\theta'(k)\cdot\theta'(z)+\sum_k\sum_z\varepsilon_n\varepsilon_n+\zeta\varepsilon_\gamma\sum_k\sum_z\theta'(z)+\sum_k\zeta\sum_z\varepsilon_n\right.\\ &\left.+\sum_k\varepsilon_\gamma\theta'(k)\sum_z\zeta+\sum_k\varepsilon_\gamma\theta'(k)\sum_z\varepsilon_n+\sum_z\zeta\sum_k\varepsilon_n+\sum_z\varepsilon_\gamma\theta'(z)\sum_k\varepsilon_n\right\}\\ &=\zeta^2K^2+\mathbf{E}\{\varepsilon_\gamma^2\}\sum_k\sum_z\theta'(k)\theta'(z)+\sum_k\sum_z\mathbf{E}\{\varepsilon_n\varepsilon_n\}+2\zeta\cdot\mathbf{E}\{\varepsilon_\gamma\}K\sum_z\theta'(z)+2\sum_k\theta'(k)\sum_z\mathbf{E}\{\varepsilon_\gamma\varepsilon_n\}.\end{aligned} \tag{A.6}$$

The second term on the right-hand-side of (A.5) is

$$\begin{aligned}\left(\sum_k\left(\zeta+\mathbf{E}\{\varepsilon_\gamma\}\theta'(k)+\mathbf{E}\{\varepsilon_n\}\right)\right)^2 &= \left(\sum_k(\zeta)\right)^2\\ &= K^2\zeta^2.\end{aligned} \tag{A.7}$$

Therefore, the error variance becomes

$$\begin{aligned}\mathbf{V}\{\hat{d}_{\delta}^{(m,s)}\} &= \frac{\mathbf{V}\{\varepsilon_{\gamma}\}\sum_{k}\sum_{k'}\theta'(k)\theta'(k')+\sum_{k}\sum_{k'}\mathbf{E}\{\varepsilon_n\varepsilon_n\}+2\sum_{k}\theta'(k)\sum_{k'}\mathbf{E}\{\varepsilon_{\gamma}\varepsilon_n\}}{K^2} \\ &= \frac{\sum_{k}\sum_{k'}\theta'(k)\theta'(k')}{K^2}\cdot\mathbf{V}\{\varepsilon_{\gamma_{LS}}^{(m,s)}\} \\ &\quad - \frac{2\sum_{k}\theta'(k)\sum_{k'}\mathbf{E}\{\varepsilon_{\gamma_{LS}}^{(m,s)}\cdot(\varepsilon_{DN(z)}^{(m,s)}-2\varepsilon_{SY}^{(m,s)})/2\}}{K^2} \\ &\quad + \frac{\sum_{k}\sum_{k'}\mathbf{E}\{(\varepsilon_{DN(z)}^{(m,s)}-2\varepsilon_{SY}^{(m,s)})\cdot(\varepsilon_{DN(z)}^{(m,s)}-2\varepsilon_{SY}^{(m,s)})\}}{4K^2} \quad . \end{aligned} \tag{A.8}$$

Simplifying,

$$\begin{aligned}\mathbf{V}\{\hat{d}_{\delta}^{(m,s)}\} &= \frac{\sum_{k}\sum_{k'}\theta'(k)\theta'(k')}{K^2}\cdot\mathbf{V}\{\varepsilon_{\gamma_{LS}}^{(m,s)}\}+\frac{\sum_{k}((N-1)K-2k)\sum_{k'}\mathbf{E}\{\varepsilon_{\gamma_{LS}}^{(m,s)}\varepsilon_{SY}^{(m,s)}\}}{K^2} \\ &\quad + \frac{\sum_{k}\mathbf{E}\{(\varepsilon_{DN(z)}^{(m,s)})^2\}+4\mathbf{E}\{(\varepsilon_{SY}^{(m,s)})^2\}}{4K^2} \\ &= \frac{\sum_{k}\sum_{k'}\theta'(k)\theta'(k')}{K^2}\cdot\mathbf{V}\{\varepsilon_{\gamma_{LS}}^{(m,s)}\}+\frac{(N-1)K\sum_{k}\sum_{k'}\mathbf{E}\{\varepsilon_{\gamma_{LS}}^{(m,s)}\varepsilon_{SY}^{(m,s)}\}}{K^2}-\frac{2\sum_{k}k\sum_{k'}\mathbf{E}\{\varepsilon_{\gamma_{LS}}^{(m,s)}\varepsilon_{SY}^{(m,s)}\}}{K^2} \\ &\quad + \frac{\mathbf{E}\{(\varepsilon_{DN(z)}^{(m,s)})^2\}+4\mathbf{E}\{(\varepsilon_{SY}^{(m,s)})^2\}}{4K} \\ &= \frac{\sum_{k}\sum_{k'}\theta'(k)\theta'(k')}{K^2}\cdot\mathbf{V}\{\varepsilon_{\gamma_{LS}}^{(m,s)}\}+(N-1)\sum_{k'}\mathbf{E}\{\varepsilon_{\gamma_{LS}}^{(m,s)}\varepsilon_{SY}^{(m,s)}\}-\frac{2\sum_{k}k\sum_{k'}\mathbf{E}\{\varepsilon_{\gamma_{LS}}^{(m,s)}\varepsilon_{SY}^{(m,s)}\}}{K^2} \\ &\quad + \frac{5\sigma_x^2(m,s)+\sigma_x^2(s,m)}{4K} \\ &= \frac{\sum_{k}\sum_{k'}\theta'(k)\theta'(k')}{K^2}\cdot\mathbf{V}\{\varepsilon_{\gamma_{LS}}^{(m,s)}\}+\left(\frac{-K(K+2K_{ST}-1)+(N-1)K^2}{K^2}\right)\cdot\sum_{k'}\mathbf{E}\{\varepsilon_{\gamma_{LS}}^{(m,s)}\varepsilon_{SY}^{(m,s)}\} \\ &\quad + \frac{5\sigma_x^2(m,s)+\sigma_x^2(s,m)}{4K} \\ &= \frac{\sum_{k}\sum_{k'}\theta'(k)\theta'(k')}{K^2}\cdot\mathbf{V}\{\varepsilon_{\gamma_{LS}}^{(m,s)}\}+\left(\frac{NK^2-2K^2+K-2K\cdot K_{ST}}{K^2}\right)\cdot\sum_{k'}\mathbf{E}\{\varepsilon_{\gamma_{LS}}^{(m,s)}\varepsilon_{SY}^{(m,s)}\} \\ &\quad + \frac{5\sigma_x^2(m,s)+\sigma_x^2(s,m)}{4K} \quad , \end{aligned} \tag{A.9}$$

where $\mathbf{V}\{\varepsilon_{SY}^{(m,s)}\}=\sigma_x^2(m,s)$ and $\mathbf{V}\{\varepsilon_{DN(z)}^{(m,s)}\}=\sigma_x^2(m,s)+\sigma_x^2(s,m)$. The coefficient, $\sum_{k}\sum_{k'}\theta'(k)\theta'(k')$ of the first term on the right-hand-side of (A.9) is expressed as

$$\begin{aligned}\sum_k\sum_{k'}\theta'(k)\theta'(k') &= \left(\sum_k \frac{(N-1)K-2k}{2}\right)\cdot\left(\sum_{k'}\frac{(N-1)K-2k'}{2}\right)\\ &= \frac{1}{4}\sum_k\sum_{k'}\left((N-1)^2K^2+4kk'-2k(N-1)K-2k'(N-1)K\right)\\ &= \frac{(N-1)^2K^4}{4}+\left(\sum_{k=K_{ST}}^{K+K_{ST}-1}k\right)^2-(N-1)K^2\sum_{k=K_{ST}}^{K+K_{ST}-1}k\\ &= \frac{(N-1)^2K^4}{4}+\left(\frac{K}{2}(K+2K_{ST}-1)\right)^2-(N-1)K^2\left(\frac{K}{2}(K+2K_{ST}-1)\right). \qquad \text{(A.10)}\end{aligned}$$

To evaluate the cross-correlation, $\sum_{k=K_{ST}}^{K+K_{ST}-1}\mathbf{E}\{\varepsilon_{\gamma_{LS}}^{(m,s)}\cdot\varepsilon_{SY}^{(m,s)}\}$ in the second term on the right-hand-side of (A.9), we make use of (2.45c) , which is

$$\varepsilon_{\gamma_{LS}}^{(m,s)}=\frac{12}{K(K^2-1)\cdot\Delta_{LS}}\sum_{k=K_{ST}}^{K+K_{ST}-1}k\cdot\varepsilon_{SY}^{(m,s)}-\frac{6(K+2K_{ST}-1)}{K(K^2-1)\cdot\Delta_{LS}}\sum_{k=K_{ST}}^{K+K_{ST}-1}\varepsilon_{SY}^{(m,s)}\ .$$

This leads to

$$\begin{aligned}\mathbf{E}\{\varepsilon_{\gamma_{LS}}^{(m,s)}\cdot\varepsilon_{SY}^{(m,s)}\} &= \frac{12}{K\cdot(K^2-1)\cdot\Delta_{LS}}\sum_{k=K_{ST}}^{K+K_{ST}-1}k\cdot\mathbf{E}\{\varepsilon_{SY}^{(m,s)}\cdot\varepsilon_{SY}^{(m,s)}\}-\frac{6(K+2K_{ST}-1)}{K(K^2-1)\cdot\Delta_{LS}}\sum_{k=K_{ST}}^{K+K_{ST}-1}\mathbf{E}\{\varepsilon_{SY}^{(m,s)}\cdot\varepsilon_{SY}^{(m,s)}\}\\ &= \frac{12}{K\cdot(K^2-1)\cdot\Delta_{LS}}\cdot k\cdot\mathbf{E}\{\varepsilon_{SY}^{(m,s)}\cdot\varepsilon_{SY}^{(m,s)}\}-\frac{6(K+2K_{ST}-1)}{K(K^2-1)\cdot\Delta_{LS}}\cdot\mathbf{E}\{\varepsilon_{SY}^{(m,s)}\cdot\varepsilon_{SY}^{(m,s)}\}\\ &= \frac{12\cdot k\cdot\sigma_x^2(m,s)}{K\cdot(K^2-1)\cdot\Delta_{LS}}-\frac{6\cdot(K+2K_{ST}-1)\cdot\sigma_x^2(m,s)}{K\cdot(K^2-1)\cdot\Delta_{LS}}\ . \qquad \text{(A.11)}\end{aligned}$$

As a result,

$$\begin{aligned}\sum_{k=K_{ST}}^{K+K_{ST}-1}\mathbf{E}\{\varepsilon_{\gamma_{LS}}^{(m,s)}\cdot\varepsilon_{SY}^{(m,s)}\} &= \sum_{k=K_{ST}}^{K+K_{ST}-1}\frac{12\cdot k\cdot\sigma_x^2(m,s)}{K(K^2-1)\cdot\Delta_{LS}}-\frac{6\cdot(K+2K_{ST}-1)\cdot\sigma_x^2(m,s)}{K(K^2-1)\cdot\Delta_{LS}}\\ &= \frac{12\cdot\sigma_x^2(m,s)}{K(K^2-1)\cdot\Delta_{LS}}\cdot\left(\frac{K}{2}\cdot(K+2K_{ST}-1)\right)-\frac{6\cdot(K+2K_{ST}-1)\cdot\sigma_x^2(m,s)\cdot K}{K(K^2-1)\cdot\Delta_{LS}}\\ &= \frac{6\cdot\sigma_x^2(m,s)\cdot(K+2K_{ST}-1)}{(K^2-1)\cdot\Delta_{LS}}-\frac{6\cdot(K+2K_{ST}-1)\cdot\sigma_x^2(m,s)}{(K^2-1)\cdot\Delta_{LS}}\\ &= 0\ . \qquad \text{(A.12)}\end{aligned}$$

Thus the sum of the cross-correlation $\sum_k\mathbf{E}\{\varepsilon_{\gamma_{LS}}^{(m,s)}\cdot\varepsilon_{SY}^{(m,s)}\}$ is zero. This allows us to express $\mathbf{V}\{\hat{d}_{\delta}^{(m,s)}\}$ as

$$\begin{aligned}
\mathbf{V}\{\hat{d}_{\delta}^{(m,s)}\} &= \frac{\left(\sum_k \theta'(k)\right)^2}{K^2}\cdot \mathbf{V}\{\varepsilon_{\gamma_{LS}}^{(m,s)}\} + \frac{5\sigma_x^2(m,s)+\sigma_x^2(s,m)}{4K} \\
&= \frac{(N-1)^2\cdot K^2\cdot \mathbf{V}\{\varepsilon_{\gamma_{LS}}^{(m,s)}\}}{4} + \frac{\mathbf{V}\{\varepsilon_{\gamma_{LS}}^{(m,s)}\}}{K^2}\left(\frac{K}{2}(K+2K_{ST}-1)\right)^2 \\
&\quad -(N-1)\cdot \mathbf{V}\{\varepsilon_{\gamma_{LS}}^{(m,s)}\}\left(\frac{K}{2}(K+2K_{ST}-1)\right) + \frac{5\sigma_x^2(m,s)+\sigma_x^2(s,m)}{4K} \\
&= \mathbf{V}\{\varepsilon_{\gamma_{LS}}^{(m,s)}\}\left(\frac{(N-1)^2\cdot K^2}{4} + \frac{(K+2K_{ST}-1)^2}{4} - \frac{(N-1)\cdot K\cdot(K+2K_{ST}-1)}{2}\right) \\
&\quad + \frac{5\sigma_x^2(m,s)+\sigma_x^2(s,m)}{4K} \\
&= \frac{12\sigma_x^2(m,s)}{K^3}\left(\frac{(N-1)^2K^2+(K+2K_{ST}-1)\cdot(K+2K_{ST}-1-2(N-1)K)}{4}\right) \\
&\quad + \frac{5\sigma_x^2(m,s)+\sigma_x^2(s,m)}{4K} \\
&= \frac{12\sigma_x^2(m,s)}{K^3}\left(\frac{(N-1)^2K^2+(K+2K_{ST}-1)\cdot(2K_{ST}-1-2NK+3K)}{4}\right) \\
&\quad + \frac{5\sigma_x^2(m,s)+\sigma_x^2(s,m)}{4K}.
\end{aligned} \tag{A.13}$$

And the variance of the estimated difference in initial offset $\hat{d}_{\delta}^{(m,s)}$ between m and slave s is

$$\mathbf{V}\{\hat{d}_{\delta}^{(m,s)}\} = \frac{3\sigma_x^2(m,s)}{K}\cdot\left((N-1)^2 + \frac{(K+2K_{ST}-1)\cdot(2K_{ST}-1-2NK+3K)}{K^2}\right) + \frac{5\sigma_x^2(m,s)+\sigma_x^2(s,m)}{4K}. \tag{A.14}$$

If $K_{ST}=0$,

$$\mathbf{V}\{\hat{d}_{\delta}^{(m,s)}\} = \frac{3\sigma_x^2(m,s)}{K}\cdot\left((N-1)^2 + \frac{(K-1)\cdot(3K-2NK-1)}{K^2}\right) + \frac{5\sigma_x^2(m,s)+\sigma_x^2(s,m)}{4K}. \tag{A.15}$$

The normalized variance $\mathbf{V}\{\hat{d}_{\delta}^{(m,s)}\}/\sigma_x^2(m,s)$ is plotted in Figure A.1 for the case $\rho_{m,s}=\rho_{s,m}$, i.e.,

$$\sigma_x^2(m,s)=\sigma_x^2(s,m). \tag{A.16}$$

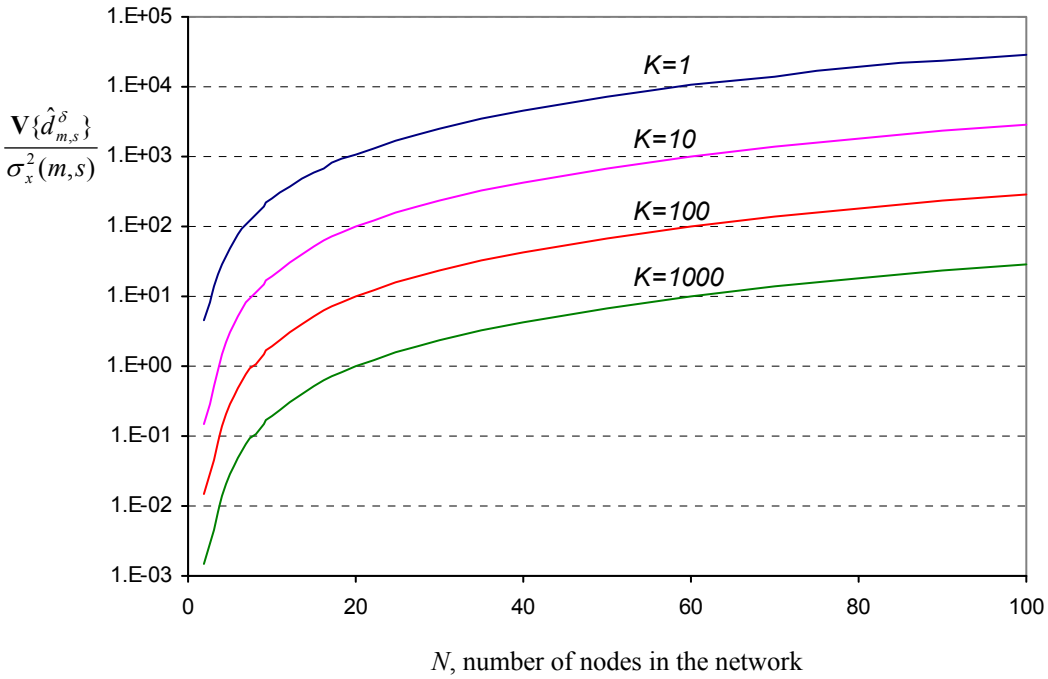

Figure A.1: The normalized variance of the estimated difference in initial offset between two nodes in a network of N nodes utilizing time-transfer scheme A. In this case, $\rho_{m,s} = \rho_{s,m}$.

APPENDIX B

VARIANCE OF TIMING ERRORS

The timing error between nodes m and s at time t' after time transfer is defined as

$$t_{(k')}^{(m)} - t_{(k')}^{(s)} = a_1^{(m)} t' + d^{(m)} + \phi_{(k')}^{(m)} - a_1^{(s)} t' - d^{(s)} - \phi_{(k')}^{(s)}, \tag{B.1}$$

where $t' = k' T_f$.

B.1 Hierarchical Master-slave Timing Error

In this section, the timing errors after time synchronization using single-master-to-multiple-slaves (SM) and hierarchical master-slaves (HM) time-transfer architectures are presented. In this analysis, the variance of the timing error is defined as

$$\mathbf{V}\{t_{(k')}^{(1)} - \tilde{t}_{HM(k')}^{(s)}\} = \mathbf{V}\{a_1^{(1)} t' + d^{(1)} - \tilde{a}_{HM}^{(s)} t' - \tilde{d}_{HM}^{(s)}\} + 2\sigma_\phi^2, \ \forall s, \ s \neq 1, \tag{B.2}$$

where $a_1^{(1)}$ and $d^{(1)}$ are the drift and initial offset of the lead master node, and $\tilde{a}_{HM}^{(s)}$, $\tilde{d}_{HM}^{(s)}$, $\tilde{t}_{HM(k')}^{(s)}$ are the "settled" drift, initial offset and timing of node s after HM time transfer.

Let $\mathbf{M}$ be an ordered set whose elements are the node label of the roving masters. The elements in the set are arranged according to the order at which node takes turn to be the roving master. The element of $\mathbf{M}$ is denoted as $\mathbf{M}(q)$ where $q = 0,...,|\mathbf{M}|-1$ and $\mathbf{M}(0) = 1$ is the lead master node. If Q is the number of hops from lead master to roving master node m', from which node s acquires its timing, then $\mathbf{M}(Q) = m'$. From section 4.3, the settled initial offset at node s after HM time-transfer is given by

$$\tilde{d}_{HM}^{(s)} = d^{(1)} + \varepsilon_{\hat{d}}^{(\mathbf{M}(Q),s)} + \tilde{\rho}_{\mathbf{M}(Q),s} + \sum_{\substack{q=1 \\ \mathbf{M}(q) \neq s}}^{Q} \varepsilon_{\hat{d}}^{(\mathbf{M}(q-1),\mathbf{M}(q))} + \tilde{\rho}_{\mathbf{M}(q-1),\mathbf{M}(q)}, \tag{B.3}$$

and the frame repetition rate $(= \tilde{a}_{HM}^{(s)} T_f)$, is

$$\widetilde{a}_{HM}^{(s)} T_f = a_1^{(1)} T_f + \varepsilon_{\gamma_{LS}}^{(\mathbf{M}(Q),s)} + \sum_{\substack{q=1 \\ \mathbf{M}(q)\neq s}}^{Q} \varepsilon_{\gamma_{LS}}^{(\mathbf{M}(q-1),\mathbf{M}(q))} , \tag{B.4}$$

for $s \neq 1$. The difference in initial offset, $d_{\delta}^{(m,s)}$ between two nodes m and s is estimated by the sample mean of $\{\vartheta^{(m,s)}(k)\}_{k=0}^{K-1}$ over K frames. From Chapter 3, this estimate is

$$\hat{d}_{\delta}^{(m,s)} = \sum_{k=0}^{K-1} (-\vartheta^{(m,s)}(k))/K , \tag{B.5}$$

and (3.23) states that $\vartheta^{(m,s)}(k) = -d_{\delta}^{(m,s)} - \widetilde{\rho}_{m,s} + (\theta(k) - K_{ST}) \cdot (a_{\delta}^{(m,s)} T_f - \hat{\gamma}_{LS}^{(m,s)}) + \varepsilon_{\vartheta}^{(m,s)}$, and $\theta(k)$ is the characteristic function of the time-transfer scheme. For $i = j$, then

$$\begin{aligned} \hat{d}_{\delta}^{(m,s)} &= \frac{1}{K} \sum_{k=0}^{K-1} d_{\delta}^{(m,s)} + \widetilde{\rho}_{m,s} + (\theta(k) - K_{ST}) \cdot \varepsilon_{\gamma_{LS}}^{(m,s)} - \varepsilon_{\vartheta}^{(m,s)} \\ &= d_{\delta}^{(m,s)} + \widetilde{\rho}_{m,s} + \frac{1}{K} \varepsilon_{\gamma_{LS}}^{(m,s)} \sum_{k=0}^{K-1} (\theta(k) - K_{ST}) - \frac{1}{K} \sum_{k=0}^{K-1} \varepsilon_{\vartheta}^{(m,s)} . \end{aligned} \tag{B.6}$$

Therefore

$$\begin{aligned} \widetilde{d}_{HM}^{(s)} &= d^{(s)} + \hat{d}_{\delta}^{(m,s)} \\ &= d^{(m)} + \widetilde{\rho}_{m,s} + \varepsilon_{\hat{d}}^{(m,s)} , \end{aligned} \tag{B.7}$$

where

$$\varepsilon_{\hat{d}}^{(m,s)} = \frac{1}{K} \varepsilon_{\gamma_{LS}}^{(m,s)} \sum_{k=0}^{K-1} (\theta(k) - K_{ST}) - \frac{1}{K} \sum_{k=K_{ST}}^{K+K_{ST}-1} \varepsilon_{\vartheta}^{(m,s)} . \tag{B.8}$$

Similarly,

$$\widetilde{a}_{HM}^{(s)} T_f = a_1^{(s)} T_f + \hat{\gamma}_{LS}^{(m,s)} , \tag{B.9}$$

where $\gamma^{(m,s)} - \hat{\gamma}_{LS}^{(m,s)} = -\varepsilon_{\gamma_{LS}}^{(m,s)}$ and

$$\mathbf{V}\{\gamma^{(m,s)} - \hat{\gamma}_{LS}^{(m,s)}\} = \mathbf{V}\{\varepsilon_{\gamma_{LS}}^{(m,s)}\} . \tag{B.10}$$

Substituting (B.3) and (B.4) into (B.2) and takes the expectation square, leads to

$$
\begin{aligned}
&\mathbf{E}\left\{\left(t_{(k')}^{(1)}-\tilde{t}_{HM(k')}^{(s)}\right)^2\right\}\\
&=\mathbf{E}\left\{\left(\left(\tilde{a}_{HM}^{(s)}-a_1^{(1)}\right)\cdot t'+\tilde{d}_{HM}^{(s)}-d^{(1)}\right)^2\right\}+2\sigma_\phi^2\\
&=\mathbf{E}\left\{\left(\tilde{a}_{HM}^{(s)}-a_1^{(1)}\right)^2\cdot(t')^2+(\tilde{d}_{HM}^{(s)}-d^{(1)})^2+2\right\}+2\sigma_\phi^2\\
&=\mathbf{V}\{\tilde{a}_{HM}^{(s)}-a_1^{(1)}\}\cdot(t')^2+\mathbf{V}\{\tilde{d}_{HM}^{(s)}-d^{(1)}\}+2\sigma_\phi^2+(\mathbf{E}\{\tilde{d}_{HM}^{(s)}-d^{(1)}\})^2\\
&\quad+2\cdot\mathbf{E}\left\{\left(\varepsilon_{\gamma_{LS}}^{(\mathbf{M}(Q),s)}+\sum_{\substack{q=1\\ \mathbf{M}(q)\neq s}}^{Q}\varepsilon_{\gamma_{LS}}^{(\mathbf{M}(q-1),\mathbf{M}(q))}\right)\cdot\left(\varepsilon_{\hat{d}}^{(\mathbf{M}(Q),s)}+\sum_{\substack{q=1\\ \mathbf{M}(q)\neq s}}^{Q}\varepsilon_{\hat{d}}^{(\mathbf{M}(q-1),\mathbf{M}(q))}+\tilde{\rho}_{\mathbf{M}(q-1),\mathbf{M}(q)}\right)\cdot\frac{t'}{T_f}\right\}\\
&=\mathbf{V}\{a_1^{(1)}-\tilde{a}_{HM}^{(s)}\}\cdot(t')^2+\mathbf{V}\{d^{(1)}-\tilde{d}_{HM}^{(s)}\}+\left(\tilde{\rho}_{\mathbf{M}(Q),s}+\sum_{\substack{q=1\\ \mathbf{M}(q)\neq s}}^{Q}\tilde{\rho}_{\mathbf{M}(q-1),\mathbf{M}(q)}\right)^2\\
&\quad+2\cdot\mathbf{E}\left\{\varepsilon_{\gamma_{LS}}^{(\mathbf{M}(Q),s)}\cdot\varepsilon_{\hat{d}}^{(\mathbf{M}(Q),s)}\right\}\cdot\frac{t'}{T_f}+2\cdot\sum_{\substack{q=1\\ \mathbf{M}(q)\neq s}}^{Q}\left(\sum_{\substack{q'=1\\ \mathbf{M}(q')\neq s}}^{Q}\mathbf{E}\left\{\varepsilon_{\gamma_{LS}}^{(\mathbf{M}(q-1),\mathbf{M}(q))}\cdot\varepsilon_{\hat{d}}^{(\mathbf{M}(q'-1),\mathbf{M}(q'))}\right\}\right)\cdot\frac{t'}{T_f}+2\sigma_\phi^2\\
&=\mathbf{V}\{a_1^{(1)}-\tilde{a}_{HM}^{(s)}\}\cdot(t')^2+\mathbf{V}\{d^{(1)}-\tilde{d}_{HM}^{(s)}\}+\left(\tilde{\rho}_{\mathbf{M}(Q),s}+\sum_{\substack{q=1\\ \mathbf{M}(q)\neq s}}^{Q}\tilde{\rho}_{\mathbf{M}(q-1),\mathbf{M}(q)}\right)^2\\
&\quad+2\cdot\mathbf{E}\left\{\varepsilon_{\gamma_{LS}}^{(\mathbf{M}(Q),s)}\cdot\varepsilon_{\hat{d}}^{(\mathbf{M}(Q),s)}\right\}\cdot\frac{t'}{T_f}+2\cdot\sum_{\substack{q=1\\ \mathbf{M}(q)\neq s}}^{Q}\mathbf{E}\left\{\varepsilon_{\gamma_{LS}}^{(\mathbf{M}(q-1),\mathbf{M}(q))}\cdot\varepsilon_{\hat{d}}^{(\mathbf{M}(q-1),\mathbf{M}(q))}\right\}\cdot\frac{t'}{T_f}+2\sigma_\phi^2 \quad . \qquad \text{(B.11)}
\end{aligned}
$$

Substituting (B.8) into (B.11) and from Appendix A,

$$
\sum_{k=K_{ST}}^{K+K_{ST}-1}\mathbf{E}\{\varepsilon_{\vartheta}^{(m,s)}\cdot\varepsilon_{\gamma_{LS}}^{(m,s)}\}=\sum_{k=K_{ST}}^{K+K_{ST}-1}\mathbf{E}\{\varepsilon_{SY}^{(m,s)}\cdot\varepsilon_{\gamma_{LS}}^{(m,s)}\}=0\ . \qquad \text{(B.12)}
$$

Therefore the cross-correlation term $\mathbf{E}\{\varepsilon_{\gamma_{LS}}^{(m,s)}\cdot\varepsilon_{\hat{d}}^{(m,s)}\}$ is

$$
\begin{aligned}
\mathbf{E}\left\{\varepsilon_{\gamma_{LS}}^{(m,s)}\cdot\varepsilon_{\hat{d}}^{(m,s)}\right\}&=\frac{1}{K}\mathbf{E}\left\{\varepsilon_{\gamma_{LS}}^{(m,s)}\cdot\varepsilon_{\gamma_{LS}}^{(m,s)}\sum_{k=0}^{K-1}(\theta(k)-K_{ST})\right\}\\
&=\frac{1}{K}\mathbf{V}\{\varepsilon_{\gamma_{LS}}^{(m,s)}\}\cdot\sum_{k=0}^{K-1}(\theta(k)-K_{ST})\ . \qquad \text{(B.13)}
\end{aligned}
$$

The variable K_{ST} is replaced with $(2N-1)KQ$ for the time transfer from the roving master, denoted by $\mathbf{M}(Q)$, to slave s. When timing is transferred from one roving master to another starting from the lead master $\mathbf{M}(0)=1$ to another roving master node denoted by $\mathbf{M}(q)$, $q>0$, then $K_{ST}=(2N-1)K(q-1)$ and (B.11) reduces to

$$\mathbf{E}\left\{\left(t_{(k')}^{(1)}-\widetilde{t}_{HM(k')}^{(s)}\right)^2\right\}=\mathbf{V}\{a_1^{(1)}-\widetilde{a}_{HM}^{(s)}\}\cdot(t')^2+\mathbf{V}\{d^{(1)}-\widetilde{d}_{HM}^{(s)}\}$$
$$+\left(\widetilde{\rho}_{\mathbf{M}(Q),s}+\sum_{\substack{q=1\\ \mathbf{M}(q)\neq s}}^{Q}\widetilde{\rho}_{\mathbf{M}(q-1),\mathbf{M}(q)}\right)^2$$
$$+2\cdot\mathbf{E}\{\varepsilon_{\gamma_{LS}}^{(\mathbf{M}(Q),s)}\cdot\varepsilon_{\hat{d}}^{(\mathbf{M}(Q),s)}\}\cdot t'/T_f+2\cdot\sum_{\substack{q=1\\ \mathbf{M}(q)\neq s}}^{Q}\mathbf{E}\{\varepsilon_{\gamma_{LS}}^{(\mathbf{M}(q-1),\mathbf{M}(q))}\cdot\varepsilon_{\hat{d}}^{(\mathbf{M}(q-1),\mathbf{M}(q))}\}\cdot t'/T_f$$
$$+2\sigma_{\phi}^2\ . \tag{B.14}$$

At the end of the hierarchical master-slave time-transfer, i.e., $|\mathbf{M}|$ number of nodes have being the roving master, then $t'=(2N-1)\cdot K\cdot|\mathbf{M}|$.

B.2 Mutually Synchronous Timing Error

In this section, the timing variance after mutually synchronous time-transfer is presented. Note that instead of measuring the difference in timing between node s with respect to a lead master node, the mean (average) of the sample variance of all nodes in the network after time transfer is of interest. From (4.10) and (4.17),

$$\widetilde{a}_{MU}^{(s)}T_f=a_1^{(1)}T_f+\sum_{n=1}^{N-1}\varepsilon_{\gamma_{LS}}^{(n,n+1)}+\varepsilon_{\gamma_{LS}}^{(N,s)}\ , \tag{B.15a}$$

$$\widetilde{d}_{MU}^{(s)}=d^{(s)}+\sum_{\substack{m=1\\ m\neq s}}^{N}\alpha_{m,s}\cdot\hat{d}_{\delta}^{(m,s)}$$
$$=\sum_{\substack{m=1\\ m\neq s}}^{N}\alpha_{m,s}\cdot(d^{(m)}+\widetilde{\rho}_{m,s})+\sum_{\substack{m=1\\ m\neq s}}^{N}\alpha_{m,s}\cdot\varepsilon_{\hat{d}}^{(m,s)}\ , \tag{B.15b}$$

where $\hat{d}_{\delta}^{(m,s)}=d_{\delta}^{(m,s)}+\widetilde{\rho}_{m,s}+\varepsilon_{\hat{d}}^{(m,s)}$ and $\hat{\gamma}_{LS}^{(m,s)}=\gamma_{LS}^{(m,s)}+\varepsilon_{\gamma_{LS}}^{(m,s)}$. For the above quantities, the variance across all nodes in the network is defined to be the sample variance. Then the mean of the variances of $\widetilde{a}_{MU}^{(s)}$, $\widetilde{d}_{MU}^{(s)}$ and $\widetilde{t}_{MU(k')}^{(s)}$ across all nodes in the network are defined as

$$\overline{\mathbf{V}\{\widetilde{a}_{MU}\}}=\mathbf{E}\left\{\frac{1}{N-1}\sum_{s=1}^{N}\left(\widetilde{a}_{MU}^{(s)}-\left(\frac{1}{N}\sum_{s=1}^{N}\widetilde{a}_{MU}^{(s)}\right)\right)^2\right\}, \tag{B.16a}$$

$$\overline{\mathbf{V}\{\widetilde{d}_{MU}\}}=\mathbf{E}\left\{\frac{1}{N-1}\sum_{s=1}^{N}\left(\widetilde{d}_{MU}^{(s)}-\left(\frac{1}{N}\sum_{s=1}^{N}\widetilde{d}_{MU}^{(s)}\right)\right)^2\right\}, \tag{B.16b}$$

$$\overline{\mathbf{V}\{\widetilde{t}_{MU(k')}\}}=\mathbf{E}\left\{\frac{1}{N-1}\sum_{s=1}^{N}\left(\widetilde{t}_{MU(k')}^{(s)}-\left(\frac{1}{N}\sum_{s=1}^{N}\widetilde{t}_{MU(k')}^{(s)}\right)\right)^2\right\}, \tag{B.16c}$$

where $\widetilde{a}_{MU}^{(s)}$, $\widetilde{d}_{MU}^{(s)}$ and $\widetilde{t}_{MU(k')}^{(s)}=\widetilde{a}_{MU}^{(s)}\cdot t'+\widetilde{d}_{MU}^{(s)}+\phi_{(k')}^{(s)}$ are the settled drift, initial offset and timing at node s after time synchronization using a MU time-transfer architecture. The oscillator timing jitter $\phi_{(k')}^{(s)}$ is assumed to be i.i.d. with zero mean and variance σ_{ϕ}^2.

To evaluate (B.16a), consider

$$\begin{aligned}
\mathbf{E}\left\{\left(\frac{1}{N}\sum_{s=1}^{N}\widetilde{a}_{MU}^{(s)}\cdot T_f\right)^2\right\}&=\frac{1}{N^2}\cdot\mathbf{E}\left\{\left(\sum_{s=1}^{N}(a_1^{(1)}\cdot T_f+\sum_{n=1}^{N\text{-}1}\varepsilon_{\gamma_{LS}}^{(n,n+1)}+\varepsilon_{\gamma_{LS}}^{(N,s)})\right)^2\right\}\\
&=\frac{1}{N^2}\cdot\mathbf{E}\left\{\left(\sum_{s=1}^{N}a_1^{(1)}T_f\right)^2+\left(\sum_{s=1}^{N}\sum_{n=1}^{N\text{-}1}\varepsilon_{\gamma_{LS}}^{(n,n+1)}\right)^2+\left(\sum_{s=1}^{N}\varepsilon_{\gamma_{LS}}^{(N,s)}\right)^2+2\sum_{s=1}^{N}\sum_{s'=1}^{N}\sum_{n=1}^{N\text{-}1}\varepsilon_{\gamma_{LS}}^{(n,n+1)}\cdot\varepsilon_{\gamma_{LS}}^{(N,s')}\right\}\\
&=(a_1^{(1)}T_f)^2+\frac{1}{N^2}\sum_{s=1}^{N}\mathbf{V}\{\varepsilon_{\gamma_{LS}}^{(N,s)}\}+\frac{1}{N^2}\sum_{s=1}^{N}\sum_{s'=1}^{N}\left(\sum_{n=1}^{N\text{-}1}\mathbf{V}\{\varepsilon_{\gamma_{LS}}^{(n,n+1)}\}\right)\\
&=(a_1^{(1)}T_f)^2+\sum_{n=1}^{N\text{-}1}\mathbf{V}\{\varepsilon_{\gamma_{LS}}^{(n,n+1)}\}+\frac{1}{N^2}\sum_{s=1}^{N}\mathbf{V}\{\varepsilon_{\gamma_{LS}}^{(N,s)}\}.
\end{aligned} \tag{B.17a}$$

Then

$$\overline{\mathbf{V}\{\widetilde{a}_{MU}\}}=\frac{1}{N}\cdot\sum_{s=1}^{N}\mathbf{E}\left\{\left(\varepsilon_{\gamma_{LS}}^{(N,s)}\right)^2\right\}/T_f^2\ . \tag{B.17b}$$

Similarly (B.16b) is evaluated as follows:

$$\begin{aligned}
\overline{\mathbf{V}\{\widetilde{d}_{MU}\}}&=\mathbf{E}\left\{\frac{1}{N-1}\sum_{s=1}^{N}\left(\widetilde{d}_{MU}^{(s)}-\sum_{s'=1}^{N}\widetilde{d}_{MU}^{(s')}/N\right)^2\right\}\\
&=\frac{1}{N-1}\mathbf{E}\left\{\sum_{s=1}^{N}\left(\left(\widetilde{d}_{MU}^{(s)}\right)^2+\frac{1}{N^2}\left(\sum_{s'=1}^{N}\widetilde{d}_{MU}^{(s')}\right)^2-\frac{2}{N}\sum_{s'=1}^{N}\widetilde{d}_{MU}^{(s)}\cdot\widetilde{d}_{MU}^{(s')}\right)\right\}\\
&=\frac{1}{N-1}\mathbf{E}\left\{\sum_{s=1}^{N}\left(\widetilde{d}_{MU}^{(s)}\right)^2+\frac{1}{N}\left(\sum_{s'=1}^{N}\widetilde{d}_{MU}^{(s')}\right)^2-\frac{2}{N}\left(\sum_{s'=1}^{N}\widetilde{d}_{MU}^{(s')}\right)^2\right\}\\
&=\frac{1}{N-1}\mathbf{E}\left\{\sum_{s=1}^{N}\left(\widetilde{d}_{MU}^{(s)}\right)^2-\frac{1}{N}\left(\sum_{s=1}^{N}\widetilde{d}_{MU}^{(s)}\right)^2\right\}\ .
\end{aligned} \tag{B.18a}$$

Taking expectation on the squared of $\sum_{s-1}^{N} d_{MU}^{(s)}$,

$$\mathbf{E}\left\{\left(\sum_{s=1}^{N}\widetilde{d}_{MU}^{(s)}\right)^2\right\}=\left(\sum_{s=1}^{N}\sum_{m=1.m\neq s}^{N}\alpha_{m,s}\cdot\left(d^{(m)}+\widetilde{\rho}_{m,s}\right)\right)^2+\mathbf{E}\left\{\left(\sum_{s=1}^{N}\sum_{m=1,m\neq s}^{N}\alpha_{m,s}\varepsilon_{\hat{d}}^{(m,s)}\right)^2\right\}$$

$$=\left(\sum_{s=1}^{N}\sum_{m=1.m\neq s}^{N}\alpha_{m,s}\cdot\left(d^{(m)}+\widetilde{\rho}_{m,s}\right)\right)^2+\sum_{s=1}^{N}\sum_{\substack{m=1\\m\neq s}}^{N}\alpha_{m,s}^2\mathbf{E}\left\{\left(\varepsilon_{\hat{d}}^{(m,s)}\right)^2\right\}. \qquad \text{(B.18b)}$$

and from (B.15b),

$$\mathbf{E}\left\{\left(\widetilde{d}_{MU}^{(s)}\right)^2\right\}=\left(\sum_{\substack{m=1,\\m\neq s}}^{N}\alpha_{m,s}\cdot(d^{(m)}+\widetilde{\rho}_{m,s})\right)^2+\mathbf{E}\left\{\left(\sum_{\substack{m=1,\\m\neq s}}^{N}\alpha_{m,s}\cdot\varepsilon_{\hat{d}}^{(m,s)}\right)^2\right\}$$

$$=\left(\sum_{\substack{m=1,\\m\neq s}}^{N}\alpha_{m,s}\cdot(d^{(m)}+\widetilde{\rho}_{m,s})\right)^2+\sum_{\substack{m=1,\\m\neq s}}^{N}\alpha_{m,s}^2\cdot\mathbf{E}\left\{\left(\varepsilon_{\hat{d}}^{(m,s)}\right)^2\right\}. \qquad \text{(B.18c)}$$

Since $\widetilde{d}_{MU}^{(s)}=\sum_{\substack{m=1\\m\neq s}}^{N}\alpha_{m,s}\cdot(d^{(m)}+\widetilde{\rho}_{m,s})+\sum_{\substack{m=1\\m\neq s}}^{N}\alpha_{m,s}\cdot\varepsilon_{\hat{d}}^{(m,s)}$, implies $\mathbf{V}\{\widetilde{d}_{MU}^{(s)}\}=\sum_{\substack{m=1,\\m\neq s}}^{N}\alpha_{m,s}^2\cdot\mathbf{V}\{\varepsilon_{\hat{d}}^{(m,s)}\}$ and $\varepsilon_{\hat{d}}^{(m,s)}$ has zero mean. Therefore

$$\overline{\mathbf{V}\{\widetilde{d}_{MU}\}}=\frac{1}{N}\sum_{s=1}^{N}\sum_{m=1,m\neq s}^{N}\alpha_{m,s}^2\mathbf{V}\{\varepsilon_{\hat{d}}^{(m,s)}\}+\frac{1}{N-1}\sum_{s=1}^{N}\left(\sum_{m=1.m\neq s}^{N}\alpha_{m,s}\cdot\left(d^{(m)}+\widetilde{\rho}_{m,s}\right)\right)^2$$

$$-\frac{1}{N\cdot(N-1)}\left(\sum_{s=1}^{N}\sum_{m=1.m\neq s}^{N}\alpha_{m,s}\cdot\left(d^{(m)}+\widetilde{\rho}_{m,s}\right)\right)^2$$

$$=\frac{1}{N}\sum_{s=1}^{N}\mathbf{V}\{\widetilde{d}_{MU}^{(s)}\}+\frac{1}{N-1}\sum_{s=1}^{N}\left(\sum_{m=1.m\neq s}^{N}\alpha_{m,s}\cdot\left(d^{(m)}+\widetilde{\rho}_{m,s}\right)\right)^2$$

$$-\frac{1}{N(N-1)}\left(\sum_{s=1}^{N}\sum_{m=1.m\neq s}^{N}\alpha_{m,s}\cdot\left(d^{(m)}+\widetilde{\rho}_{m,s}\right)\right)^2 . \qquad \text{(B.18d)}$$

To obtain the timing variance, we note that

$$\widetilde{t}_{MU(k')}^{(s)}=\widetilde{a}_{MU}^{(s)}\cdot t'+\widetilde{d}_{MU}^{(s)}+\phi_{(k')}^{(s)}, \qquad \text{(B.19a)}$$

$$\left(\widetilde{t}_{MU(k')}^{(s)}\right)^2=\left(\widetilde{a}_{MU}^{(s)}\cdot t'\right)^2+\left(\widetilde{d}_{MU}^{(s)}\right)^2+2\cdot\widetilde{a}_{MU}^{(s)}\cdot\widetilde{d}_{MU}^{(s)}\cdot t'+\left(\phi_{(k')}^{(s)}\right)^2+2\cdot\widetilde{a}_{MU}^{(s)}\cdot t'\cdot\phi_{(k')}^{(s)}+2\cdot\widetilde{d}_{MU}^{(s)}\cdot\phi_{(k')}^{(s)}, \qquad \text{(B.19 b)}$$

$$\left(\sum_{s=1}^{N}\widetilde{t}_{MU(k')}^{(s)}\right)^2=\sum_{s=1}^{N}\sum_{s'=1}^{N}(\widetilde{a}_{MU}^{(s)}t'+\widetilde{d}_{MU}^{(s)}+\phi_{(k')}^{(s)})\cdot(\widetilde{a}_{MU}^{(s')}t'+\widetilde{d}_{MU}^{(s')}+\phi_{(k')}^{(s')})$$
$$=\left(\sum_{s=1}^{N}\widetilde{a}_{MU}^{(s)}t'\right)^2+\left(\sum_{s=1}^{N}\widetilde{d}_{MU}^{(s)}\right)^2+\left(\sum_{s=1}^{N}\phi_{k'}^{(s)}\right)^2+2\sum_{s=1}^{N}\sum_{s'=1}^{N}a_{MU}^{(s')}d_{MU}^{(s)}t'$$
$$+2\sum_{s=1}^{N}\sum_{s'=1}^{N}a_{MU}^{(s')}\phi_{(k')}^{(s)}t'+2\sum_{s=1}^{N}\sum_{s'=1}^{N}d_{MU}^{(s')}\phi_{(k')}^{(s)}\ . \tag{B.19c}$$

Taking the expectation of (B.19b), we arrive at

$$\mathbf{E}\left\{\left(\widetilde{t}_{MU(k')}^{(s)}\right)^2\right\}=\mathbf{E}\left\{\left(\widetilde{a}_{MU}^{(s)}\right)^2\right\}\cdot(t')^2+\mathbf{E}\left\{\left(\widetilde{d}_{MU}^{(s)}\right)^2\right\}+\mathbf{E}\left\{\left(\phi_{(k')}^{(s)}\right)^2\right\}+2\cdot\mathbf{E}\left\{\widetilde{a}_{MU}^{(s)}\cdot\widetilde{d}_{MU}^{(s)}\right\}\cdot t'\ , \tag{B.19d}$$

and the timing variance at individual node after time transfer is

$$\mathbf{V}\left\{\widetilde{t}_{MU(k')}^{(s)}\right\}=\mathbf{V}\left\{\left(\widetilde{a}_{MU}^{(s)}\right)^2\right\}\cdot(t')^2+\mathbf{V}\left\{\left(\widetilde{d}_{MU}^{(s)}\right)^2\right\}+\mathbf{V}\left\{\left(\phi_{(k')}^{(s)}\right)^2\right\}. \tag{B.19e}$$

From (B.15a),

$$\mathbf{E}\left\{\left(\widetilde{a}_{MU}^{(s)}\right)^2\right\}=\left(a_1^{(1)}\right)^2+\mathbf{E}\left\{\left(\sum_{n=1}^{N-1}\varepsilon_{\gamma_{LS}}^{(n,n+1)}\right)^2\right\}/T_f^2+\mathbf{E}\left\{\left(\varepsilon_{\gamma_{LS}}^{(N,s)}\right)^2\right\}/T_f^2$$
$$+2\sum_{n=1}^{N-1}\mathbf{E}\left\{\varepsilon_{\gamma_{LS}}^{(n,n+1)}\cdot\varepsilon_{\gamma_{LS}}^{(N,s)}\right\}/T_f^2$$
$$=\left(a_1^{(1)}\right)^2+\sum_{n=1}^{N-1}\mathbf{E}\left\{\left(\varepsilon_{\gamma_{LS}}^{(n,n+1)}\right)^2\right\}/T_f^2+\mathbf{E}\left\{\left(\varepsilon_{\gamma_{LS}}^{(N,s)}\right)^2\right\}/T_f^2\ . \tag{B.20a}$$

The cross-correlation is evaluated as follows

$$\mathbf{E}\left\{\widetilde{a}_{MU}^{(s)}\cdot\widetilde{d}_{MU}^{(s)}\right\}=a_1^{(1)}\sum_{\substack{m=1,\\ m\neq s}}^{N}\alpha_{m,s}\cdot d^{(m)}+a_1^{(1)}\sum_{\substack{m=1,\\ m\neq s}}^{N}\alpha_{m,s}\cdot\rho_{m,s}+\sum_{n=1}^{N-1}\sum_{\substack{m=1,\\ m\neq s}}^{N}\frac{\alpha_{m,s}}{T_f}\cdot\mathbf{E}\{\varepsilon_{\gamma_{LS}}^{(n,n+1)}\cdot\varepsilon_{\hat{d}}^{(m,s)}\}$$
$$+\sum_{\substack{m=1,\\ m\neq s}}^{N}\frac{\alpha_{m,s}}{T_f}\cdot\mathbf{E}\{\varepsilon_{\gamma_{LS}}^{(N,s)}\cdot\varepsilon_{\hat{d}}^{(m,s)}\}\ , \tag{B.20b}$$

and

$$\mathbf{E}\left\{\widetilde{a}_{MU}^{(s')}\cdot\widetilde{d}_{MU}^{(s)}\right\}=a_1^{(1)}\sum_{\substack{m=1,\\ m\neq s}}^{N}\alpha_{m,s}\cdot d^{(m)}+a_1^{(1)}\sum_{\substack{m=1,\\ m\neq s}}^{N}\alpha_{m,s}\cdot\rho_{m,s}+\sum_{n=1}^{N-1}\sum_{\substack{m=1,\\ m\neq s}}^{N}\frac{\alpha_{m,s}}{T_f}\cdot\mathbf{E}\{\varepsilon_{\gamma_{LS}}^{(n,n+1)}\cdot\varepsilon_{\hat{d}}^{(m,s)}\}$$
$$+\sum_{\substack{m=1,\\ m\neq s}}^{N}\frac{\alpha_{m,s}}{T_f}\cdot\mathbf{E}\{\varepsilon_{\gamma_{LS}}^{(N,s)}\cdot\varepsilon_{\hat{d}}^{(m,s')}\}\cdot\delta(s-s')\ , \tag{B.20c}$$

where $\delta(s-s')=1$ if $s=s'$, otherwise $\delta(s-s')=0$. Moreover it can be shown that

$$\sum_{\substack{m=1,\\ m\neq s}}^{N} \frac{\alpha_{m,s}}{T_f}\cdot \mathbf{E}\{\varepsilon_{\gamma_{LS}}^{(N,s)}\cdot \varepsilon_{\hat{d}}^{(m,s)}\} = \frac{\alpha_{N,s}}{T_f}\cdot \mathbf{E}\{\varepsilon_{\gamma_{LS}}^{(N,s)}\cdot \varepsilon_{\hat{d}}^{(N,s)}\}\,, \tag{B.21a}$$

and

$$\sum_{n=1}^{N-1}\sum_{\substack{m=1,\\ m\neq s}}^{N} \frac{\alpha_{m,s}}{T_f}\cdot \mathbf{E}\{\varepsilon_{\gamma_{LS}}^{(n,n+1)}\cdot \varepsilon_{\hat{d}}^{(m,s)}\} = \frac{\alpha_{s-1,s}}{T_f}\cdot \mathbf{E}\{\varepsilon_{\gamma_{LS}}^{(s-1,s)}\cdot \varepsilon_{\hat{d}}^{(s-1,s)}\},\ 1<s<=N\,. \tag{B.21b}$$

The variance of the timing $\mathbf{E}\{(\tilde{t}_{MU(k')}^{(s)})^2\}$ at individual node s after MU time-transfer can be evaluated by substituting (B.20a), (B.20b) and (B.20c) into (B.19c).

From (B.16c), the variance of the timing across all nodes in the network evaluates to

$$\begin{aligned}\overline{\mathbf{V}\{\tilde{t}_{MU(k')}\}} = {} & \overline{\mathbf{V}\{\tilde{a}_{MU}\}}\cdot (t')^2 + \overline{\mathbf{V}\{\tilde{d}_{MU}\}} + \frac{2}{N-1}\sum_{s=1}^{N}\mathbf{E}\{\tilde{a}_{MU}^{(s)}\cdot \tilde{d}_{MU}^{(s)}\}\cdot t' \\ & - \frac{2}{N(N-1)}\sum_{s=1}^{N}\sum_{s'=1}^{N}\mathbf{E}\{\tilde{a}_{MU}^{(s')}\cdot \tilde{d}_{MU}^{(s)}\}\cdot t' + \mathbf{E}\left\{\left(\phi_{(k')}^{(s)}\right)^2\right\}.\end{aligned} \tag{B.22}$$

Substituting (B.20c) and (B.20d) into (B.22), equation (B.22) becomes

$$\begin{aligned}\overline{\mathbf{V}\{\tilde{t}_{MU(k')}\}} = {} & \overline{\mathbf{V}\{\tilde{a}_{MU}\}}\cdot (t')^2 + \overline{\mathbf{V}\{\tilde{d}_{MU}\}} \\ & + \frac{2\cdot t'}{N-1}\sum_{s=1}^{N}\Bigg(a_1^{(1)}\sum_{\substack{m=1,\\ m\neq s}}^{N}\alpha_{m,s}\cdot d^{(m)} + a_1^{(1)}\sum_{\substack{m=1,\\ m\neq s}}^{N}\alpha_{m,s}\cdot \rho_{m,s} + \sum_{n=1}^{N-1}\sum_{\substack{m=1,\\ m\neq s}}^{N}\frac{\alpha_{m,s}}{T_f}\cdot \mathbf{E}\{\varepsilon_{\gamma_{LS}}^{(n,n+1)}\cdot \varepsilon_{\hat{d}}^{(m,s)}\} \\ & \qquad + \frac{\alpha_{N,s}}{T_f}\cdot \mathbf{E}\{\varepsilon_{\gamma_{LS}}^{(N,s)}\cdot \varepsilon_{\hat{d}}^{(N,s)}\}\Bigg) \\ & - \frac{2\cdot t'\cdot N}{N(N-1)}\sum_{s=1}^{N}\Bigg(a_1^{(1)}\sum_{\substack{m=1,\\ m\neq s}}^{N}\alpha_{m,s}\cdot d^{(m)} + a_1^{(1)}\sum_{\substack{m=1,\\ m\neq s}}^{N}\alpha_{m,s}\cdot \rho_{m,s} + \sum_{n=1}^{N-1}\sum_{\substack{m=1,\\ m\neq s}}^{N}\frac{\alpha_{m,s}}{T_f}\cdot \mathbf{E}\{\varepsilon_{\gamma_{LS}}^{(n,n+1)}\cdot \varepsilon_{\hat{d}}^{(m,s)}\} \\ & \qquad + \frac{1}{N}\cdot\frac{\alpha_{N,s}}{T_f}\cdot \mathbf{E}\{\varepsilon_{\gamma_{LS}}^{(N,s)}\cdot \varepsilon_{\hat{d}}^{(N,s)}\}\Bigg) + \sigma_{\phi}^2 \\ = {} & \overline{\mathbf{V}\{\tilde{a}_{MU}\}}\cdot (t')^2 + \overline{\mathbf{V}\{\tilde{d}_{MU}\}} + \frac{2\cdot t'}{N}\sum_{s=1}^{N-1}\frac{\alpha_{N,s}}{T_f}\cdot \mathbf{E}\{\varepsilon_{\gamma_{LS}}^{(N,s)}\cdot \varepsilon_{\hat{d}}^{(N,s)}\} + \sigma_{\phi}^2\ ,\end{aligned} \tag{B.23}$$

where $K_{ST} = (2N-1)KQ$ and $\mathbf{M}(Q) = m$ if nodes take turn to be the roving master in the natural order. For MU, $k' = (2N-1)K\cdot N$ and $t' = (2N-1)KT_f N$.

APPENDIX C

SIMULATION RESULTS FOR HIERARCHICAL MASTER-SLAVE TIME-TRANSFER ARCHITECTURE

This appendix reports the simulation results obtained from simulating the hierarchical master-slave time transfer architecture. Unless otherwise specified, the Monte Carlo simulations are performed with the following simulation parameters:

1.) Number of nodes in network, $N = 20$.

2.) Nominal frame repetition rate, $T_f = 10^{-3}$ seconds.

3.) Approximate pulse width of UWB monocycle, $\sigma_w = 0.067 \times 10^{-9}$ seconds.

4.) Order of Gaussian derivative waveform, $n = 8$.

5.) Number of frames per slot, $K = K_s = K_r = 1000$.

6.) Uplink and downlink index, $i = j$.

7.) Oscillator phase noise, $\sigma_\phi = 0$.

8.) Path-loss exponent, $\rho_L = 2$.

For the HM time-transfer architecture, simulations are performed with 5 and 19 roving masters (including the lead master node). If nodes are aware of the signal propagation distances from themselves to all other nodes in the network, i.e., nodes have complete knowledge of the network topology, for 5 roving masters, the roving masters will be taken from the ordered set {1,8,12,4,2}. Similarly, for 19 roving masters, the nodes take turn to be the roving masters in the order {1,8,12,4,2,6,20,17,18,9,13,16,11,10,5,7,15,14,19}.

The initial offset before time-transfer is,

$d^{(s)}$ = { -0.15398521972836, 0.10680338700882, 0.17076648855833,
0.07034841669641, -0.07829529943844, -0.02252087387333,
0.05095257661642, 0.25459580650917, 0.23084002368445,

0.09858776012560, 0.11177512414205, 0.10387650348619,

0.28858078810527, 0.01802540503429, 0.10627836711161,

0.12694466466843, 0.00301192281376, 0.07173229031455,

0.27131321961697, 0.14643006878572} $\times 10^{-9}$ secs.

The normalized drift before time transfer is,

$\eta^{(s)}$ = { 1×10^{-6}, 7×10^{-6}, -4×10^{-6}, 9×10^{-6}, 5×10^{-6},

4×10^{-6}, -8×10^{-6}, -5×10^{-6}, 2×10^{-6}, -7×10^{-6},

8×10^{-6}, 1×10^{-6}, 7×10^{-6}, -4×10^{-6}, 8×10^{-6},

5×10^{-6}, 7×10^{-6}, 4×10^{-6}, 3×10^{-6}, -2×10^{-6} }.

Therefore the drift of the nodes in the network before time-transfer is $a_1^{(s)} = 1+\eta^{(s)}$.

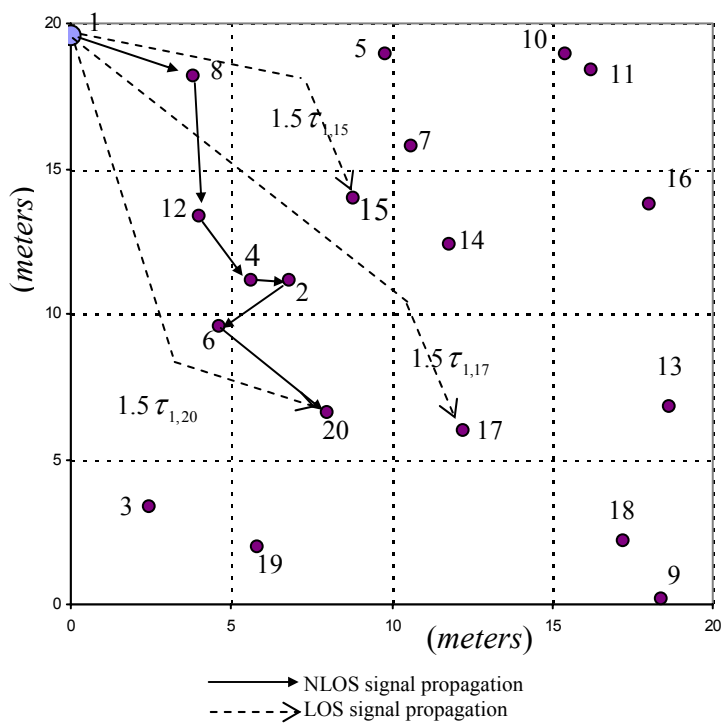

Figure C.1: Network topology used for time transfer simulations. The simulations parameters are listed in the beginning of this Appendix. Node 1 is the lead master node.

C.1 Known Network Topology

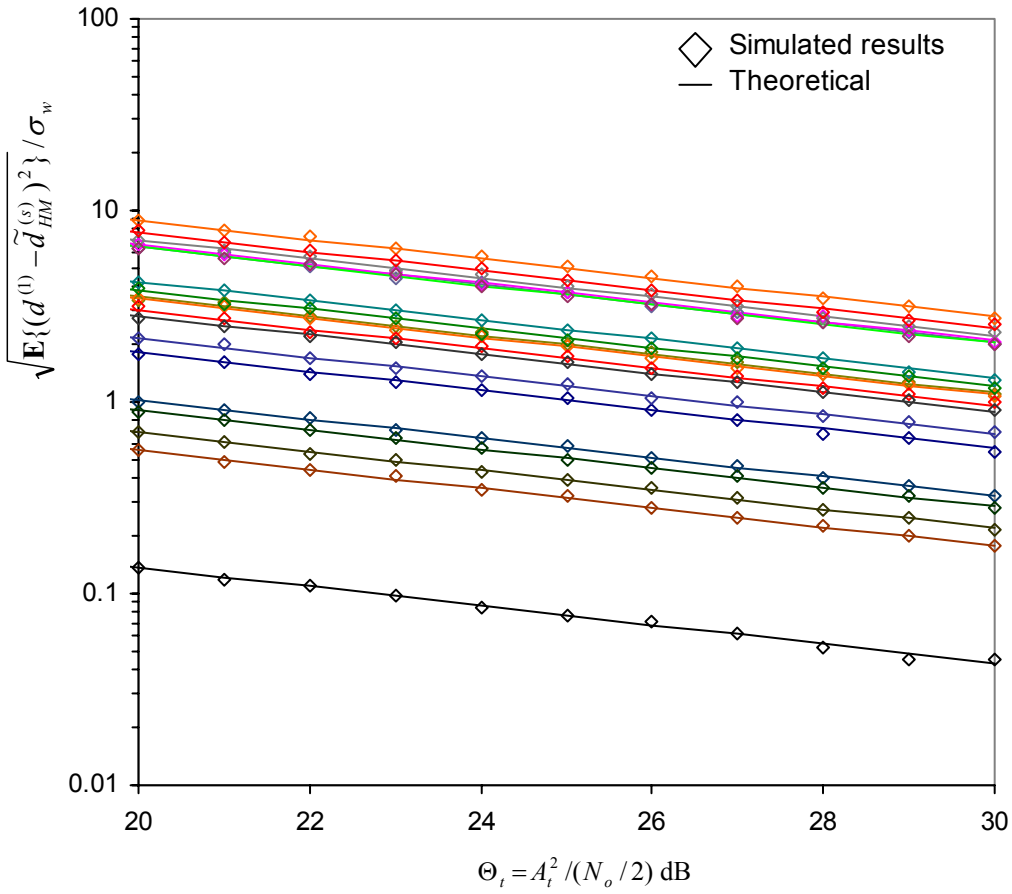

Figure C.2: Normalized standard deviation of difference in initial offset estimate after HM time transfer with 5 roving masters, $\mathbf{M} \in \{1,8,12,4,2\}$. In this simulation, it is assumed that the distances between all nodes are known. Results obtained using time-transfer scheme A.

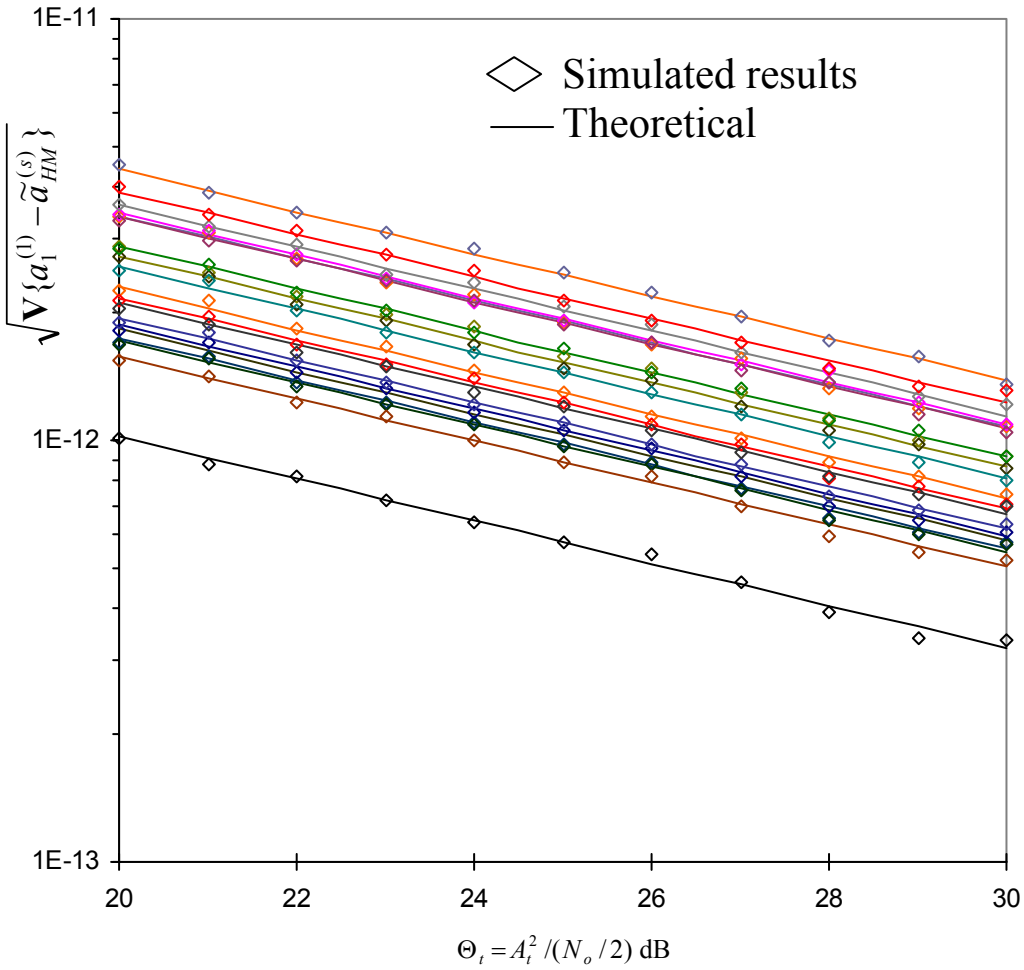

Figure C.3: Normalized standard deviation of difference in drift estimate after HM time transfer with 5 roving masters, $\mathbf{M} \in \{1,8,12,4,2\}$. In this simulation, it is assumed that the distances between all nodes are known. Results obtained using time-transfer scheme A.

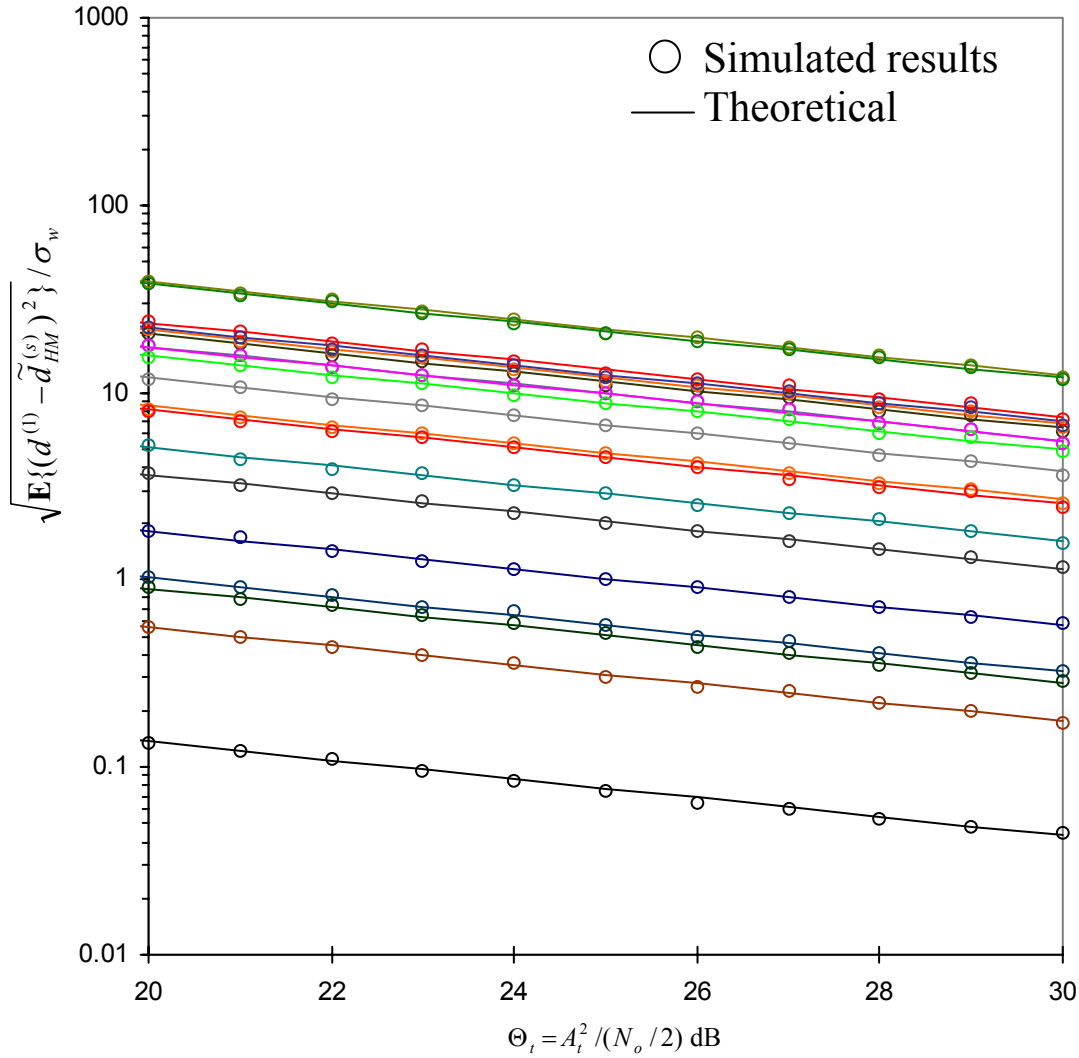

Figure C.4: Normalized standard deviation of difference in initial offset estimate after HM time transfer with 19 roving masters. In this simulation, it is assumed that the distances between all nodes are known. The roving master are:

$$\{1,8,12,4,2,6,20,17,18,9,13,16,11,10,5,7,15,14,19\}.$$

Results obtained using time-transfer scheme A.

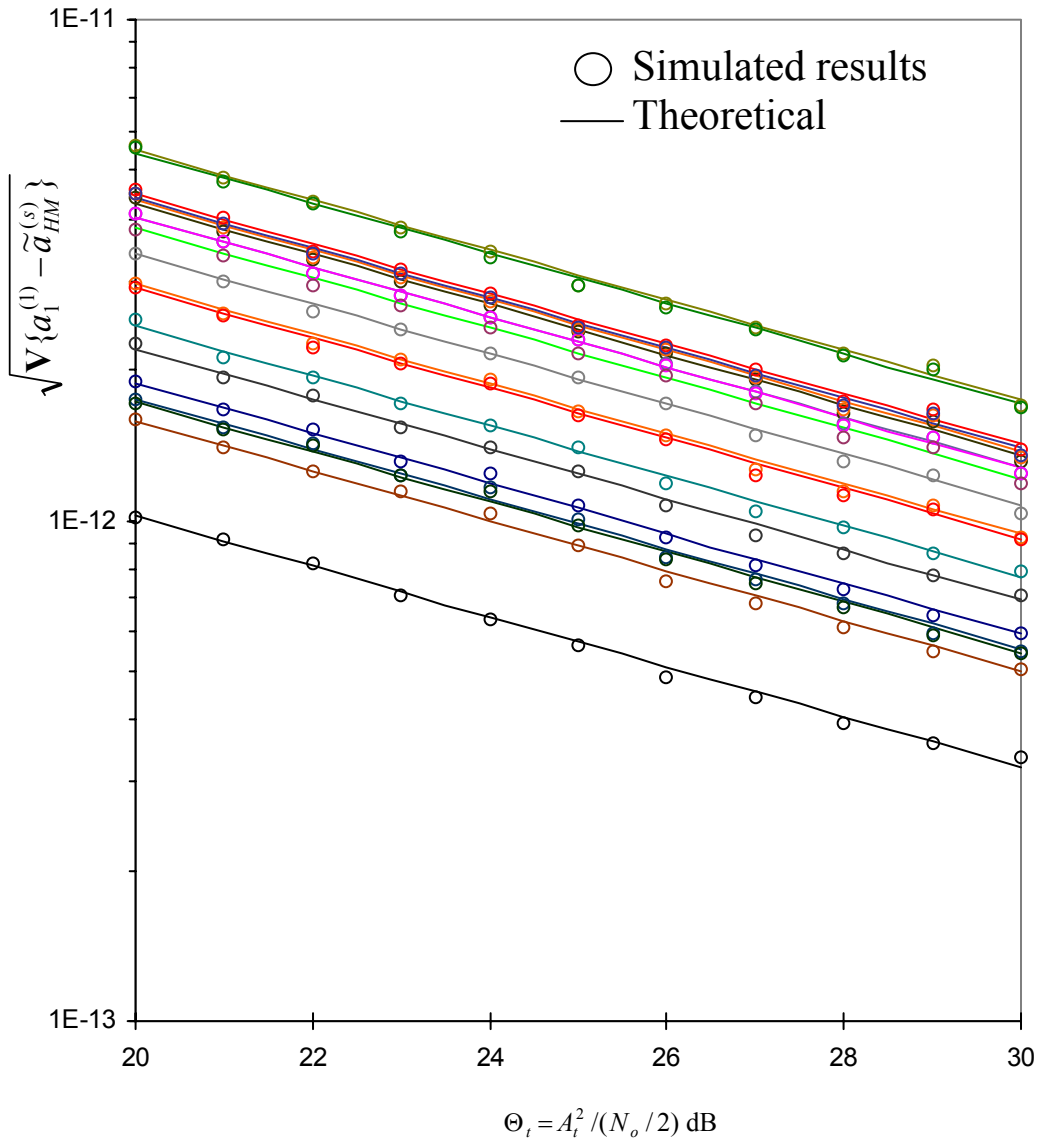

Figure C.5: Normalized standard deviation of difference in drift estimate after HM time transfer with 19 roving masters. In this simulation, it is assumed that the distances between all nodes are known. The y-axis is in log scale. Results obtained using time-transfer scheme A.

C.2 Unknown Network Topology

With unknown network topology and a finite K, not only the roving masters are not selected optimally based on the shortest signal propagation distance, slave node also did not select optimally the roving master from which it acquires its timing.

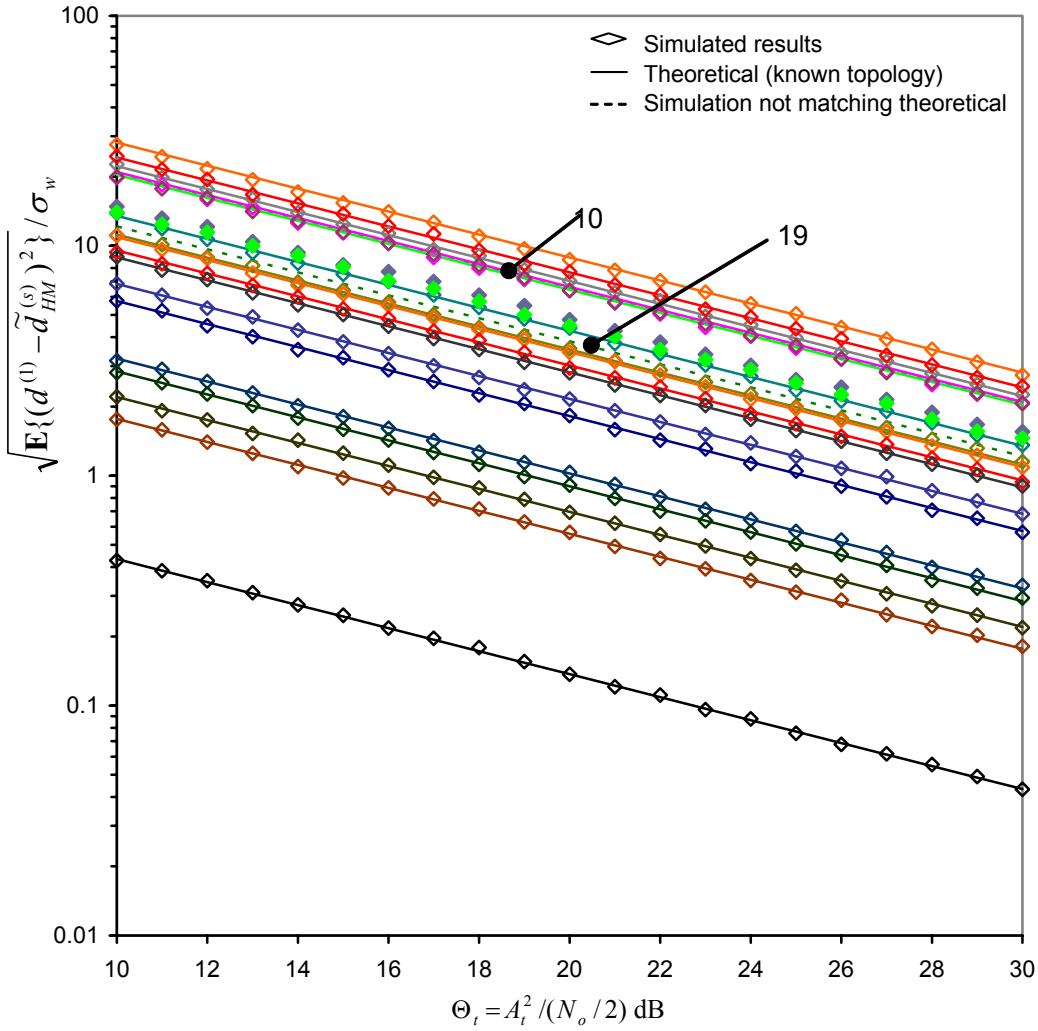

Figure C.6: Normalized standard deviation of difference in initial offset estimate after HM time transfer with 5 roving masters. Nodes 10 and 19 do not agree with theoretical results computed with known network topology. Results obtained using time-transfer scheme A.

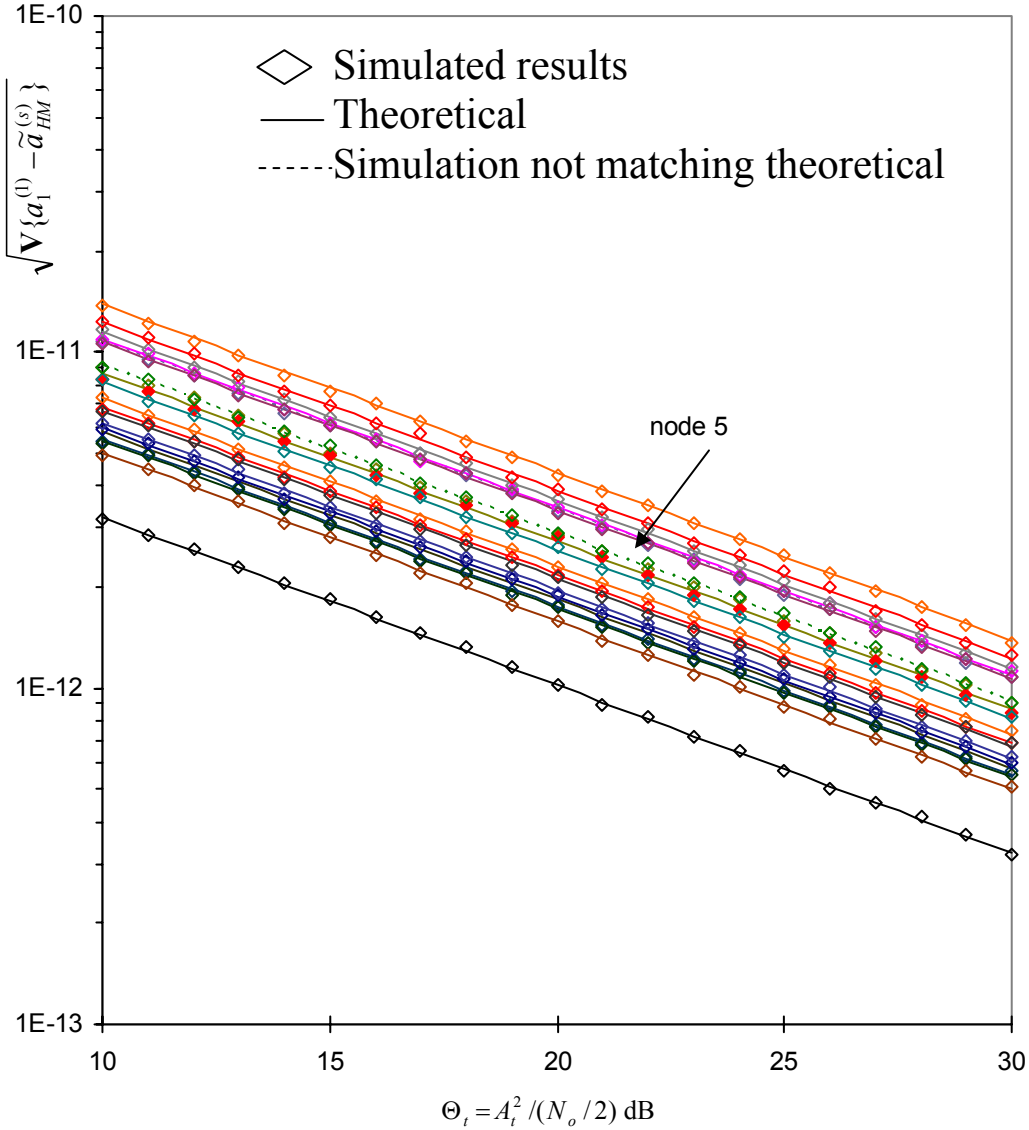

Figure C.7: Normalized standard deviation of difference in drift estimate after HM time transfer with 5 roving masters. Unlike variance of difference in initial offset, only node 5 deviates significantly from theoretical results computed with known network topology. Results obtained using time-transfer scheme A.

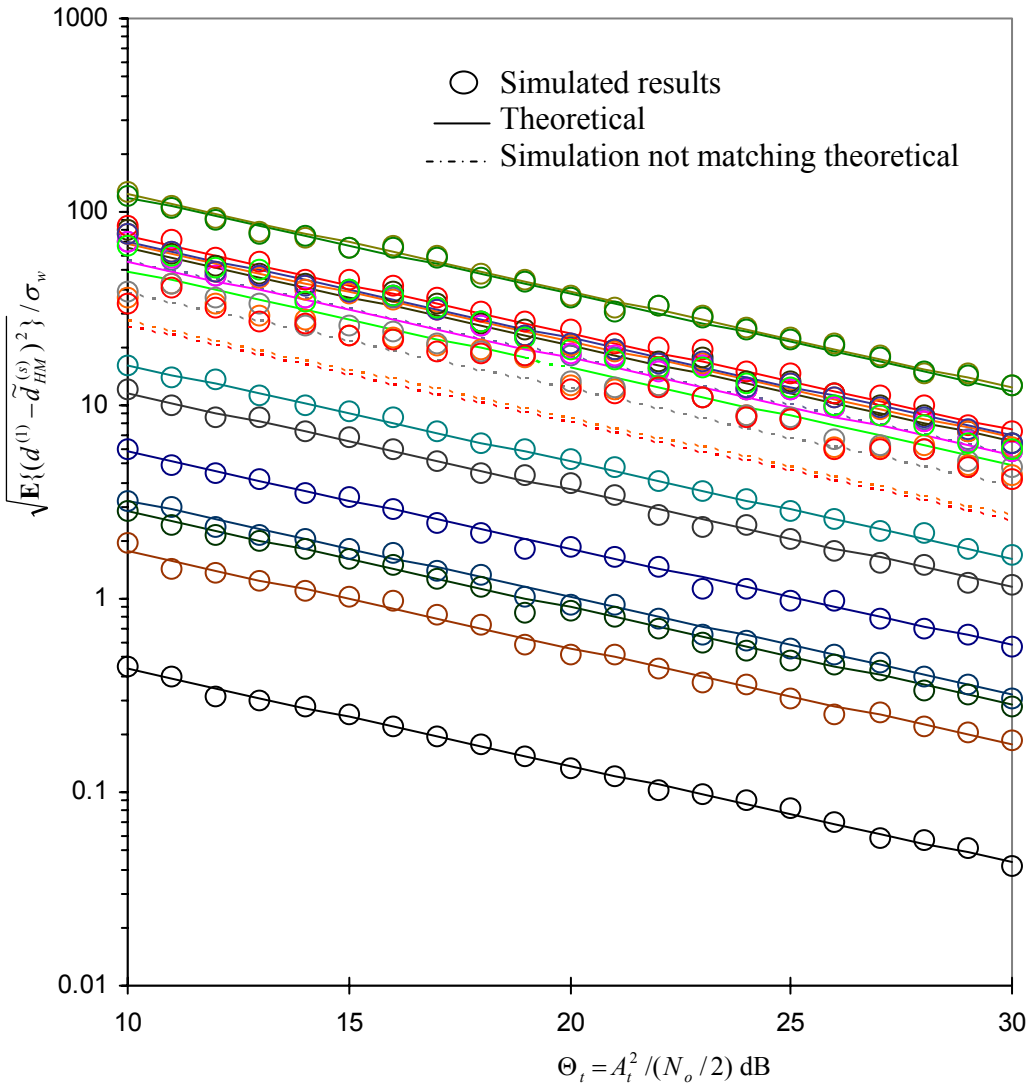

Figure C.8: Normalized standard deviation of difference in initial offset estimate after HM time transfer with 19 roving masters. More nodes deviates significantly from theoretical results computed with known network topology compared to having only 5 roving masters. Results obtained using time-transfer scheme A.

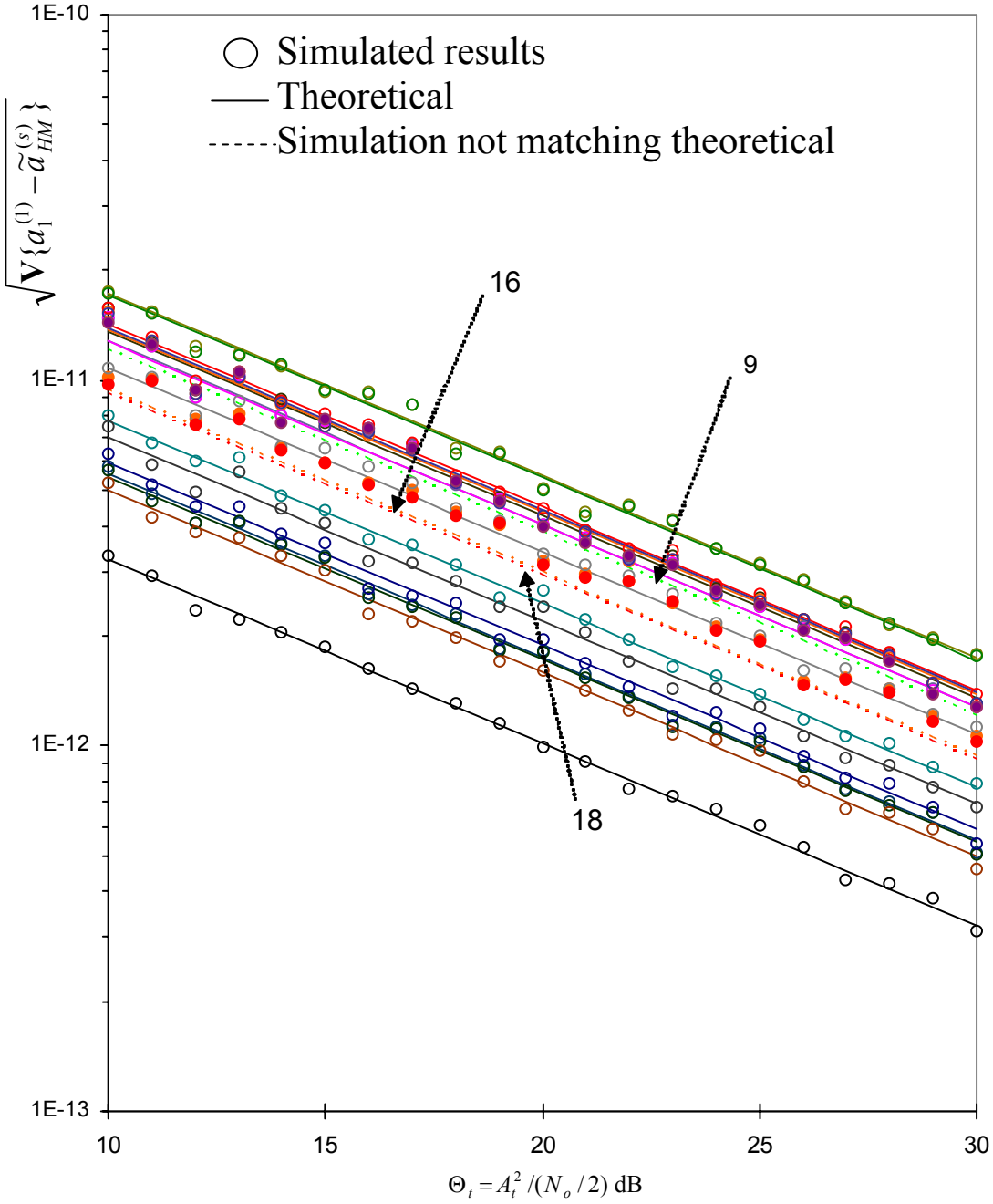

Figure C.9: Normalized standard deviation of difference in drift estimate after HM time transfer with 19 roving masters. Nodes 9, 16 and 18 deviates significantly from theoretical results computed with known network topology. Results obtained using time-transfer scheme A.

APPENDIX D

SIMULATION RESULTS FOR MUTUALLY SYNCHRONOUS TIME-TRANSFER ARCHITECTURE

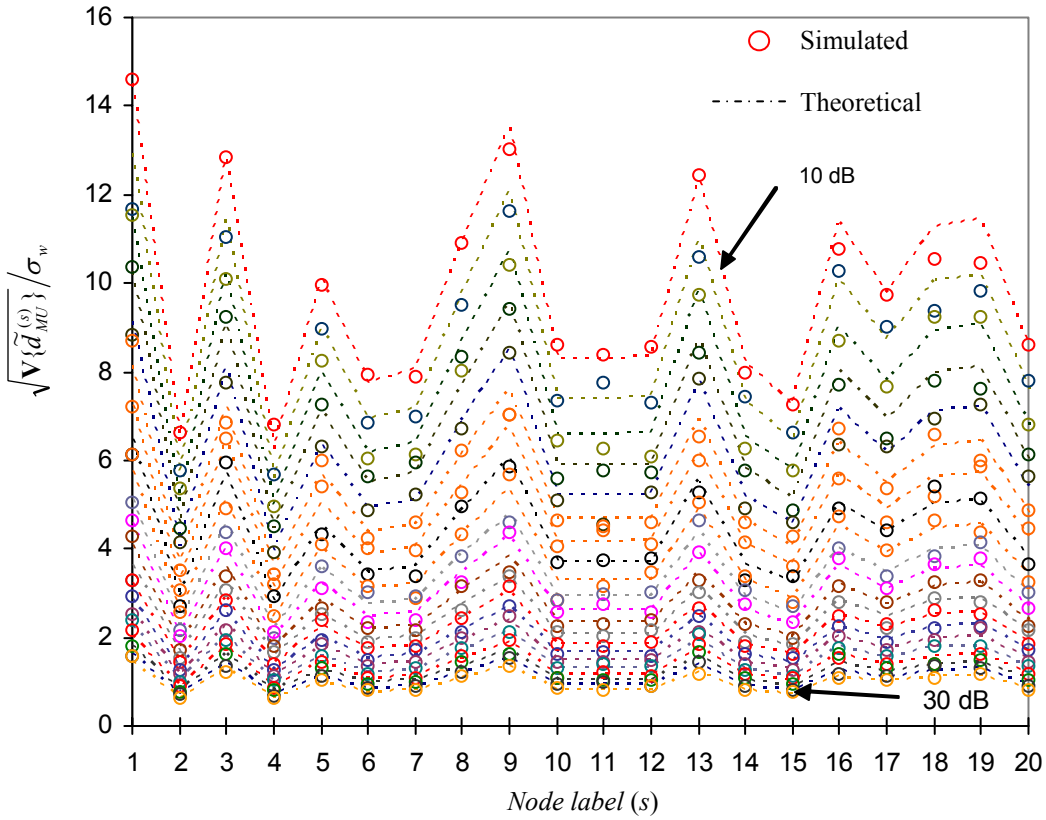

Figure D.1: Normalized standard deviation of the settled initial offset estimate for individual nodes in the network after MU (without NLoS propagation). The y-axis is in linear scale and the standard deviation is normalized with respect to σ_w. The top most 'simulated' points are obtained at $\Theta_t = 10$ dB, and in increment of 1 dB, the bottom most 'simulated' points are obtained at $\Theta_t = 30$ dB. Results obtained using time-transfer scheme A.

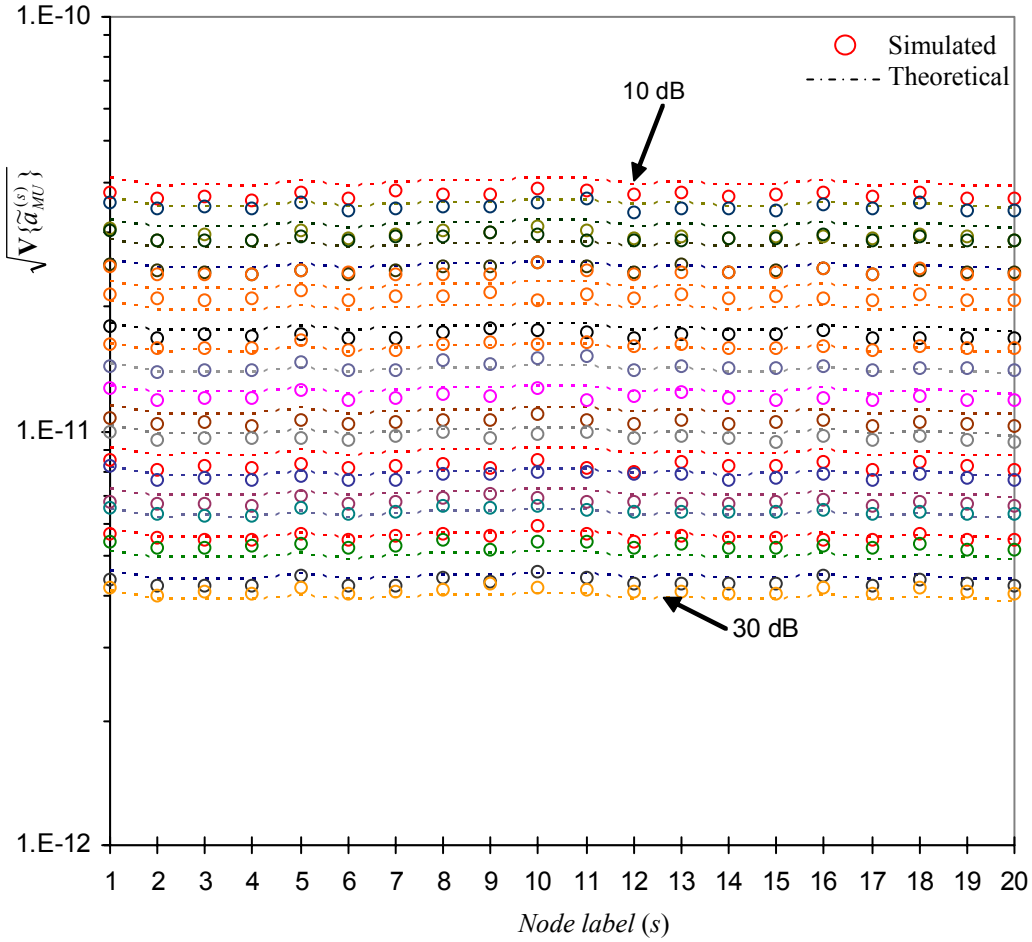

Figure D.2: Standard deviation of the settled drift estimate after MU (without NLoS propagation) obtained from simulation and compared with theoretical analysis. The y-axis is in log scale. The top most 'simulated' points are obtained at $\Theta_t = 10$ dB, and in increment of 1 dB, the bottom most 'simulated' points are obtained at $\Theta_t = 30$ dB. Results obtained using time-transfer scheme A.

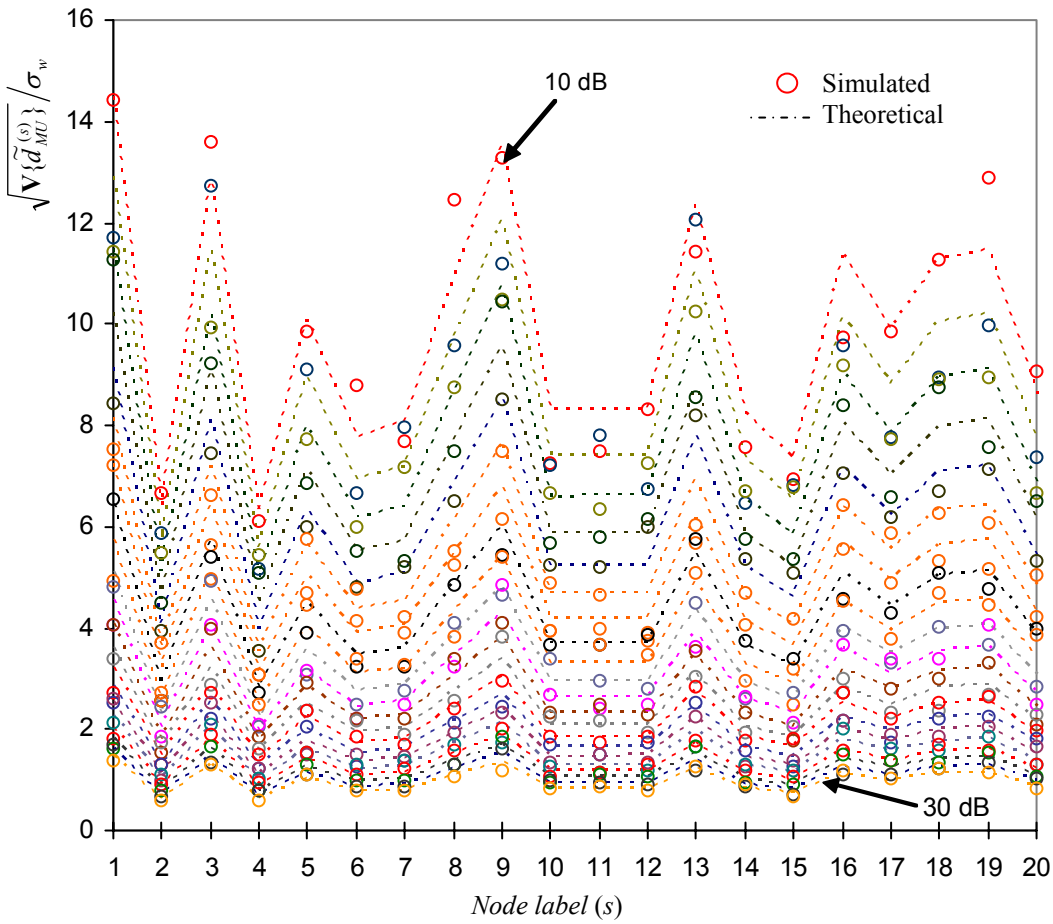

Figure D.3: Normalized standard deviation of the settled initial offset estimate after MU for individual nodes in the network obtained from simulation and compared with theoretical analysis. In this simulation, NLoS propagation is introduced between nodes 1 and 15, 17 and 20 with receiver measurement error. The y-axis is in linear scale and the initial offset is normalized with respect to σ_w. The top most 'simulated' points are obtained at $\Theta_t = 10$ dB, and in increment of 1 dB, the bottom most 'simulated' points are obtained at $\Theta_t = 30$ dB. Results obtained using time-transfer scheme A.

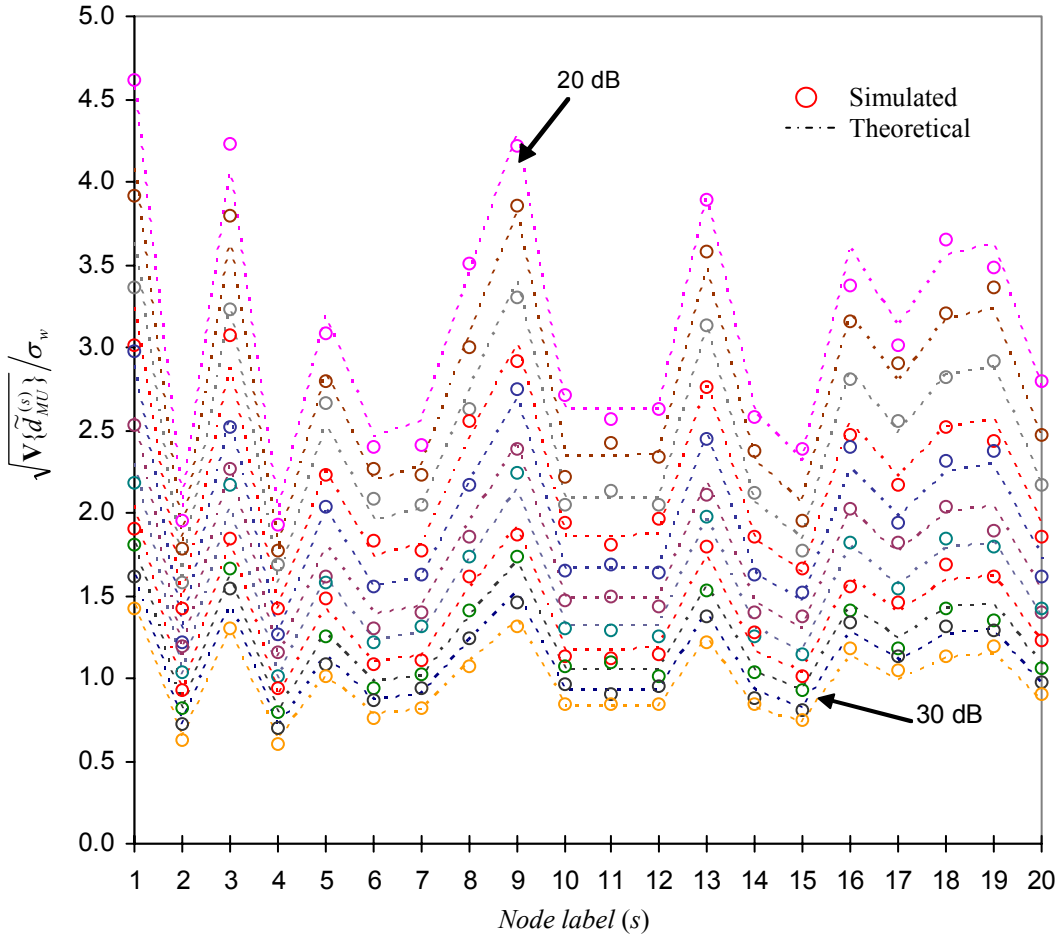

Figure D.4: Normalized standard deviation of the settled initial offset estimate after MU for individual nodes in the network obtained from simulation and compared with theoretical analysis. In this simulation, NLoS propagation is introduced between nodes 1 and 15, 17 and 20 with receiver measurement error. The y-axis is in linear scale and the initial offset is normalized with respect to σ_w. The top most 'simulated' points are obtained at $\Theta_t = 10$ dB, and in increment of 1 dB, the bottom most 'simulated' points are obtained at $\Theta_t = 30$ dB. In order to verify the theoretical derivations, each network node is assumed to know the signal propagation distance from itself to all other nodes in the network. The simulated results agree well with the results obtained from the analytical equations. Results obtained using time-transfer scheme A.

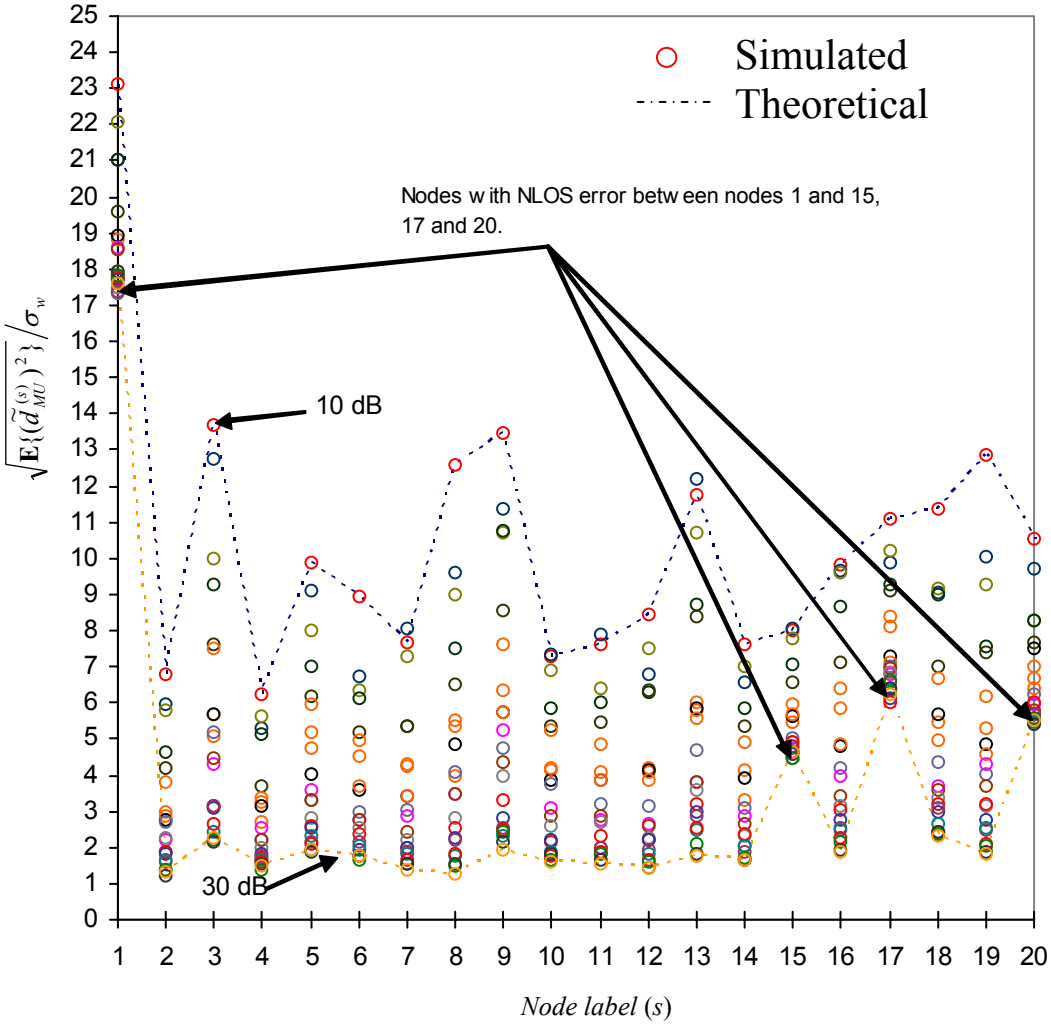

Figure D.5: Normalized standard deviation of the settled initial offset estimate after mutual synchronization. In this simulation, NLoS propagation is introduced between nodes 1 and 15, 17 and 20 with receiver measurement error. The expectation-square, $\sqrt{\mathbf{E}\{(\tilde{d}_{MU}^{(s)})^2\}}/\sigma_w$ is plotted in this figure instead of the $\sqrt{\mathbf{V}\{\tilde{d}_{MU}^{(s)}\}}/\sigma_w$ of Fig. D.3. The top most 'simulated' points are obtained at $\Theta_t = 10dB$, and in increment of 1 dB, the bottom most 'simulated' points are obtained at $\Theta_t = 30dB$. Results obtained using time-transfer scheme A.

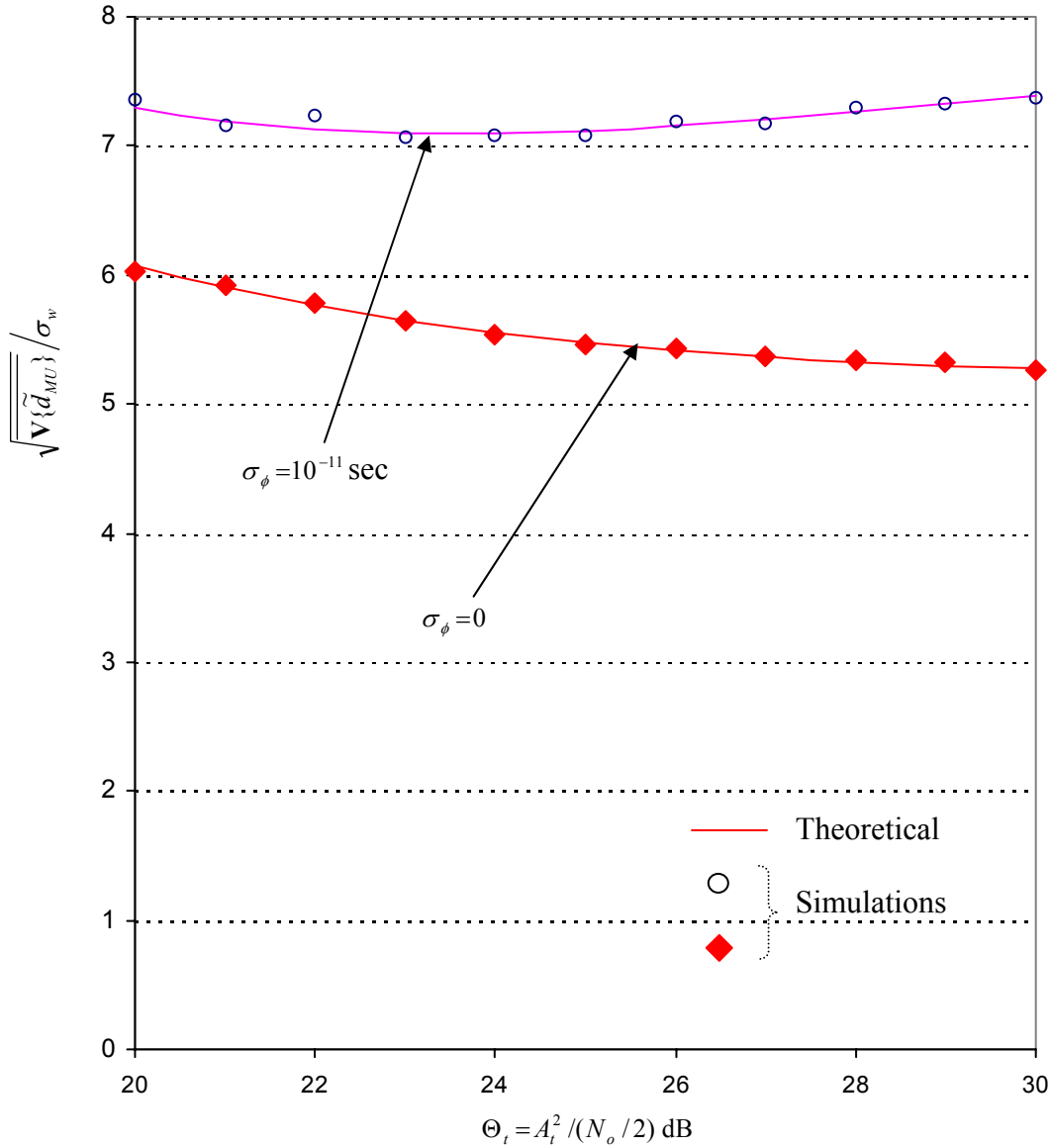

Figure D.6: Square-root of the sample variance of the settled initial offset estimate after MU is plotted as a function of Θ_t. The y-axis is in linear scale and normalized by σ_w. In this simulation, NLoS propagation is introduced between nodes 1 and 15, 17 and 20 with receiver measurement error. The simulation assumes that each network node knows the signal propagation distance from itself to all other nodes in the network. The theoretical formulation agrees with the simulation results. Results obtained using time-transfer scheme A.

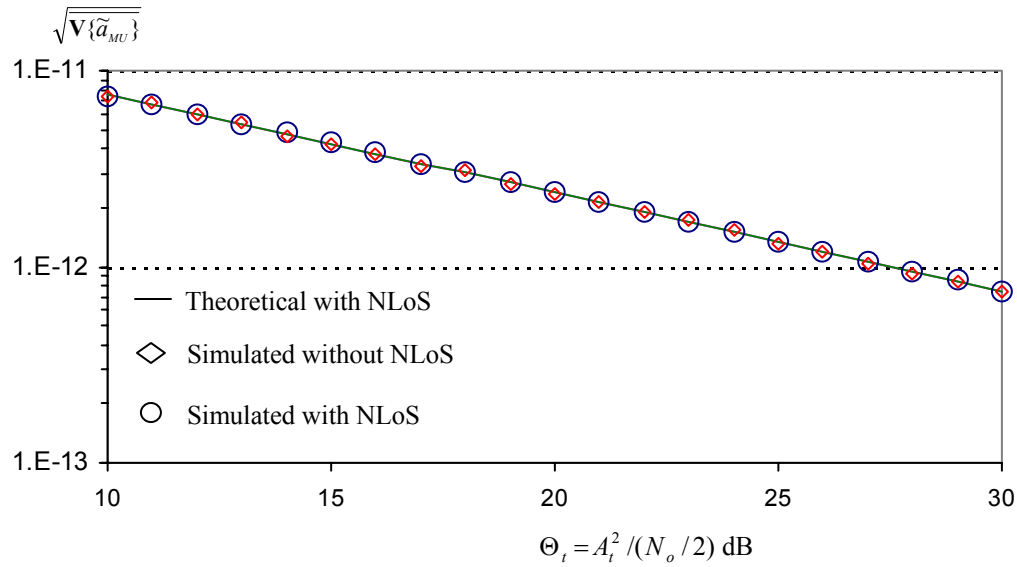

Figure D.7: Square-root of the sample variance of the settled drift estimate across all nodes in the network after MU is plotted as a function of Θ_t. The y-axis is in log scale. As expected, there is no difference between propagations with LoS and without LoS. Results obtained using time-transfer scheme A.

APPENDIX E

SIMULATION RESULTS ON TIME-TRANSFER ERRORS USING TIME-TRANSFER SCHEME A

This appendix reports the timing errors of the SM, HM and MU time-transfer architectures obtained from simulation. The simulation parameters are identical to those listed in Appendix C. The network topology is shown in Fig. C.1.

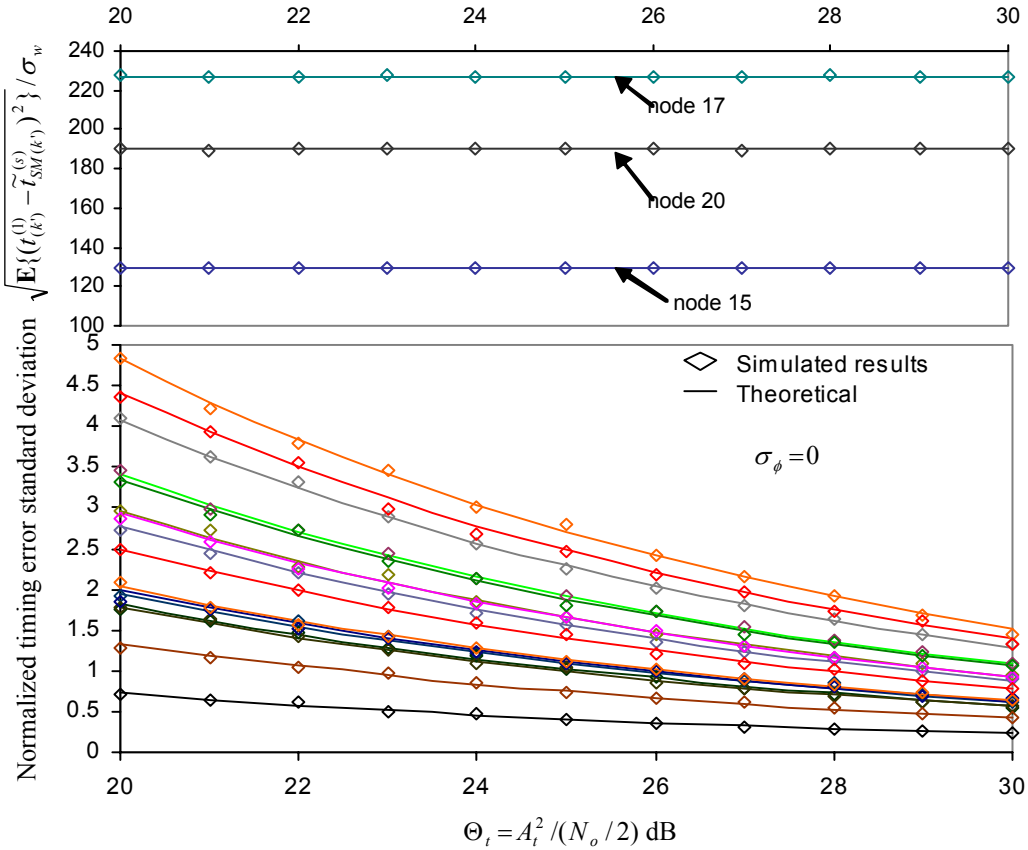

Figure E.1: Normalized timing error standard deviation after SM time transfer, i.e., there is no roving of master nodes and $t' = (2N-1)KT_f$. Time transfer from node 1 to nodes 15, 17 and 20 is impaired by receiver measurement error. In this simulation, in order to verify the theoretical derivations, each network node is assumed to know the signal propagation distance from itself to all other nodes in the network. Results obtained using time-transfer scheme A.

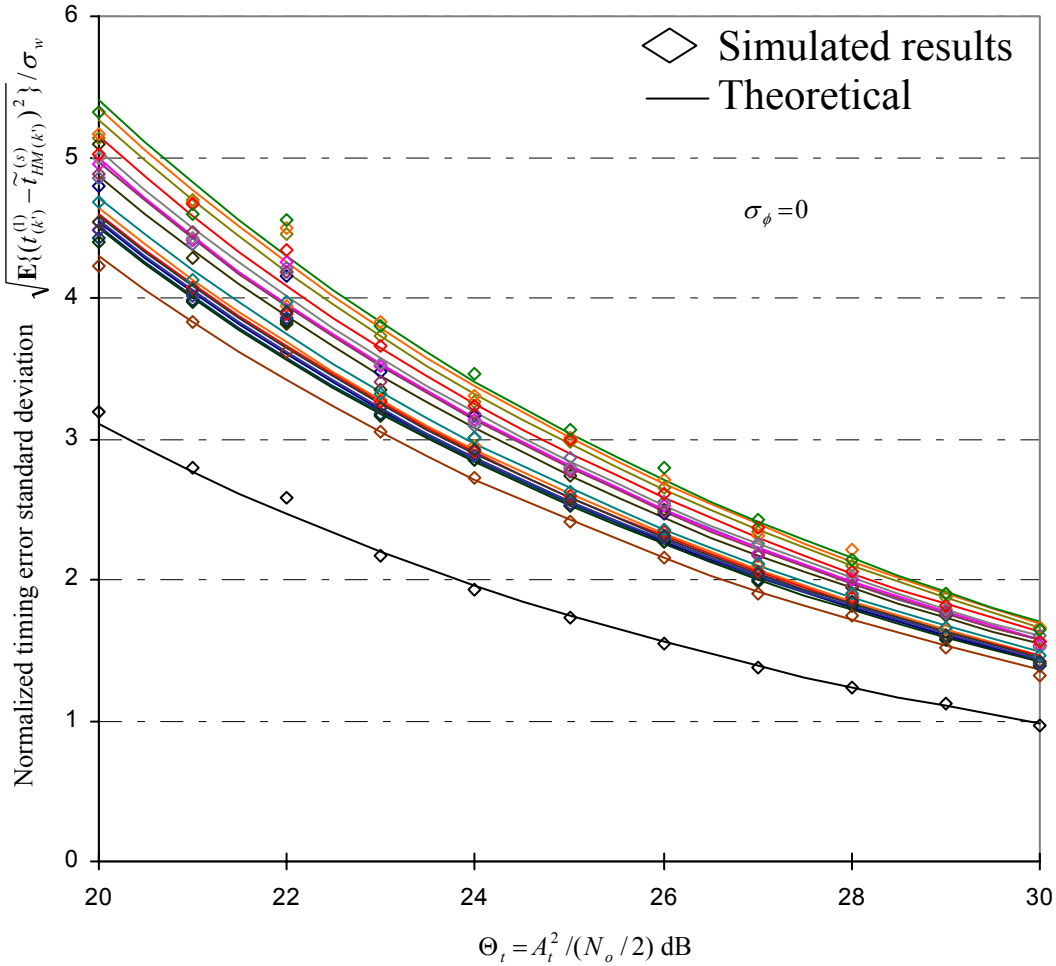

Figure E.2: Normalized timing error standard deviation after HM time transfer with 5 roving masters. The roving master nodes are $\mathbf{M} \in \{1,8,12,4,2\}$. Here $t' = (2N-1)KT_f \cdot 5$. In this simulation, in order to verify the theoretical derivations, each network node is assumed to know the signal propagation distance from itself to all other nodes in the network. The theoretical formulation agrees with the simulation results. Results obtained using time-transfer scheme A.

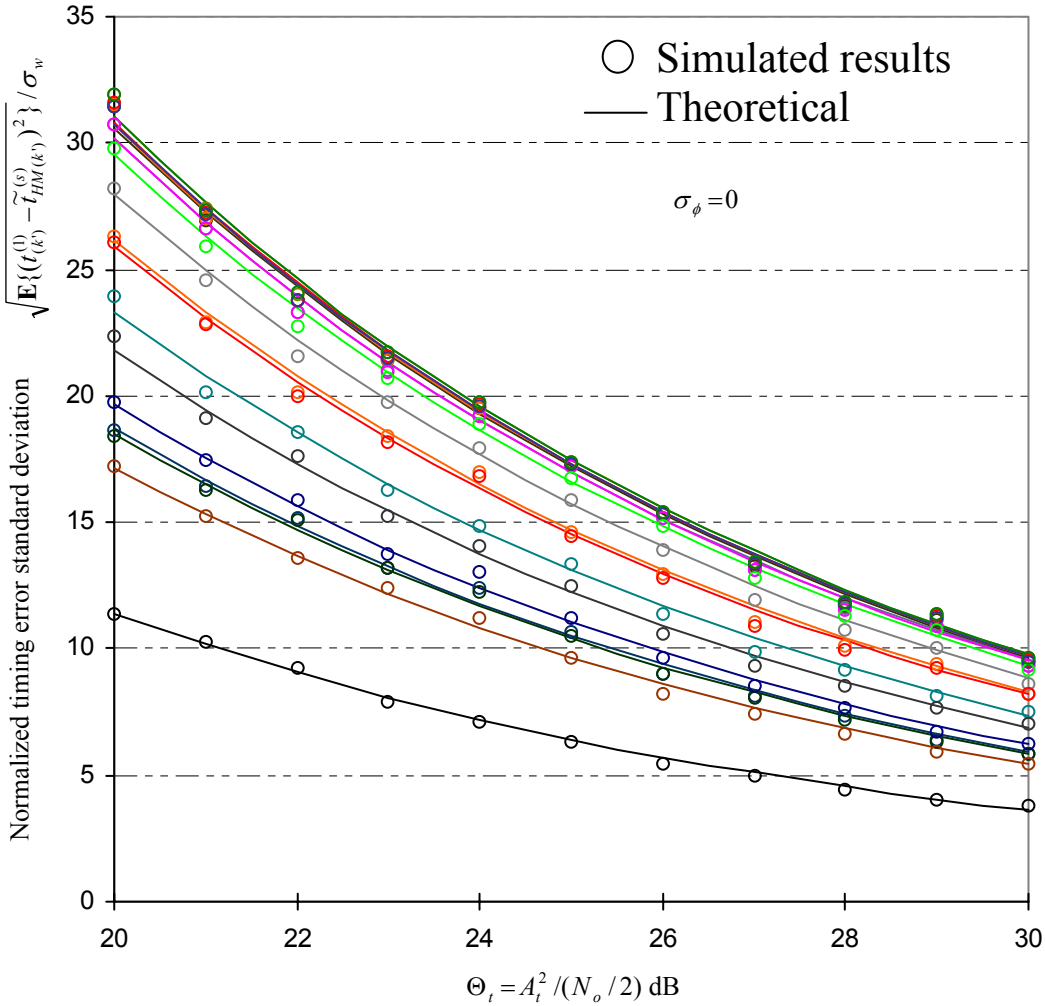

Figure E.3: Normalized timing error standard deviation after HM time transfer with 19 roving masters. The nodes take a turn as the roving master in the order: 1,8,12,4,2,6,20,17,18,9,13,16,11,10,5,7,15,14,19. And $t' = (2N-1)KT_f \cdot 19$. In this simulation, in order to verify the theoretical derivations, each network node is assumed to know the signal propagation distance from itself to all other nodes in the network. The theoretical formulation agrees well with the simulation results. Results obtained using time-transfer scheme A.

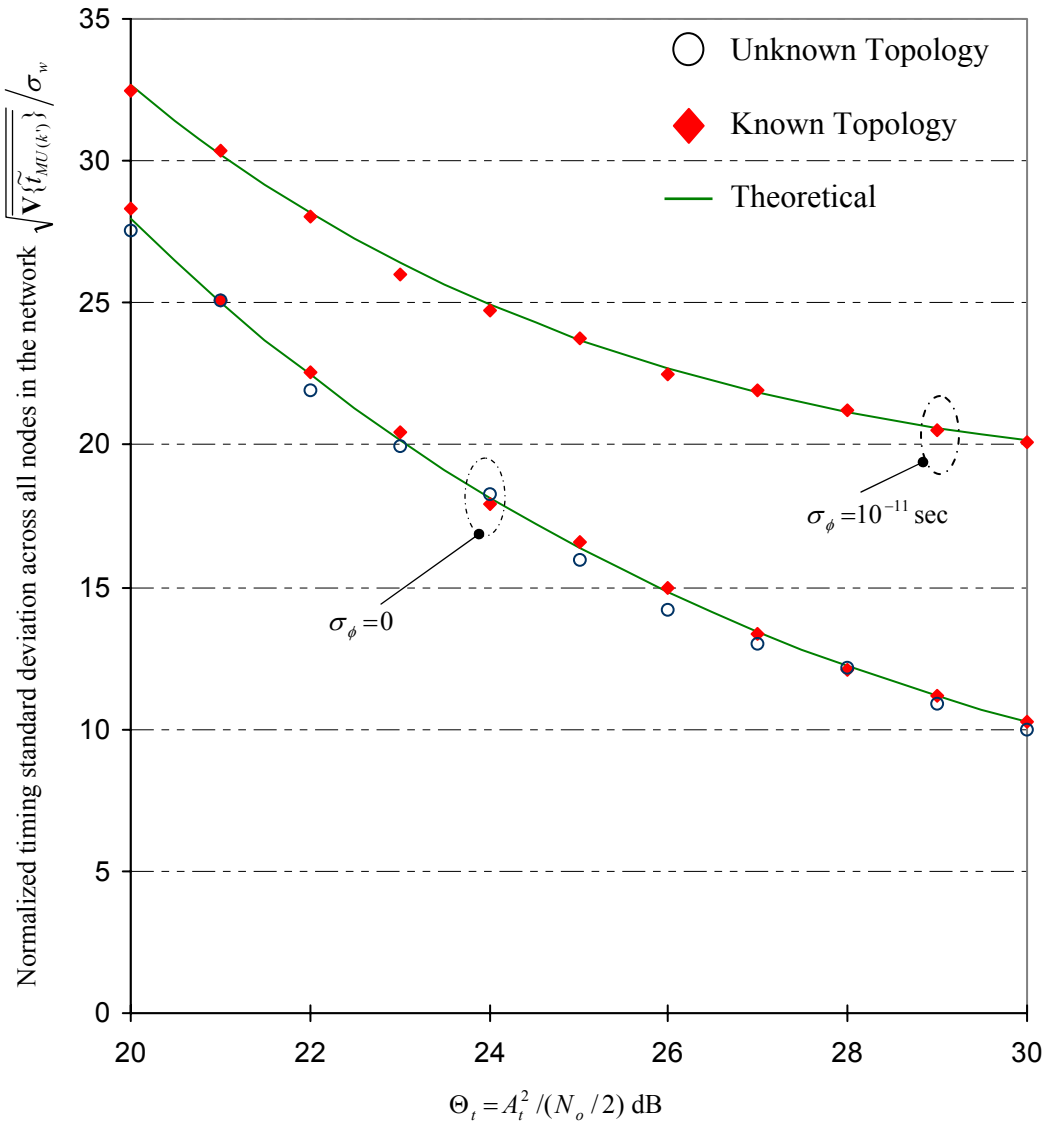

Figure E.4: Normalized timing sample variance across all nodes in the network after MU time transfer. Points labeled with 'known topology' refer to the simulation results when each network node is assumed to know the signal propagation distance from itself to all other nodes in the network. 'Unknown topology' refers otherwise. And $t' = (2N-1)KT_f \cdot 20$ for $N = 20$. Results obtained using time-transfer scheme A.

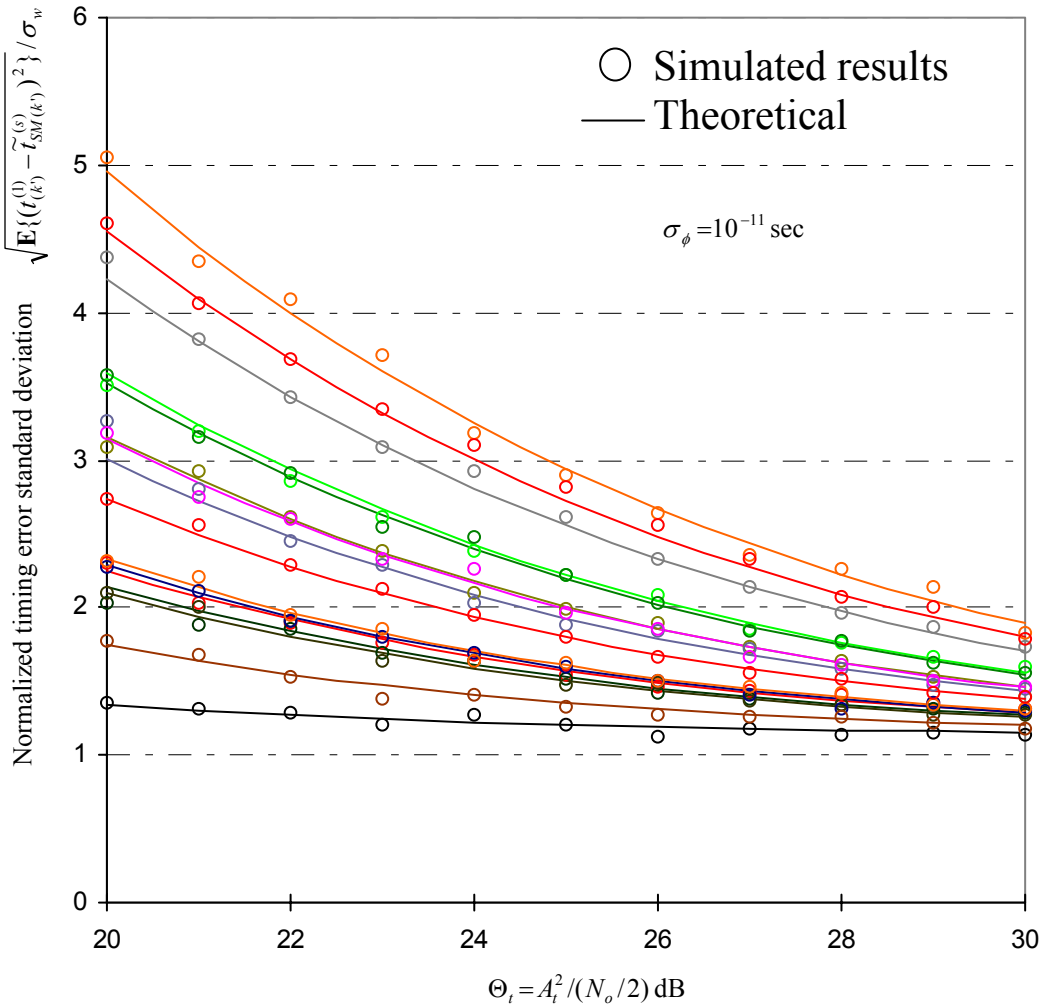

Figure E.5: Normalized timing error standard deviation after SM time transfer, i.e., there is no roving of master nodes and $t'=(2N-1)KT_f$. Here the standard deviation of the oscillator phase noise is $\sigma_\phi = 10^{-11}$ sec. Time transfer from node 1 to nodes 15, 17 and 20 is impaired by receiver measurement error (not shown in this figure). In this simulation, in order to verify the theoretical derivations, each network node is assumed to know the signal propagation distance from itself to all other nodes in the network. Results obtained using time-transfer scheme A.

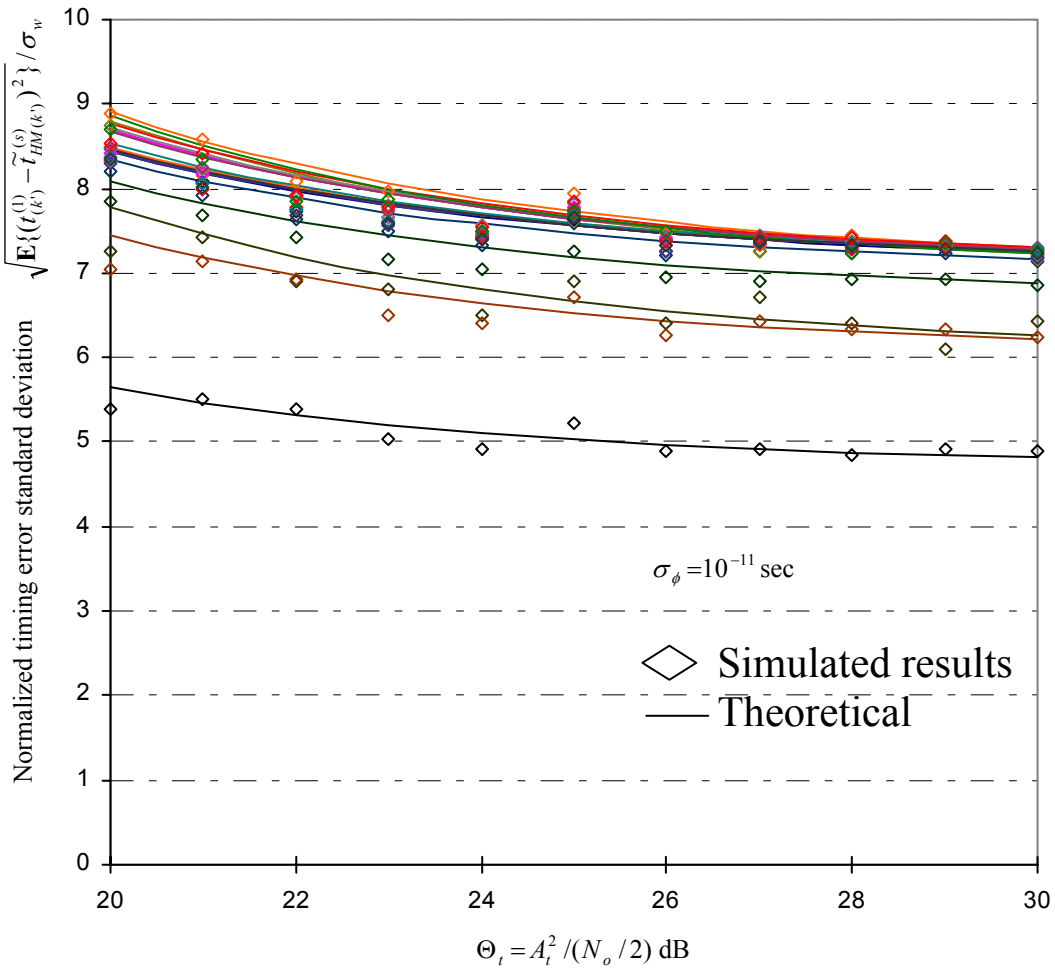

Figure E.6: Normalized timing error standard deviation after HM time transfer with 5 roving masters. The roving master nodes are $\mathbf{M} \in \{1,8,12,4,2\}$. Here the standard deviation of the oscillator phase noise is $\sigma_\phi = 10^{-11}$ sec and $t' = (2N-1)KT_f \cdot 5$. In this simulation, in order to verify the theoretical derivations, each network node is assumed to know the signal propagation distance from itself to all other nodes in the network. The theoretical formulation agrees with the simulation results. Results obtained using time-transfer scheme A.

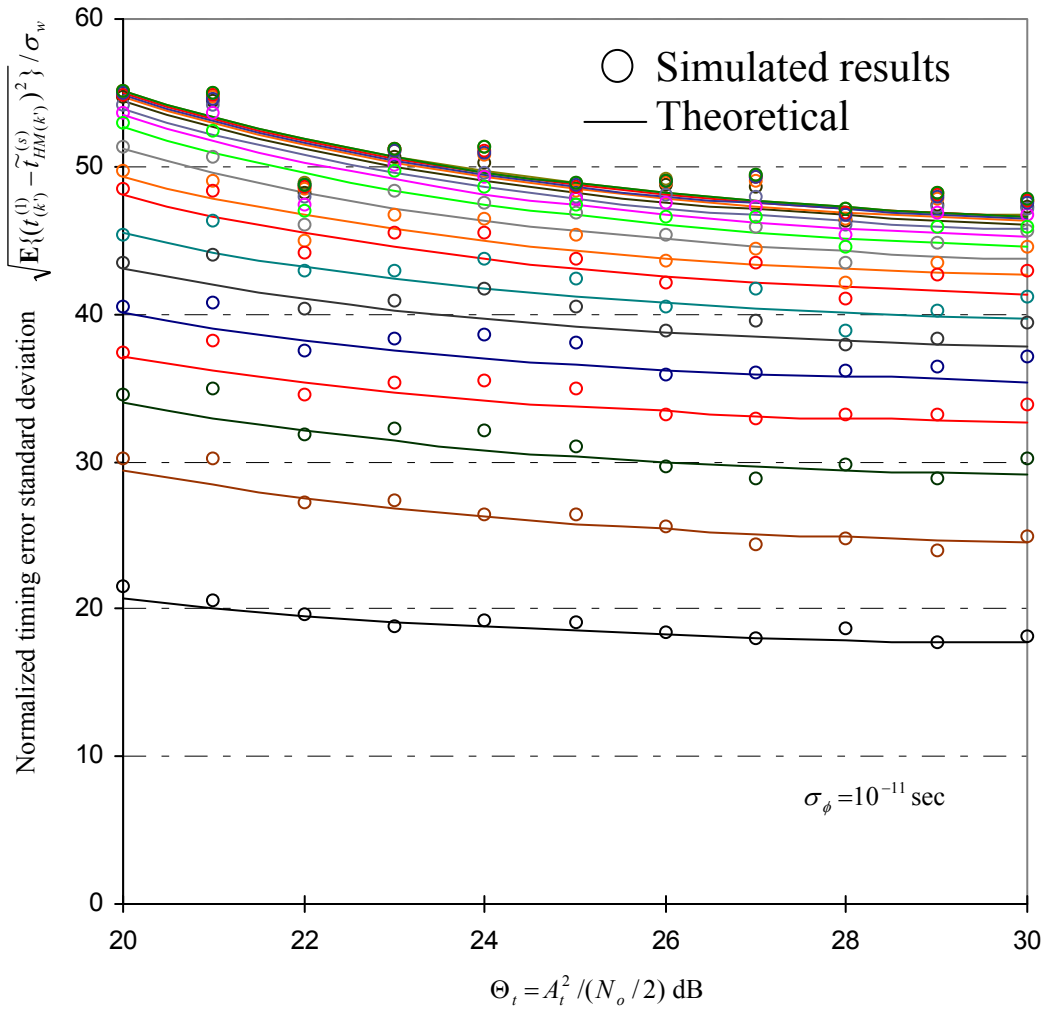

Figure E.7: Normalized timing error standard deviation after HM time transfer with 19 roving masters. The nodes take a turn as the roving master in the order: 1,8,12,4,2,6,20,17,18,9,13,16,11,10,5,7,15,14,19. And $t' = (2N-1)KT_f \cdot 19$. Here the standard deviation of the oscillator phase noise is $\sigma_\phi = 10^{-11}$ sec. In this simulation, in order to verify the theoretical derivations, each network node is assumed to know the signal propagation distance from itself to all other nodes in the network. The theoretical formulation agrees well with the simulation results. Results obtained using time-transfer scheme A.

APPENDIX F

SIMULATION RESULTS ON TIME-TRANSFER ERRORS USING TIME-TRANSFER SCHEME C

This appendix reports the timing errors of the SM, HM and MU time-transfer architectures obtained from simulation and using time-transfer scheme C. The simulation parameters are identical to those listed in Appendix C. The network topology is shown in Fig. C.1.

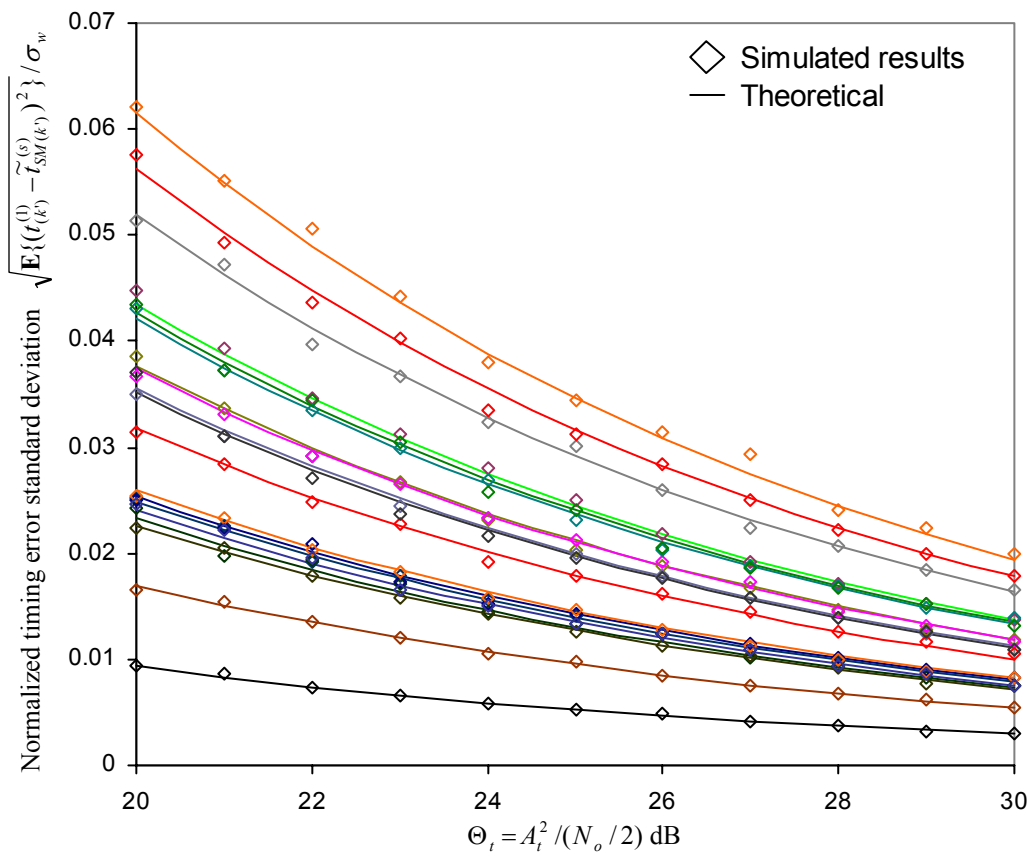

Figure F.1: Normalized standard deviation of timing error after SM time transfer. In this simulation no NLoS propagations are introduced, and $t' = (2N-1)KT_f$, $K = 1000$, $\sigma_\phi = 0$ and $\rho_L = 2$. In order to verify the theoretical derivations, each network node is assumed to know the signal propagation distance from itself to all other nodes in the network. Results obtained using time-transfer scheme C.

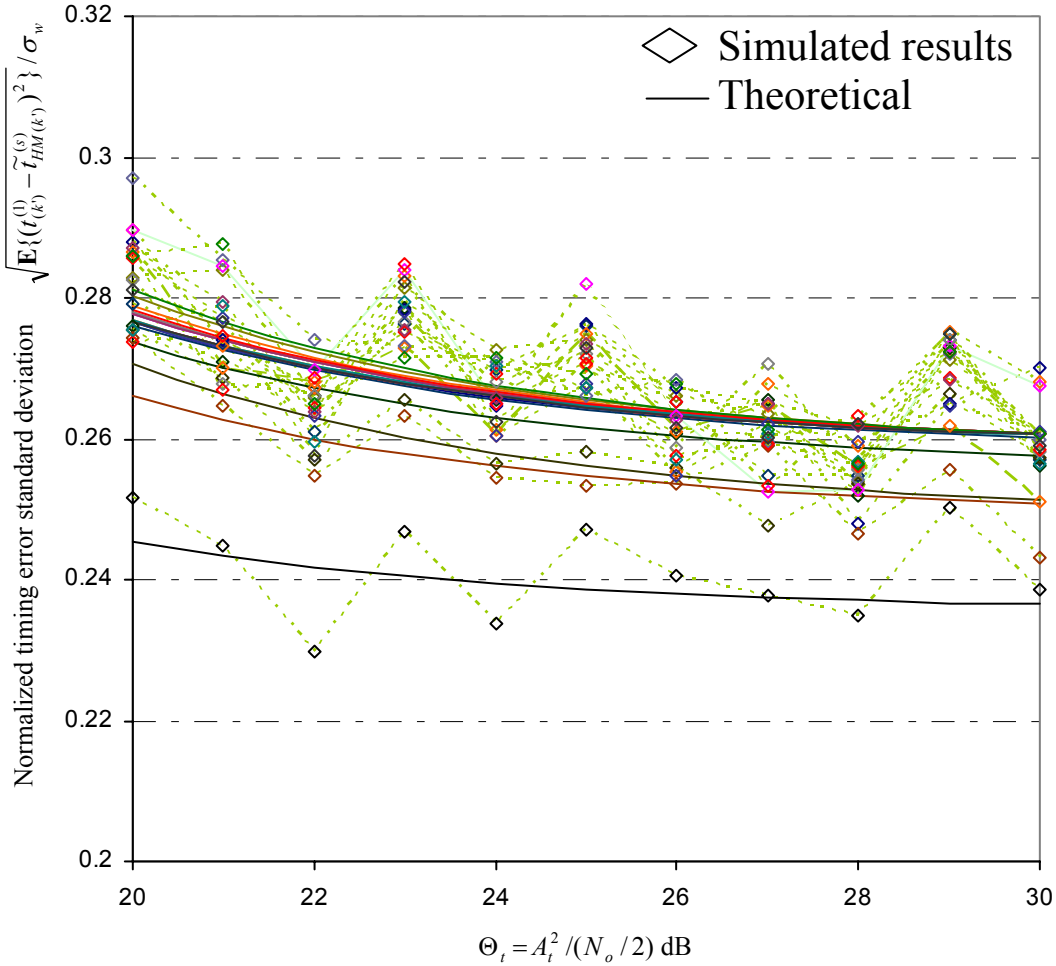

Figure F.2: Normalized timing error standard deviation after HM time transfer with 5 roving masters. The roving master nodes are $\mathbf{M} \in \{1,8,12,4,2\}$. The network nodes have no knowledge of the distances between themselves. Here $t' = (2N-1)KT_f \cdot 5$, $K = 1000$, $\sigma_\phi = 10^{-11}$ sec and $\rho_L = 2$ and no NLoS propagation is introduced. Results obtained using time-transfer scheme C and 2100 Monte Carlo steps.

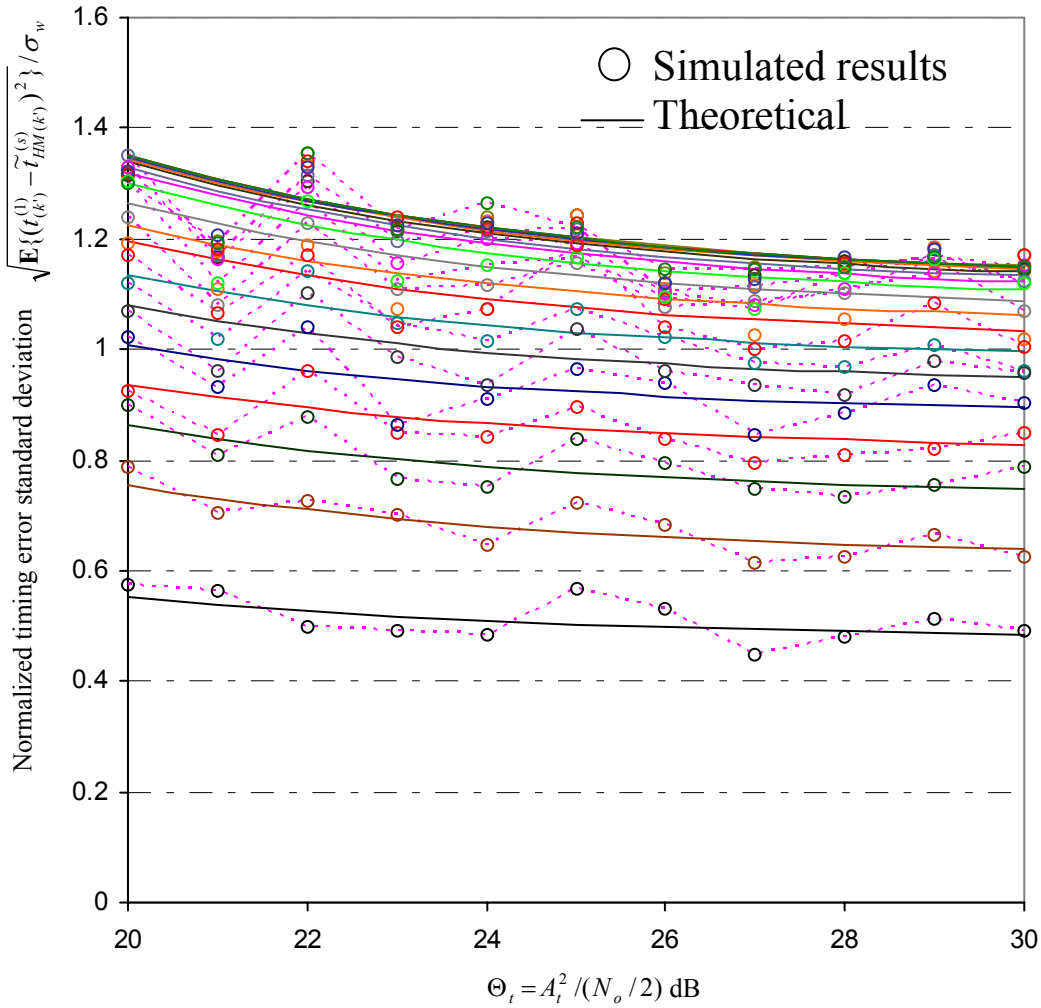

Figure F.3: Normalized timing error standard deviation after HM time transfer with 19 roving masters. The roving master nodes are $\mathbf{M} \in \{1,8,12,4,2,6,20,17,18,9,13,16,11,10,5,7,15,14,19\}$. Here $t' = (2N-1)KT_f \cdot 19$, $K = 1000$, $\sigma_\phi = 10^{-11}$ sec and $\rho_L = 2$ and no NLoS propagation is introduced. Results obtained using time-transfer scheme C and 200 Monte Carlo steps. In this simulation, in order to verify the theoretical derivations, each network node is assumed to know the signal propagation distance from itself to all other nodes in the network.

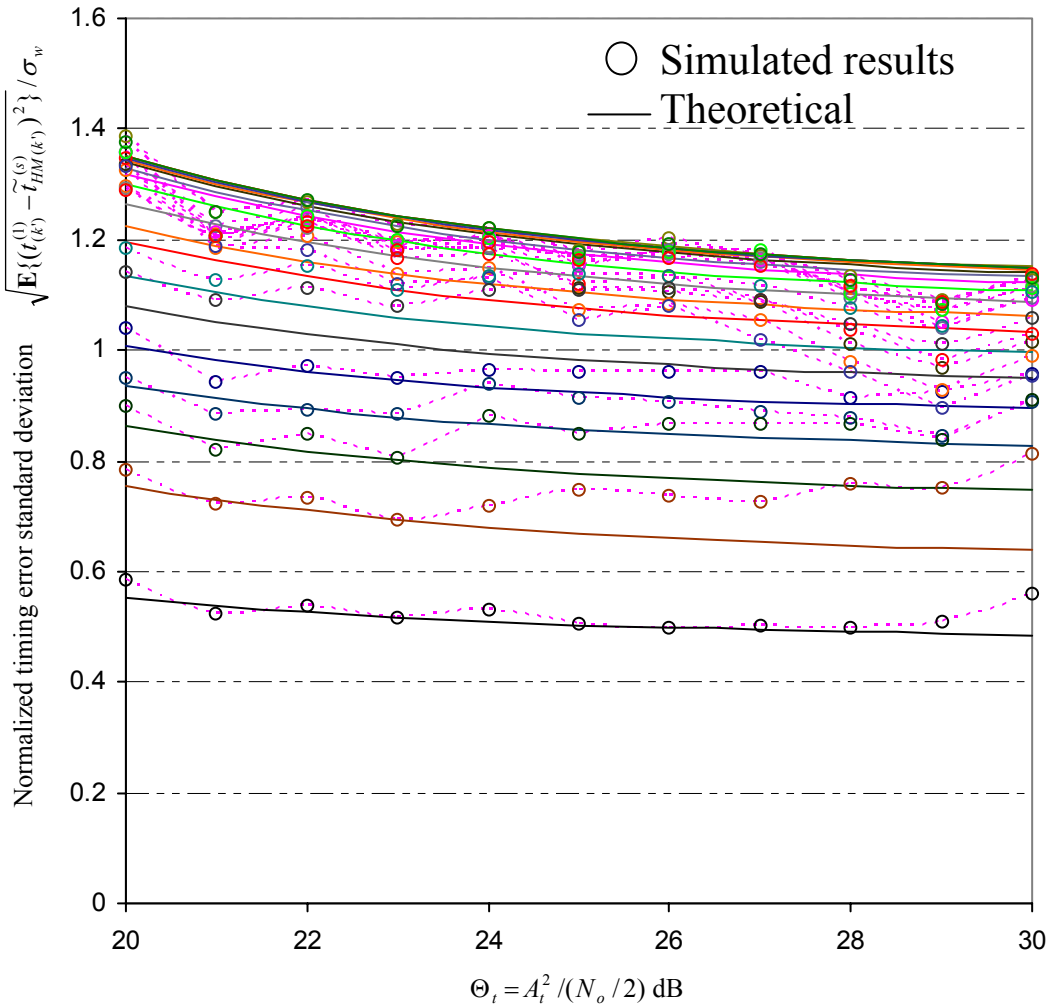

Figure F.4: Normalized timing error standard deviation after HM time transfer with 19 roving masters. The roving master nodes are $\mathbf{M} \in \{1,8,12,4,2,6,20,17,18,9,13,16,11,10,5,7,15,14,19\}$. The network nodes have no knowledge of the distances between themselves. Here $t' = (2N-1)KT_f \cdot 19$, $K = 1000$, $\sigma_\phi = 10^{-11}$ sec and $\rho_L = 2$ and no NLoS propagation is introduced. Results obtained using time-transfer scheme C and 1700 Monte Carlo steps.